UNIVERSITY OF SOUTHAMPTON

Faculty of Engineering and Physical Sciences
School of Physics & Astronomy

A Data-Driven Approach to Understanding Supernovae as Astrophysical Probes

DOI: 10.1002/0470841559.ch1???

Volume n of m

by

Tomás Enrique Müller Bravo
M.Sc. in Astrophysics
B.Sc. in Astronomy
ORCiD: 0000-0003-3939-7167

A thesis for the degree of
Doctor of Philosophy

January 2022

University of Southampton

Abstract

Faculty of Engineering and Physical Sciences
School of Physics & Astronomy

Doctor of Philosophy

A Data-Driven Approach to Understanding Supernovae as Astrophysical Probes

by Tomás Enrique Müller Bravo

Forthcoming time-domain surveys, such as the Rubin Observatory Legacy Survey of Space and Time, will vastly increase samples of supernovae (SNe) and other optical transients. This large stream of photometric data will allow the development and improvement of machine-learning techniques for analysing their light curves and provide a better understanding of these phenomena as astrophysical probes.

In this thesis, I present PISCOLA, an open-source data-driven/machine-learning light-curve fitter. Although PISCOLA can be used to estimate the rest-frame light curves of any transient, without the need for an underlying light-curve model, here I present an application to type Ia supernovae (SNe Ia) as distance indicators. I tested PISCOLA on simulations of SNe Ia to validate its performance, showing it successfully retrieves rest-frame peak magnitudes for average data qualities of current cosmological surveys. When compared to the existing light-curve fitter SALT2 on real data, I find small differences in the estimated light curve parameters.

I introduce an original analysis by decomposing the estimated rest-frame light curves of SNe Ia from the Pantheon sample with Non-Negative Matrix Factorization. This decomposition is used as a new way of standardising SNe Ia that provides similar scatter in the measured distances as SALT2. Additionally, I use PISCOLA to study the wavelength-dependent variation of colour in SNe Ia to have a better understanding of their intrinsic variation, finding no disagreement with the SALT2 model.

I also present the study of SN 2016aqf, a low-luminosity type II SN (LL SN II) with extensive photometric and spectral coverage. I use nebular (late-time) spectra to estimate a progenitor mass of $12 \pm 3\,M_{\odot}$, and measure the [Fe II] λ7155 and [Ni II] λ7378 lines, mainly found in LL SNe II, to estimate its Ni/Fe abundance ratio, a parameter sensitive to the inner progenitor structure and explosion mechanism dynamics. Placing this measurement in the context of a sample of SNe II, I find that the measured distribution of Ni/Fe abundance ratio does not agree with those predicted by theoretical modelling.

Contents

List of Figures

List of Tables

Declaration of Authorship

I declare that this thesis and the work presented in it is my own and has been generated by me as the result of my own original research.

I confirm that:

1. This work was done wholly or mainly while in candidature for a research degree at this University;
2. Where any part of this thesis has previously been submitted for a degree or any other qualification at this University or any other institution, this has been clearly stated;
3. Where I have consulted the published work of others, this is always clearly attributed;
4. Where I have quoted from the work of others, the source is always given. With the exception of such quotations, this thesis is entirely my own work;
5. I have acknowledged all main sources of help;
6. Where the thesis is based on work done by myself jointly with others, I have made clear exactly what was done by others and what I have contributed myself;
7. Claudia Gutiérrez obtained and reduced the photometric and spectroscopic data of SN 2016aqf.
8. Parts of this work have been published as: Müller-Bravo et al. (2020) and Müller-Bravo et al. (2021).

Signed:..... Date:.....

To my beloved wife Vicky, who accompanied and supported me throughout this tough journey. To my entire family who supported me from the distance, especially Erica and Patricio, my parents, and Nicolás, Maximiliano and Agustín, my brothers.

Acknowledgements

I would like to thank Mark Sullivan, my supervisor, and Mat Smith, who I consider as my second supervisor, for their guidance throughout my entire PhD and help developing PISCOLA.

To the entire Southampton+Portsmouth Supernova group, past and present members I shared my stay with: Mark, Mat, Claudia, Cosimo, Charlotte, Phil, Chris, Maria, Lizi, Miika, Lisa, Matt, Marcus and Zoe. Thanks for all the discussions, help and supports throughout these years. It was nice to know you and hope to continue sharing moments with you in the future.

To the friends I have made as part of my stay in the UK: Noel, Lore, Paula, Javier, Felipe, David, Romi and Vale, to name just a few. Thank you for all the trips, adventures, beers and asados we shared together. I am looking forward to repeating all of this in the future.

To those in the Southampton Astronomy department whose company I enjoyed and shared more than a few pints with: Noel, Lorenzo, Claudia, Miika, Kevin, Mayukh, Daniel, Federico, Jakub, Alex and several others. Thank you for your friendship. More pints will come in the future.

To my friends in Chile and those who I have met as part of my career in Astronomy but are scattered around the world. Thank you for the time we have shared (remotely and in person). Fate will get us together again.

To Jules, Root and Cisco (RIP). Thanks for sharing your house with two complete strangers, a place I can call home.

My PhD was funded by the CONICYT PFCHA/DOCTORADOBECAS CHILE/2017-72180113.

Abbreviations

AB	**AB**solute
ASASSN	**A**ll-**S**ky **A**utomated **S**urvey for **S**uper**N**ovae
BAO	**B**aryon **A**coustic **O**scillation
BH	**B**lack **H**ole
CANDELS	**C**osmic **A**ssembly **N**ear-infrared **D**eep **E**xtragalactic **L**egacy **S**urvey
CCSN	**C**ore-**C**ollapse **S**uper**N**ova
CfA	**C**enter **f**or **A**strophysics
CL	**C**olour-variation **L**aw
CLASH	**C**luster **L**ensing **A**nd **S**upernova Survey with **H**ubble
CSM	**C**ircum**S**tellar **M**aterial
CSP	**C**arnegie **S**upernova **P**roject
DES	**D**ark **E**nergy **S**urvey
ECSN	**E**lectron-**C**apture **S**uper**N**ova
EFOSC2	**E**SO **F**aint **O**bject **S**pectrograph and **C**amera version **2**
ePESSTO	**e**xtended **P**ublic **E**SO **S**pectroscopic **S**urvey of **T**ransient **O**bjects
ESO	**E**uropean **S**outhern **O**bservatory
EW	**E**quivalent **W**idth
FLRW	**F**riedmann-**L**emaître-**R**obertson-**W**alker
FTS	**F**aulkes **T**elescope **S**outh
FWHM	**F**ull-**W**idth at **H**alf **M**aximum
GOODS	**G**reat **O**bservatories **O**rigins **D**eep **S**urvey
GP	**G**aussian **P**rocess
HR	**H**ubble **R**esidual
HST	**H**ubble **S**pace **T**elescope
Ia	type **Ia**
Ib	type **Ib**
Ic	type **Ic**
II	type **II**
II-L	type **II L**inear
II-P	type **II P**lateau
IR	**I**nfra**R**ed
LL	**L**ow **L**uminosity

LSST	**L**egacy **S**urvey of **S**pace and **T**ime
MCMC	**M**arkov **C**hain **M**onte **C**arlo
MJD	**M**odified **J**ulian **D**ay
MW	**M**ilky **W**ay
NED	**N**ASA/IPAC **E**xtragalactic **D**atabase
NGC	**N**ew **G**eneral **C**atalogue of nebulae and clusters of stars
NIR	Near **I**nfra**R**ed
NMF	**N**on-negative **M**atrix **F**actorization
NS	**N**eutron **S**tar
NTT	**N**ew **T**echnology **T**elescope
Pan-STARRS	**Pan**oramic **S**urvey **T**elescope **A**nd **R**apid **R**esponse **S**ystem
PCA	**P**rincipal **C**omponent **A**nalysis
PISCOLA	**P**ython for **I**ntelligent **S**upernova-**CO**smology **L**ight-curve **A**nalysis
PS1	**P**an-**S**TARRS Data Release **1**
PSF	**P**oint-**S**pread-**F**unction
r.m.s	**r**oot-**m**ean-**s**quare
RSS	**R**obert **S**tobie **S**pectrograph
S/N	**S**ignal-to-**N**oise ratio
SALT	**S**outhern **A**frican **L**arge **T**elescope (only used in Chapter 7)
SALT	**S**pectral **A**daptive **L**ight-curve **T**emplate
SALT2	**S**pectral **A**daptive **L**ight-curve **T**emplate **2**
SDSS	**S**loan **D**igital **S**ky **S**urvey
SED	**S**pectral **E**nergy **D**istribution
SFR	**S**tar-**F**ormation-**R**ate
SN	**S**uper**N**ova
SNLS	**S**uper**N**ova **L**egacy **S**urvey
UV	**U**ltra**V**iolet
WD	**W**hite **D**warf
ZAMS	**Z**ero **A**ge **M**ain **S**equence
ZP	**Z**ero**P**oint
ZTF	**Z**wicky **T**ransient **F**acility

Chapter 1

Introduction

1.1 Supernovae

Supernovae (SNe) are extremely energetic explosions and the ultimate fate of many stars in the universe. These phenomena, as we know them today, have been studied for almost a hundred years (since the early 1930s), with Fritz Zwicky and Walter Baade some of the first to address this field (Baade & Zwicky, 1934b,a,c), giving birth to the word "supernova" (introduced by Lundmark 1932). However, there are records of these events that are hundreds to thousands years old (e.g., SN 1054; Chevalier, 1977) as their relatively high luminosity and variation on human time scales make them relatively easy to observe.

The light curves (evolution of the luminosity as a function of time) of SNe are powered in a small part by the shock (explosion) energy, but mostly by the radioactive decay of ^{56}Ni. This element is produced in the explosion and decays into ^{56}Co (via β^+-decay), with a half-life of 6.1 days, which subsequently decays into ^{56}Fe (via electron capture and β^+-decay), with a half-life of 77.7 days (Colgate & McKee, 1969; Arnett, 1979). The radioactive decay produces a large amount of γ-rays and positrons, prior to peak light, which are then trapped within the ejecta and then reprocessed into longer-wavelength photons (e.g., ultraviolet, optical, infrared), producing the full electromagnetic spectrum. The extreme conditions found in the inside of the SN event produce explosive nucleosynthesis, where a large portion of the elements produced during the stellar nucleosynthesis (Burbidge et al., 1957; Arnett, 1978) gives birth to intermediate-mass and iron-group elements (e.g., Arnett & Clayton, 1970; Woosley et al., 1973), but also leads to the synthesis of neutron-rich heavy isotopes through the *r*-process (e.g., Sumiyoshi, 2002; Cowan & Thielemann, 2004).

SNe light curves go through two main phases: the *photospheric* (optically thick) phase and *nebular* (optically thin) phase. The former covers the first part of the light-curve

evolution, including peak luminosity, and is characterised by spectra dominated by broad absorption lines, produced by the outer, thicker ejecta layers, with high expansion velocities. The latter phase starts during the ^{56}Co exponential-decay tail and is characterised by spectra dominated by narrow emission lines, produced by the inner layers of the ejecta, when the outer layers have already diffuse into the surroundings. The time of transition between the photospheric phase and nebular phase is not strictly defined as there is a smooth transition between both phases. Additionally, it depends on the characteristics of each SN (e.g., explosion physics, progenitor).

The typical bolometric (total radiation emitted across all wavelengths of the electromagnetic spectrum) luminosity of these events is of the order of 10^{43}erg s^{-1} ($\sim 10^{9}$–10^{10}L$_{\odot}$, comparable to the luminosity of the host galaxy), while the total energy is of the order of 10^{51} erg (unit equivalent to 1 Bethe or 1 foe); $\sim$ 99 per cent kinetic energy and $\sim$ 1 per cent (10^{49} erg) radiation energy. Their peak luminosity is approximately proportional to the amount of ^{56}Ni synthesised as it is the main power source of the light curve (Arnett's rule; Arnett 1982; although see Khatami & Kasen 2019).

The study of SNe has been mainly focused at optical wavelengths ($\sim 4000 - 7000$ Å), where they are brightest, concentrating $\gtrsim$ 80 per cent of the total luminosity, and easiest to observe from the ground.

SNe come in many different flavours, given by the wide variety of progenitor stars they can have. The first classification was introduced by Minkowski (1941) who designated two main groups: Type II SNe, events with signatures of hydrogen (e.g., H I λ6563/Hα; the ionisation nomenclature is 'I' for neutral elements, 'II' for singly ionised, etc.), and Type I SNe, as those without hydrogen.

This classification has since evolved with new sub-types, adapting to the ever evolving field and our increasing understanding of these phenomena. Elias et al. (1985) coined the terms Type Ia SNe for the dominant group of Type I events, showing signatures of Si II (e.g., Si II λ6355), and Type Ib SNe, showing signatures of He I (e.g., He I λ5876, He I λ6678 and He I λ7065; Harkness et al., 1987). Wheeler & Harkness (1990) introduced the term Type Ic SNe for a subgroup of Type Ib SNe without signatures of He I. Type II SNe were initially sub-divided by the properties of their optical light curves by Barbon et al. (1979): those showing a prominent plateau (II-P) and those with a fast, linear decline (II-L), although a whole continuum has been found between both sub-types (e.g., Anderson et al., 2014; Sanders et al., 2015).

Other sub-types were later introduced: SNe IIb, transitioning from a H-rich early spectra to SNe Ib-like He-dominated spectra within a few weeks of explosion (Filippenko, 1988), and SNe IIn, showing relatively narrow emission lines of H attributed to circumsetallar interaction (Schlegel, 1990). The classification in types can sometimes be unclear and has led to, for instance, SNe Ib and SNe Ic sometimes being combined into

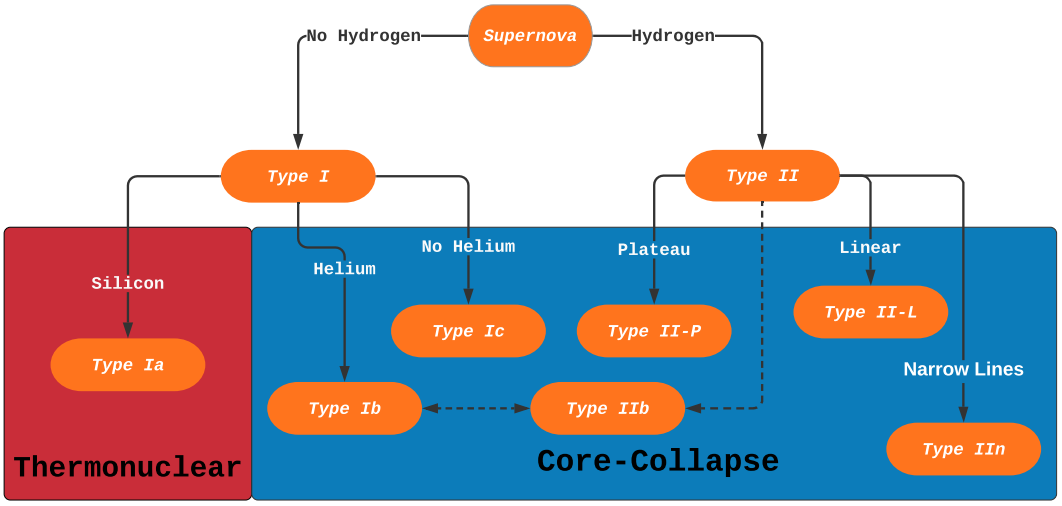

FIGURE 1.1: General classification of SNe. Types are mainly divided according to the presence or absence of certain chemical elements in their spectrum around the time of peak brightness. Classification of SNe II into II-P and II-L is based on light-curve shape. Most SN types belong to the core-collapse class (massive star progenitors), while only a subset belong to the thermonuclear class (WD progenitors. See Figure 1.3 for the intrinsic rates of SNe.

a single SNe Ib/c type. For a classical review on SN classification, see Filippenko (1997) and for a more recent review see Gal-Yam (2017).

The classification of these objects is not only limited to their observables, but also the physics driving their explosions, where we distinguish two main classes: core-collapse (CC) SNe and thermonuclear SNe. In Figure 1.1, I present a chart summarising the main types and classes of SNe.

1.1.1 Core-Collapse Supernovae

As the name suggests, CCSNe are produced by the rapid collapse of the Fe core of massive stars, with a Zero-Age Main Sequence mass $M_{ZAMS} \gtrsim 8\,M_{\odot}$, when the electron degeneracy is no longer sufficient to counter the gravitational compression. These stars release $\sim 10^{53}$ erg of gravitational potential energy in the form of neutrinos during their collapse, from which $\sim$ 1 per cent is deposited in the ejecta layers, powering a CCSN explosion (e.g., Colgate & White, 1966; Arnett, 1966; Bethe & Wilson, 1985; Janka, 2017), leaving behind a core that either turns into a neutron star (NS) or a black hole (BH; e.g., Baade & Zwicky, 1934b; Burrows & Lattimer, 1986; Ugliano et al., 2012; Pejcha & Thompson, 2015; Ertl et al., 2016; Sukhbold et al., 2016). Kochanek (2014) estimates that, in order to have an agreement between simulations and observations, ∼20 per cent of massive stars might fail to explode as CCSNe and instead collapse to a BH with no or negligible electromagnetic display.

The neutrino heating mechanism is the leading theory in explaining the explosion mechanism in CCSNe (e.g., Woosley et al., 2002; Pejcha & Thompson, 2012; Sukhbold et al., 2016). It introduces neutrinos as a source of energy that helps reproduce the explosion in SN simulations (e.g., Janka & Mueller, 1996; Janka, 2001; Couch, 2017). One of the main evidences in favour of this theory is the type II SN 1987A, in the Large Magellanic Cloud (the closest SN observed in the last few centuries), the only stellar collapse with detections of neutrinos (Hirata et al., 1987; Bionta et al., 1987; Alekseev et al., 1987, 1988).

Different mechanisms contribute to the light curves of CCSNe. In here, I will only present those in common to all CCSNe. The mechanisms are summarised in Figure 1.2 and described below:

- *Shock breakout*: before any electromagnetic emission emerges, a shock is created by the rebound of in-falling material on the newly formed proto-NS and propagates through the envelope, depositing mechanical and thermal energy, until it reaches the surface of the star, briefly emitting, on time scales of seconds to a fraction of an hour, X-ray and UV radiation (e.g., Falk & Arnett, 1977; Klein & Chevalier, 1978; Waxman et al., 2007; Waxman & Katz, 2017).
- *Shock cooling and ejecta recombination*: after shock breakout, the heated and ionised ejecta cools due to the emission radiation (diffusion cooling) and the expansion of the ejecta (adiabatic cooling). This also triggers the recombination of the ejected layers (e.g., H and He layers in the case of SNe II and Ib, respectively).
- *Radioactive decay*: the shock also produces synthesis of heavy elements, some of which decay and radiate (Arnett, 1980, 1982), with ^{56}Ni the main radioactive product. The decay of ^{56}Ni into ^{56}Co and then ^{56}Fe powers the late-time light curve of most SNe (alternative powering mechanisms are out of the scope of this thesis).

The main exponents of this class of SNe are the H-rich type II and H-poor type Ib/c (also referred to as striped-envelope) SNe. The progenitors of SNe II-P have been observed to be red supergiants (e.g., Smartt, 2009, 2015), while type II-L, IIn and some peculiar type II SNe (e.g., SN 1987A) are associated to stars such as yellow supergiants (e.g., Elias-Rosa et al., 2010), blue supergiants (e.g., Podsiadlowski, 1992) and luminous blue variables (e.g., Gal-Yam et al., 2007), respectively, although their progenitor populations are still unclear. Type Ib/c SNe are associated to more massive stars, such as Wolf-Rayet stars (e.g., Groh et al., 2013; Gal-Yam et al., 2014).

In Figure 1.3), I show the observed and (estimated) intrinsic rates of different types of SNe, taken from Li et al. (2011). SNe II are the most common type (>50 per cent, Figure 1.3) of all SNe (e.g., Li et al., 2011; Shivvers et al., 2017) due to the nature of their

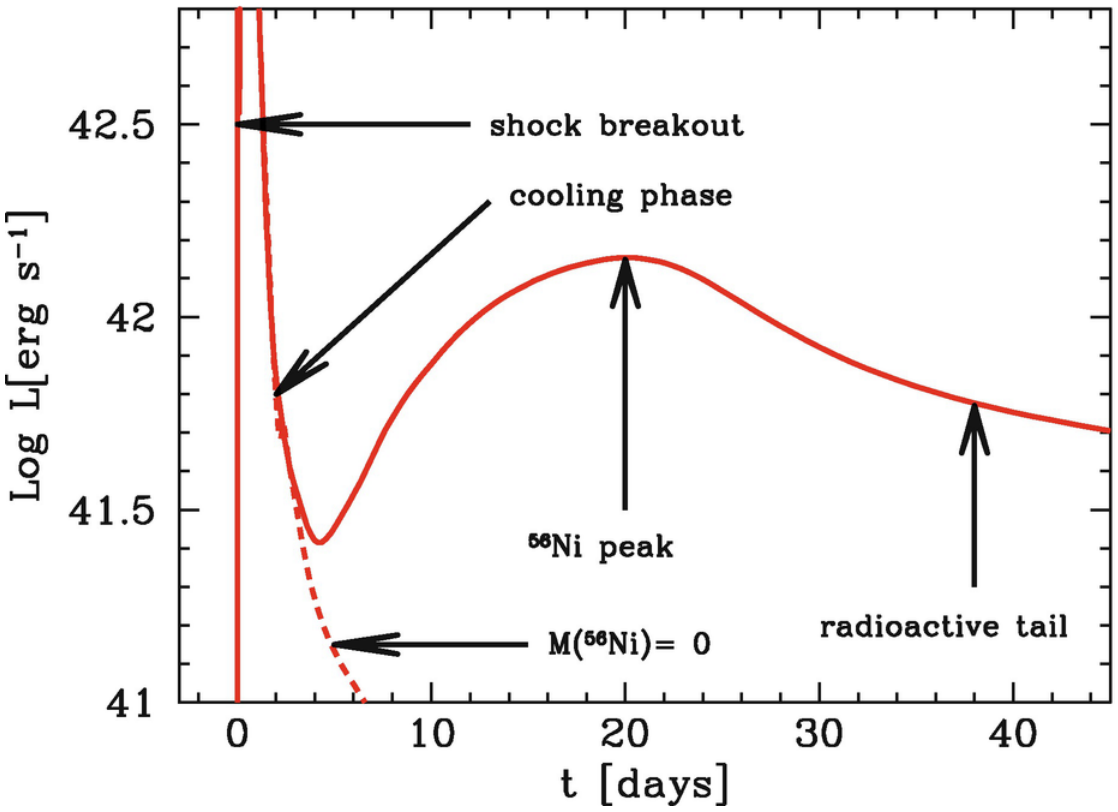

FIGURE 1.2: This figure is taken from Bersten & Mazzali (2017) and summarises the mechanisms that contribute to the bolometric light curve a SN I calculated using a hydrodynamical code (Bersten et al., 2011).

progenitors, being close to the lower end of the mass range of the initial mass function, thus being intrinsically a larger population (e.g., Salpeter, 1955; Kroupa, 2001; Kroupa et al., 2013), while SNe Ib/c are only ∼20 per cent of all SNe and approximately 25 per cent of all CCSNe (see Figure 1.3).

The ^{56}Ni yields and optical light curves of SNe are important as they help characterise and understand the physics of SNe in general. Type II SNe produce on the order of $10^{-3} - 10^{-1}$ M$_\odot$ of ^{56}Ni (e.g., Hamuy, 2003; Spiro et al., 2014; Müller et al., 2017; Anderson, 2019), while SNe Ib/c produce around an order of magnitude more (e.g., Prentice et al., 2016; Taddia et al., 2018; Anderson, 2019).

In Figure 1.4, I show examples of V-band light curves of different types of CCSNe. The optical light curves of SNe II-P present a large diversity, reaching peak luminosity in ∼4–17 days after explosion (e.g., González-Gaitán et al., 2015) and displaying a plateau which lasts ∼70–120 days (e.g., Anderson et al., 2014, see Figure 1.4), before transitioning to the exponential-decay tail, with an approximate drop of 0.98 mag per 100 days, assuming full γ-ray trapping (Woosley et al., 1989). This plateau is produced by the recombination of hydrogen, initially ionised by high energy γ-rays and positrons. On the other hand, the optical light curves of SNe II-L, Ib and Ic display faster declines due

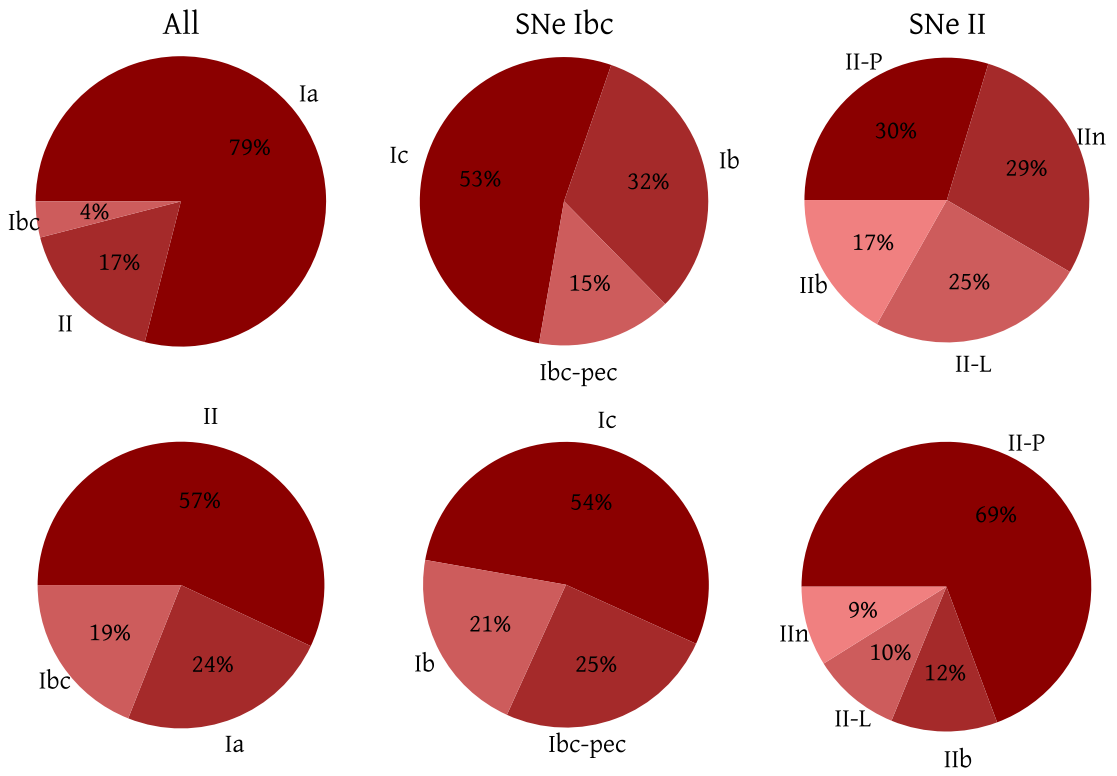

FIGURE 1.3: Observed (**top** row) and (estimated) intrinsic (**bottom** row) rates for all (*left* column), type Ib/c (*middle* column) and type II SNe (*right* column). This figure is adapted from Figures 7 & 9 in Li et al. (2011). Note that the values in some of the charts from the original figures do not add to 100 per cent, so I slightly modified these for visualisation (this does *not* affect the rates in any significant way at all).

to the lack of thick H or He envelopes, which produces shorter and steeper recombination phases (see Figure 1.4). The V-band average peak absolute magnitudes of SNe II, Ib and Ic are -16.7 ± 1.0 mag, -17.1 ± 0.6 mag and -17.6 ± 0.2 mag, respectively (Anderson et al., 2014; Taddia et al., 2018).

In Figure 1.5, I show examples of spectra of the different types of CCSNe. These show distinct features for the different types. The spectra of SNe II during the plateau phase present H I (Balmer series) with clear P Cygni line profiles (Oke, 1974) and Fe II λ4924, Fe II λ5108, Fe II λ5169 lines (see Figure 1.5). During the nebular phase (several months after explosion), the spectra become dominated by relatively narrow emission lines, and new forbidden spectral lines appear, such as the [Ca II] $\lambda\lambda$7291, 7323 and [O I] $\lambda\lambda$6300, 6364 doublets.

As a note, the nomenclature for spectral lines is λ for singlets, $\lambda\lambda$ for doublets, etc., produced due to electron spin. The two square brackets (e.g., [Ca II]) refer to *forbidden* lines, which are lines not observed in the 'laboratory spectra' on Earth as they are highly improbable. Elements with one square bracket (e.g., Mg I]) denote *semi-forbidden* lines.

[1] https://sne.space/

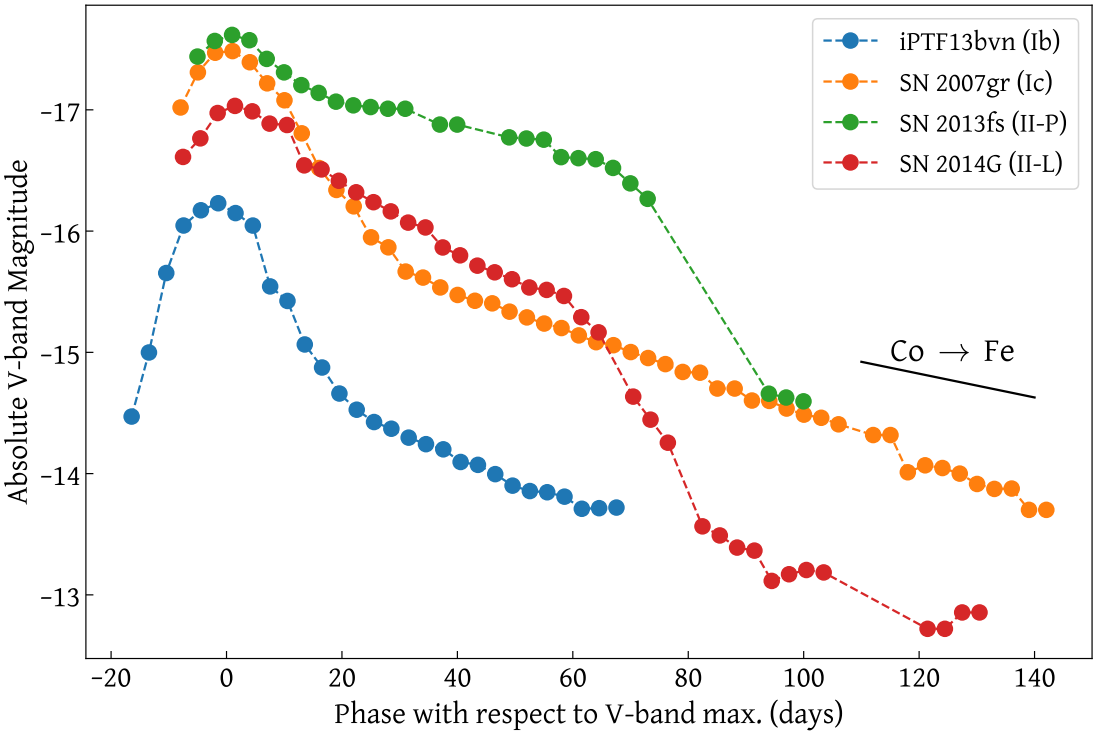

FIGURE 1.4: V-band light curves of different types of CCSNe: SN 2007Y (Ib; Cao et al., 2013), SN 2007gr (Ic; Hunter et al., 2009), SN 2004et (II-P; Sahu et al., 2006; Maguire et al., 2010) and SN 1980K (II-L; Buta, 1982). SN 2004et shows the characteristic plateau of its type produced by the H recombination. SN 1980K shows a more rapid decline into the radioactive decay tail than SN 2004et. SN 2007Y and SN 2007gr show light curves with faster decline rates than the former. The light curves of some SNe Ib/c have relatively similar shape to those of SNe Ia (SNe Ic even have similar brightness). The ^{56}Co $\rightarrow$ ^{56}Fe decay is shown as a reference. Data taken from the Open Supernova Catalog[1](OSC).

The photosphere is the surface at which the optical depth reaches a value of 2/3. It is of great importance as it is where most of the light is emitted and where the continuum of the spectral energy distribution (SED) is formed (Hubeny & Mihalas, 2014). For SNe II, the expansion velocity of the photosphere is measured from the absorption minima of the Fe II λ5169 line, a good tracer of it (Hamuy et al., 2001). The expansion velocity reaches values of $\sim$10000 km s^{-1} around peak luminosity and drops to a few 1000 km s^{-1} during the exponential decay tail as we are looking deeper into the ejecta.

Type Ib and Ic have relatively similar spectra, showing lines such as Mg II, Ca II and Si II around peak luminosity. However, the main difference is that SNe Ib show He I lines, while SNe Ic do not. During the nebular phase, SNe Ib/c present lines such as the [Ca II] $\lambda\lambda$7291, 7323 and [O I] $\lambda\lambda$6300, 6364 doublets, but also other lines not found or not commonly detected in SNe II (e.g., Mg I] λ4571). The expansion velocities of the photosphere of SNe Ib/c are relatively similar to SNe II, with some SNe Ic having relatively larger velocities of $\sim$15000 km s^{-1} around peak luminosity (e.g, Taddia et al., 2018; Prentice et al., 2019).

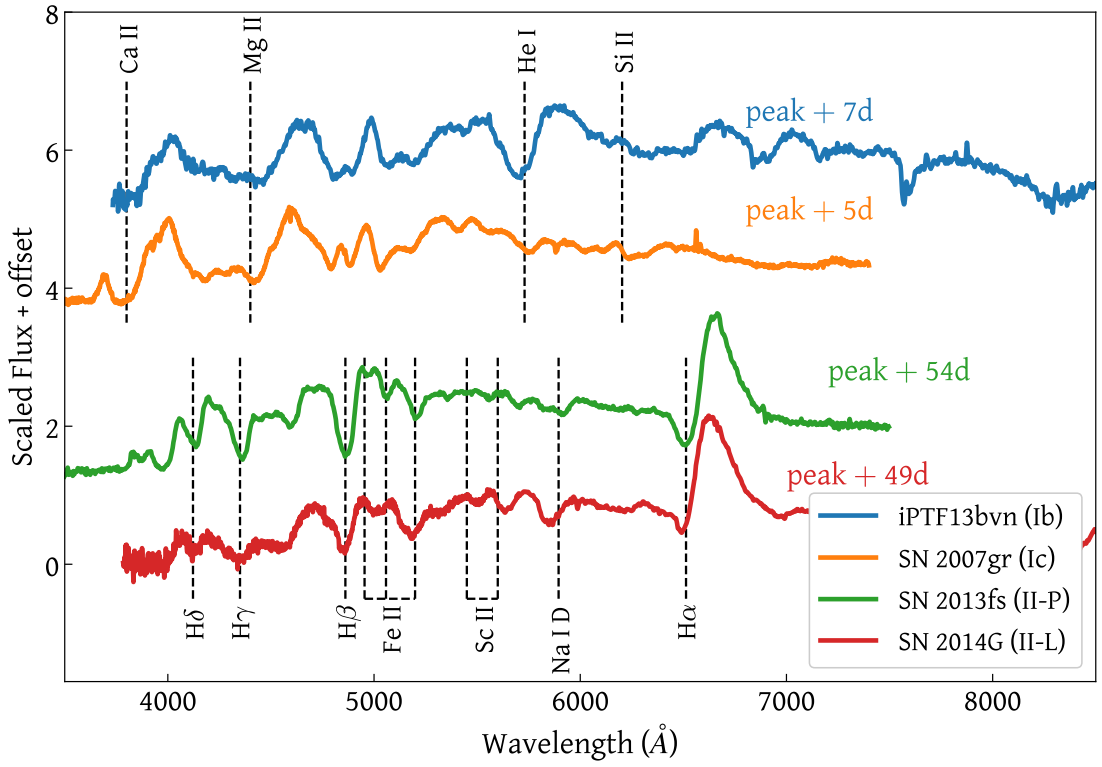

FIGURE 1.5: A series of spectra of different types of CCSNe: SN 2007Y (Ib; Cao et al., 2013), SN 2007gr (Ic; Hunter et al., 2009), SN 2004et (II-P; Sahu et al., 2006; Maguire et al., 2010) and SN 1980K (II-L; Buta, 1982). The vertical dashed lines mark the positions of their characteristic spectral lines, labelled with their respective names. The spectra of the H-poor SNe (2007Y and 2007gr) are around peak brightness in the V band, while the spectra of the H-rich SNe (2004et and 1980K) are several weeks after peak brightness in the V band (roughly mid plateau), when they present many of the characteristic spectral lines of their respective types. Data taken from the OSC.

Theoretical studies have shown that the nebular [O I] $\lambda\lambda$6300, 6364 doublet is a good tracer of the progenitor core mass of CCSNe, and, therefore, of the progenitor ZAMS mass (e.g., Jerkstrand et al., 2012, 2014, 2018, hereafter J12, J14 and J18; and some other studies as well, e.g., Mazzali et al. 2010; Lisakov et al. 2017, 2018), making the late-time spectral evolution extremely important for the study of SN progenitors. Furthermore, nebular nucleosynthesis diagnosis is so far consistent with the lack of massive progenitors above $\sim$18 $M_\odot$ for SNe II found by Smartt (2015) from observational constraints (e.g., J14, Valenti et al. 2016). In addition to the study of the nebular [O I] $\lambda\lambda$6300, 6364 doublet as a progenitor mass estimator, the Ni/Fe abundance ratio, measured from the [Fe II] λ7155 and [Ni II] λ7378 lines, mainly found in SNe II, has been shown to be important for the understanding of the inner structure of the progenitor and the explosion mechanism dynamics, as the observed iron-group yields are linked to the temperature, density and neutron excess of the layers that become fuel for the rapid burning process of the explosion (Jerkstrand et al., 2015b,a, hereafter J15a, J15b). However, there are few studies of this ratio, mainly due to the lack of late-time spectra and the absence of these features in the available data in the literature.

Several (spectroscopic) sub-divisions of CCSNe have appeared with time, such as SNe Ibn (e.g., Pastorello et al., 2007), which are Ib-like events with narrow lines produced by interaction, and broad-line SNe Ic (Ic-BL; e.g., Mazzali et al., 2002; Gal-Yam et al., 2002; Foley et al., 2003), with broad spectral features, showing the complexity of the SN population; however, these are not discussed in this thesis.

1.1.2 Thermonuclear Supernovae

Thermonuclear SNe are known to come from C/O white dwarfs (WDs; e.g., Hoyle & Fowler, 1960; Woosley et al., 1986; Nomoto et al., 1984; Hoeflich et al., 1996; Hillebrandt & Niemeyer, 2000; Bloom et al., 2012; Maoz et al., 2014) in a binary system with a non-degenerate companion star (single-degenerate scenario; e.g., Webbink, 1984; Iben & Tutukov, 1984), or another WD (double-degenerate scenario; e.g., Whelan & Iben, 1973). These explosions are produced by the ignition of carbon fusion as the WD approaches the *Chandrasekhar* mass limit, $M_{\rm Ch} \sim 1.4\,{\rm M}_{\odot}$. However, many other alternative theoretical models exist that can help explain thermonuclear SNe, such as sub-Chandrasekhar, super-Chandrasekhar and core-degenerate models (e.g., Fink et al., 2007, 2010; Sim et al., 2010; Howell et al., 2006; Hicken et al., 2007; Scalzo et al., 2010; Kashi & Soker, 2011; Ilkov & Soker, 2012).

Shortly after the initiation of nuclear fusion, a large fraction of the matter in the WD undergoes a runaway reaction, releasing immense amounts of energy, unbinding the star in a thermonuclear explosion. These SNe are the main producers of Fe-group elements and therefore, contribute to the chemical evolution of the universe (e.g., Nomoto et al., 1997; Seitenzahl & Townsley, 2017). The mechanisms that contribute to the light curve of SNe Ia are the same as those described for CCSNe: shock breakout, shock cooling and ejecta recombination, and radioactive decay. There are several explosion scenarios that try to explain the initial explosion mechanism of SNe Ia and until shock breakout, which occurs in a different manner than for CCSNe. Some involve deflagration (subsonic wave front), detonation (supersonic wave front) or a combination of both. However, the shock breakout in SNe Ia is still under debate as specific conditions need to be met by the explosion mechanism. High cadence and deep observations can be key in discerning between the different models and the presence of shock breakout in these SNe (see, e.g., Piro et al., 2010). For reviews on the different explosion models, see Nomoto et al. (2003); Höflich et al. (2013).

Thermonuclear SNe are the most commonly observed class ($\gtrsim$ 80 per cent, see Figure 1.3) in magnitude-limited surveys (which most surveys are), such as the Zwicky Transient Facility (ZTF; Perley et al., 2020) and Dark Energy Survey (DES; Smith et al., 2020), due to their intrinsically high average luminosity. The main exponent of this class are SNe Ia, representing $\sim$ 70 per cent of all thermonuclear SNe (e.g., Li et al., 2011), and will be the main focus of this thesis hereon.

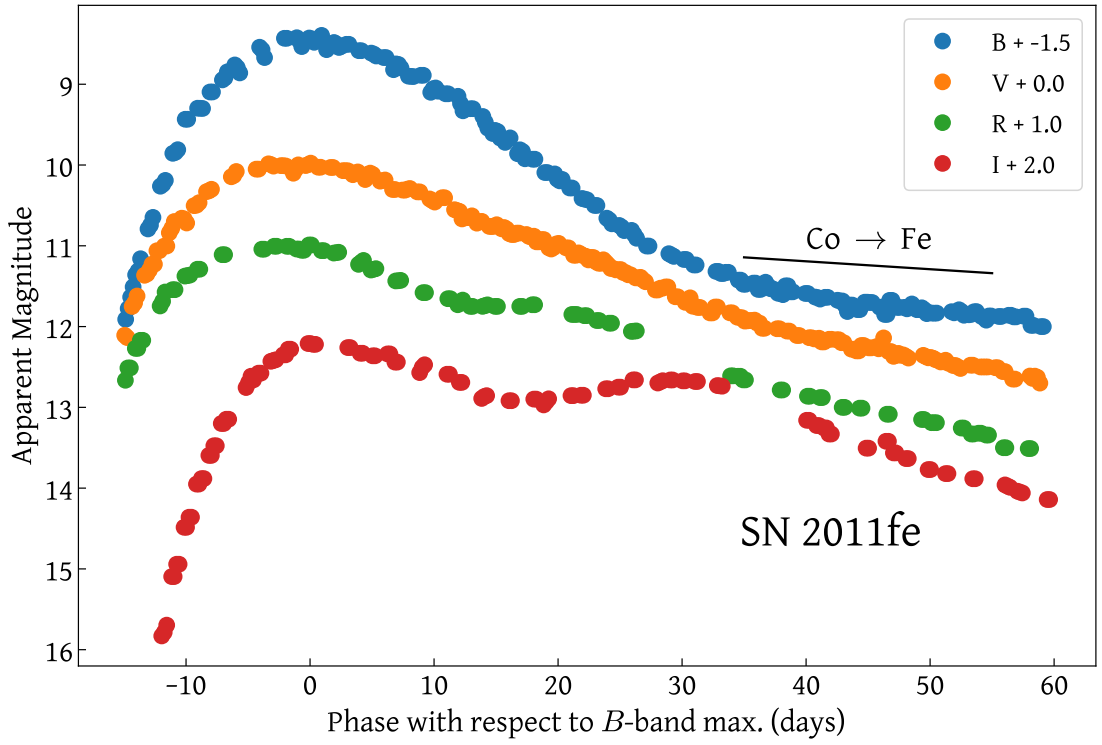

FIGURE 1.6: *BVRI*-bands light curves of Type Ia SN 2011fe (Pereira et al., 2013). The ^{56}Co $\rightarrow$ ^{56}Fe decay is shown as a reference. Data taken from the OSC.

SNe Ia produce on the order of $0.1 - 1.0\,M_{\odot}$ of ^{56}Ni (e.g., Wang et al., 2008; Childress et al., 2015). They display relatively homogeneous optical light curves, rising to peak brightness in ∼17–20 days in the *B* band (e.g., Conley et al., 2006; Ganeshalingam et al., 2011; Firth et al., 2015), declining afterwards for $\sim$ 50 days before starting the exponential decay (^{56}Co $\rightarrow$ ^{56}Fe; see Figure 1.6). The mean absolute *B*-band magnitude of 'normal' SNe Ia (i.e., not including sub-types) is around −19.1 mag with a low intrinsic root-mean-square (r.m.s.) scatter, $\lesssim$0.3 mag (e.g, Betoule et al., 2014; Ashall et al., 2016).

The spectrum around peak brightness is uniform and displays characteristic features, such as Si II (e.g., Si II λ6355), S II, Ca II and other intermediate-mass elements (e.g., Filippenko, 1997; Nugent et al., 2011, but see also Figure 1.7). The spectral features of SNe Ia have broad profile lines due to their high expansion velocities. They possess expansion velocities of the photosphere between ∼15000 km s^{-1} at early epochs (before peak) and several 1000 km s^{-1} at later epochs (e.g., Benetti et al., 2005; Altavilla et al., 2009). During the nebular phase, as the layers expand and become optically thin, the inner layers become visible and Fe-group elements (produced close to the core of the ejecta) start dominating the spectra.

Other thermonuclear SNe include: 1991T-like (Filippenko et al., 1992a), with higher luminosity than average SNe Ia and pre-peak spectrum dominated by Fe III lines; 1991bg-like (Filippenko et al., 1992b; Ruiz-Lapuente et al., 1993), with absorption at ∼4000–4500 Å in their spectra and lower luminosity than average SNe Ia; 2002cx-like/Iax (Li

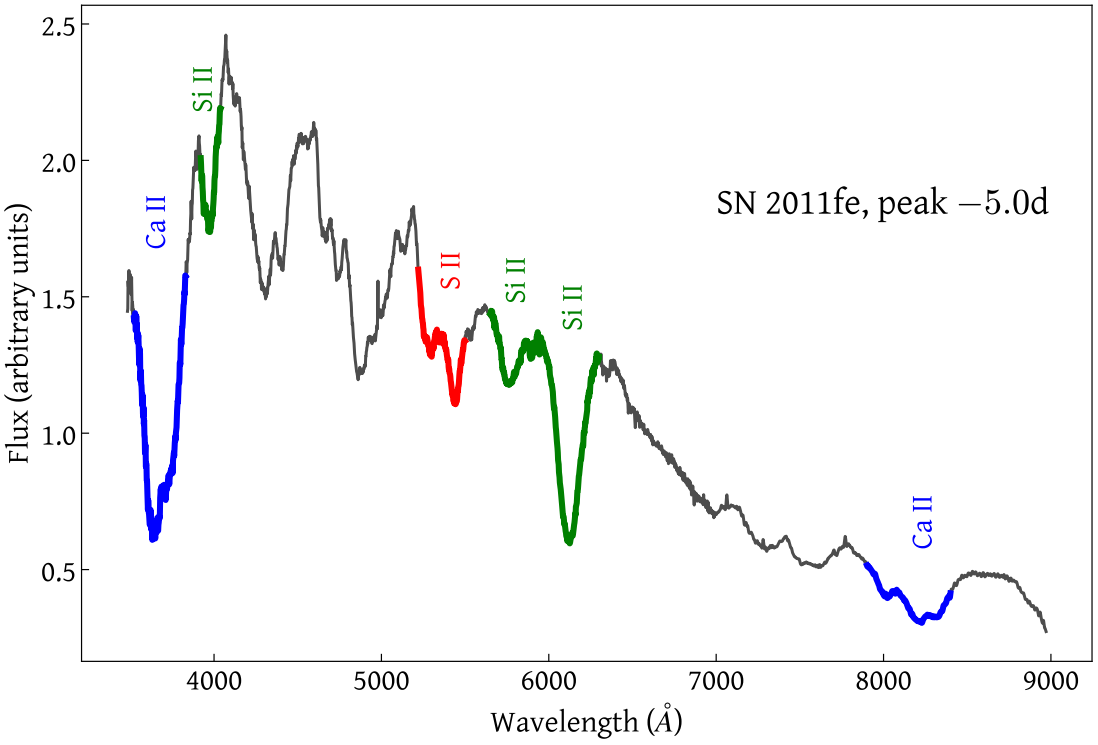

FIGURE 1.7: Spectrum of Type Ia SN 2011fe (Pereira et al., 2013). Some of the most characteristic spectral lines are shown, respectively labelled. The spectrum is around peak brightness in the *B* band, when it presents many of the characteristic spectral lines of its type. Data taken from the OSC.

et al., 2003; Foley et al., 2013), with 1991T-like spectra, but lower expansion velocities; and Ia-CSM (Hamuy et al., 2003), with H Balmer lines indicating interaction with an envelope of circumstellar material (CSM). These other types of thermonuclear SNe are not discussed in this thesis.

1.2 Supernovae as Distance Indicators

SNe Ia were found to exhibit relatively uniform peak luminosity, with an intrinsic r.m.s. scatter $\lesssim 0.3$ mag (e.g., Barbon et al., 1973; Cadonau et al., 1985; Doggett & Branch, 1985; Tammann & Leibundgut, 1990), which raised the idea of using them as distance indicators. This is demonstrated by a Hubble diagram (Hubble, 1929), which can be plotted as observed peak magnitude or distance vs recessional velocity or redshift. An incomplete list of early versions of the Hubble diagram with SNe Ia can be found in Zwicky (1965); Kowal (1968) and Barbon et al. (1975). Additionally, SNe Ia show a clear correlation between their (optical) *peak luminosity* and the *rate of decline* after peak light (expressed through a stretch parameter) and *colour* at *B*-band peak (e.g., Pskovskii, 1977, 1984; Phillips, 1993; Hamuy et al., 1995; Riess et al., 1995; Perlmutter et al., 1997;

Tripp, 1998; Phillips et al., 1999; Goldhaber et al., 2001; Kattner et al., 2012). Furthermore, correlations have been found between peak luminosity and host galaxy properties, such as *stellar mass* (e.g. Kelly et al., 2010; Lampeitl et al., 2010; Sullivan et al., 2010). These correlations can be used to correct light curves of SNe Ia, producing increasing uniformity and reducing the scatter in the Hubble diagram (e.g., Betoule et al., 2014). Consequently, SNe Ia have been studied for many decades as standardisable candles for cosmological distance measurements (e.g., Kowal, 1968; Elias et al., 1985; Phillips, 1993; Hamuy et al., 1995; Riess et al., 1996; Hamuy et al., 1996).

SNe II have been used as distance indicators for almost as long as SNe Ia, although they present a larger diversity and scatter (e.g., Barbon et al., 1979). Leonardo Searle developed one of the first methods, called the Expanding Photosphere Method (also referred to as "Baade-Wesselink" method), based on pulsating stars, which relates the expansion of the photosphere to its physical size (assuming an isotropic expansion). This was first attempted for SNe II by Kirshner & Kwan (1974) and was later on improved by other works (e.g., Hamuy, 2001a). Hamuy & Pinto (2002a) established an independent method, the Standard Candle Method, which uses the relation between the expansion velocity and observed brightness at 50 days after explosion to derive a normalised luminosity during the plateau phase of SNe II-P. Several other methods have since been developed, such as the Photospheric Magnitude Method (Rodríguez et al., 2014) and Photometric Candle Method (de Jaeger et al., 2015), the latter being a purely photometric method. However, despite the improvement in reducing the scatter in distances measured with SNe II in recent years (Gall et al., 2016; de Jaeger et al., 2020b,a), they are not as competitive as SNe Ia (e.g., Abbott et al., 2019) and other methods, such as Tully-Fisher relation (e.g., Kourkchi et al., 2020), geometric distance measurements to megamaser-hosting galaxies (e.g., Pesce et al., 2020) and gravitationally lensed quasars (e.g., Wong et al., 2020).

Sandage (1961), using the brightest galaxies in clusters, laid out one of the first methods to estimate the deceleration parameter as a measure of the matter density and geometry of the universe. Later on, Kowal (1968) used the same method on a sample of SNe I, leading to their use as standardisable candles. The increasing number and size of SNe Ia samples produced by systematic surveys over the last 30 years, such as Calán/Tololo (Hamuy et al., 1996) and Supernova Cosmology Project (SCP; Perlmutter et al., 1999), led to the discovery of the accelerated expansion of the universe (Riess et al., 1998; Perlmutter et al., 1999) and the Nobel Price of Physics award in 2011. In more recent years, other surveys, such as the Harvard-Smithsonian Center for Astrophysics (CfA) 1–4 (Riess et al., 1999; Jha et al., 2006; Hicken et al., 2009b,a, 2012) and Carnegie Supernova Project (CSP; Contreras et al., 2010), have led to the development of light-curve fitters, such as MLCS2k2 (Riess et al., 1996, 1998; Jha et al., 2007), SiFTO (Conley et al., 2008), SALT2 (Guy et al., 2005, 2007) and SNooPy (Burns et al., 2011), refining the standardisation of these object. These are usually trained on samples of well-observed SNe

and are then used to fit light-curves of other SNe Ia to extract light-curve parameters for their standardisation.

The current focus in the field is the understanding of systematic biases affecting the distance measurements as, with the increasing sample of SNe Ia, statistical uncertainties are no longer dominating the uncertainty budget in the cosmological analyses (e.g., Scolnic et al., 2018b; Abbott et al., 2019).

1.3 Cosmology

Cosmology is the study of the universe at large scales, from the beginning (Big Bang), evolution and its ultimate fate. In this section, I will mainly focus on the theory behind the standard cosmological model. For more detailed derivations, I refer the reader to others textbooks and notes in cosmology (e.g., Narlikar, 2002; Dodelson, 2003; Tytgat, 2009; Lambourne, 2010).

1.3.1 Cosmological Principle

The cosmological principle, which has been the basis of the development of modern cosmology, states that the universe is homogeneous (invariant under ones displacement) and isotropic (invariant under rotation) at large-enough scales. For instance, this implies the the laws of physics are the same in all parts of the universe and the Earth holds no special place. The cosmological principle derives from the Copernican principle but has no strong theoretical foundations. However, it has been supported by numerous observations, such as the isotropy of the cosmic microwave background (CMB; e.g., Planck Collaboration et al., 2014a, 2016a,c, 2020a) and the large-scale distribution of matter (e.g., Maddox et al., 1990; Doroshkevich et al., 2004).

1.3.2 Einstein Field Equations

The Einstein field equations describe the relation between the geometry of space-time and the distribution of matter within it:

$$G_{\mu\nu} + \Lambda g_{\mu\nu} = \frac{8\pi G}{c^4} T_{\mu\nu} \tag{1.1}$$

where $G_{\mu\nu}$ is the Einstein tensor, Λ the cosmological constant (I will sometimes refer to this as Dark Energy), $g_{\mu\nu}$ is the metric tensor (it specifies the space-time geometry), G is Newton's gravitational constant, c is the speed of light and $T_{\mu\nu}$ is the stress-energy

or energy-momentum tensor, which describes the matter content. These set of equations, together with the geodesic equation, dictate how a falling particle moves through space-time, and form the foundations of general relativity. Additionally, the current cosmological model is directly derived from these equations.

1.3.3 Friedmann-Lemaître-Robertson-Walker Metric

The metric used to describe the universe on large scales is the Friedmann-Lemaître-Robertson-Walker (FLRW) metric and has the following form in spherical coordinates:

$$ds^2 = -c^2dt^2 + a(t)^2\left[\frac{dr^2}{1-kr^2} + r^2d\Omega^2\right] = -c^2dt^2 + a(t)^2d\Sigma \tag{1.2}$$

where k is the spacial curvature (constant), c is the speed of light, a is the *scale factor* and $d\Omega^2 = d\theta^2 + \sin^2\theta d\phi^2$. This is also known as the Robertson-Walker metric. The present-time value of the scale factor is $a(t=0) = 1$. We can redefine $d\Sigma^2$, to obtain a more general form of the metric, as:

$$d\Sigma^2 = d\chi^2 + \chi^2\, d\Omega^2, \tag{1.3}$$

where $d\Omega$ is as before and:

$$\chi = \begin{cases} \sqrt{k}^{-1}\sin(r\sqrt{k}), & k > 0 \\ r, & k = 0 \\ \sqrt{|k|}^{-1}\sinh(r\sqrt{|k|}), & k < 0. \end{cases} \tag{1.4}$$

The curvature k can take values between -1 and +1. For example, in the case of $k > 0$, $d\chi = \cos(r\sqrt{k})dr$. As can be seen, the metric changes depending on the curvature of the universe, which has implications on its evolution. We will further discuss this in the next section.

1.3.4 Friedmann Solutions

One of the Friedmann solutions to the time component of Einstein equations is given by:

$$H(t)^2 \equiv \left(\frac{\dot{a}(t)}{a(t)}\right)^2 = \frac{8\pi G}{3}\rho, \tag{1.5}$$

where H is the Hubble parameter (measurement of the expansion of the universe in units of inverse time) and ρ is the *energy* density of the universe (I will refer to it simply as density). The dot represents the time derivative. Here on, we will make the time dependence implicit (e.g., $a(t) = a$) for simplicity. The density of the universe can be divided into its different components: radiation ($\rho_{\rm rad}$; this includes relativistic matter, such as neutrinos), matter ($\rho_{\rm m}$; non-relativistic matter), spatial curvature ($\rho_{\rm k}$; this is mainly defined with mathematical purposes and has no physical interpretation) and Dark Energy (ρ_Λ). Equation (1.5) can then be re-written as:

$$H^2 = \frac{8\pi G}{3}(\rho_{\rm rad} + \rho_{\rm m} + \rho_{\rm k} + \rho_\Lambda). \tag{1.6}$$

The spatial curvature and Dark Energy densities are respectively defined as:

$$\begin{aligned} \rho_{\rm k} &\equiv -\frac{kc^2}{a^2} \\ \rho_\Lambda &\equiv \frac{\Lambda c^2}{3}. \end{aligned} \tag{1.7}$$

We can define the *critical density*, the average density of matter required for the universe to just halt its expansion (but only after an infinite time), as:

$$\rho_{\rm crit} \equiv \frac{3H^2}{8\pi G}. \tag{1.8}$$

If the matter density in the universe is high, gravity slows the expansion until it halts, and ultimately re-collapses. This is known as a *closed* universe. If the matter density in the universe is low , gravity is insufficient to stop the expansion, and the Universe continues to expand forever. This is known as an *open* universe. If the matter density is 'just right' (equal to the critical density), the expansion is halted only after an infinite time. This is known as a *flat* universe. The geometries for each of these universes are presented in Figure 1.8.

Substituting $\rho_{\rm crit}$ in equation (1.6) we obtain:

$$1 = \left(\frac{\rho_{\rm rad} + \rho_m + \rho_k + \rho_\Lambda}{\rho_{\rm crit}}\right). \tag{1.9}$$

Note that all these components are time dependent, except for ρ_Λ, which may or may not be constant. The *dimensionless* densities (also known as *fractional* densities) are defined as the density over the critical density:

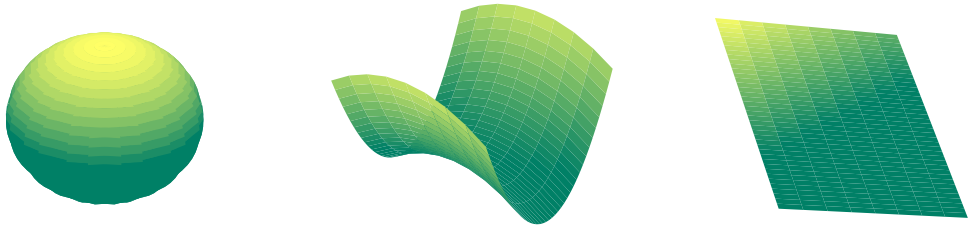

FIGURE 1.8: Three possible geometries for the universe: spherical space (closed universe; **left**), hyperbolic space (open universe; **middle**) and flat space (flat universe; **right**).

$$\begin{aligned}
\Omega_r &\equiv \frac{\rho_r}{\rho_{\text{crit}}} \\
\Omega_m &\equiv \frac{\rho_m}{\rho_{\text{crit}}} \\
\Omega_k &\equiv \frac{\rho_k}{\rho_{\text{crit}}} = -\frac{kc^2}{a^2H^2} \\
\Omega_\Lambda &\equiv \frac{\rho_\Lambda}{\rho_{\text{crit}}} = \frac{\Lambda c^2}{3H_0^2},
\end{aligned} \tag{1.10}$$

which turn equation (1.9) into:

$$1 = \Omega_m + \Omega_r + \Omega_\Lambda + \Omega_k \tag{1.11}$$

1.3.5 Raychaudhuri Solution

An important solution derived from Einstein field equations is the Raychaudhuri equation or acceleration equation:

$$\frac{2\ddot{a}}{a} + \frac{\dot{a}^2}{a^2} = -8\pi G p \tag{1.12}$$

where p is the pressure of the universe. If we use the Friedmann equation, equation (1.5), in the Raychaudhuri equation, equation (1.12), and re-arrange some terms, we obtain:

$$\frac{\ddot{a}}{a} = -\frac{4\pi G}{3c^2}(\rho + 3p), \tag{1.13}$$

where the factor of 3 represents the three spatial dimensions.

The equation of state that relates the pressure and energy density of a physical system is given by $p = \omega\rho$. So, if $\rho + 3p > 0$, or, equivalently $1 + 3\omega > 0$, the expansion of the universe is decelerated.

We can explicitly solve for the density ρ and see its dependence on the scale factor, a. From the first law of thermodynamics (conservation of energy) applied to $E = \rho V$ (remember that ρ is the *energy* density), where E is the energy of the universe and V its volume, one obtains that:

$$\rho \propto a^{-3(1+\omega)}. \tag{1.14}$$

The value of ω will depend on the nature of the component. For non-relativistic matter, $p = 0$, therefore, $\omega = 0$, so $\rho \propto a^{-3}$ (given the three spatial dimensions). For radiation (including relativistic matter), $\omega = 1/3$, so $\rho \propto a^{-4}$ (given the three spatial dimensions plus the wavelength dependence of photons). If dark energy is described by a cosmological constant, then $\omega = -1$ and $\rho = const$. If Dark Energy evolves as a function of time, then $w \neq -1$. It is common to refer to ω as the Dark Energy equation-of-state parameter.

From equation (1.14), the present-day density and the density at a given time are related by the scale factor: $\rho_m = \rho_{m,0}a^{-3}$, $\rho_{\text{rad}} = \rho_{\text{rad},0}a^{-4}$, $\rho_k = \rho_{k,0}a^{-2}$ (as defined in equation (1.7)) and $\rho_\Lambda = \rho_{\Lambda,0}$, for a constant Λ, where the 0 subscript denotes the present-time ($a = 1$) values and H_0 is the present-time Hubble parameter, also known as the *Hubble constant*, the value of the expansion of the universe today. Additionally, if we re-define the normalisation factor of the dimensionless densities Ω to be the present-time critical density $\rho_{\text{crit},0}$, i.e., $\Omega = \rho/\rho_{\text{crit},0}$, we can re-write equation (1.5) as:

$$\begin{aligned} H^2 &= H_0^2(\Omega_{\text{rad},0}a^{-4} + \Omega_{m,0}a^{-3} + \Omega_{k,0}a^{-2} + \Omega_{\Lambda,0}) \\ &= H_0^2E^2(a), \end{aligned} \tag{1.15}$$

where $E^2(a) \equiv (\Omega_{\text{rad},0}a^{-4} + \Omega_{m,0}a^{-3} + \Omega_{k,0}a^{-2} + \Omega_{\Lambda,0})$. Alternatively, Ω_Λ can be written as a function of ω for a more general expression, i.e., $\Omega_\Lambda = \Omega_{\Lambda,0}a^{-3(1+\omega)}$.

1.3.6 The Standard Cosmological Model

The standard cosmological model is known as the Λ Cold Dark Matter (ΛCDM) model and is made up of mostly Dark Energy (Λ) and Dark Matter. In the last decades, several works have estimated the cosmological parameters from observational data, obtaining values of $\Omega_\Lambda \sim 0.7$, $\Omega_{m,0} \sim 0.3$ and $\Omega_{\text{rad},0} \sim \Omega_{k,0} \sim 0.0$ (Betoule et al., 2014; Planck Collaboration et al., 2014b, 2016b; Alam et al., 2017; Carter et al., 2018; Scolnic et al., 2018b; Abbott et al., 2019; Planck Collaboration et al., 2020b; Tröster et al., 2020). In other

words, the universe contains ∼70 per cent Dark Energy, ∼30 matter and a tiny fraction of radiation, and is approximately spatially flat. Out of the 30 per cent of matter content in the universe, only 1/6 is in the form of 'common' matter, i.e., baryons, and the rest is in the form of non-visible matter, which can only be 'seen' indirectly through its gravitational interaction with the visible matter as it does not interact with electromagnetic radiation. This non-visible matter is now termed Dark Matter ('discovery' attributed to Vera C. Rubin, but see also, e.g., Zwicky 1933; White et al. 1993; Navarro et al. 1996; Schuecker et al. 2003; Gao et al. 2004) and it is mainly found in galaxies and galaxy clusters, constituting most of their content. The word 'cold' in the ΛCDM model refers to the nature of Dark Matter being non-relativistic, contrary to hot Dark Matter, which refers to a relativistic nature.

1.3.7 Cosmological distances in the universe

The comoving (time/expansion-independent) distance travelled by a photon from a distant object (e.g., galaxy) to an observer can be computed by the following formula, derived directly from equation (1.2) (the FLRW metric):

$$\chi = \int_{t_e}^{t_o} c\frac{dt}{a}, \tag{1.16}$$

where t_e is the time of emission of the photon and t_o is the time of observation of the photon. We can re-write this equation to include equation (1.15):

$$\chi = \int_{a_e}^{1} c\frac{da}{a^2 H_0 E(a)}, \tag{1.17}$$

or in terms of redshift, z, and that $a = 1/(1+z)$:

$$\chi = \frac{c}{H_0}\int_0^{z_e}\frac{dz}{E(z)} = d_H\int_0^{z_e}\frac{dz}{E(z)}, \tag{1.18}$$

where $d_H \equiv c/H_0$ is the *Hubble distance*. The comoving distance between comoving observers is by definition a fixed, unchanging quantity independent of time, while the dynamic, changing distance between them is called *proper distance*, d. The relation between both at a given time, t, is simply $d(t) = \chi/a(t) = \chi(1+z)$, assuming a flat ($k = 0$) universe. The distance d is also referred to as the *luminosity distance* as it is the distance travelled by a photon and is a very important notion of distance for observations. SNe Ia are commonly used to measure luminosity distances.

1.3.8 Measuring distances with Type Ia Supernovae

We know that the relation between the luminosity, L, and flux, F, of an object is given by:

$$F = \frac{L}{4\pi d^2}, \tag{1.19}$$

where d is the (luminosity) distance. Additionally, the flux can be measured in magnitudes (m), a logarithmic scale (see Chapter 2), by using the following equation:

$$m = -2.5 \log_{10}(F) + m_0, \tag{1.20}$$

with m_0 an arbitrary reference value.

Using the two relations above, the distance modulus is defined as the difference between the apparent (observed) magnitude and absolute magnitude (the magnitude as if the object was at a distance of 10 pc):

$$\mu = m - M = -2.5 \log_{10}\left(\frac{F}{F_{10\,\mathrm{pc}}}\right) = -2.5 \log_{10}\left(\frac{(10\,\mathrm{pc})^2}{d^2}\right) = 5 \log_{10}\left(\frac{d}{10\,\mathrm{pc}}\right), \tag{1.21}$$

where d is measured in parsec. Using SNe Ia as standardisable candles, we first need to correct the apparent magnitude using the correlations described in Section 1.2:

$$m_B^{\mathrm{corr}} = m_B + \alpha s - \beta C + \Delta_{\mathrm{Mass}} + \Delta_{\mathrm{Bias}}, \tag{1.22}$$

where m_B is the peak brightness in the rest-frame B band, s is a stretch-like parameter and c is a colour-like parameter. α and β are nuisance parameters representing the contribution from the stretch and colour corrections, respectively. Δ_{Mass} is a correction due to host galaxy stellar mass, where it has been found that brighter SNe (after stretch and colour correction) tend to explode in more massive galaxies (e.g., Kelly et al., 2010; Lampeitl et al., 2010; Sullivan et al., 2010). Δ_{Bias} is the distance bias correction, a correction due to *selection* effects, also known as *Malmquist* bias (Malmquist, 1922, 1925), which describes how astronomical (magnitude-limited) observations preferentially detect intrinsically bright objects.

By using equation (1.22), one can simply express the distance modulus measured from SNe Ia as:

$$\mu_{\rm SN} = m_B^{\rm corr} - M, \tag{1.23}$$

where, this time, M is another nuisance parameter, but also represents the average absolute magnitude of SNe Ia. The distance modulus measured from the cosmological model is given by:

$$\mu_{\rm cosmo} = 5\log_{10} d(z,\, \omega,\, \Omega_{m,0},\, \Omega_{\rm rad,0},\, \Omega_\Lambda,\, \Omega_{k,0}) - 5, \tag{1.24}$$

and will depend on the value of the different cosmological parameters and redshift. Finally, the cosmological parameters, together with the nuisance parameters, can be measured by minimising the following function (a reduced chi-squared):

$$\bar{\chi}^2 = (\mu_{\rm SN} - \mu_{\rm cosmo})^\dagger A^{-1} (\mu_{\rm SN} - \mu_{\rm cosmo})\,/\,DoF, \tag{1.25}$$

where DoF are the degrees of freedom (number of data points minus number of parameters) and A is the covariance matrix of $\mu_{\rm SN}$, where most of the off-diagonal components are zero. There are several factors that contribute to A:

$$\begin{aligned} A =& \sigma_{m_B}^2 + \alpha^2\sigma_s^2 + \beta^2\sigma_C^2 + 2\alpha{\rm Cov}_{m_B,s} - 2\beta{\rm Cov}_{m_B,C} - 2\alpha\beta{\rm Cov}_{s,C} \\ &+ \sigma_{\rm Mass}^2 + \sigma_{\rm Bias}^2 + \sigma_{\rm vpec}^2 + \sigma_z^2 + \sigma_{\rm lens}^2 + \sigma_{\rm int}^2, \end{aligned} \tag{1.26}$$

where $\sigma_{m_B}^2$, σ_s^2 and σ_C are the uncertainties in the light-curve parameters, ${\rm Cov}_{m_B,s}$, ${\rm Cov}_{m_B,C}$ and ${\rm Cov}_{s,C}$ are the covariances between light-curve parameters, $\sigma_{\rm Mass}^2$ is the uncertainty from $\Delta_{\rm Mass}$, $\sigma_{\rm Bias}^2$ is the uncertainty from $\Delta_{\rm Bias}$, $\sigma_{\rm vpec}^2$ is the uncertainty on redshift from peculiar velocities of the host galaxies (usually assumed to be $\sim$150 – 300 km s^{-1}, i.e., $\sim$0.0005–0.001 in redshift; e.g., Scolnic et al. 2014; Betoule et al. 2014; Scolnic et al. 2018b), σ_z^2 is the uncertainty in the redshift measurement and $\sigma_{\rm lens}^2$ is the uncertainty from stochastic weak gravitational lensing (usually assumed to be $\sigma_{\rm lens} = 0.055 \times z$, as given in Jönsson et al. 2010). $\sigma_{\rm int}^2$ is the intrinsic scatter, the remaining variation unexplained by the standardisation of SNe Ia, and is fitted such that equation (1.25) is equal to 1, i.e., $\bar{\chi}^2 = 1$.

1.3.9 Recent Cosmological Analyses

Recent work (e.g., Betoule et al., 2014; Scolnic et al., 2018b; Abbott et al., 2019) shows that SN Ia measurements, in combination with other methods, e.g., the CMB (e.g., Planck Collaboration et al., 2020b) and baryon acoustic oscillations (e.g., Alam et al., 2017; Carter et al., 2018), are in agreement with the standard ΛCDM cosmological

model and with a dark energy equation-of-state with $w = -1$ (i.e., a cosmological constant), within the uncertainties.

In the last decade, there has been a joint effort to increase the sample of SNe Ia for cosmological analyses. Betoule et al. (2014) compiled SNe Ia from different surveys to create the Joint Light-curve Analysis (JLA) sample of 720 SNe Ia, with a detailed cross-calibration. A few years later, Scolnic et al. (2018b) expanded the JLA sample, creating the Pantheon sample of 1048 SNe Ia. However, both analyses presented an uncertainty budget dominated by statistical uncertainties. More recently, (Abbott et al., 2019) used a combination of low-redshift SNe used in the previous samples with those from DES, obtaining one of the latest constraints on Ω_m and w from DES (Abbott et al., 2019), as shown in Figure 1.3.9, but with almost identical contribution from the systematic and statistical uncertainties. Assuming, a flat universe, they obtained that $w = -0.978 \pm 0.059$ ($\sim$ 6 per cent uncertainty), value consistent with a cosmological constant. Thus, current effort is focused on reducing this uncertainty in w to less than 1 per cent to properly exclude the evolution of the cosmological constant.

The uncertainty budget of SN Ia cosmology is reaching a point where it is starting to be dominated by systematic uncertainties (e.g., Abbott et al., 2019), such as the selection effects, light-curve standardisation of SNe Ia and cross-calibration of photometric systems. Surveys like the Rubin Observatory Legacy Survey of Space and Time (LSST) and Foundation Supernova Survey (Foley et al., 2018; Jones et al., 2019) are aiming to reduce the uncertainties on the selection effect and photometric calibration. However, biases and uncertainties coming from light-curves standardisation need to be addressed in a different way.

1.3.10 Light-Curve Fitters

Systematic uncertainties can be further reduced by applying proper light curve corrections. Cosmological studies of SNe Ia use light-curve fitters for their standardisation, e.g., MLCS2k2 (Riess et al., 1996, 1998; Jha et al., 2007), SALT2 (Guy et al., 2005, 2007), SiFTO (Conley et al., 2008) and SNooPy (Burns et al., 2011, 2014).

MLCS2k2 is an empirical model based on a set of light-curve templates created from a training sample of SNe Ia. The light-curves are parametrized by a luminosity/light-curve shape parameter (Δ) that modifies the underlying model (fiducial light curves). Additionally, this model separates the intrinsic colour component of the SN Ia and the extrinsic component, coming from the host-galaxy dust.

SiFTO is another empirical model trained of a sample of SNe Ia. The SED model describes the light-curve shape with a stretch parameter (stretch in the rest-frame B band, s_B). The colours of a SN are described by a set of normalisation parameters (one per

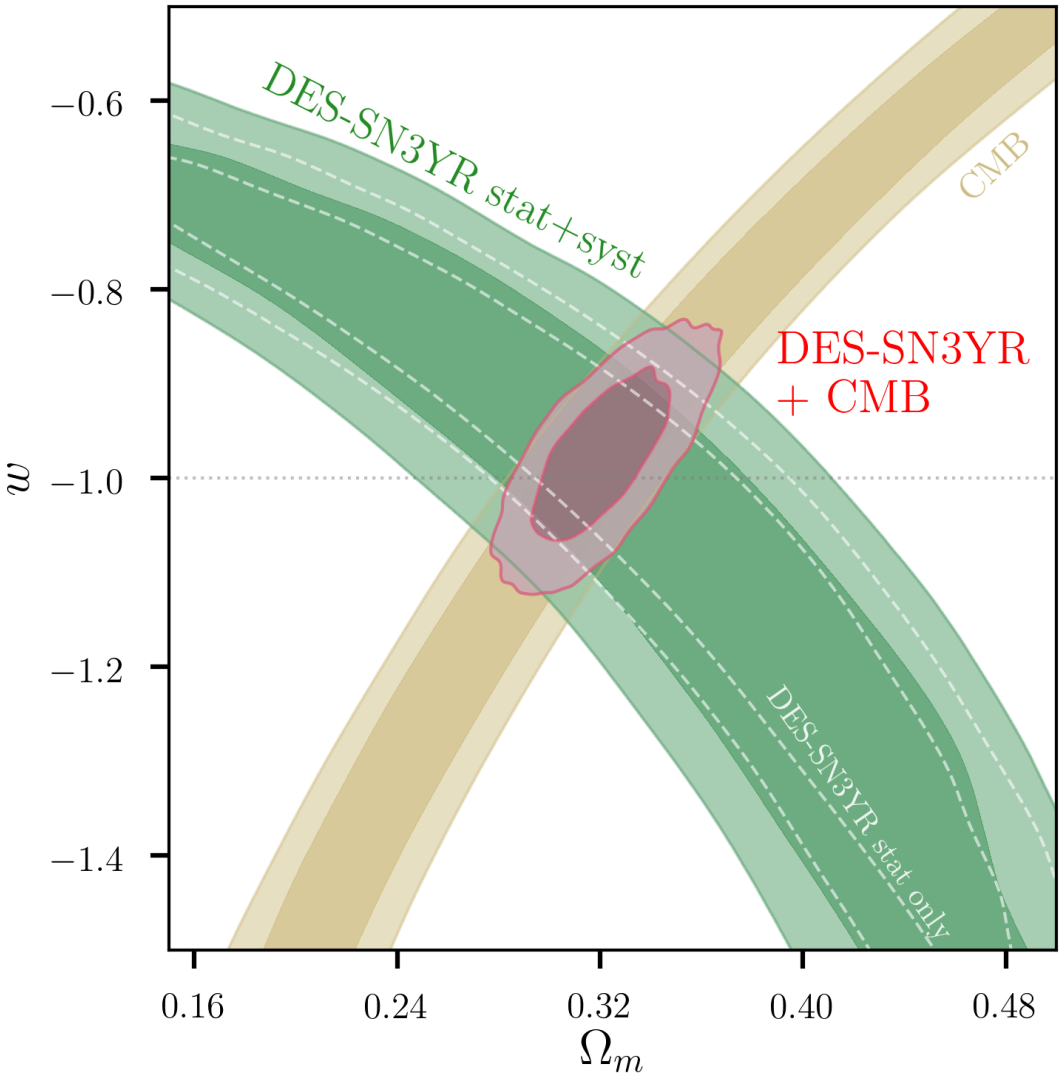

filter), from which a colour-like parameter can be extracted taking information from the multiple wavelengths.

SNooPy is similar to MLCS2k2 and SiFTO, but presents some key differences. First, it is trained on a sample of SNe Ia with optical and near-infrared (NIR) data, allowing it to fit NIR light curves. Second, SNooPy can use the standard stretch parameter $\Delta m_{15}(B)$, but also a colour-stretch parameter (s_{BV}; Burns et al. 2014), which describes the shape of the colour curve (evolution in time). Last, it incorporates different fitting models with different assumptions, for example, considering reddening as a parameter, making it a very versatile light-curve fitter.

In this thesis, I will focus on SALT2 as it is one of the most widely used light-curve fitters in current cosmological analyses (e.g., Betoule et al., 2014; Scolnic et al., 2018b; Abbott et al., 2019), although most fitters work in a similar way, as I already described.

SALT2 is an empirical SN Ia model, trained on a spectro-photometric sample of these objects, and describes the flux of a SN Ia with the following functional form:

$$F(p,\lambda)_{\rm SN} = x_0 \times [M_0(p,\lambda) + x_1 M_1(p,\lambda) + \ldots] \times \exp[c \times CL(\lambda)], \tag{1.27}$$

where p is the rest-frame time with respect to B-band peak, λ is the rest-frame wavelength, M_0 is the average spectral sequence, M_1 is an additional component that describes further variability (the contribution of high-order components is less significant) and CL represents the average colour variation law of a SN Ia (see Chapter 6). Note that the SALT2 model essentially comes from a Principal Component Analysis (PCA) decomposition that includes a colour term (the exponential).

The terms x_0, x_1 and c are the SALT2 light-curve parameters, which are used for the standardisation of SNe Ia, where x_0 is related to the peak apparent magnitude in the B band via $-2.5\ log_{10}(x_0) + 10.635 = m_B^{\rm max}$, x_1 is a measurement of the stretch of the light curve, and c is the colour of the SN. Note that c is essentially an approximate measurement of $(B-V)$ at the time of B-band peak brightness, measured with respect to the base template, M_0.

Template-based light-curve fitters have shown to be an excellent tool for standardising SNe Ia, however, they are not free from limitations. For instance, most of them work with optical data only (except for SNooPy), which may not properly characterise the full multi-colour light-curve variation of SNe Ia. Additionally, SNe Ia are better suited for cosmology in the NIR as they show more homogeneous light curves and are less affected by dust extinction (e.g., Elias et al., 1981, 1985; Freedman et al., 2009), although they are also fainter (i.e., harder to observe). Furthermore, these light-curve fitters are susceptible to biases (Kessler et al., 2009b) given the need of a training sample of SNe Ia, which may not be representative of the overall population (e.g., Ellis et al., 2008; Maguire et al., 2012).

To summarise this chapter, SNe come in many different flavours, with different progenitors and explosion mechanisms. A sub-set of these, known as SNe Ia, show remarkably high uniformity in their optical light curves and have been used as distance indicators for decades. Furthermore, thanks to these the accelerating expansion of the universe was discovered.

SNe Ia, in combinations with other probes, are in agreement with a flat ΛCDM model with cosmological constant. However, higher accuracy and precision is required to properly exclude any evolution of the cosmological constant. With the increasing sample of SNe Ia, the uncertainty budget is no longer dominated by statistical uncertainties, but by systematic uncertainties. Future surveys will help decrease these. Additionally, the use of light-curve fitters for the standardisation of SNe Ia also improves the

precision in distance measurements, although the uncertainties coming from this will dominate the uncertainty budget in the near future.

Thus, the aim of this thesis is to search for an alternative standardisation of SNe Ia to further improve the precision in the distance measurements. In the next chapter, I will describe how photometry works and how observations are calibrated. Then, I will introduce and describe a new light-curve fitter developed as part of this work, which does not suffer from the limitations other light-curve fitters suffer, as mentioned above. Later, I will present some tests with simulations and real data to help validate my code and then proceed to analyse the light curves of SNe Ia with a machine-learning algorithm to present a new, alternative and competitive standardisation/framework. I will study the colour evolution of SNe Ia and compare it with the SALT2 model to have a better understanding of their physics, putting this in perspective with future cosmological SN analyses. I will finalise, moving to a broader context in the 'SN landscape', by presenting the study of a low-luminosity SN II with extended photometric and spectroscopic coverage, showing that late-time spectra is key for understanding the progenitors and explosion mechanisms of SNe II and possibly of CCSNe in general.

Chapter 2

Photometry

In this chapter, I will introduce photometry, the main technique used to measure the light of astrophysical objects. As one of the main pillars in astronomy, photometry is one of the bases of how we gather data across the sky. Thus, a proper calibration is fundamental for the analysis and comparison of different datasets, such as those of SNe Ia. I will start by giving some historical background and continue by introducing the main concepts to understand how photometry works.

2.1 Photometric System

Astronomers use *filters* to measure the flux in a given range of the spectrum of a celestial body (e.g., a star). The amount of the spectrum that a filter allows through is known as the *bandpass*. However, the measured flux depends on the combination of atmosphere, telescope (mirrors), instrument, filter (bandpass) and detector (quantum efficiency). I will refer to the combination of all these effects as *response* or *transmission function*.

Filters are usually divided in three main categories: narrow-band, intermediate-band and broad-band filters. For the purpose of this thesis, I will focus on the latter, those with bandpasses widths in the order of 1000 Å, as these are the most commonly used filters in the field of SNe.

The photometry of a source provides a coarse measurement of its spectrum through a set of filters, or transmission functions to be more precise (considering external factors, such as the atmosphere). The advantage over spectroscopy, the technique of splitting light into its constituent wavelengths (i.e., a spectrum), is that photometry allows the collection of a larger amount of photons over a shorter period of time, therefore, increasing the signal-to-noise (S/N), but with a trade-off for spectral resolution.

One of the most widely use photometric systems is the $UBVR_CI_C$ system, also known as the Johnson-Morgan-Cousins system. The first filters, UBV ("Ultraviolet", "Blue" and "Visual") were introduced by Johnson & Morgan (1953) (see also Johnson & Harris 1954; Johnson 1955). Kron et al. (1953) added two further filters, R_KI_K ("Red", "Infrared"), improved by Johnson et al. (1966), but later superseded by the shorter effective-wavelength R_C and I_C filters introduced by Cousins (1976) (the subscript C is commonly dropped for simplicity).

The introduction of charge-coupled devices (CCDs), which have different spectral sensitivities to the photomultiplier tubes that were used to define the original $UBRVI$ system, led Bessell (1990) to publish new $UBVRI$ filters that closely reproduce the original Johnson-Morgan-Cousins filter transmissions, when used with CCDs. Bessell's UBVRI filters are a common set of filters and are considered *standard* filters. In Figure 2.1 (*top* panel), I show the transmission functions of the Bessell filters.

Gunn et al. (1998) introduced the United States Naval Observatory (USNO)/Sloan Digital Sky Survey (SDSS) $u'g'r'i'z'$ ("ultraviolet", "green", "red", "infrared" and "near-infrared") filters, which were then superseded by the *ugriz* (*unprimed*) filters (Doi et al., 2010), widely used and also considered as *standard* filters. In Figure 2.1 (*bottom* panel), I show the transmission functions of the SDSS filters. These filters have less overlap between them than the Johnson-Morgan-Cousin filters, providing better understanding of the underlying SED, and cover a broader range, providing more information, making them better suited for photometry. For reviews of standard photometric systems see Johnson (1966) and Bessell (2005).

2.2 Magnitude System

The apparent magnitude of a source is a relative measurement. This means that one must chose a *zeropoint*, i.e., a reference source, like a star, to compare the brightness with, defining the scale of the system. The apparent magnitude is defined as:

$$m - m_\star = -2.5 \log_{10}(F/F_\star), \tag{2.1}$$

where m and F are the observed magnitude and flux of the source, and $m_\star$ and $F_\star$ are the observed magnitude and flux of the reference star. We can re-write this equation to incorporate all the values from the reference star in a single, constant term:

$$m = -2.5 \log_{10}(F) + [m_\star + 2.5 \log_{10}(F_\star)] = -2.5 \log_{10}(F) + ZP, \tag{2.2}$$

where ZP is the zeropoint that defines the magnitude system.

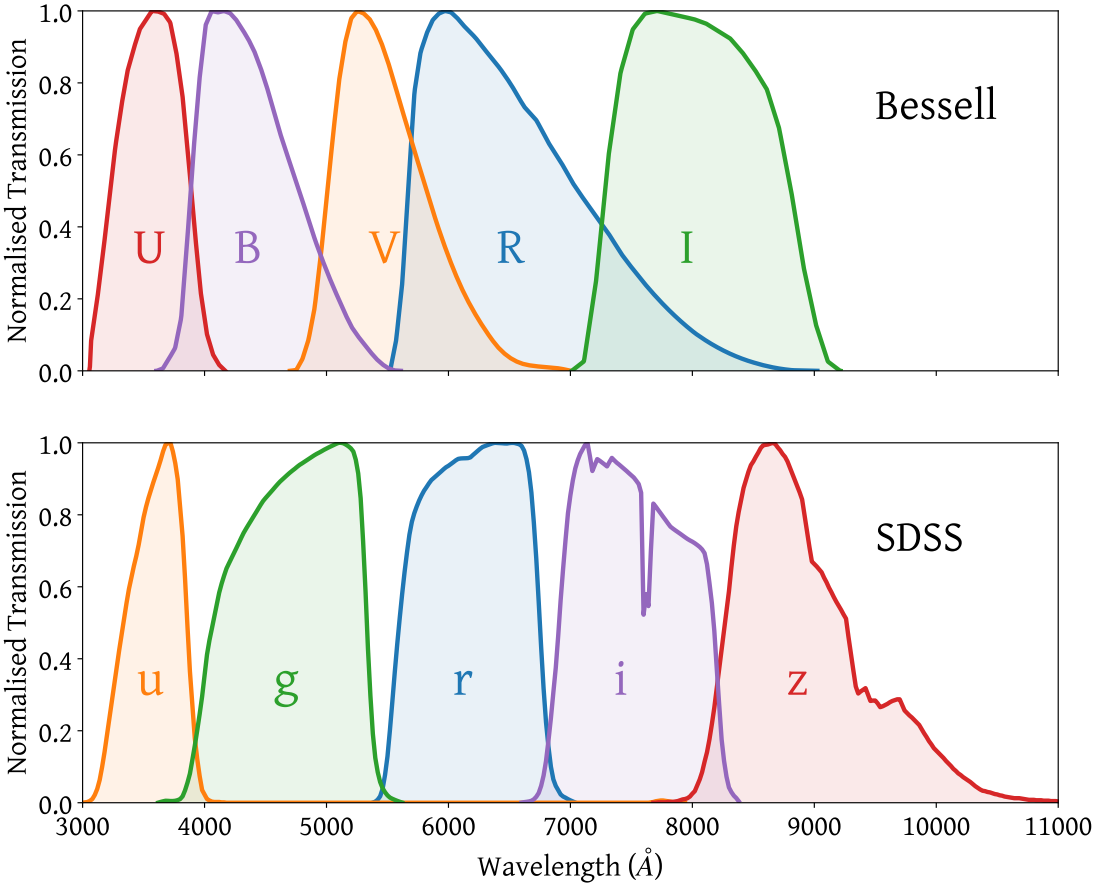

FIGURE 2.1: *UBVRI* filter transmission functions from Bessell (1990) (**top panel**) and *ugriz* filter transmission functions from Doi et al. (2010) (**bottom panel**).

2.2.1 Vega System

The A0V star *Vega/Alpha Lyrae/αLyr.* (e.g., Bohlin & Gilliland, 2004b) was chosen as the reference star (also called a primary standard) for the *UBVRI* system as it has a magnitude close to zero in Hipparchos' magnitude scale, it is observable throughout most of the year in the northern hemisphere, it is relatively bright, non-variable, and with a reasonably flat and smooth optical spectrum. However, Vega is too bright for most modern telescopes, so a set of secondary stars was defined with their magnitudes calibrated relative to Vega.

As the measurements became more precised and accurate, it became apparent that Vega actually had a magnitude of ∼0.03 mag in *V* band and that its luminosity was slightly variable, thus limiting the precision of these. In Figure 2.2, I show the spectrum of Vega around optical wavelengths.

2.2.2 Johnson System

By definition of this system, Vega has a V-band magnitude of 0.03 mag and all colour indices (or simply, colour; difference in magnitude between two filters) are equal to zero, i.e.:

$$U - B = B - V = V - R = R - I = 0, \tag{2.3}$$

where it is standard practice to refer to the apparent magnitude of a source observed through a filter by the name of the filter, e.g., $m_V = V$. In general, photometric systems with $UBVRI$ filters are tied to Vega.

2.2.3 Gunn System

This system adopts BD $+17°4708$ (e.g., Bohlin & Gilliland, 2004a), an F subdwarf star, as its reference star and is defined to have all colours equal to zero, with all magnitudes equal to 9.50, which is approximately equal to its Johnson V-band magnitude.

2.2.4 AB System

In the ABsolute (AB) system (e.g., Oke, 1965, 1974; Oke & Gunn, 1983; Fukugita et al., 1996), a monochromatic magnitude is defined such that:

$$m_{\rm AB}(\nu) = -2.5 \log_{\rm I0} \left(\frac{f_\nu}{3631 {\rm Jy}} \right) = -2.5 \log_{\rm I0} \left(\frac{f_\nu}{1 {\rm Jy}} \right) + 8.90 \, {\rm mag}, \tag{2.4}$$

in units of janskys (Jy), or alternatively, in units of erg $\mathrm{cm}^{-2}\,\mathrm{s}^{-1}\,\mathrm{Hz}^{-1}$:

$$m_{\rm AB} = -2.5 \log_{10} f_\nu - 48.60. \tag{2.5}$$

In other words, the AB spectrum has constant flux per unit frequency, and has $V_{\rm AB} \approx V_{\rm Vega}$. In general, photometric systems with $ugriz$ filters are tied to AB via BD $+17°4708$. In Figure 2.2, I show the AB spectrum around optical wavelengths.

2.2.5 Flux Measurement

The flux of a source through a given filter is usually measured as a function of frequency (F_ν, in units of erg $\mathrm{cm}^{-2}\,\mathrm{s}^{-1}\,\mathrm{Hz}^{-1}$), wavelength ($F_\lambda$, in units of erg $\mathrm{cm}^{-2}\,\mathrm{s}^{-1}\,\mathrm{\AA}^{-1}$) or photons ($N_\lambda$, in units of photons $\mathrm{cm}^{-2}\,\mathrm{s}^{-1}\,\mathrm{\AA}^{-1}$), using one of the following equations:

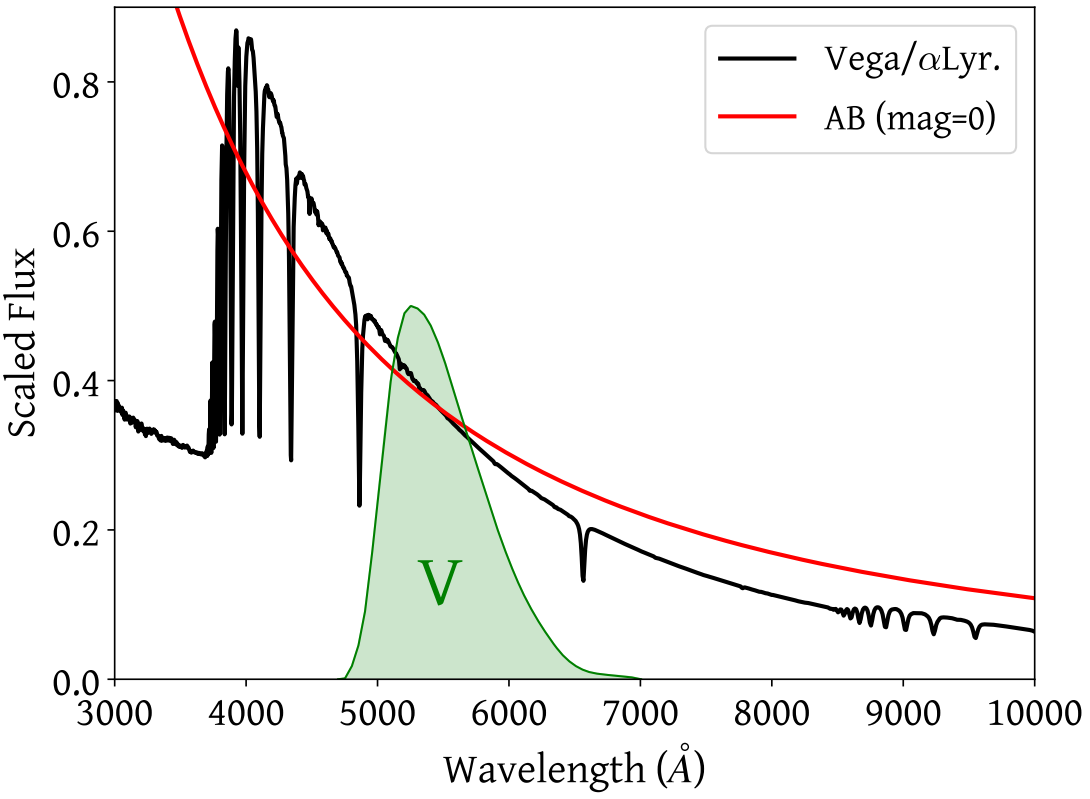

FIGURE 2.2: Spectrum of Vega (black) and AB (red) systems. Both systems have approximately the same zero magnitude in the V band. A V-band transmission function (green) is shown as a reference.

$$
\begin{aligned}
F_\nu &= \frac{\int \nu^{-1} f_\nu T_\nu d\nu}{\int \nu^{-1} T_\nu d\nu}, \\
F_\lambda &= \frac{\int \lambda f_\lambda T_\lambda d\lambda}{\int \lambda T_\lambda d\lambda}, \\
N_\lambda &= \frac{1}{ch} \int \lambda f_\lambda T_\lambda d\lambda,
\end{aligned}
\tag{2.6}
$$

where T is the transmission function of the filter, f is the spectral energy distribution (SED, i.e., spectrum) of the source, c is the speed of light and h is Planck's constant. Note that some transmission functions may be pre-multiplied by λ (informally referred to as going from photon sensitivity to energy sensitivity), including the Bessell filters, which modifies the above equations ($T_\lambda \to T_\lambda / \lambda$).

One can convert between flux units using $\nu\lambda = c$ and the relation between f_ν and f_λ:

$$
f_\nu = \frac{\lambda^2}{c} f_\lambda. \tag{2.7}
$$

In the SN community, SEDs are commonly presented as a function of wavelength.

2.3 Photometric Calibration

Every set of observations must be photometrically calibrated to be able to compare them with other observations, e.g., from another telescope. This process is explained in the following subsections.

2.3.1 Standard Stars

To calibrate a magnitude system, a set of standard stars is required. These are well-observed stars (with known standard magnitudes) whose SEDs are well calibrated and known with precision. These standard stars are divided into different "categories":

- *Primary standards*: these are the main stars used to define a magnitude system. Vega (α Lyr), the F subdwarf BD $+17°4708$, and a few other Hubble Space Telescope (HST) CALSPEC sources (Bohlin et al., 2014) fall in this category.
- *Secondary standards*: these are stars distributed all around the sky, calibrated with the primary stars. As the primary stars are not observed all year round, historically, these have been used to calibrate observations. These stars have well-measured standard magnitudes and can be found in catalogues, e.g., Landolt (1992, 2007) and Smith et al. (2002).
- *Tertiary standards*: these are local stars in each SN field. They are calibrated using secondary standards. As individual observations do not usually include secondary stars in the field of view, tertiary stars can be used to easily calibrate each individual observation.

The main standard stars for optical photometric systems are: Landolt standards (Landolt, 1992, 2007), which are tied to Vega, and Smith standards (Smith et al., 2002), which are tied to AB via BD $+17°4708$.

2.3.2 Atmospheric extinction

Every ground-based observation will be subject to atmospheric extinction, which must be accounted for during photometric calibration. The amount of extinction will depend on altitude; the larger the distance between our line of sight and the zenith, the larger the atmospheric extinction. The magnitude of an object as if measured from above the atmosphere, m_0, is estimated as:

$$m_0 = m - k\sec(z) = m - kX \tag{2.8}$$

where k is the filter-dependent extinction coefficient and z is the angle with respect to the zenith (Bouguer's Law) and m is the observed magnitude. The term sec(z) is also known as the *airmass*, X, with values of 1 at the zenith and 2 at $z = 60°$. As the atmospheric extinction is wavelength dependent ($\propto \lambda^{-4}$), it affects bluer filters more than redder filters. A colour term can also be included for improved accuracy. This terms corrects for the fact that atmospheric extinction strongly depends on colour, so bluer objects lose more light than redder objects. However, I will not include the colour term for simplicity.

One can calculate k by observing a star at two different positions during the same photometric night (e.g., positions 1 and 2). As m_0 does not change, then:

$$m_2 - m_1 = k(X_2 - X_1), \tag{2.9}$$

from which k can be calculated. Clearly, an improved precision is obtained if this is done for several different positions and stars.

2.3.3 Natural Magnitudes

The signal of an object in an image is measured in counts, N_c, integrated along the length of the exposure, t_{exp}. N_c/t_{exp} is sometimes referred to as *raw* flux and is proportional to the flux of the object. The instrumental magnitude is defined as:

$$m_{inst} = -2.5\log_{10}(N_c/t_{exp}) = -2.5\log_{10}(\alpha F_0), \tag{2.10}$$

where α is the constant of proportionality and F_0 is the above-the-atmosphere flux. If we re-arrange the above equation we obtain:

$$m_{inst} = -2.5\log_{10}(F_0) + 2.5\log_{10}(\alpha) = m_{nat} + [kX - ZP] \tag{2.11}$$

where m_{nat} is the *natural* (calibrated) magnitude containing the above-the-atmosphere flux of the object, and the other term contains the atmospheric extinction (kX) and a zeropoint (ZP). The magnitude is called natural because it is specific/intrinsic to the combination of atmosphere-telescope-instrument-filter-detector. Different observing setups at different observatories produce different response functions, which can be accounted for using colour terms (e.g., Harris et al., 1981). For instance, the relation between the natural magnitude of a facility and a standard magnitude is given by:

$$m_{nat} = m_{std} - \epsilon C, \tag{2.12}$$

where ϵ is the colour term (a band-dependent constant) and C is a colour index (e.g., $B - V$). If we replace equation (2.12) in equation (2.11), we obtain:

$$m_{\rm inst} = [m_{\rm std} - \epsilon\, C] + [kX - ZP] \tag{2.13}$$

with ϵ and ZP as the only unknowns. Using a set of standard stars (see Section 2.3.1) and re-arranging the above equation, we can fit a model, such as a straight line, with ϵ as the slope and the ZP as the intercept, to obtain these parameters:

$$y = -m_{\rm inst} + m_{\rm std} + kX = \epsilon\, C + ZP. \tag{2.14}$$

Finally, with ZP in equation (2.11), we can calculate $m_{\rm nat}$.

2.4 Cross-Calibration of Multiple Photometric Systems

A photometric systems is tied to an specific combination of atmosphere-telescope-instrument-filter-detector, so a proper calibration of it is not trivial. Padmanabhan et al. (2008) introduced a method to photometrically calibrate wide-field optical imaging surveys, called *Ubercal*, achieving $\lesssim$2 per cent relatively accuracy for SDSS. Schlafly et al. (2012), using this same method, achieved $\lesssim$1 per cent relatively accuracy for the Panoramic Survey Telescope and Rapid Response System (Pan-STARRS) survey. However, most SN analyses that attempt to constrain cosmological parameters combine different SN samples to cover a wider range in redshift and improve statistics (e.g, Betoule et al., 2014).

A cross-calibration of photometric systems can be performed where one or more systems are tied to a single system (e.g., Betoule et al., 2013; Scolnic et al., 2015), the one with best precision and accuracy in the zeropoints. This is a very challenging step in current cosmological analyses with SNe Ia as the systematic uncertainties coming from the calibrations are one of the largest contributors to the uncertainty budget (e.g, Betoule et al., 2014; Scolnic et al., 2018b). Scolnic et al. (2015) performed one of the most recent cross-calibration between different SNe Ia surveys, called *Supercal*, taking advantage of the uniform calibration of Pan-STARRS (Schlafly et al., 2012), and used by Scolnic et al. (2018b).

In the near-future, the LSST and Foundation Supernova Survey (Foley et al., 2018; Jones et al., 2019) will reduce the uncertainties from photometric calibration with all the observations coming from only two different facilities, also providing a much larger sample of SNe Ia, at high and low redshift, respectively. However, other sources of systematic uncertainties will start dominating, such as the standardisation of SNe Ia, the main focus of this work.

2.5 Observational Corrections

When observing astronomical objects, one must always consider biases in the measurement due to different factors outside of the atmosphere. In this section, I will describe the concepts of dust extinction and K-correction.

2.5.1 Dust Extinction

Interstellar dust absorbs and re-emit photons, scattering them in random directions. This occurs when the typical size of dust grains is comparable to the wavelength of photons, producing an apparent dimming or 'extinction' of the light from objects in the line-of-sight (the direction in which one is observing). This effect is larger at bluer wavelengths, producing an apparent reddening in addition to extinction. Trumpler (1930) was one of the first works showing evidence of dust extinction in observations. The degree of reddening is measured by comparing the colour of an object, e.g., $(B - V)$, to its true colour, $(B - V)_O$, through the equation:

$$E(B - V) = (B - V) - (B - V)_O, \tag{2.15}$$

where $E(B - V)$ is the colour excess. In the last few decades, many works have focused on mapping the Milky-Way (MW) interstellar-dust reddening across the sky. Schlegel et al. (1998) built MW dust maps based on far-infrared emission of dust, modelling the temperature and optical depth of the dust, and then calibrating a relationship between the dust's far-infrared optical depth and optical reddening. This calibration was later updated by Schlafly & Finkbeiner (2011), scaling it by 0.86. The MW dust maps of Schlafly & Finkbeiner (2011) are the most widely used by the SN community nowadays.

Extinction and reddening are linked through the following equation:

$$A_V = R_V \times E(B - V), \tag{2.16}$$

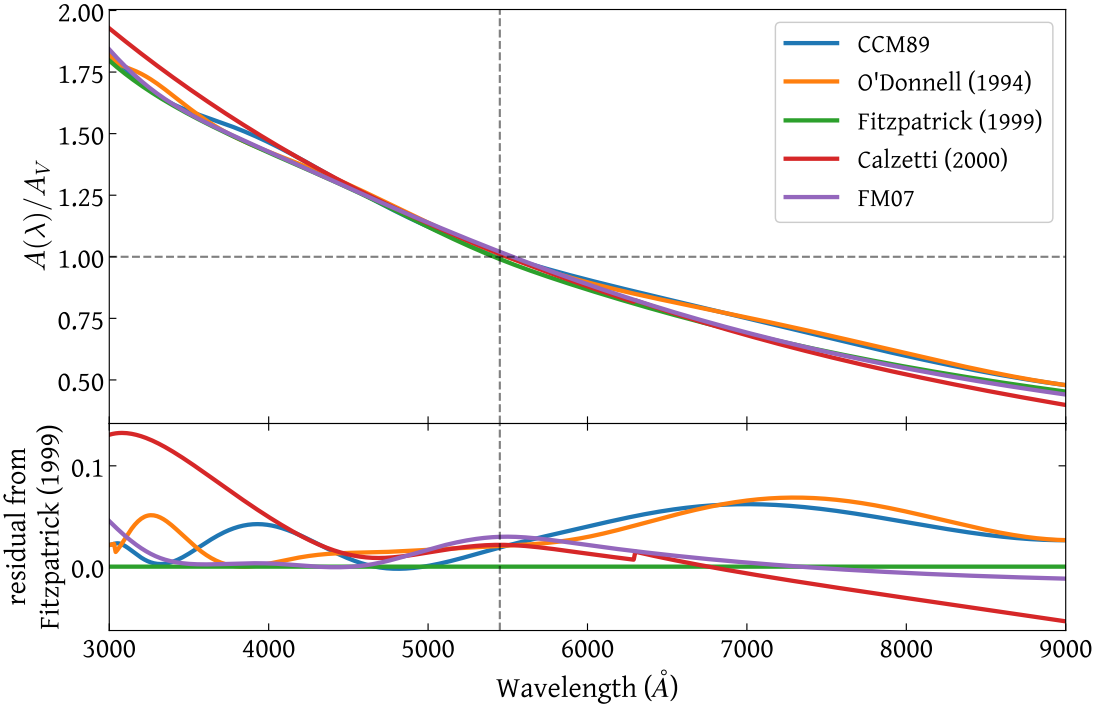

FIGURE 2.3: Comparison of different dust extinction laws: Cardelli et al. (CCM89, 1989, blue), ODonnell (1994, orange), Fitzpatrick (1999, green), Calzetti et al. (2000, red) and Fitzpatrick & Massa (FM07, 2007, purple). The *bottom* panel shows the residuals with respect to Fitzpatrick (1999). The vertical dashed grey line marks the approximate effective wavelength of the V band (∼5450 Å).

where A_V is the extinction in the V band, measured in units of magnitudes, and R_V is the total-to-selective extinction ratio, with a typical value in the MW of 3.1 (e.g., Schultz & Wiemer, 1975). Several works measured the variation of dust extinction as a function of wavelength (e.g., Cardelli et al., 1989; ODonnell, 1994; Fitzpatrick, 1999; Calzetti et al., 2000; Fitzpatrick & Massa, 2007), caused by the composition of the dust, known as *dust extinction law*. In Figure 2.3, I compare different dust extinction laws around optical wavelengths. Although they look relatively similar and have similar shape at optical wavelengths (top panel), they can differ in detail by up to several (∼10) per cent (bottom panel).

In Figure 2.4, I show a comparison of a Fitzpatrick (1999) dust extinction law for different values of R_V. As R_V is proportional to A_V, any difference in the total-to-selective extinction value directly translates to a difference in extinction. Determining R_V for other galaxies apart from the MW is very difficult as their detailed composition becomes harder to resolve with increasing distance, and has only being done with relatively high accuracy for nearby galaxies, such as the Small Magellanic Cloud and Large Magellanic Cloud (Gordon et al., 2003).

Dust extinction affects all extragalactic observations and thus should always be taken into account.

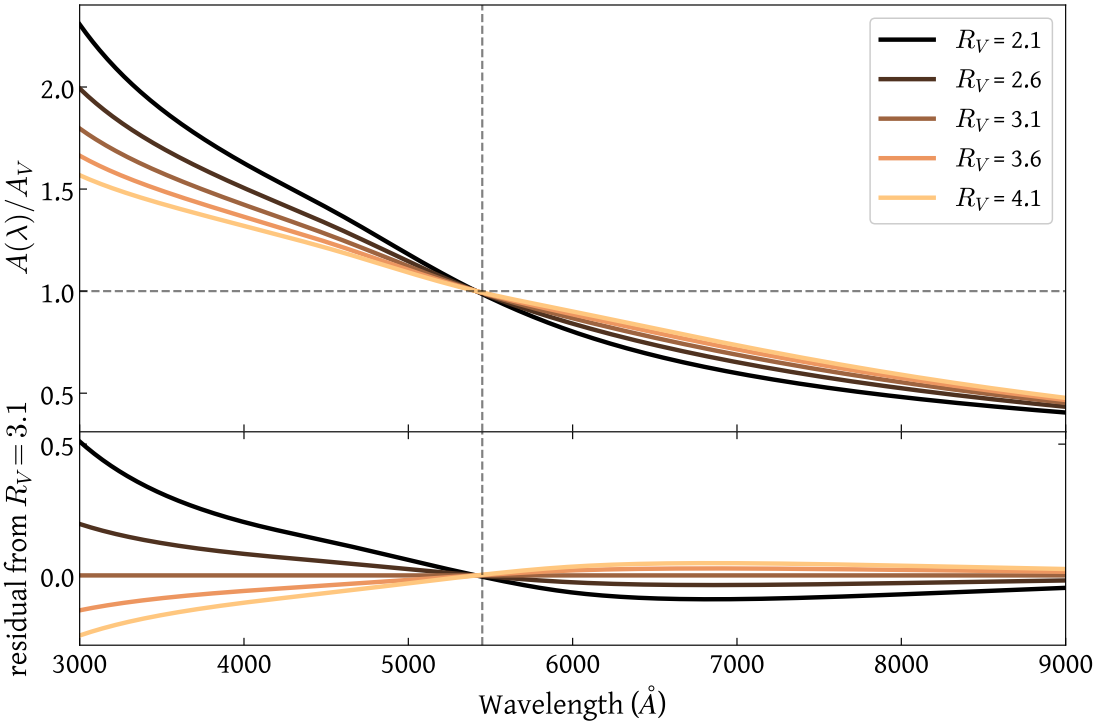

FIGURE 2.4: Comparison of a Fitzpatrick (1999) extinction law with different values of R_V. The *bottom* panel shows the residuals with respect to an $R_V = 3.1$, the typical value found in the MW (e.g., Schultz & Wiemer, 1975). The vertical dashed grey line marks the approximate effective wavelength of the V band (∼5450 Å).

2.5.2 *K*-correction

For objects with a non-zero redshift, the light of a rest-frame object is redshifted to longer wavelengths and is observed with an observer-frame filter. The *K*-correction (e.g., Oke & Sandage, 1968; Leibundgut, 1990; Hamuy et al., 1993; Kim et al., 1996) is used to calculate the apparent magnitude in some x filter of an object at a redshift z using the following equation:

$$m_x\left(z, t_{\text{obs}}\right) = M_x\left(t_{\text{rest}}\right) + \mu(\text{z}) + K_x\left(z, t_{\text{res}}\right), \tag{2.17}$$

where μ is the distance modulus, M_x is the absolute magnitude in x filter, t_{rest} is the time in the rest frame of the object, and $t_{\text{obs}} = (1+z)t_{\text{rest}}$ is the time in the observer frame. In other words, it is used to convert measurements into their respective rest frames.

At relatively low z, the observer-frame filters partially overlap with the same wavelength range of the observer-frame and rest-frame SEDs of an object. This is seen in the *middle* panel of Figure 2.5 for a SN Ia SED, where the observer-frame B filter observes approximately the same wavelength range of the observer-frame (solid black

lines) and rest-frame (dashed black line) SEDs. In this case, a single-filter *K*-correction is calculated by using the following equation:

$$K_x = 2.5\log(1+z) + 2.5\log\left(\frac{\int F(\lambda)T_x(\lambda)d\lambda}{\int F(\lambda/(1+z))T_x(\lambda)d\lambda}\right), \tag{2.18}$$

where F is the SED of an object and T is the transmission function of x filter. Therefore, the *K*-correction value will change depending on the SED of the observed object as well as its redshift. As z continues increasing, the observer-frame SED starts shifting further towards redder wavelengths. This is clearly shown in the *bottom* panel of Figure 2.5. At z =0.3, the observer-frame V filter observes approximately the same wavelength range of the observer-frame SED as a B filter would observe the rest-frame SED. In this case, a cross-filter *K*-correction for filters x and y is calculated by using:

$$\begin{aligned} K_{xy}(t,z) = &-2.5\log\frac{\int \lambda T_x(\lambda)Z(\lambda)d\lambda}{\int \lambda T_y(\lambda)Z(\lambda)d\lambda} \\ &+2.5\log\frac{\int \lambda T_x(\lambda)F(\lambda,t)d\lambda}{\int \lambda T_y(\lambda)\{F[\lambda/(1+z),t]/(1+z)\}d\lambda}, \end{aligned} \tag{2.19}$$

where F and T are as before, and Z is the SED of an object with known $x-y$ colour.

To summarise:

- photometry is the technique used to measure the light of astrophysical objects through filters. A combination of photometric system, defined by a given set of filters, and magnitude system, defined by a reference star (given that magnitudes are relative measurements), is used for this.
- The calibration of magnitude systems is performed by measuring the flux of several standard stars and depends on the total system response, i.e., on a combination of atmosphere-telescope-instrument-filter-detector. However, the combination of multiple systems is not trivial as the calibration will be different for each of these. Supercal is a method developed for the cross-calibration of multiple photometric systems. This is an important step as current cosmological SN analyses gather different SN samples to cover a wider range in redshift and improve statistics.
- Additionally, extinction- and *K*-correction are fundamental for all extragalactic observations as they bias the measurements. This is of great importance for SNe Ia observations when used for distance measurement, as high (sub-percent) precision and accuracy are required for current cosmological analyses. However, as the era of new survey is approaching, the systematic uncertainties will no longer

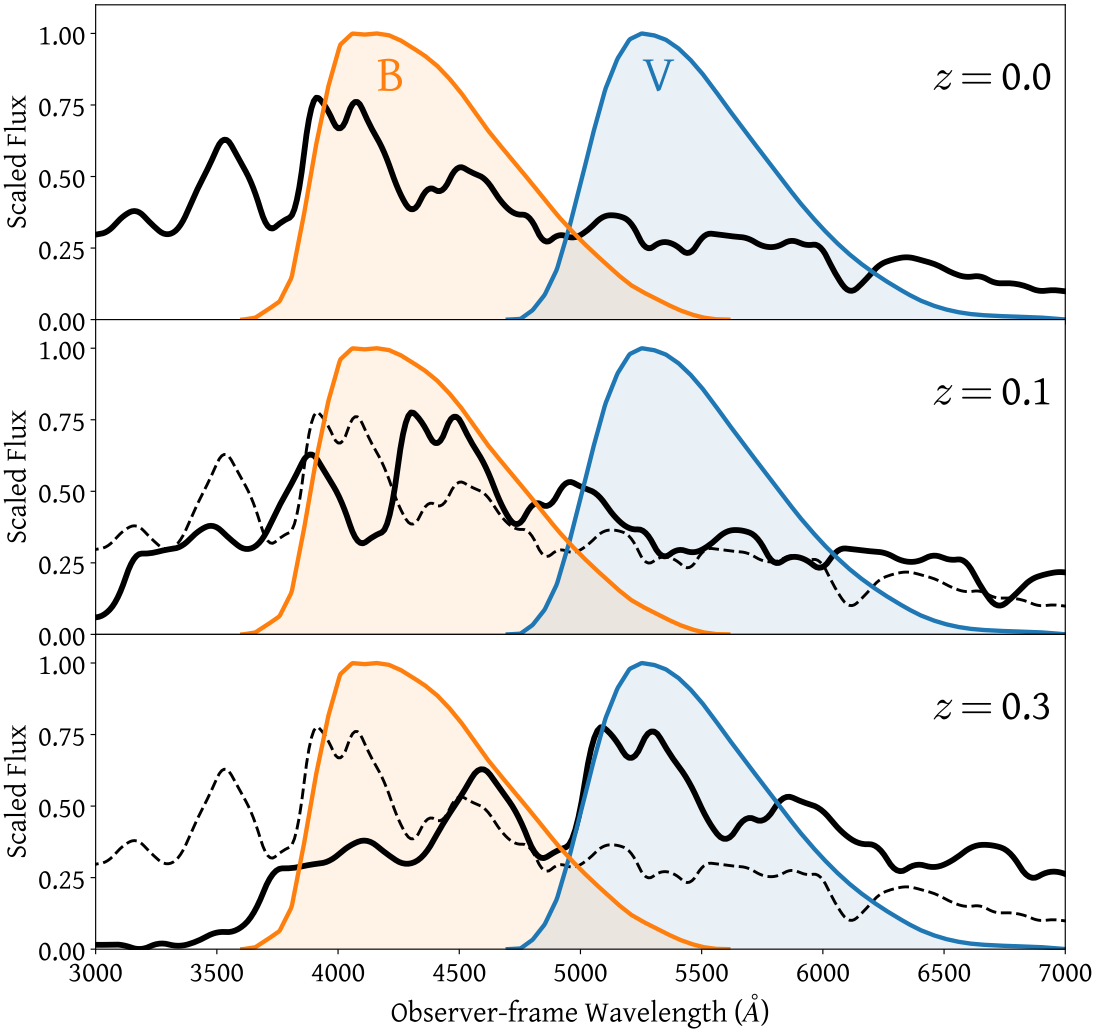

FIGURE 2.5: Observer-frame SED of a SN Ia at redshifts 0.0 (**top** panel), 0.1 (**middle** panel) and 0.3 (**bottom** panel). The observer-frame filters B (orange) and V (blue) and a rest-frame SED (dashed black line) are shown for reference. The observer-frame SED at z =0.0 completely overlaps with the rest-frame SED. As one observes at higher redshifts, the observer-frame SED starts shifting towards redder wavelengths.

be dominated by calibration, but by other sources, such as the standardisation of SNe Ia.

In the next chapter, I will present a new light-curve fitter, with the aim of improving the current standardisation of SNe Ia.

Chapter 3

PISCOLA: Python for Intelligent Supernova-COsmology Light-curve Analysis

In this chapter, I describe my new SN Ia light-curve fitter: **P**ython for **I**ntelligent **S**upernova-**CO**smology **L**ight-curve **A**nalysis (PISCOLA; Müller-Bravo et al., 2021). The code is open source[1] and written in PYTHON 3, a language widely used in the astronomy community. PISCOLA is intended to be simple and transparent in operation, allowing the user the opportunity to understand every step of the light-curve fitting and correction process. The full documentation can be found online[2]. In Figure 3.1, I show the main steps in PISCOLA, described in the following sections.

I wrote PISCOLA because most of the light-curve fitters that the community currently uses suffer from several limitations: they work with optical data only while SNe Ia are better suited for cosmology in the NIR (e.g., Elias et al., 1981, 1985; Freedman et al., 2009), they are susceptible to biases, e.g., due to the samples used for their training (e.g., Kessler et al., 2009b), and the light-curve parameters used for the standardisation of SNe might not extract all the underlying information, providing limited correction only. Therefore, PISCOLA provides an alternative to these other light-curve fitters.

In the next section, I describe Gaussian Processes (GPs), the backbone of PISCOLA, and motivate its implementation.

[1] https://github.com/temuller/piscola
[2] https://piscola.readthedocs.io/en/latest/

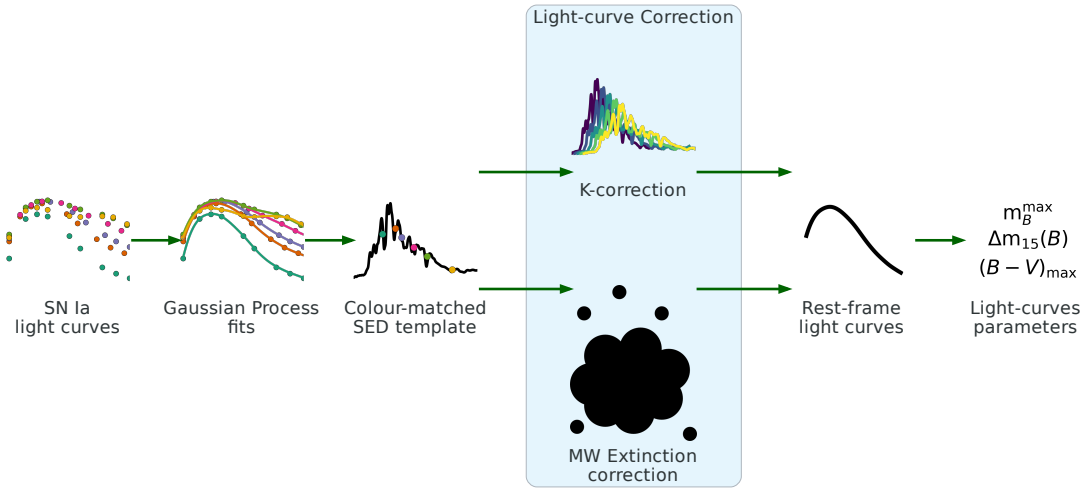

FIGURE 3.1: Flowchart of the main steps in the PISCOLA process. Gaussian Process (Section 3.1) is used to fit the SN Ia light-curves as a function of wavelength and time (Section 3.2). An spectral energy distribution time-series template is then 'warped' to match the observed SN colours, corrected for redshift (*K*-correction) and then MW dust extinction (Section 3.3). Finally, rest-frame light curves are obtained and the light-curve parameters estimated (Sec 3.4).

3.1 Gaussian Processes

GP is an excellent tool for data regression as it provides a more robust and natural way of interpolating and extrapolating data, and propagating errors than other methods, such as polynomials. The underlying assumption with GPs is that the data distributes as a multi-variate Gaussian distribution (see below), which is the case for most astronomical observations. This is because photons counts, which have Poisson distributions, are usually far from being scarce (specially in the optical regime), so the central limit theorem establishes that the sum of all these distributions tends towards a Gaussian distribution.

Polynomials, unlike GPs, can be undesirably global, i.e., data at one range of the model can have a strong influence on what the model does at a different range (Magee, 1998), which is usually something not desired. Splines, which are often preferred to polynomials, due to similar reasons, are just a special case of GP regression (Kimeldorf & Wahba, 1970).

PISCOLA uses GPs, a Bayesian method, to model the SN Ia light curves (Section 3.2) and SED time-series (Section 3.3). A GP is a random process where any point $\mathbf{x} \in \mathbb{R}^d$ is assigned a random variable $f(\mathbf{x})$ with Gaussian distribution and where the joint distribution of a finite number of these variables $p\left(f\left(\mathbf{x}_1\right), \ldots, f\left(\mathbf{x}_N\right)\right)$ is itself Gaussian. A GP model, $p(\mathbf{f} \mid \mathbf{X}) = \mathcal{N}(\mathbf{f} \mid \boldsymbol{\mu}, \mathbf{K})$, is defined by a mean function, $\boldsymbol{\mu}$, and a covariance function (also called a kernel), $\mathbf{K}$.

There are different types of kernels, e.g., 'squared exponential', 'rational quadratic', 'periodic', the 'Matérn family', etc., each with its own set of hyperparameters, parameters that cannot be learnt during the fitting process, but are set beforehand (however, these can be optimised). PISCOLA makes use of GEORGE (Ambikasaran et al., 2016), a GP implementation in PYTHON that allows the user to choose between several well-known kernels. My code implements three of these: squared exponential (SE), Matérn 3/2 (M32) and Matérn 5/2 (M52). The Matérn family is broadly used in different areas of research as it is effective at describing different physical processes (e.g., Rasmussen & Williams, 2006), such as light curves, while the Squared Exponential kernel provides a smoother fit for the mangling function (see Section 3.3). These kernels are defined as follows:

$$k_{SE}(x, x') = \sigma^2 \exp\left(- \frac{|x - x'|^2}{2\ell} \right), \tag{3.1}$$

$$k_{M32}(x, x') = \sigma^2 \left(1 + \frac{\sqrt{3}\,|x - x'|}{\ell} \right) \exp\left(- \frac{\sqrt{3}\,|x - x'|}{\ell} \right), \tag{3.2}$$

$$k_{M52}(x, x') = \sigma^2 \left(1 + \frac{\sqrt{5}\,|x - x'|}{\ell} + \frac{5\,|x - x'|}{3\ell^2} \right) \exp\left(- \frac{\sqrt{5}\,|x - x'|}{\ell} \right), \tag{3.3}$$

where the length-scale, ℓ, and variance, σ^2, are the hyperparameters of the kernels. Figure 3.2 shows a comparison between the three kernels. The main difference between them is the covariance between points, being higher for the Squared Exponential kernel than for the other two (for two data points at a fixed distance, for a fixed set of hyperparameters).

Figures 3.3 & 3.4 show a comparison between different length scales and variances, respectively, for the Squared Exponential kernel, for a fixed mean function equal to zero. The length scale determines the length of the 'wiggles' in a function, giving also a sense of how far one can extrapolate the data. The variance determines the average distance of the function away from its mean. For more details about the GP method, see Rasmussen & Williams (2006).

3.2 The Light-Curve Model

With PISCOLA, unlike many other SN light curve fitters, there is no underlying SN template or model that is directly fit to the observed light curves; the observer-frame modelling is entirely data driven. This allows PISCOLA to fit any band (ultraviolet, optical, NIR, etc.) as long as data is available. GP has also been used in the context

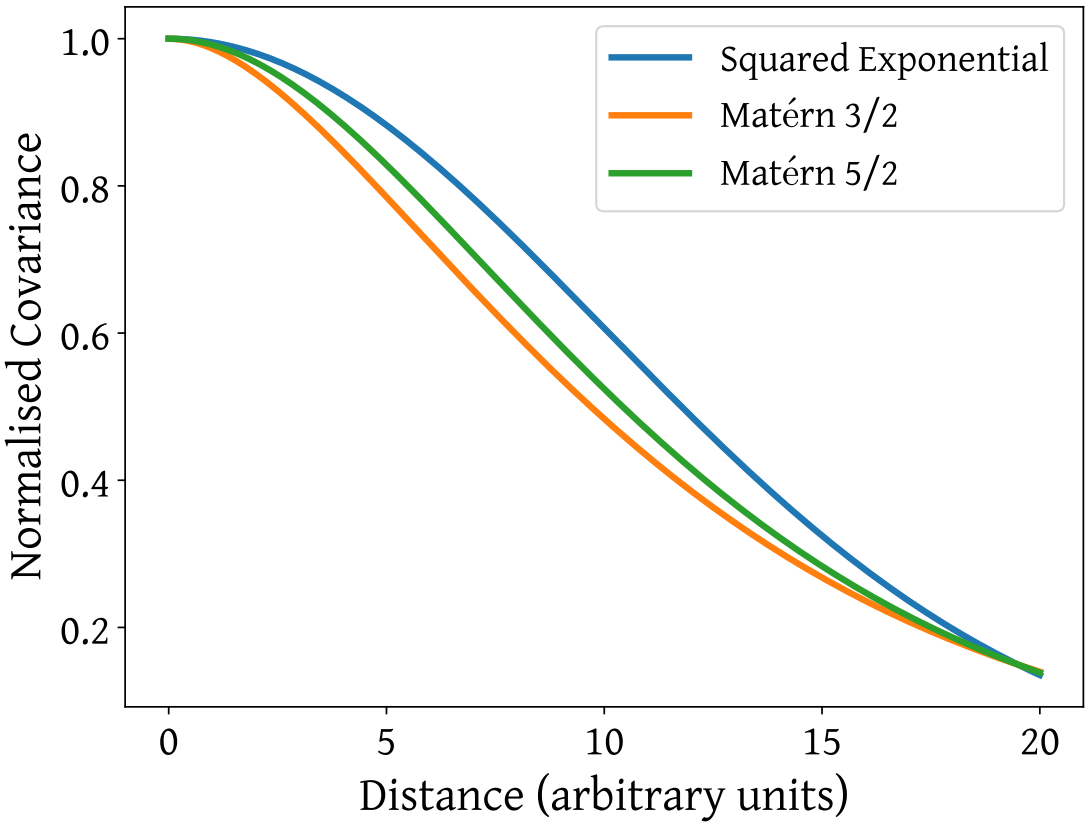

FIGURE 3.2: Comparison of the covariance between three kernels, with fixed hyperparameters, available with PISCOLA: Squared Exponential (blue), Matérn 3/2 (orange) and Matérn 5/2 (green).

of SN light curves before, in cases where the underlying model is not well known or no assumptions wants to be made about it (e.g., Kim et al., 2013; Dhawan et al., 2018; Inserra et al., 2018; Angus et al., 2019; Avelino et al., 2019) or to build templates/models (e.g., Kim et al., 2013; Avelino et al., 2019), with excellent results in both cases. PISCOLA falls in the former cases as I do not want to make any assumptions of the underlying model.

The fitting of the SN multi-colour observer-frame light curves is performed in two dimensions, as a function of time and wavelength. All three hyperparameters are optimised at this stage: length scales for the time and wavelength axes, and the variance. I fit in magnitude space as the logarithmic scale provides smoother and more accurate GP fits than using fluxes directly; when fitting in flux space, the large difference in flux between rest-frame B-band and other bands can produce fits with an under-estimated B-band peak (this happens for different choices of kernel).

One disadvantage of fitting in magnitude space is that non-detections are not used as they cannot be represented correctly in magnitude space (some non-detections can have negative values as well). This also means that data around peak luminosity will have more weight than data in the tails of the light curves, for measurements with the

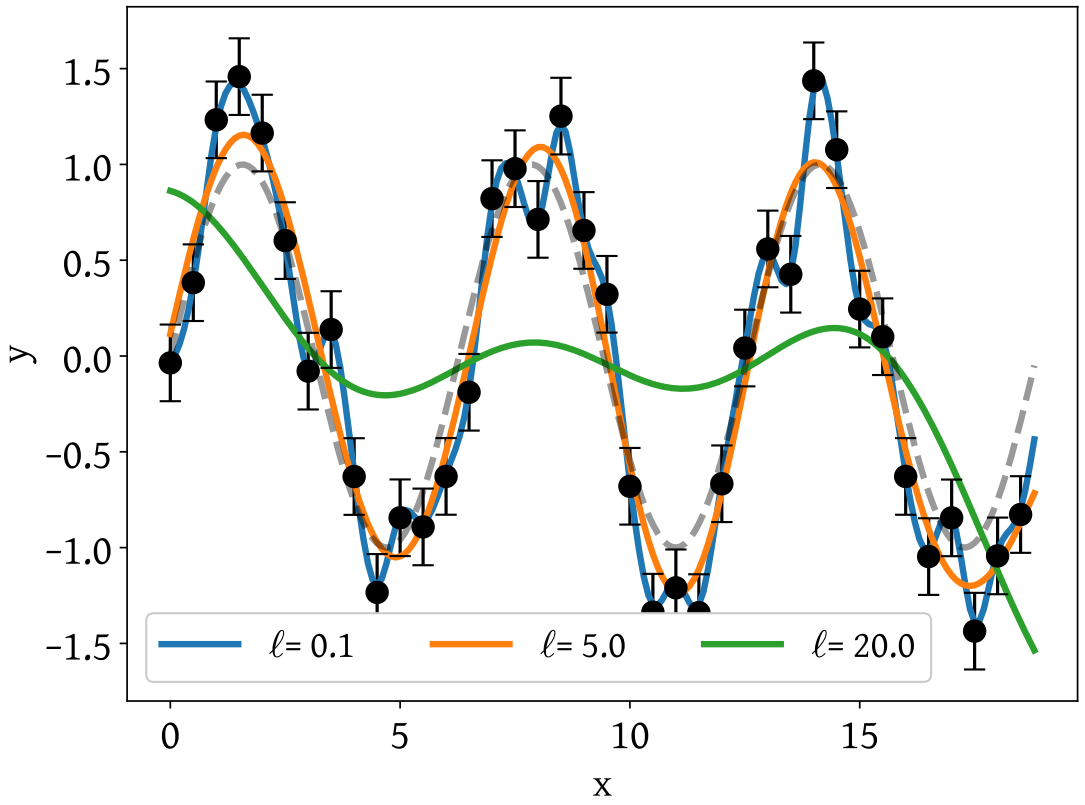

FIGURE 3.3: Comparison between different length scale values (ℓ) for a Squared Exponential kernel with fixed variance: 0.1 (blue), 5.0 (orange) and 20.0 (green). GP fits (solid lines) were performed on simulated data (black circles). Only the mean GP model is shown in each case for visualisation. The underlying function, from which the simulated data was extracted from, is shown as well (dashed grey line).

same uncertainty in flux space, during the regression. I note that it is the data around peak that interests me most in the light-curve fitting for the application shown in this work.

Another disadvantage of fitting in magnitude space is that lower S/N observations have asymmetric errors, which represent an issue for GP regression. However, these can be removed by masking out these observations (see Chapter 4), although this reduces the amount of useful data.

Multi-colour light curves trace different wavelengths of the same underlying SED. Thus, a 2D regression provides more robust results than fitting in one dimension at a time (flux as a function of time, for each band independently), as it uses information from multiple bands to cover gaps in the data, allowing a better interpolation and extrapolation. An example is shown in Figure 3.5, where I compare the three different kernels implemented in PISCOLA. The fits with Matérn 5/2 and Squared Exponential kernels produce almost identical results, with the former having slightly larger (more conservative) uncertainties, while the fits with a Matérn 3/2 kernel produces

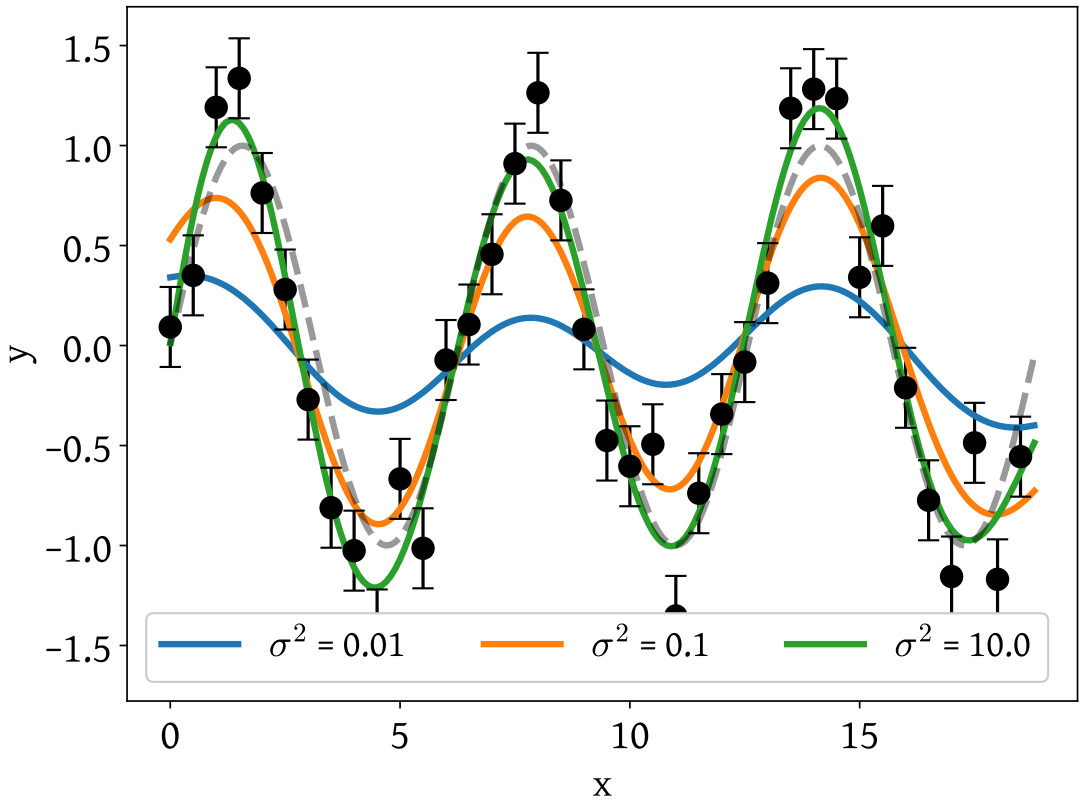

FIGURE 3.4: Comparison between different variance values (σ^2) for a Squared Exponential kernel with fixed length scale: 0.01 (blue), 0.1 (orange) and 10.0 (green). GP fits (solid lines) were performed on simulated data (black circles). Only the mean GP model is shown in each case for visualisation. The underlying function, from which the simulated data was extracted from, is shown as well (dashed grey line).

less smooth light curves. A Matérn 5/2 kernel is the default option in PISCOLA as it produces flexible yet smooth fits.

A further advantage of fitting in 2D is that a more accurate estimation of the time of B-band maximum light ($t_B^{\max}$) is obtained compared to 1D fits by naturally interpolating the rest-frame B band. The time of peak luminosity in a given band is estimated from the GP fit by calculating the time at which the derivative becomes zero at the effective wavelength of the desired band. For the case of the rest-frame B band, we denote the time of peak luminosity as parameter $t_B^{\max}$. This is important as the light-curve correction process depends on this (see Section 3.3).

Moreover, PISCOLA can produce excellent results with low-redshift ($z \lesssim 0.1$) SNe Ia, i.e., objects with relatively well-sample light curves and high-S/N. This is of great importance for the estimation of the Hubble constant, measurement of peculiar velocities in the local universe, and the extraction of astrophysics from the SNe Ia light curves, to name just a few of many applications. In Figure. 3.6, I show the PISCOLA fit to a low-z SN, SN 2004ey from the CSP survey. We see that PISCOLA produces great results. In Figure 3.7, we show the SALT2 fit we performed to the same SN, using the

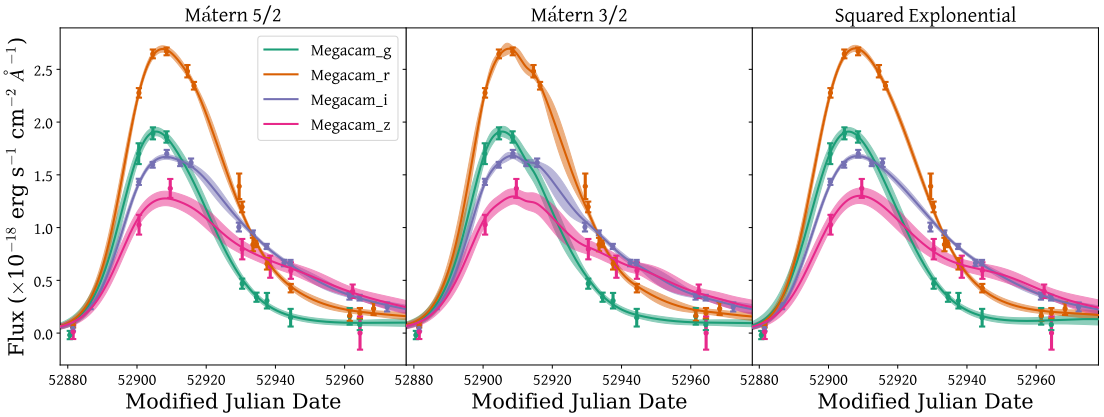

FIGURE 3.5: GP model of the observer-frame multi-colour light curve of the SN Ia SNLS-03D1au using Matérn 5/2 (**left** panel), Matérn 3/2 (**midde** panel) and Squared Exponential kernels (**right** panel). The original data, from the supernova legacy survey, observed in the Canada–France–Hawaii Telescope MegaCam *griz* filters are shown as points with uncertainties. The solid lines show the mean of the GP model, and the shaded areas represent one standard deviation (1σ).

implementation of the code in `sncosmo` (Barbary et al., 2016). In this case, we see that SALT2 produces larger residuals compared to PISCOLA.

I see that PISCOLA outperforms SALT2 when fitting the CSP u and r, which are on the blue and red limits, respectively, of the effective training range of SALT2 (∼3000–7000 Å), although it stretches out to redder bands (∼9000 Å), but with less precision. Furthermore, PISCOLA produces great results with the i band, even fitting the secondary peak, showing the potential of fitting NIR light curves. I also note that PISCOLA produces better results in bands like CSP g and V (`csp_o` in Figure 3.7), important for the estimation of colour and colour evolution in SNe Ia.

It is of interest to see the comparison of light-curve fits for SNe from different surveys as well. In Figures 3.8 & 3.9, I show fits and residuals using PISCOLA, with default parameters, and SALT2, using the sncosmo implementation, with the light-curve parameters from Scolnic et al. (2018b), respectively, for SNe 2004eo, 2008ar , SDSS-6936, SDSS-6057, SNLS-03D1au, SNLS-04D3fq, PS1-000174 and PS1-520022, from different surveys used in Chapter 4. The SALT2 fits of SNe 2004eo and 2008ar are in disagreement with the data in almost every band (especially g-band for SN 2004eo), presumably because the SALT2 template is a poor match to the data. For SNe SDSS-6936 and SDSS-6057, both sets of fits (PISCOLA and SALT2) produce relatively similar results in *gri*-bands. However, for SN SDSS-6936, the u band is wider, more luminous and peaks later for PISCOLA. In the case of SN SDSS-6057, the u band is more luminous for SALT2. The z bands for these SNe are outside the valid range of SALT2 (3000 – 7000 Å in the rest-frame). For the rest of the SNe, the fits look relatively similar, with some differences in shape (specially SNLS-04D3fq, the highest redshift object between these SNe), mainly driven by the poorer coverage (compered to the lower-z SNe). The

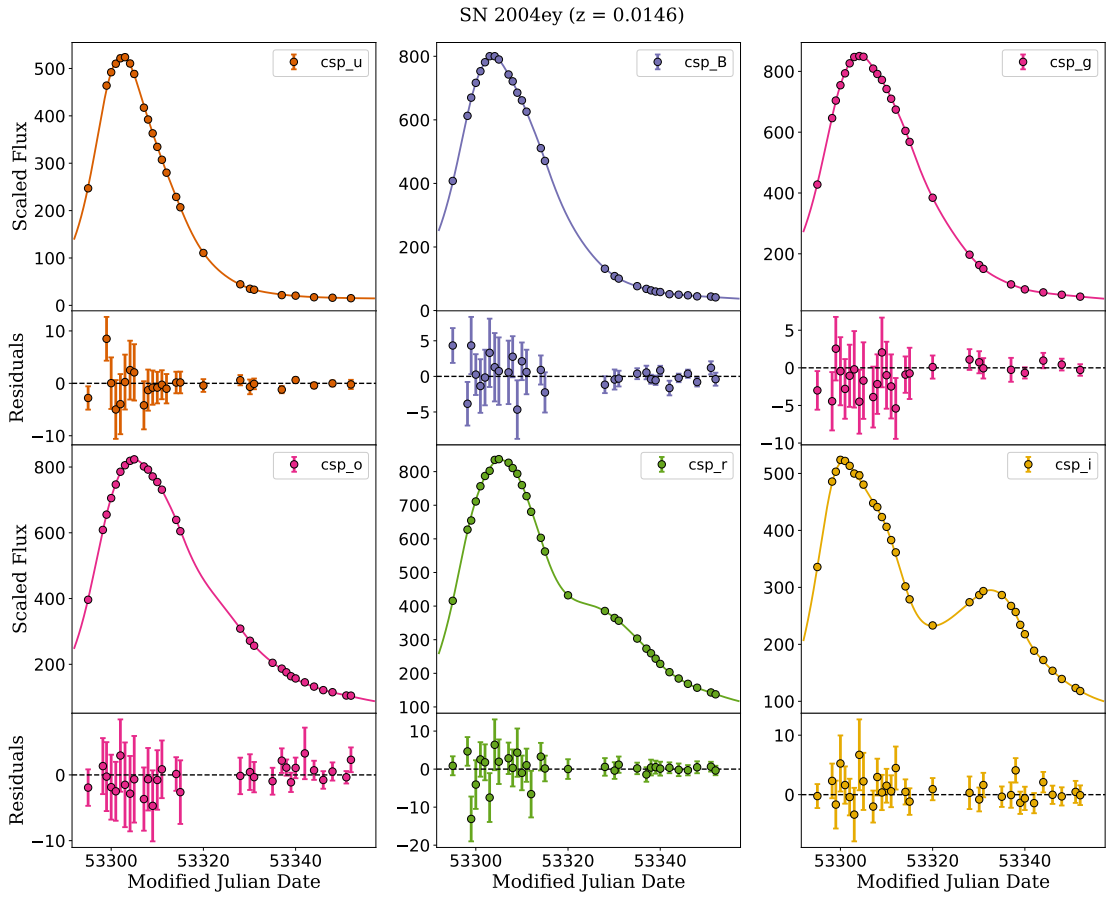

FIGURE 3.6: PISCOLA light-curves fits and residuals of SN 2004ey from the CSP survey. The observational uncertainties for this SN are small so they are only seen in the residual plots. The label `csp_o` is used by PISCOLA to refer to one of the three available CSP V-bands[3].

PISCOLA fits of g and r bands of PS1-520022 have a box-like shape, in part due to the lack of data in these bands, but also driven by the data in i band.

In terms of residuals, PISCOLA produces better results, especially for the low-z SNe, most likely due to the data-driven nature of the GP model. One can clearly see that the advantage of PISCOLA also relies on being able to fit any band, contrary to SALT2, which is only valid in the 3000 – 7000 Å range in the rest-frame.

3.3 The SED Model

The observer frame light-curve models from PISCOLA can then be used to estimate rest-frame light curve quantities, usually through K-corrections (see Section 2.5.2). This is performed using a SN Ia SED time-series template (e.g., Nugent et al., 2002; Hsiao et al., 2007), which PISCOLA adjusts (or 'mangles') so that it reproduces the colours of

[3]see `https://csp.obs.carnegiescience.edu/data/filters` for more details.

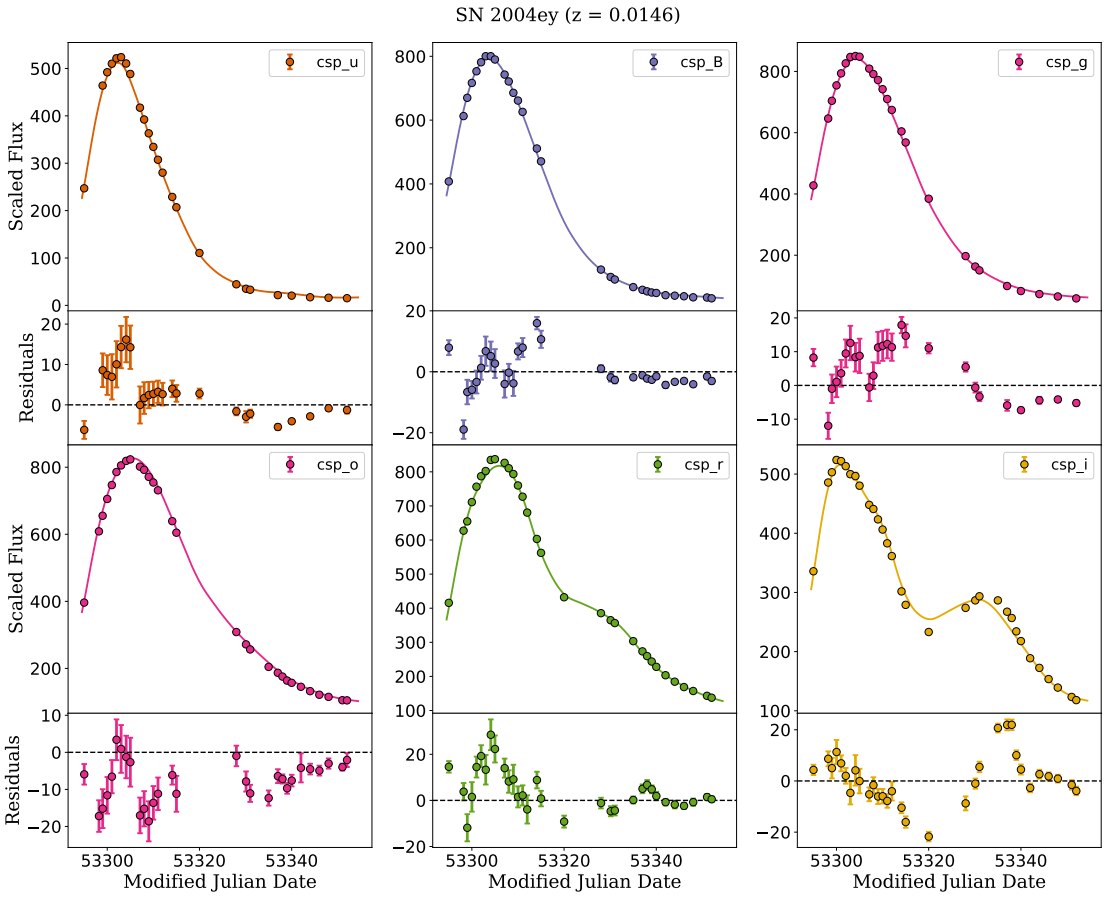

FIGURE 3.7: SALT2 light-curves fit and residuals of SN 2004ey from the CSP survey. The rest of the description is the same as in Figure 3.6.

the observed light curve at each epoch, as estimated by the GP model (see also Hsiao et al., 2007; Conley et al., 2008). The result is a colour-matched SED template, i.e., a SN Ia SED time-series which reproduces the observed light curves of the SN being fit.

The colour-matching is performed by multiplying the SED template by a wavelength-dependent function at the desired phases (time with respect to $t_B^{\max}$), after which the template reproduces the observed light-curve when integrated through the observed filters. This wavelength-dependent function is often represented by a spline in the literature, but PISCOLA makes use of GPs with (by default) a Squared Exponential kernel, resulting in a smooth function and a natural way of propagating uncertainties in the process. The steps for developing the mangling function are as follows:

1. The SED template is redshifted to the SN redshift;
2. MW dust extinction (see Section 2.5.1) is then applied to the redshifted SED template;
3. The filters used in the observations are used to calculate the fluxes in those bands;

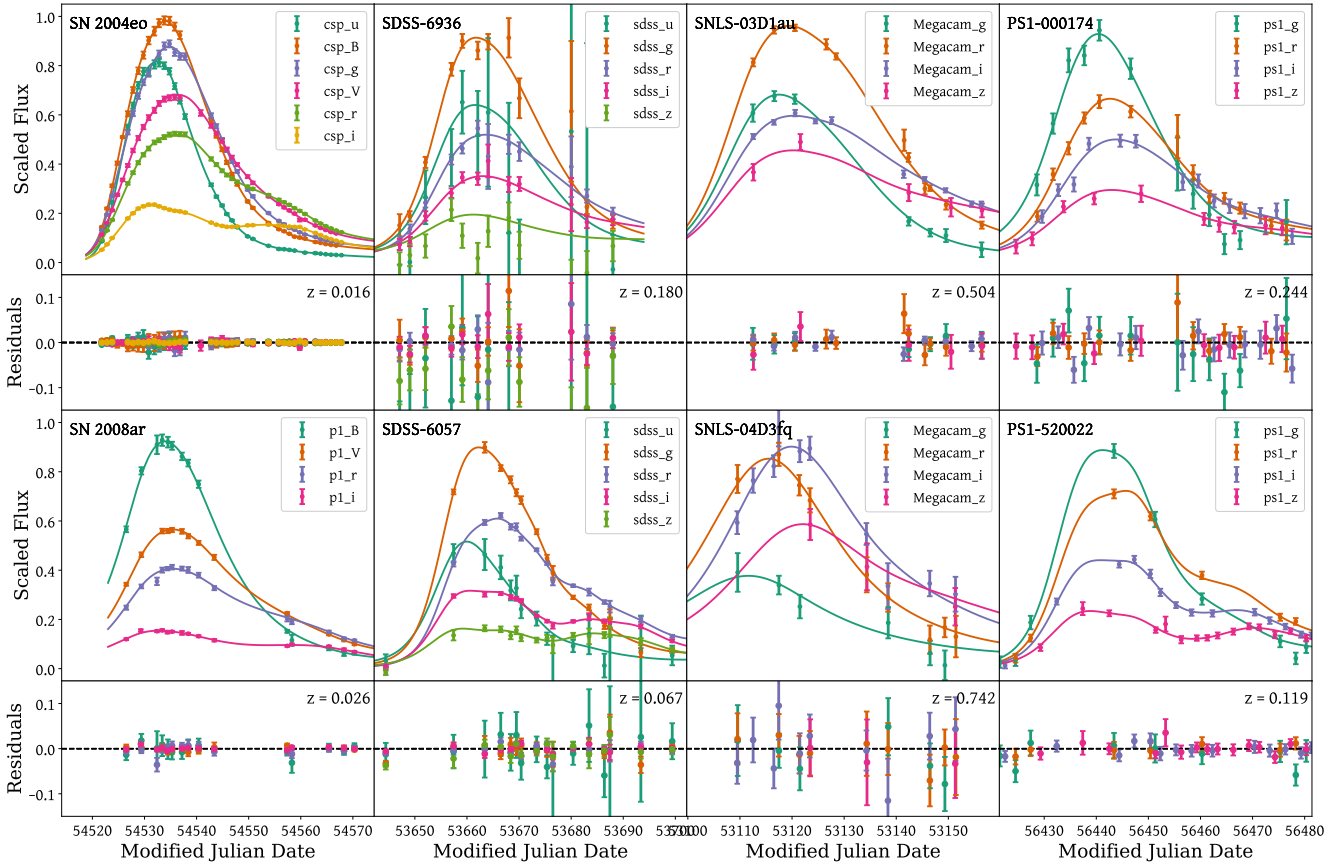

FIGURE 3.8: PISCOLA fits and residuals, using the default parameters, for SNe 2004eo (**top left** panels), SDSS-6936 (**top middle left** panels), SNLS-03D1au (**top middle right** panels), PS1-000174 (**top right** panels), 2008ar (**bottom left** panels), SDSS-6057 (**bottom middle left** panels), SNLS-04D3fq (**bottom middle right** panels), PS1-520022 (**bottom right** panels), from different surveys used in Chapter 4. The bands used for each SN are included the legends, while their redshifts are included in the residual panels. Some of the fits appear trimmed as PISCOLA does not extrapolate far beyond the data range (a few days in the time-axis). The uncertainties of the fits are not shown for visualisation.

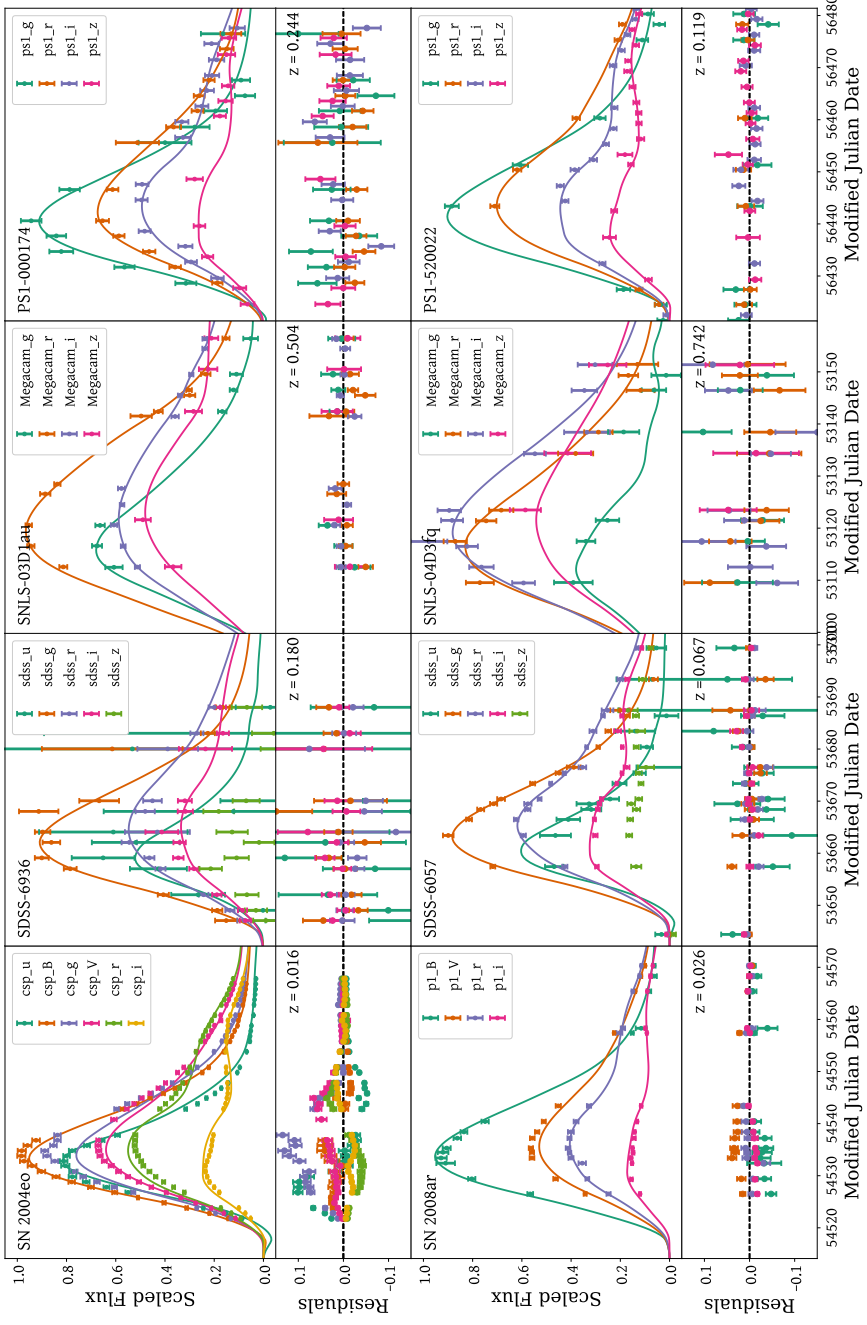

FIGURE 3.9: Same as Figure 3.8, but for SALT2, using the `sncosmo` implementation and the light-curve parameters from Scolnic et al. (2018b). The SALT2 fit of the SDSS-z band of SNe SDSS-6936 and SDSS-6057 are not displayed as they are outside the valid range of the light-curve fitter (3000 – 7000 Å in the rest-frame). The uncertainties of the fits are not shown for visualisation.

4. The ratios between the fluxes of the observed SN and the SED template are calculated for each band and centred at their respective effective wavelengths;

5. The mangling function is then calculated by modelling the flux ratios with GPs using an squared exponential kernel.

The first two steps reproduce the effects that the photons experience from their origin in the SN until they reach us (without considering other sources of extinction other than MW dust). The SED template is then multiplied by the mangling function to produce a colour-matched SED. An example of the resulting mangling function and SED template is shown in Figure 3.10.

As this process does not ensure a perfect agreement between the observed magnitudes and those from the colour-matched SED per-se, an optimisation routine is used, where the flux ratios are the parameters to be adjusted to improve the agreement. Given that the mangling function is required to be smooth as a function of wavelength (assuming that all SNe Ia have relatively similar SEDs), there is a trade-off between smoothness and the accuracy of the recovered magnitudes. However, any difference between the observed and recovered magnitudes is propagated in the error budget.

As a final step, the colour-matched SED template is corrected for MW extinction and blueshifted back to the rest-frame to obtain a final, rest-frame SED model. PISCOLA corrects for MW dust extinction using the Schlafly & Finkbeiner (2011) dust maps and a Fitzpatrick (1999) extinction law as default. Other implementations of the dust maps (Schlegel et al., 1998) and extinction laws are also available. The SFDMAP[4] and EXTINCTION (Barbary, 2016) PYTHON packages are used to perform the corrections. PISCOLA does not correct for any other sources of extinction, such as host galaxy extinction or circumstellar dust.

This procedure is repeated for as many phases as desired, depending on the data coverage.

3.4 Light-Curve Parameters

The output of the previous sections is a rest-frame time-series SED SN Ia template that reproduces the observer-frame light curves of the SN Ia being fit. From this, rest-frame light curves in any required band can be calculated (within the wavelength and phase limitations of the input data), together with various light-curve parameters. The choice of rest-frame light-curve parameters to measure is arbitrary; in this analysis, I calculate traditional light curve parameters: the B-band peak apparent magnitude ($m_B^{\max}$), the decline in magnitudes in the 15 days following $t_B^{\max}$ ($\Delta m_{15}(B)$; Phillips, 1993), and the

[4] https://github.com/kbarbary/sfdmap

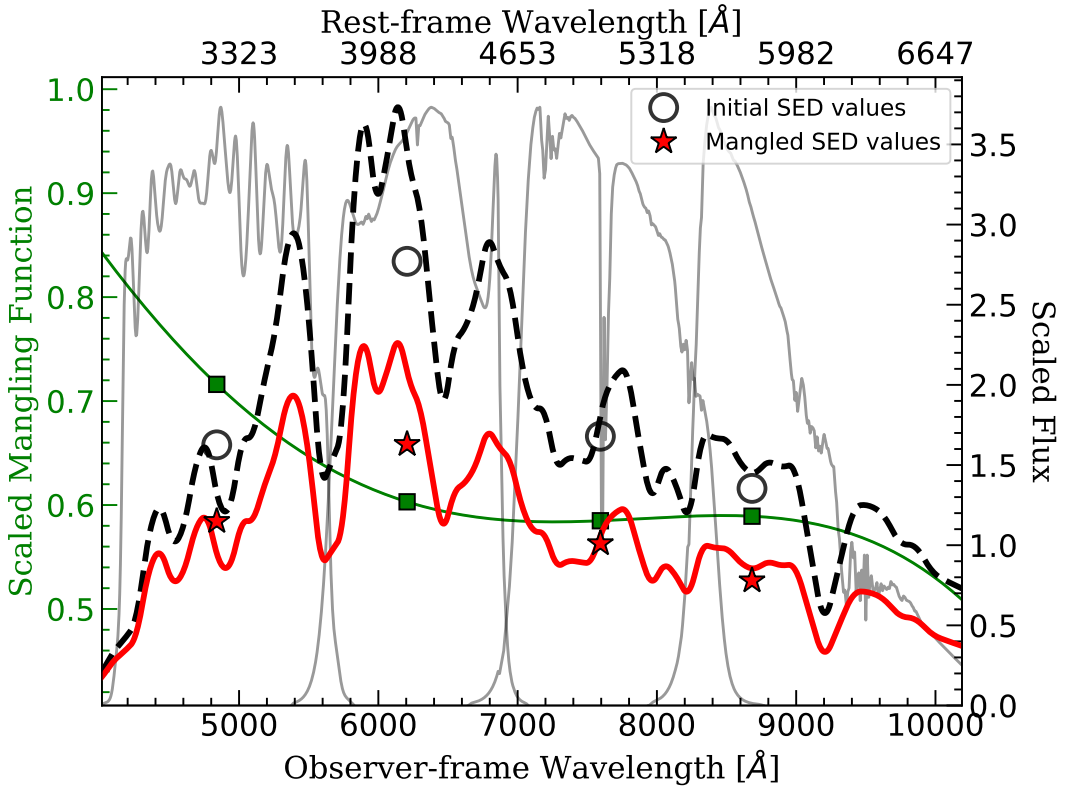

FIGURE 3.10: Mangling function (solid green line) for SNLS-03D1au at $t_B^{\max}$. The green squares represent the flux ratios of the different bands centred at their respective effective wavelengths. The initial SED (dashed black line) is compared to the SED multiplied by the mangling function (solid red line). The initial (black open circles) and mangled (red stars) SED fluxes are also shown. The transmission functions of the filters used are plotted in grey. The scaling is arbitrary for visualisation.

$B-V$ colour at $t_B^{\max}$ ($(B-V)_{\max}$; Tripp, 1998). In Figure 3.11, I show an example of a resulting rest-frame B-band light curve of a SN Ia (hereafter, B-band refers to the rest-frame B-band).

Note that the procedure described depends on an initial estimate of $t_B^{\max}$, which is updated from the final rest-frame light curve. If the initial and updated estimate of $t_B^{\max}$ are not consistent, the process is repeated with the new estimate until convergence is reached or after a given number of iterations.

3.5 Calibration

Several aspects of the light curve fitting process are affected by the choices in the analysis, including the extinction law, the SN Ia SED time-series template and the transmission functions of the filters. In Chapter 4, I will compare PISCOLA with results from the SALT2 light curve fitter, thus, I need to ensure a proper calibration for a robust comparison.

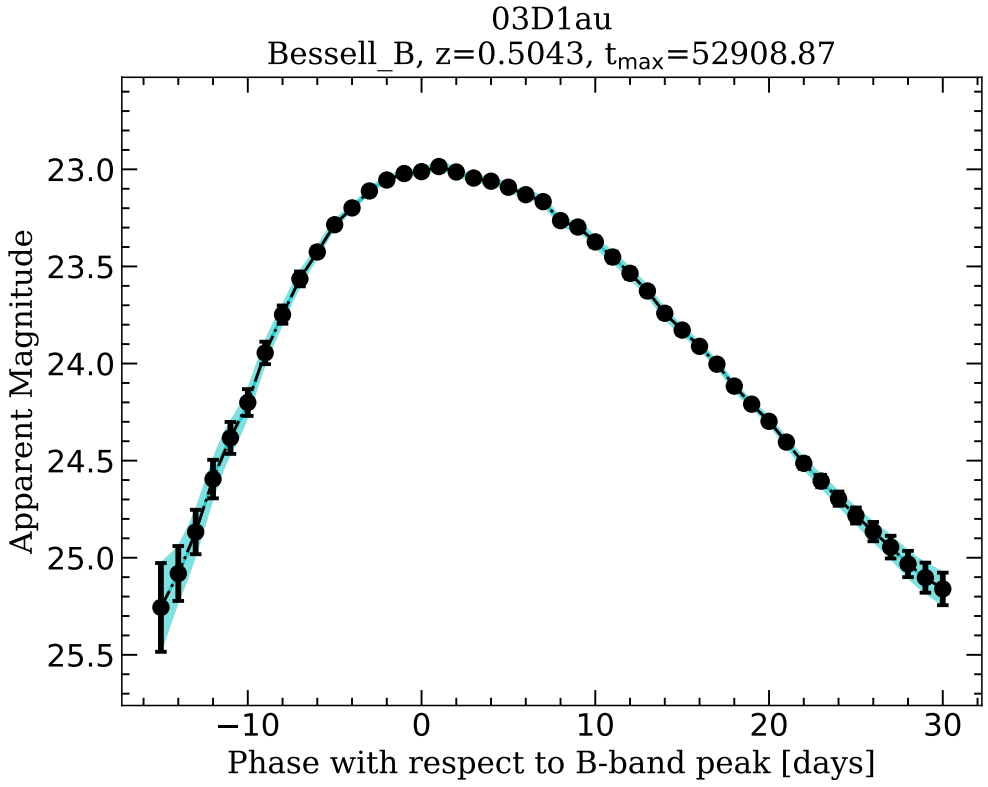

FIGURE 3.11: Rest-frame *B*-band light curve of SNLS-03D1au. In this case, observations with Megacam-*griz* filters were used to construct the *B*-band light curve.

To minimise the sources of discrepancy for the comparison between codes, I ensure my choices follow Scolnic et al. (2018b) as much as possible:

- A reddening law from Fitzpatrick (1999) is adopted;
- The SN Ia SED time-series template is the M_0 components from the SALT2 model (`salt2_template_0.dat`). I do not include the SALT2 x_1-dependent component in the SED as PISCOLA does not measure this parameter (i.e., a template with $x_1 = C = 0.0$ is used). In principle, this may lead to small differences in the *K*-corrections when compared to SALT2. For instance, when including the x_1-dependent component (assuming the x_1 values from Scolnic et al. 2018b), the differences in the rest-frame *B*-band light curve, compared to not including it, are on average $\lesssim 0.01$ mag around peak and $\lesssim 0.03$ mag at earlier or later phases. However, note that there is no reason to assume that both codes agree on the measurement of stretch for every SN;
- The same filter transmission functions as in Scolnic et al. (2018b) are used for the observed light curves;
- The same photometric calibration systems (e.g., AB using BD $+17°4708$ as primary standard) are used for magnitude systems from different surveys;

- The Bessell filters (Bessell, 1990), shifted to match Landolt (1992) observations of standard stars, (i.e., to match the Landolt transmission functions, which are nominally a realisation of the Johnson–Morgan-Cousins system), as included in SALT2 (see Betoule et al., 2014), are used to estimate the light-curve parameters (for more information about the shifts, see Appendix A of Conley et al. 2011).

In this chapter I presented PISCOLA, a new SN Ia light curve fitting tool. The light-curve model is based on GP, a data-driven regression method, which presents several advantages over other commonly used methods, such as polynomials and splines, and even other light-curve fitters. I also compared the light-curve fits produced by PISCOLA against those of SALT2. This comparison showed that PISCOLA has the advantage of fitting any band, regardless of the the effective wavelength (contrary to SALT2), producing slightly better (lower) residuals. Additionally, PISCOLA implements GPs for its SED model to produce a colour-matched SED time-series template for the correction (dust extinction and K-corrections) of the light curves in order to extract light-curve parameters for the standardisation of SNe Ia.

In the following chapter, I will test PISCOLA with simulations and real data in search of possible biases and to validate this new light-curve fitter.

Chapter 4

Validation

Having introduced PISCOLA, I present in this chapter a series of extensive tests, with simulations and real data of SNe Ia, performed on PISCOLA to validate this light-curve fitter.

4.1 Pantheon SN Ia Sample

Throughout this and most of the following chapters, I make use of the Pantheon SNe Ia sample (Scolnic et al., 2018b), representing one of the most comprehensive compilations of SNe Ia to date. Pantheon comprises many SNe Ia surveys: the Harvard Center for Astrophysics (CfA) surveys 1–4 (Riess et al., 1999; Jha et al., 2006; Hicken et al., 2009b,a, 2012), the Carnegie Supernova Project (CSP; Contreras et al., 2010; Folatelli et al., 2010; Stritzinger et al., 2011), the Sloan Digital Sky Survey SN Survey (SDSS; Frieman et al., 2008; Kessler et al., 2009b; Sollerman et al., 2009; Sako et al., 2018), the Supernova Legacy Survey (SNLS; Astier et al., 2006; Guy et al., 2010), the Panoramic Survey Telescope and Rapid Response System 1 (Pan-STARRS1/PS1) Medium Deep Survey (Rest et al., 2014; Scolnic et al., 2014) and different *Hubble Space Telescope* (HST) surveys: the Supernova Cosmology Project (SCP; Suzuki et al., 2012), the Great Observatories Origins Deep Survey (GOODS; Riess et al., 2007), and the Cosmic Assembly Near-infrared Deep Extragalactic Legacy Survey + Cluster Lensing And Supernova Survey with Hubble (CANDELS+CLASH; Graur et al., 2014; Rodney et al., 2014; Riess et al., 2018).

I denote the compilation of the CfA1–4 and CSP surveys as the 'low-z' sample (or survey), as they only contain SNe Ia at $z < 0.1$. For a more detailed description of the surveys, see Scolnic et al. (2018b) or their respective references. I use the SALT2 light-curve parameters for these SNe Ia from Scolnic et al. (2018b)[1].

[1] https://archive.stsci.edu/prepds/ps1cosmo/

4.2 SNANA

I use the SuperNova ANAlysis software (SNANA; Kessler et al., 2009a), version `v10_75c`, to simulate transient surveys and produce light curves of simulated transient events, accounting for the survey observing pattern, limiting magnitudes, pointing on the sky, and so forth. The generated SNe are based on light-curve models – in this case I used the SALT2 model from Betoule et al. (2014, version 2.4) as this is one of the most widely used light-curve fitters and was also used by Scolnic et al. (2018b). More precisely, the light curves are generated from an SED time series template with a given value of x_1 and c (SALT2 light-curve parameters; see equation (1.27)), which are randomly drawn from observational distributions as found in Scolnic & Kessler (2016), and given a z value and observational patterns according to the specifications of every survey. The distributions of x_1, c and z are different for each survey due to a combination of several factors, such as Malmquist bias; for more details, see Scolnic & Kessler (2016). Additionally, I restrict my simulations to the ground-based surveys (low-z, SDSS, SNLS and PS1), which make up 98 per cent of the sample, as PISCOLA does not perform well with poorly-sampled light curves from the *HST* surveys. Approximately 500 SNe are simulated for each SN survey and for each individual test. In other words, each simulated Pantheon-like sample contains a total of ∼2000 SNe Ia (the choice of this number is explained in Section 4.3.4). A flat ΛCDM cosmology with $H_0 = 70\,\mathrm{km\,s^{-1}\,Mpc^{-1}}$, $\Omega_\mathrm{m} = 0.3$ and $\Omega_\Lambda = 0.7$ is used throughout this chapter.

4.3 Validation with simulations

I test PISCOLA through a comparison between the fits and the simulations based on $\mathrm{m}_B^{\max}$, i.e., the residual between simulated $\mathrm{m}_B^{\max}$ value and the estimated value obtained with PISCOLA, which I will sometimes refer to as $\Delta\mathrm{m}_B^{\max} \equiv m_{B,\mathrm{PISCOLA}}^{\max} - m_{B,\mathrm{simulations}}^{\max}$. I focus on the effects of cadence, the mean time between consecutive observations of an object in the same filter, and observational uncertainties or, equivalently, S/N.

SNe are fitted in an automated way with the default GP kernels and over -15 to $+30$ days with respect to $t_B^{\max}$ (default phases). In addition, I include some constraints to ensure a sufficient coverage of the peak: at least one data point in any band over -7 and 0 days, one from 0 to $+7$ days, and one from -3.5 and $+3.5$ days (this final constraint can overlap with one or both previous constraints). We also mask out observations with a S/N ≤ 5 to prevent poor-quality fits and asymmetric errors. We note that applying cuts in S/N does not bias the light-curves fits around $t_B^{\max}$ or the estimation of $\mathrm{m}_B^{\max}$ (tested on real data and simulations from the following sections), although it could possibly bias the fits at earlier or later epochs. However, for the analysis in this work, we are mainly concerned about the data around peak. Note that the cuts applied are

different, but more stringent than those applied in other analyses using SALT2 (e.g., Scolnic et al., 2018b), discarding more SNe. However, these are required given the nature of how PISCOLA works.

These constraints reduce the sample of SNe, but they ensure a relatively good quality light curve data required by GP interpolation. The chosen values are somewhat arbitrary, but small changes do not significantly alter the results. We note that, although template-driven fitters can fit SNe with different S/N, they may introduce biases as, in case of low S/N, the fitters will mainly retrieve the light-curve parameters of the templates being used.

4.3.1 Pantheon-like sample simulation

The first step is to test PISCOLA with a simulation with the same characteristics as the Pantheon sample. This allows me to check what survey characteristics work best for my code. Example light curves from simulated SNe with the characteristic of the low-z, SDSS, SNLS and PS1 surveys are shown in Figure 4.1. These help to visually check if the simulations can properly reproduce the observations.

After simulating the SNe Ia, I proceed to fit them with PISCOLA. I discard some SNe at different stages of the fitting process for several reasons:

1. The observer-frame wavelength coverage does not cover the rest-frame B-band at the redshift of the SN (e.g., SNe at high redshift);
2. The temporal coverage does not allow an initial estimation of $t_B^{\max}$ (e.g., many low-z do not have data prior to the B-band peak);
3. PISCOLA is unable to estimate an accurate B-band light curve. This happens when PISCOLA does not converge to an estimation of $t_B^{\max}$; e.g., several low-z SNe have their B-band peak only partially covered, and $t_B^{\max}$ can fall close to the limits of the coverage, producing a failure to estimate a new peak;
4. The light-curve does not satisfy the additional constraints on peak coverage (Section 4.3), mainly due to a combination of low cadence and/or masking of low S/N data;
5. Visual inspection reveals poor PISCOLA fits, mainly caused by remaining poor data quality.

The first three reasons are automated by PISCOLA. Discarding SNe after visual inspection is only feasible due to the relatively low number of SNe. This is a limitation, and for future implementations I aim to automate it with a statistically-motivated metric,

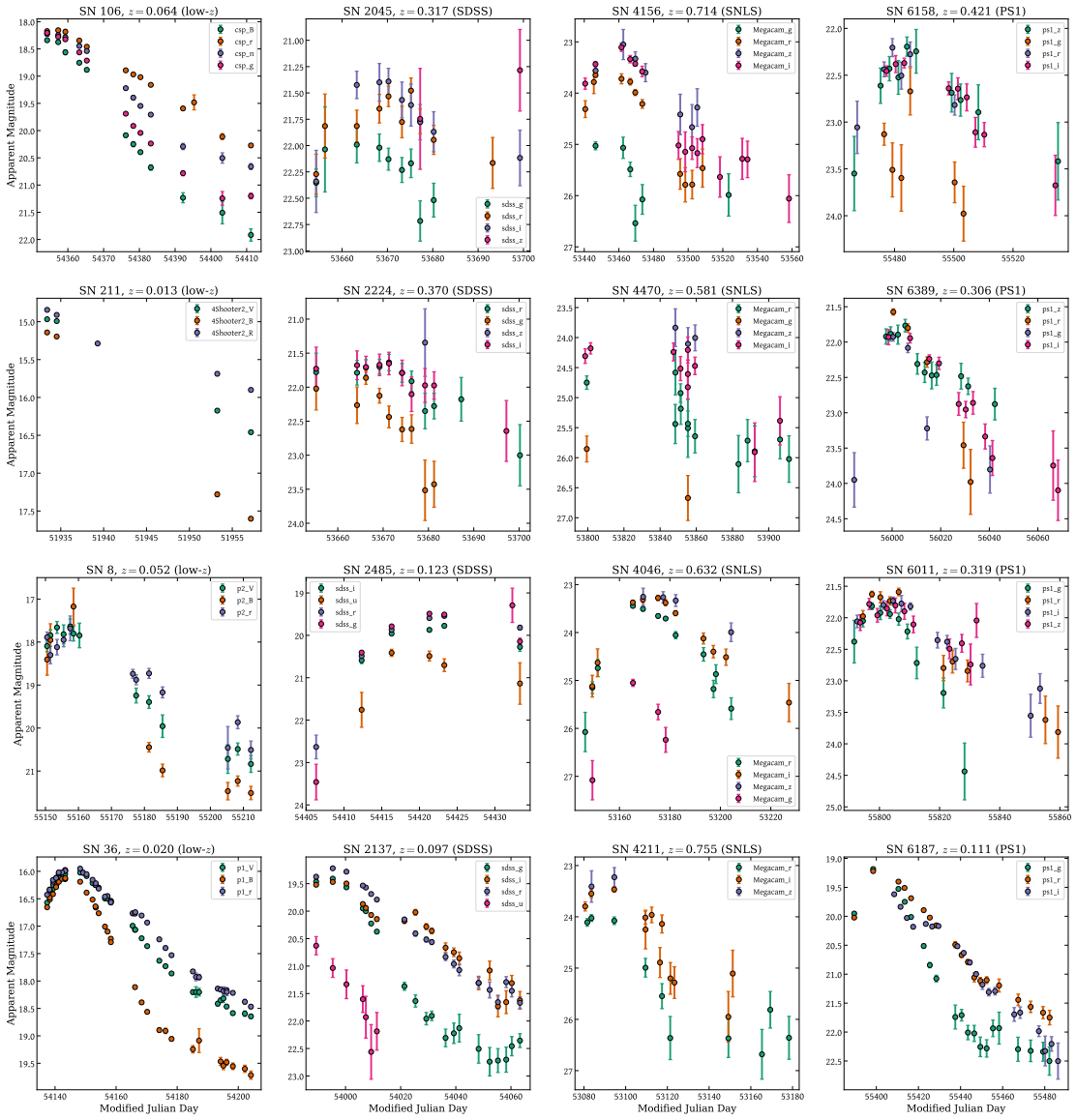

FIGURE 4.1: Example light curves of representative simulated SNe with the characteristic of the low-z (**left**), SDSS (**middle left**), SNLS (**middle right**) and PS1 (**right**) surveys. Four SNe per survey are shown with their respective redshifts.

which is the aim of this set of tests. I note that future surveys, such as LSST, will produce higher quality observations with lower uncertainties and better cadences (e.g., Lochner et al., 2018; Scolnic et al., 2018a).

I successfully fitted (obtained m_B^{max}) ∼50 per cent of the SNe. This is a low number compared to other light-curve fitters, but highlights the relatively poor data quality of some historical surveys that SNANA simulates. Stages (2) and (4) are the main causes of discarding SNe (see Section 4.4). I note that these discarding reasons do not strongly depend on redshift but mainly on the observation strategy of each survey.

The comparison between the PISCOLA-measured and simulated m_B^{max} values is shown in Figure 4.2. In Table 4.1, I show the values of Δm_B^{max}. There are no significant (i.e.,

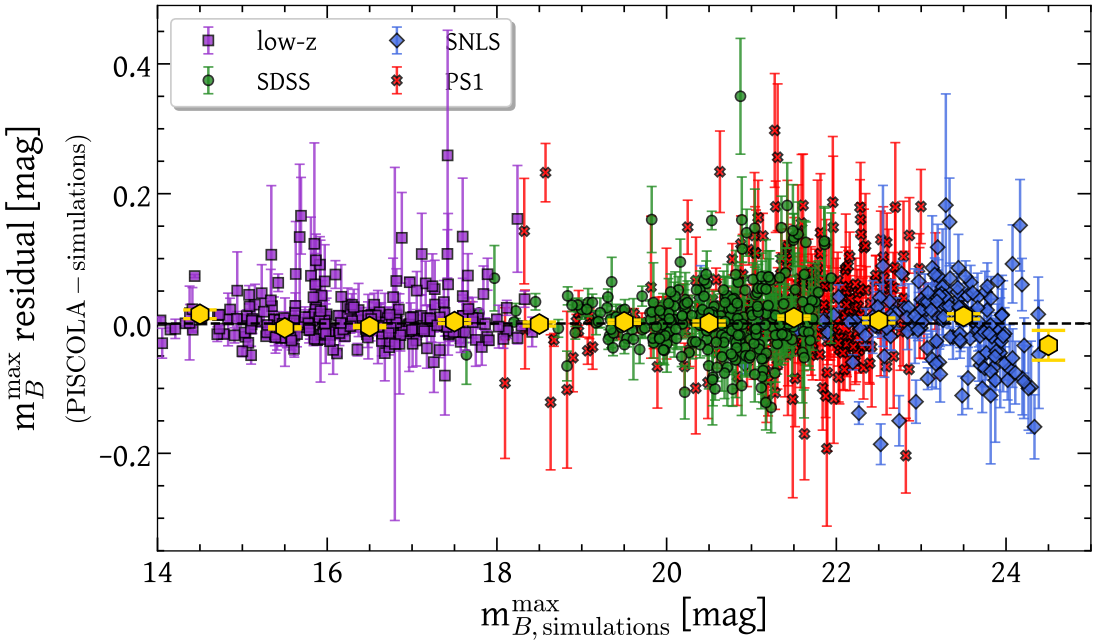

FIGURE 4.2: $\Delta m_B^{max} \equiv m_{B,PISCOLA}^{max} - m_{B,simulations}^{max}$ for a Pantheon-like simulation. Each point represents a single simulated SN, colour-coded according to the legend. The uncertainties are 1σ and are taken from the PISCOLA fits. The golden hexagons represent the weighted mean in bins of 1 mag with their respective uncertainties (1σ). SNe for which PISCOLA over-predicts the luminosity have negative residuals and vice versa.

TABLE 4.1: Weighted mean, uncertainty on the weighted mean and weighted standard deviation of Δm_B^{max} for a Pantheon-like simulation (Section 4.3.1).

survey	weighted mean (mmag)	error on the weighted mean (mmag)	weighted standard deviation (mmag)
low-z	1	1	24
SDSS	4	2	34
SNLS	3	2	29
PS1	7	2	35

$<3\sigma$) deviations from $\Delta m_B^{max} = 0.0$ mag for all surveys, except for PS1 at 3.5σ significance but small (< 0.01 mag) deviation. This is mainly caused by a few SNe with underestimated m_B^{max} and small uncertainty. Additionally, Figure 4.2 shows that some low-z SNe have underestimated m_B^{max} values, while some SNLS SNe have the opposite. This is most likely due to a combination of cadence and S/N and is further investigated in the following section. Generally, I conclude that PISCOLA is successful at retrieving accurate m_B^{max} values at < 0.01 mag.

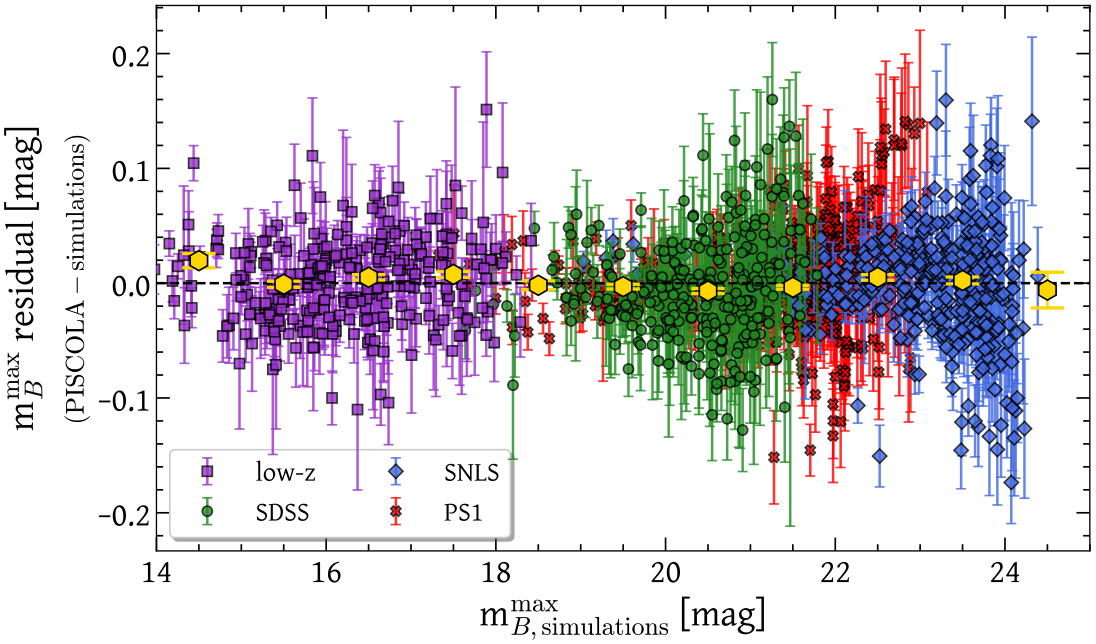

FIGURE 4.3: The description is the same as in Figure 4.2, but for a 7-day cadence Pantheon-like simulation.

4.3.2 Effect of observational cadence

As PISCOLA is a data-driven fitting method, the cadence is important as the GP model has no prior for the true shape of the SN light curves. I therefore simulated a set of Pantheon-like samples with cadences between 1 and 10 days in steps of 1 day, and took the 1-day cadence simulation as my benchmark. Observations are equally spaced for all bands (e.g., simultaneous/same-day *griz*-bands observations every x days) and with random characteristics drawn from survey-dependent distributions. I then estimated the reliability of PISCOLA as the cadence becomes poorer. An example comparison for PISCOLA-measured and simulated m_B^{max} values for the 7-day cadence simulation is shown in Figure 4.3. The results for all the simulations, with different cadences, are shown in Figure 4.4.

I successfully fitted (obtained m_B^{max}) ∼75–85 per cent of the SNe in each of the 1- to 7-day cadence simulations, and ∼60–75 per cent for the 8- to 10-day cadence simulations (SALT2 fits $\gtrsim$98 per cent of the simulated SNe in all cases). The unsuccessful SNe are mainly due to low-S/N light curves in the SDSS, SNLS and PS1 simulated samples and B-band peak not well covered (e.g., data only after peak) in the case of low-z objects. SNe were discarded for the same reasons as in Section 4.3.1. At relatively high cadence ($\lesssim$7 d), PISCOLA is accurate when estimating m_B^{max} for the different surveys (i.e., $\lesssim$ 3σ deviations from $\Delta m_B^{max} = 0.0$ mag; see bottom panel of Figure 4.4). However, the accuracy is improved for SNLS and PS1 compared to low-z and SDSS samples, given their superior S/N and/or rest-frame cadence.

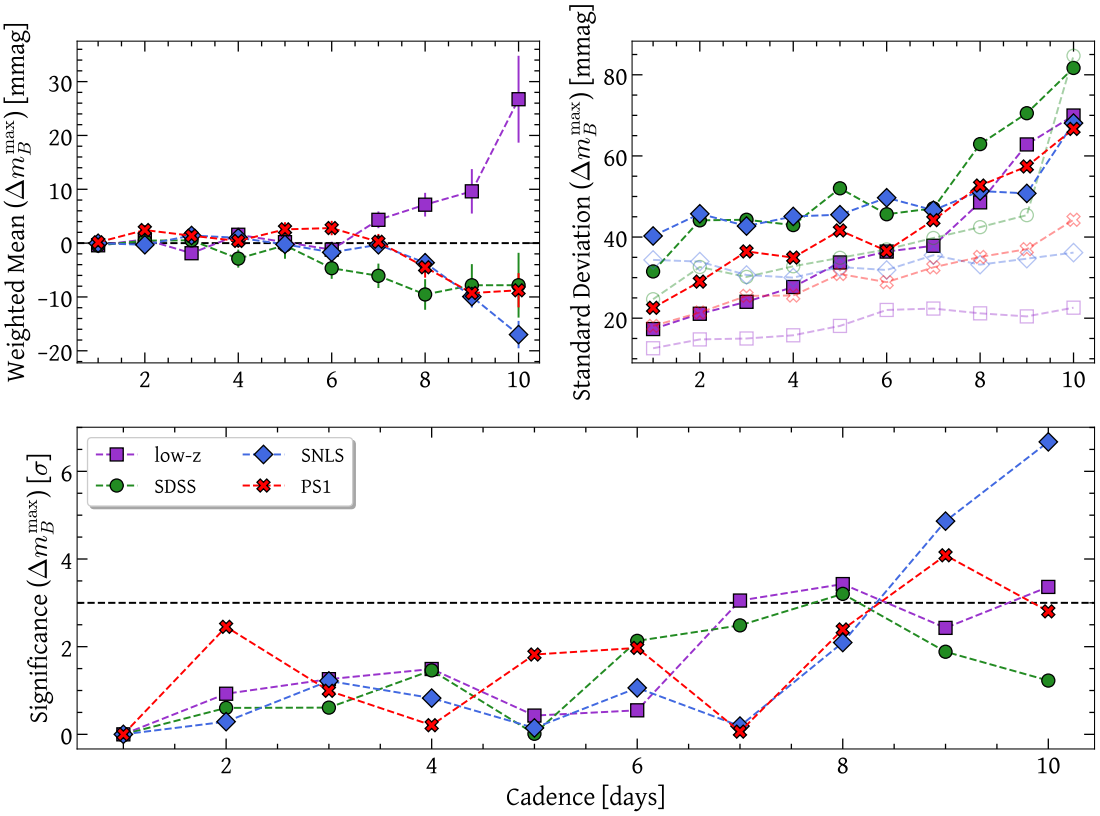

FIGURE 4.4: Weighted mean with uncertainty on the weighted mean (**top left** panel) and standard deviation (**top right** panel) of $\Delta m_B^{\max}$ for simulations with cadences between 1 and 10 days. The standard deviation of $\Delta m_B^{\max}$ for SALT2-measured $m_B^{\max}$ values, i.e., $m_{B,\mathrm{SALT2}}^{\max} - m_{B,\mathrm{simulations}}^{\max}$, are also shown for comparison (transparent symbols in the **top right** panel). Measured significant deviations of $\Delta m_B^{\max} = 0.0$ mag in units of σ are also shown (**bottom** panel). The horizontal line in the bottom panel marks a significance of 3σ.

As redshift increases, the rest-frame cadence increases (i.e., time between consecutive rest-frame measurements decreases) for fixed observer-frame cadence, due to time dilation ($\Delta t_{\mathrm{obs}} = (1+z)\Delta t_{\mathrm{rest}}$). This gives improved light-curve coverage, but with a trade-off of S/N. I examined $\Delta m_B^{\max}$ versus redshift, but see no clear trend. The surveys at different redshifts also generally perform similarly as a function of cadence. I find that PISCOLA accurately retrieves $m_B^{\max}$ ($\lesssim 3\sigma$ deviations from $\Delta m_B^{\max} = 0.0$ mag) for cadences similar to those of most high-redshift transient surveys, which have a typical cadence of about 7 days in the observer frame (e.g., DES).

However, when the cadence is $\gtrsim$7 days, the performance of PISCOLA on the low-z simulated sample is quantitatively different to the performance on the higher-redshift simulations. At low-z, PISCOLA under-predicts $m_B^{\max}$ ($\Delta m_B^{\max}$ is positive). This is because the peaks of the light curves are smoothed out: the GP model has no information about their true shape and thus does not recover the peak given a lack of information. In the other simulations (SDSS, SNLS and PS1), the opposite trend is seen: $\Delta m_B^{\max}$ is

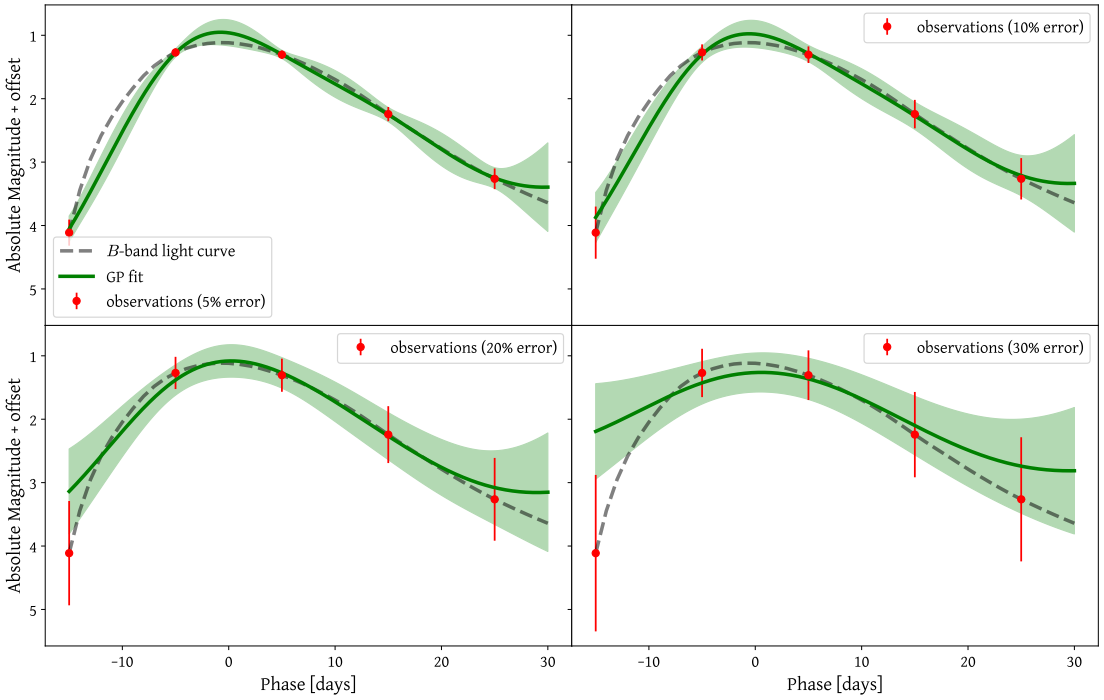

FIGURE 4.5: 10-day cadence 'observations' (red circles) extracted from the rest-frame *B*-band light curve (dashed grey line) of a SN Ia SED template. GP fits (in green) were performed for cases with simulated fractional errors of the observations of 5, 10, 20 and 30 per cent. The exact values of the uncertainties depends on the apparent magnitude of the SN. For instance, for two SNe with peak apparent magnitudes of 17 and 14, a 1 per cent error turns into 0.17 mag and 0.14 mag, respectively.

systematically negative at low cadences. This is due to the lower S/N in these data, despite the higher rest-frame cadence.

SNe with the lowest S/N, which would normally produce slightly under-predicted m_B^{max} values (see Figure 4.5), are not successfully fit, and therefore, not included in the comparison, producing the effect of an apparent over-prediction of m_B^{max} for these samples instead of just an increase in scatter. The masking of low-S/N data in part produces a similar effect. This explains some of the discrepancies seen for some SNLS SNe in Section 4.3.1. SNe with high S/N, but relatively low cadences, can sometimes have their m_B^{max} values slightly over-predicted due to measurements with low uncertainty at each side of the light-curve peak, which can produces sharper peaks (top left panel of Figure 4.5). However, this is not the general case (see the top left panel of Figure 4.4) as it very much depends on the time of the observations with respect to the actual light-curve peak and the apparent luminosity of the SN.

These effects can be reduced by tightening the constraints of the observations around peak, although this would in turn reduce the number of usable SNe. In practice, real observations are not evenly spaced, so these tests just provide a more general idea of how well PISCOLA performs.

4.3.3 Effect of observational uncertainties

The GP interpolation depends on the uncertainties of the observations. Thus, I tested the effect of observational uncertainties by simulating two Pantheon-like samples with half and twice the observational uncertainties ($\sigma_{\rm obs}$) of the data in the original Pantheon sample, with a fixed cadence of 7 days.

The weighted mean and weighted standard deviation of $\Delta m_B^{\rm max}$ for the 7-day cadence simulations with original, half and twice the observational uncertainties are shown in Table 4.2. From this comparison, I can see that a deviation from $\Delta m_B^{\rm max} = 0.0$ mag (at $\sim 3\sigma$) for the SDSS sample is persistent for different values of $\sigma_{\rm obs}$, which may be caused by a generally low S/N despite the S/N$\geq$ 5 selection used. For the low-z sample, a significant (3.5σ) deviation from $\Delta m_B^{\rm max} = 0.0$ mag (PISCOLA under-predicts $m_B^{\rm max}$) is only observed for half $\sigma_{\rm obs}$ given the relatively low cadence which smooths out the peak, despite the high S/N, as discussed in Section 4.3.2. In the case of SNLS, a significant deviation (4.5σ) in the estimation of $m_B^{\rm max}$ is only seen for twice $\sigma_{\rm obs}$ given that the SNe with the lowest S/N, which would normally produce slightly under-predicted $m_B^{\rm max}$ values, are not successfully fit and therefore not included (as discussed in Section 4.3.2). In the case of PS1 no significant deviations are observed.

Despite having some disagreement in the estimation of $m_B^{\rm max}$, these are all < 0.01 mag: PISCOLA is in good agreement with established light-curve fitters. However, the characteristics of surveys like SNLS and, especially, PS1, are ideal for fitting SNe with PISCOLA as they have relatively high S/N and the high-z observations allow a good light-curve coverage due to the relatively high rest-frame cadence. Surveys with the characteristics of the low-z sample require high cadences ($\lesssim$6 days). Future surveys, such as the LSST, will produce high-quality data with good S/N and cadence (e.g., Lochner et al., 2018; Scolnic et al., 2018a), overcoming some of the limitations found in this work, thus allowing PISCOLA to produce reliable fits

These comparisons help validate my code. However, I note the caveat that the simulations are based on the SALT2 model, which differs from other light-curve fitters. Nonetheless, the results of the tests performed throughout these sections are promising as they help establish the reliability of PISCOLA. Furthermore, for many astrophysical applications, the level of disagreement becomes less significant (e.g., the discussion in Chapter 6).

TABLE 4.2: Weighted mean, uncertainty on the weighted mean and weighted standard deviation of Δm_B^{max} for the 7-day cadence simulations with initial, half and twice the observational uncertainties (σ_{obs}; see Section 4.3.3).

survey	weighted mean (mmag)	error on the weighted mean (mmag)	weighted standard deviation (mmag)
Initial simulation			
low-z	4	2	26
SDSS	-6	2	39
SNLS	0	2	29
PS1	0	1	30
half σ_{obs} simulation			
low-z	7	2	26
SDSS	-8	2	34
SNLS	4	2	29
PS1	1	1	29
twice σ_{obs} simulation			
low-z	4	2	28
SDSS	-8	3	45
SNLS	-9	2	36
PS1	-4	2	36

4.3.4 Computational considerations

PISCOLA is a computationally intensive light-curve fitter. Fitting the light curves is fast (of the order of seconds); however, calculating the mangling function can take longer (of the order of minutes for the default phase between -15 and 30 days with respect to t_B^{max}). This is because a fixed GP model is used inside a minimization routine to calculate the mangling function. The length-scale of the GP model is fixed to a value of 20 to produce a smooth function, however, the ratios between the observed and model fluxes (see Section 3.3) are treated as parameters for the minimisation routine. I note that the wavelength axis is divided by 1000 before the minimization routine, and before setting the GP length-scale, to ensure better results by avoiding large numbers, as these are not always properly handled by the routine used. The results are then re-scaled by 1000.

The large covariance between the different bands, given by the Squared Exponential kernel used (see Figure 3.2), and the precision required, make the calculation of the mangling function a slow process as the minimisation routine takes longer to converge. Additionally, if the whole light-curve correction process needs to be repeated with an improved estimation of t_B^{max} (see Section 3.3), the time increases further.

As a result, the number of SNe that can be fit in a 'reasonable' amount of time is limited to a few thousands or tens of thousands. For instance, fitting 1000 simulated SNe Ia takes at least $\sim$2000 minutes ($\sim$33 hours) on a single CPU core, depending on various

factors. This motivated my choice of ∼2000 simulated SNe per test, allowing me to fit objects in a reasonable amount of time.

4.4 Comparison with SALT2

I next test PISCOLA on real data, using the 1022 SNe Ia from the Pantheon sample (excluding HST objects) for these tests. Unlike the simulations in the previous sections, there is no 'ground truth' for these tests, so instead I compare the outputs of PISCOLA against those of SALT2 using the light-curve parameter estimations as given in Scolnic et al. (2018b). I fit the SNe in the same way as I previously described (using default PISCOLA parameters) and applied the same constraints as for the simulations (see Section 4.3). SNe were discarded at different stages of the fitting process following Section 4.3.1.

Of the 1022 initial SNe Ia, I obtain successful fits, with m_B^{max} values, for 620, of which 413 have a $(B-V)_{max}$ estimate. Table 4.4 shows a summary of the discarded SNe. The percentage of successfully fitted SNe (∼60 per cent) is larger than for the Pantheon-like simulation in Section 4.3.1 (∼50 per cent), which is explained by the different relative numbers of SNe for the different surveys: in the simulations, all surveys have approximately the same number of SNe.

In this section, I focus on the comparisons of m_B^{max}, $\Delta m_{15}(B)$ and $(B-V)_{max}$, some of which are not directly comparable between SALT2 and PISCOLA. The outputs from different light-curve fitters are difficult to compare on a SN-by-SN basis due to, for example, different internal calibrations in the fitters producing offsets in some parameters. These are not important for cosmology as long as each code is self-consistent.

4.4.1 *B*-band peak magnitude comparison

Before comparing m_B^{max} values between PISCOLA and SALT2, an offset of $\simeq 0.27$ mag needs to be applied as the version of SALT2 used in Scolnic et al. (2018b) incorporates this global offset. On close inspection, I also found that the MW reddening values adopted by Scolnic et al. (2018b), using the Schlafly & Finkbeiner (2011) dust maps, had some inconsistencies, principally in the low-z sample where most SNe have lower reddening values than expected. In other words, I calculated the MW reddening values (using SFDMAP) for the SNe in the Pantheon sample and found a disagreement with a subset of them when comparing to the published values. I therefore use the same reddening values as Scolnic et al. (2018b) for comparison purposes.

In Figure 4.6, I show the results of the comparison between m_B^{max}. The weighted average and weighted standard deviation of $\Delta m_B^{max} \equiv \Delta m^{max}_{B,\mathrm{PISCOLA}} - \Delta m^{max}_{B,\mathrm{SALT2}}$ are shown

TABLE 4.3: Weighted mean, uncertainty on the weighted mean and weighted standard deviation of Δm_B^{max}, Δs and $(B-V)_{max} - c$ for the Pantheon sub-sample used in this work (see Sec. 4.4).

survey	weighted mean (mmag)	error on the weighted mean (mmag)	weighted standard deviation (mmag)
		Δm_B^{max}	
low-z	10	4	31
SDSS	-26	2	31
SNLS	-8	2	25
PS1	-9	2	34
		Δs	
low-z	-48	10	81
SDSS	-45	6	78
SNLS	-35	9	96
PS1	-22	9	118
		$(B-V)_{max} - c$	
low-z	45	1	8
SDSS	35	3	38
SNLS	9	5	27
PS1	4	4	44

in Table 4.3. There is a general formal disagreement ($>3\sigma$) for all the surveys except the low-z sample.

The differences are typically small, but there are some important details. The apparent offset observed for the low-z sample is mainly driven by one SN, 2004ey (in the [14, 15] mag bin in the top panel of Figure 4.6), due to its large discrepancy with SALT2 (m_B^{max} residual of $\sim$ 0.1 mag), but small uncertainties. If this object is removed, the weighted average of the m_B^{max} residual for the low-z sample is reduced to 0.005 mag. Using SALT2 to fit this SN, I obtained relatively good fits to the light curves (see Fig. 3.7), but with a different value of m_B^{max} compared to that published by Scolnic et al. (2018b), although in better agreement with the PISCOLA value. I do not know the exact source of this difference and do not have any reason from the PISCOLA fit, which results in better residuals than SALT2 (see Figure 3.6), to discard this SN.

The discrepancy in m_B^{max} for the SDSS sample is the largest, expected due to its relatively larger uncertainties. The lower S/N may cause an apparent over-prediction of PISCOLA-measured m_B^{max} values for these SNe (see discussion in Section 4.3.2). However, there is also milder disagreement for the SNLS and PS1 surveys, perhaps due to unidentified issues with photometric calibration given the results of Section 4.3, or due to differences in the SED models between SALT2 and PISCOLA. Despite thoroughly

TABLE 4.4: Number of supernovae discarded at different stages in the PISCOLA fitting.

Discarding reason	low-z	SDSS	SNLS	PS1	Total	Cumulative number discarded
(a)	1	3	33	9	46	46
(b)	58	21	7	11	97	143
(c)	22	18	1	13	54	197
(d)	15	39	57	32	143	340
(e)	2	24	8	28	62	402
Initial sample	172	335	236	279	1022	
Total discarded	98	115	106	93	402	
Remaining SNe	74	230	130	186	620	

Notes. The reasons for discarding SNe are:
(a) Poor wavelength coverage that does not allow the calculation of the rest-frame B-band light curve.
(b) Poor time coverage that does not allow an initial estimation of $t_B^{\max}$.
(c) Unable to estimate an accurate B-band light curve after light-curve fit and correction.
(d) Unable to satisfy extra constrains on peak coverage (see the last paragraph of Section 4.3).
(e) Poor PISCOLA fits checked by visual inspection of SNe with large discrepancy in $m_B^{\max}$ compared to SALT2 values.

checking the analysis and my tests, I am unable to identify the source of this discrepancy. I note that the differences could be due to unidentified issues in PISCOLA, SALT2 or both.

4.4.2 Stretch comparison

I compare the 'stretch' parameters in Figure 4.7. The weighted average and weighted standard deviation for the stretch parameters residual (between PISCOLA and SALT2), $\Delta s \equiv \Delta m_{15}(B)_{\text{PISCOLA}} - \Delta m_{15}(B)_{\text{SALT2}}$, are shown in Table 4.3. Given the data-driven nature of PISCOLA, not every SN with an estimation of $m_B^{\max}$ has enough temporal coverage to estimate its $\Delta m_{15}(B)$. The parameter $\Delta m_{15}(B)_{\text{SALT2}}$ was calculated using the x_1 values from Scolnic et al. (2018b) and the transformation from Guy et al. (2007). I can see a general disagreement ($>3\sigma$ significance) between PISCOLA and SALT2 for all surveys, except PS1 (only $\sim 2\sigma$), where SALT2 shows on average larger $\Delta m_{15}(B)$ values. Although there are intrinsic differences in the way the stretch is calculated, I note that there is one big caveat to this comparison: the estimation of $\Delta m_{15}(B)_{\text{SALT2}}$ is very indirect and the transformation from Guy et al. (2007) is most likely not well calibrated given that it comes from an older version of SALT2 (i.e., outdated), so a bias

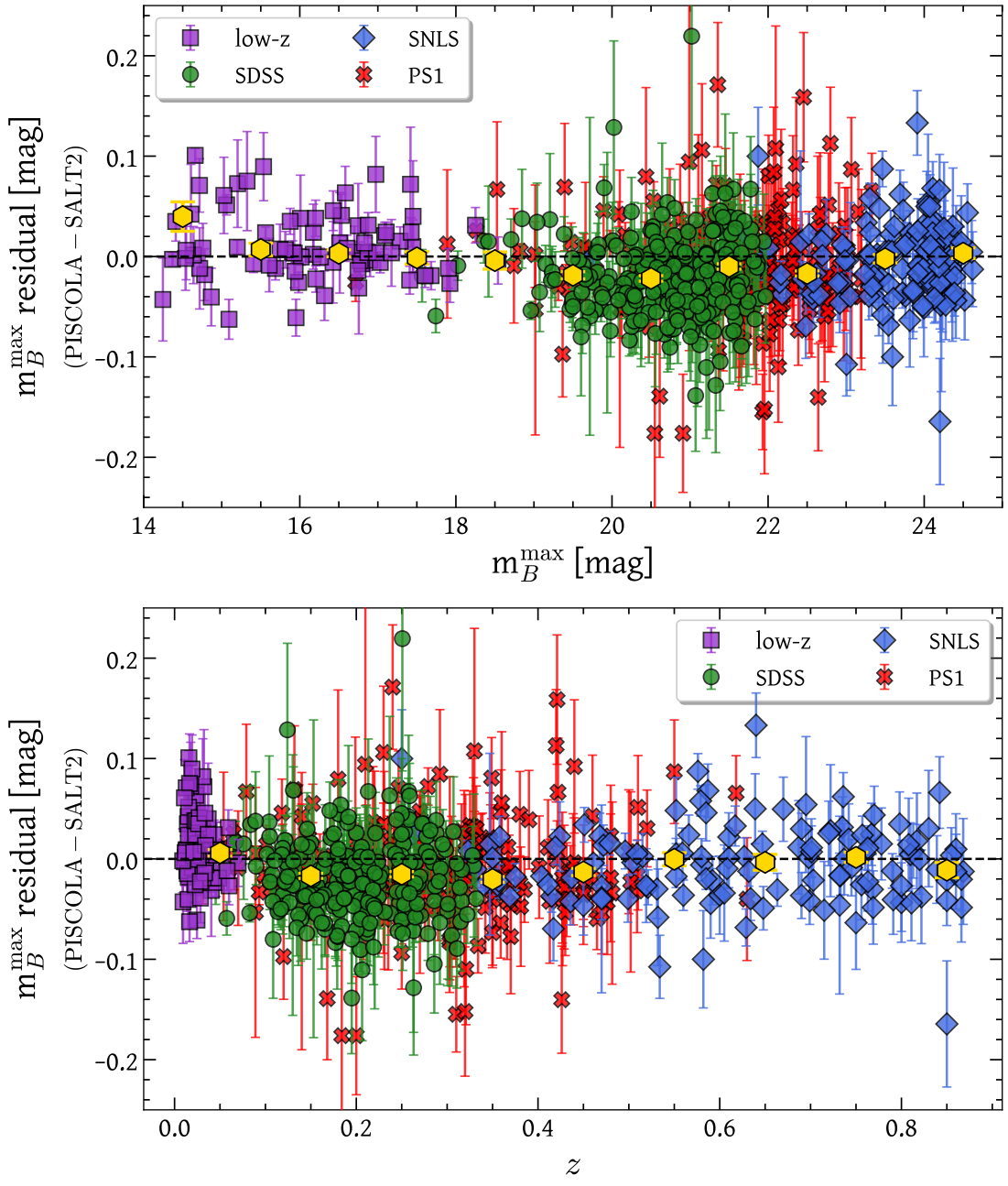

FIGURE 4.6: Comparison between m_B^{max} obtained from the SALT2 light-curve fitter and that obtained using PISCOLA as a function of m_B^{max} (**top** panel) and z (**bottom** panel) for SNe Ia from the Pantheon sample. The error bars are 1σ uncertainties from PISCOLA. The yellow hexagons represent the weighted mean in bins of 1 mag with their respective uncertainties (1σ).

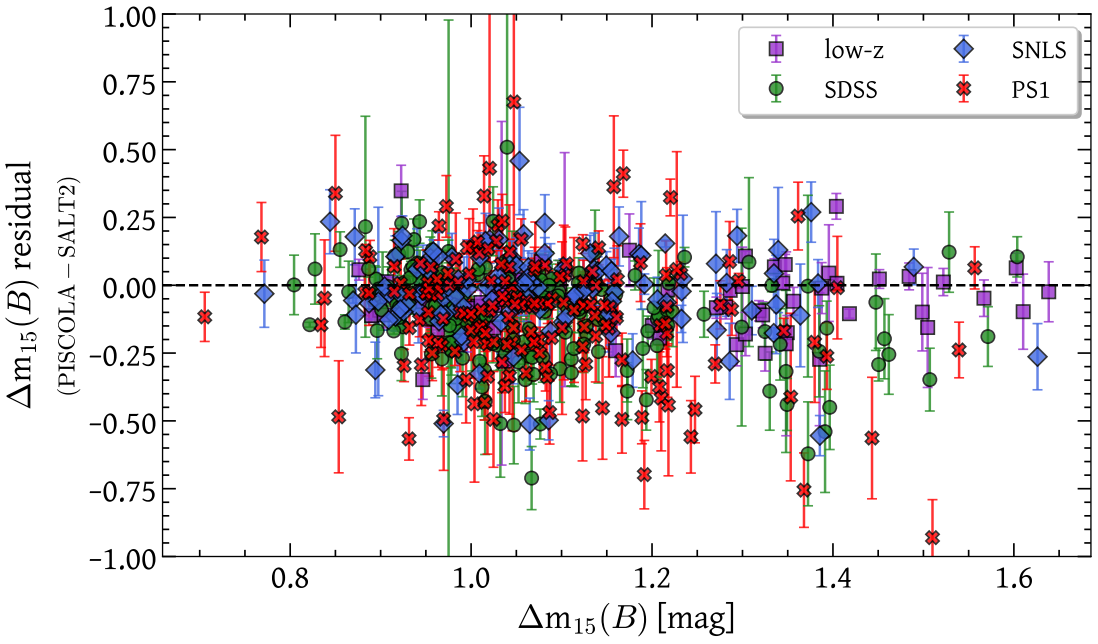

FIGURE 4.7: Stretch comparison between PISCOLA and SALT2. The parameter $\Delta m_{15}(B)$ for SALT2 was calculated using x_1 and the transformation from Guy et al. (2007). The error bars are 1σ uncertainties from PISCOLA.

can be expected. Additionally, this transformation is not linear, so some scatter is also expected, but this is not given. Thus, this comparison does not properly help validate PISCOLA.

4.4.3 Colour comparison

I compare the colour parameters in Figure 4.8. Given the data-driven nature of PISCOLA, not every SN with an estimation of m_B^{max} has sufficient wavelength coverage to also estimate its $(B-V)_{max}$, particularly at high redshift. I also note that the colour parameters are fundamentally different (see, e.g., Kessler et al., 2013), and thus a detailed comparison between colour parameters is difficult. SALT2 estimates $(B-V)_{max}$ through the c parameter using information across the 3000–7000 Å range, where c is *approximately* $(B-V)_{max} - \langle (B-V)_{max} \rangle$, and $\langle (B-V)_{max} \rangle$ is the average colour of the training sample of SNe Ia. On the other hand, PISCOLA makes a direct measurement of $(B-V)$ at t_B^{max}.

The weighted average and weighted standard deviation for the colour parameter residuals are shown in Table 4.3. As expected, some differences are seen between the colour parameters, particularly in the low-z and SDSS samples, where PISCOLA measures redder SNe than SALT2. A global offset would be expected given the definition of c,

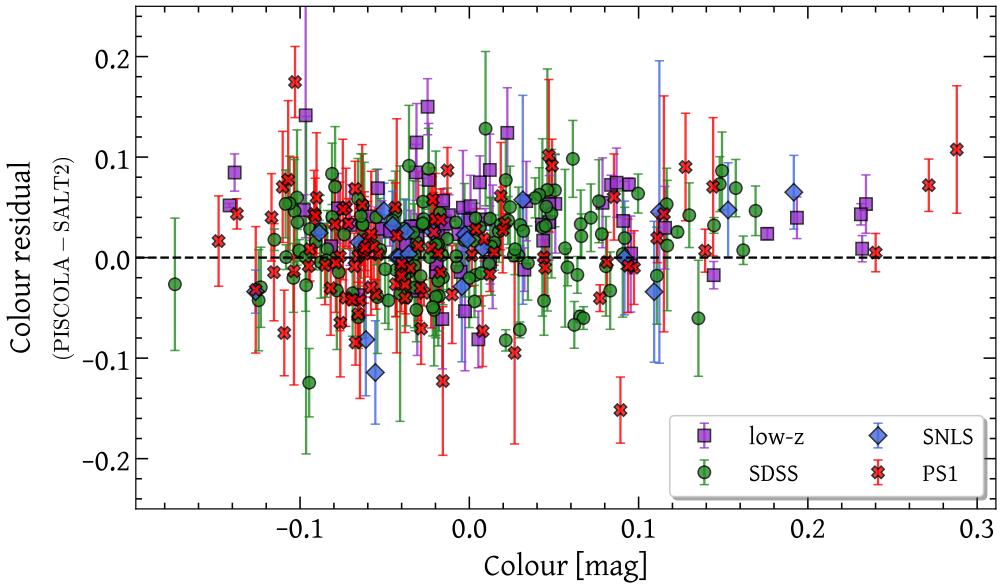

FIGURE 4.8: Colour comparison between PISCOLA ($(B-V)_{\max}$) and SALT2 (c). The error bars are 1σ uncertainties from PISCOLA. Despite some differences, a general agreement can be seen.

but the discrepancies are different for each survey, possibly implying issues with calibration as for $m_B^{\max}$ or differences between the SED models of PISCOLA and SALT2. However, the latter is not likely (see Chapter 6).

In summary for this section, I find some differences between light-curve parameters for SNe Ia measured using PISCOLA and SALT2, some of which were anticipated. For the most straight forward comparison, i.e., $m_B^{\max}$, differences between PISCOLA and SALT2 were small (a few per cents). A detailed comparison for stretch and colour is more difficult due to slightly varying definitions. Taking the results from this and the previous sections, I conclude that the performance of PISCOLA is satisfactory and validates my code.

With PISCOLA validated, the next step is to use it to measure distances with SNe Ia. In the next chapter, I present a proof-of-concept machine-learning analysis of SN Ia light curves in search of an alternative, improved standardisation.

Chapter 5

Light-Curve Analysis

In the previous chapter I validated PISCOLA as a competitive light-curve fitter. In this chapter, I demonstrate its use applied to the standardisaton of SNe Ia for distance estimation.

Many current and previous cosmological analyses (e.g., Astier et al., 2006; Guy et al., 2010; Betoule et al., 2014; Scolnic et al., 2018b) have used SALT/SALT2 light-curve parametrizations to standardise SNe Ia using the Tripp-like formula (Tripp, 1998):

$$\mu = m_B - M + \alpha \times x_1 - \beta \times c. \tag{5.1}$$

where μ is the SN Ia distance modulus, m_B, x_1 and c are the SALT2 light-curve parameters, and α, β and M are nuisance parameters, as described in Section 1.3.8.

Current cosmological analyses incorporate an additional intrinsic dispersion term, σ_{int} in the error budget, which encapsulates additional SN Ia variability that cannot be explained by their standardisation (e.g., Perlmutter et al., 1997; Tonry et al., 2003; Riess et al., 2004; Guy et al., 2010; Betoule et al., 2014; Scolnic et al., 2018b). In this chapter, I analyse SN Ia light curves from the Pantheon sample using Non-negative Matrix Factorization (NMF), an unsupervised machine-learning method, in search of an alternative parametrizations to explain the remaining variability in these objects (i.e., reduce σ_{int}).

5.1 Non-negative Matrix Factorization

NMF was first introduced by Paatero & Tapper (1994), back then called Positive Matrix Factorization, and popularised by the work of Lee & Seung (1999). It is a tool widely used in the analysis of high dimensional data, similar to the more well-known PCA.

NMF factorises a non-negative matrix, $\boldsymbol{X}$, with dimensions $m \times n$, in a set of two non-negative matrices, $\boldsymbol{W}$ and $\boldsymbol{H}$, with dimensions $m \times k$ and $k \times n$ (where $k < min(n, m)$), respectively, such that:

$$\boldsymbol{X} = \boldsymbol{W} \times \boldsymbol{H}. \tag{5.2}$$

However, as this algebra problem cannot be solved analytically, due to the non-negative constraints, it is approximated numerically, i.e., $\boldsymbol{X} \approx \boldsymbol{W} \times \boldsymbol{H}$. If one thinks of $\boldsymbol{X}$ as a matrix containing n data points, each with m features, then $\boldsymbol{W}$ contains the basis elements (representation of the features, i.e., eigenvectors), while $\boldsymbol{H}$ contains the contribution (eigenvalues) of these basis elements for each of the data points. k represents the number of NMF components obtained from the factorisation.

NMF, like PCA, is commonly used for dimensionality reduction and features extraction. PCA has been widely used in the context of SNe Ia (e.g., Cormier & Davis, 2011; Kim et al., 2013; He et al., 2018; Saunders et al., 2018). However, there are no reported works using NMF on SNe Ia and relatively few (compared to PCA) in other areas of astronomy (e.g., Blanton & Roweis, 2007; Allen et al., 2011; Zhu & Ménard, 2013; Ren et al., 2018). However, NMF is better suited for many applications in astronomy as most astrophysical signals are non-negative, thus, granting the advantage of extracting features that are easier to interpret. In addition, NMF decomposition does not produce orthogonal components, as is the case for PCA, which is ideal for this analysis as I want to find correlations between light-curve parameters.

5.2 Light-Curve Decomposition with NMF

The light-curve decomposition depends on the phase coverage being used. I present my analysis for 214 SNe which have rest-frame data over the phase range -10 to $+15$ d. In this proof-of-concept investigation, I also discarded 50 SNe (this are not considered in the 214 SNe just mentioned) which did not have straight-forwardly rising and then declining light curves, flagged by visual inspection of the fits. There are many reasons why such fits may result, including astrophysical reasons such as the presence of secondary peaks in SN Ia light curves, or experimental reasons such as lower S/N data (an example is shown in Figure 5.1). However, this decomposition application is deliberately designed to be simple in scope; future work will examine the more complicated morphology of SN Ia light curves. The sample selection for this analysis is summarised in Table 5.1. In Section 5.4, I explain in more detail the phase range chosen, and explore other phase ranges. The rest-frame B-band light curves for this sample are shown in Figure 5.2.

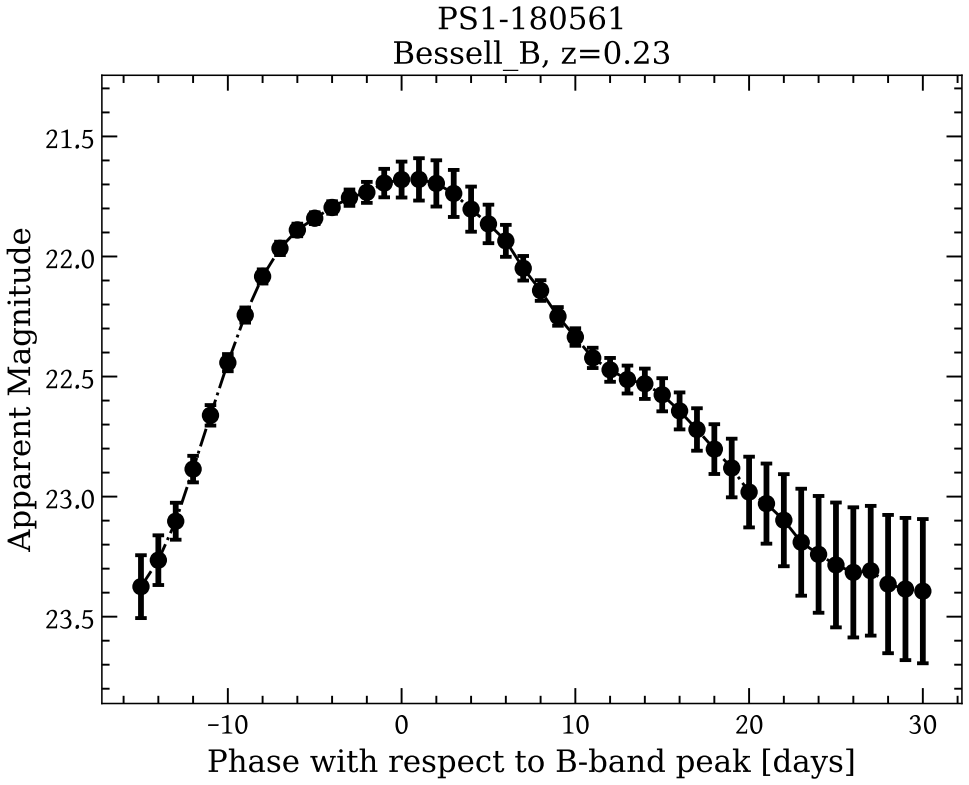

FIGURE 5.1: Rest-frame *B*-band light curve of the PISCOLA-fitted SN PS1-180561. This SN shows bumps that are not seen in SNe Ia due to an unreliable fit.

I decomposed these light curves in absolute-magnitude space, multiplied by -1 to obtain positive values. To calculate the absolute magnitudes, I use distance modulii calculated with the assumed cosmology used in the previous chapter and the redshifts from Scolnic et al. (2018b). As the NMF algorithm used does not incorporate uncertainties, I used a Monte Carlo approach, generating sets of light curves for each SN from the uncertainties estimated by PISCOLA, and applying NMF decomposition to each of these sets. This generates a distribution of coefficients from which I used the mean value and the standard deviation to propagate uncertainties.

The following analysis is described for a decomposition with three components (i.e., k =3), although I consider further components in Section 5.4. In Figure 5.3, I show the components obtained with NMF, with their respective explained variance (in percentage) with respect to the total variance of all components. Each eigenvector contains specific information about the *B*-band of an 'average' SN Ia. Component 0 contributes to the general scale of the light curve, thus correlating with the *B*-band peak absolute magnitude, M_B^{max}. Component 1 contributes to the rise of the light curve, while component 2 mainly contributes to the decline of the light curve (therefore, one would expect it to correlate with $\Delta m_{15}(B)$). Component 1 also contributes to the decline, but to a lesser degree than component 2. I note that from this data-driven decomposition, one

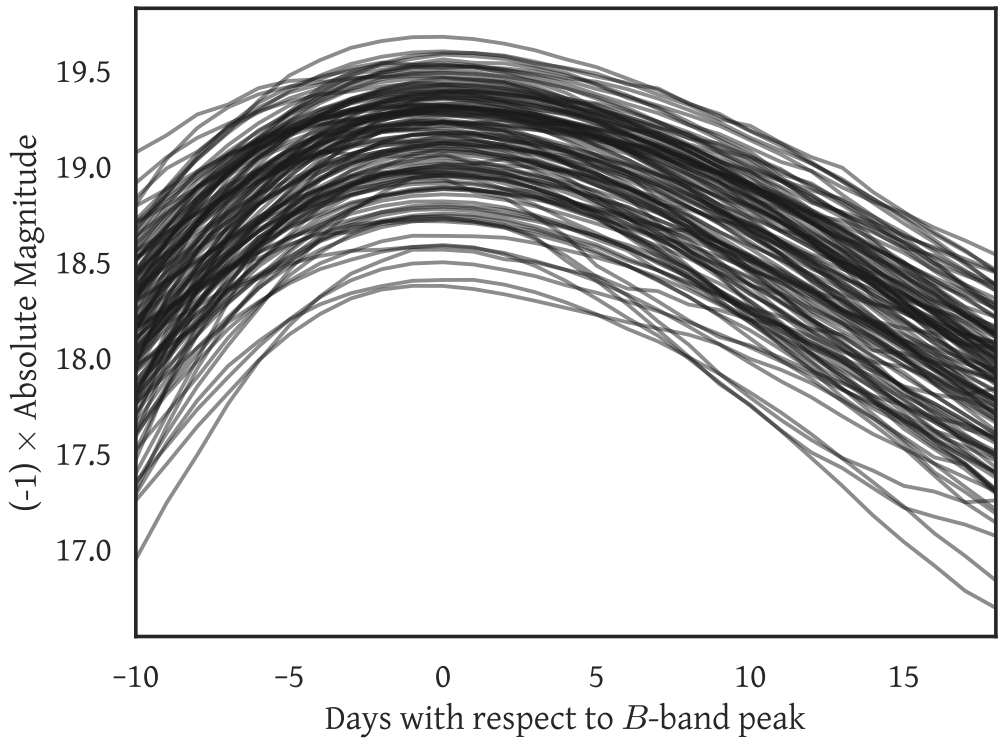

FIGURE 5.2: B-band light curves of 214 PISCOLA-fitted SNe Ia used in the decomposition analysis. Values are in absolute-magnitude multiplied by -1.

naturally retrieves components related to the rise and decline of the B-band light curve, in agreement with the findings of Hayden et al. (2010) and Ganeshalingam et al. (2011).

I am principally interested in the relative values of the components rather than the absolute values, which have no direct physical interpretation. I labelled the coefficients p_0, p_1 and p_2, associated to components 0, 1 and 2, respectively. Their distributions are shown in Figure 5.4.

In Figure 5.5, I show an example of B-band light curve from one of the SNe of the sample together with a reconstructed light curve, using the NMF components and coefficients, and their residuals. The residuals show that the reconstructed light curve has some small differences ($\lesssim$0.05 mag) with the original light curve around rise time, but much better agreement around peak ($\sim$0.02 mag residuals) and at later times ($\sim$0.00 mag residuals). The reconstructed light curves and the original light curves for the sample of 214 SNe are in excellent agreement, with mean residuals of $\sim$0.00 mag and standard deviation of $\sim$0.03 mag for all phases. This demonstrates that the NMF decomposition with 3 components is able to properly capture most of the variation in the light curves of SNe Ia.

The coefficients (eigenvalues) tell us about the contribution (or weight) of each of the components on the light curve of a SN Ia. By comparing these with different light-curve

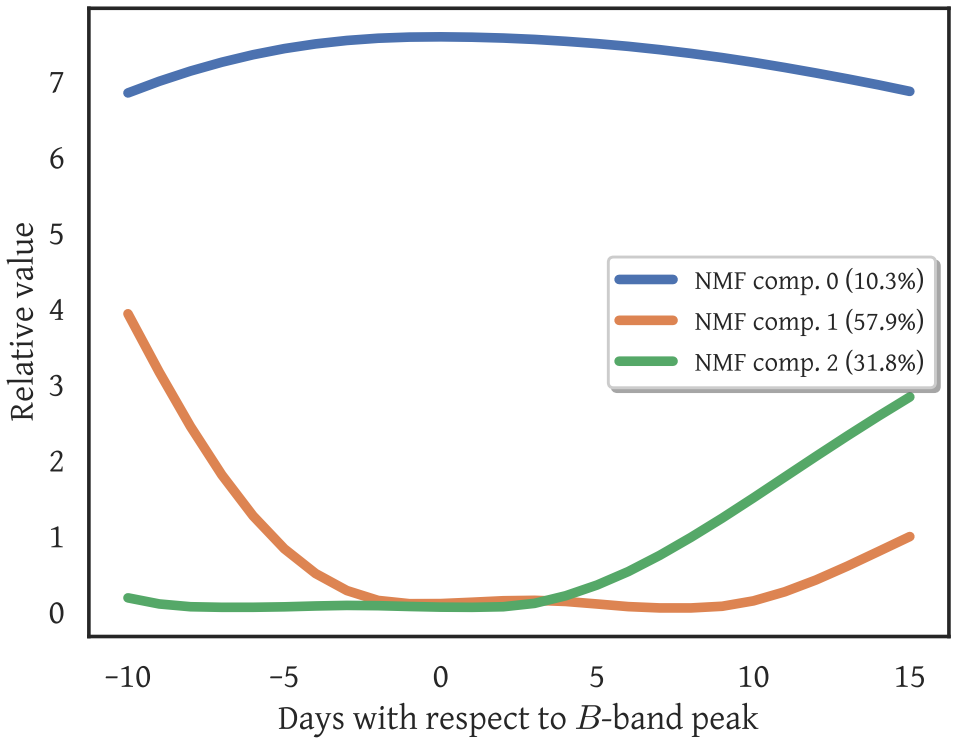

FIGURE 5.3: Three NMF components obtained from the decomposition of the B-band light curves shown in Figure 5.2. In parenthesis are the percentages of the explained variance for each component with respect to the total variance of all components. The absolute values of the components are of no importance for the analysis in this work.

parameters, one can better understand their physical interpretation. This is shown in Figure 5.6. As expected, there is a clear correlation between p_0 and M_B^{max}, and thus $(B-V)_{max}$ (e.g., Tripp, 1998). Coefficient p_1, which contributes to the rise of the light curve, has a small correlation with $(B-V)_{max}$, but not with M_B^{max}. On the other hand, coefficient p_2 clearly correlates with $\Delta m_{15}(B)$, as expected, and shows minor correlations with M_B^{max} and $(B-V)_{max}$. None of the components correlates with host-galaxy stellar mass. The decomposition is somewhat analogous to the SALT2 model, which contains x_0 and x_1 terms, although here I have two stretch components. In my case, the average (B-band light-curve) model has stretch parameters $p_1 \sim p_2 \sim 0.2$, while in the case of SALT2 it has $x_1 = 0$.

I note that NMF, unlike PCA, does not produce orthogonal components given the constraints of non-negative values, i.e., correlations between the components can be expected. From the coefficients, I find that p_1 and p_2 are anti-correlated (correlation of ~ -0.5).

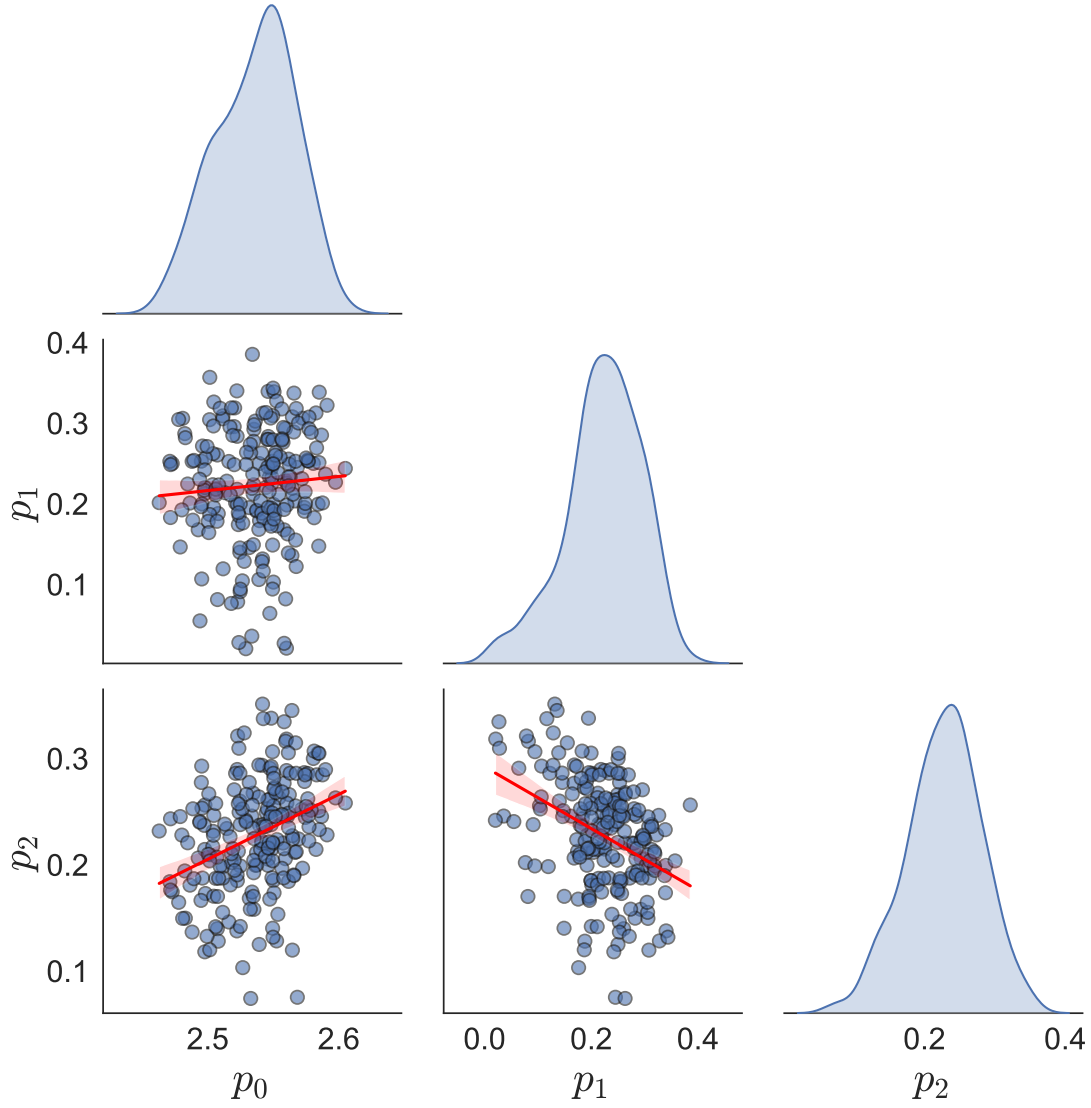

FIGURE 5.4: NMF coefficients (p_0, p_1 and p_2) for the SN Ia sample in Figure 5.2. Uncertainties are not shown for visualisation. Linear regressions between coefficients are represented by red lines.

5.3 Distance estimation

I follow an analogous approach to equation (5.1), using the PISCOLA components:

$$\mu = m_B - M + \eta_1 \times \hat{p}_1 + \eta_2 \times \hat{p}_2 - \beta \times (B-V)_{\max}, \tag{5.3}$$

where m_B and $(B-V)_{\max}$ are the PISCOLA-measured light-curve parameters (i.e., measured from the fits), $\hat{p} = p - \langle p \rangle$, and $\langle p \rangle$ is the average NMF coefficient value of the sample.

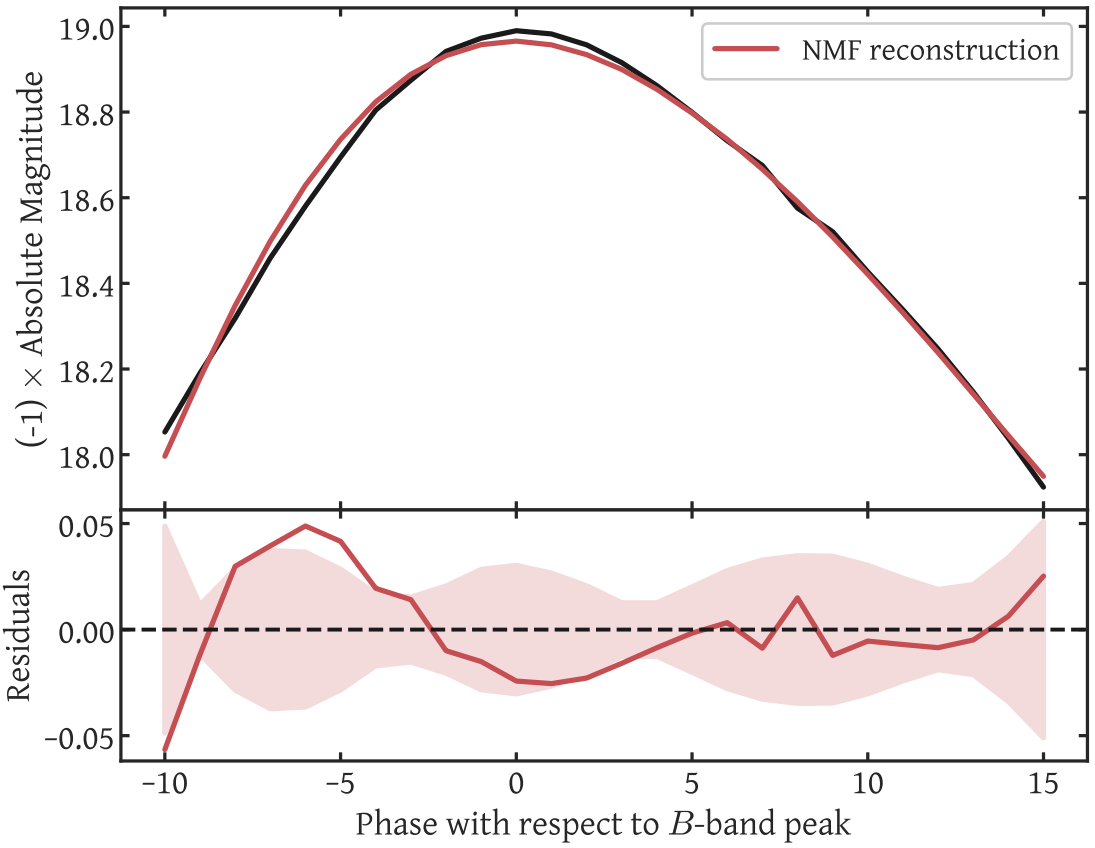

FIGURE 5.5: **Top:** example of B-band light curve from one of the SNe of the sample (black) together with a reconstructed light curve using the NMF components and coefficients (red). Values are in absolute-magnitude multiplied by -1. **Bottom:** residuals from the light curves shown in the top panel. The shaded area shows the standard deviation of the residuals for the entire sample in Figure 5.2.

5.3.1 Hubble Diagram

To build a Hubble diagram, I adopt my standard cosmology and use Markov Chain Monte Carlo (MCMC) to find the optimal values for the nuisance parameters M, η_1 , η_2 and β, adopting uniform priors without bounds (except for M, where I require $M < 0$). Note that I used only SNe with $(B-V)_{\rm max}$ values (156 out of 214) for the Hubble diagram. See Table 5.1 for more details regarding the cuts applied to the SNe sample and the end of Section 5.4 for a summary. The need of colour limits the range of redshift, as I require rest-frame V-band coverage to estimate $(B-V)_{\rm max}$, which can be redshifted out of the filters' coverage for high-z SNe. I tried using alternative colour parameters, such as the slope of the mangling function, which contains information about $(B-V)_{\rm max}$ in a narrow range ($\sim$ 4500–5500 Å), allowing me to incorporate higher-redshift SNe. However, it provided a more limited standardisation compared to $(B-V)_{\rm max}$.

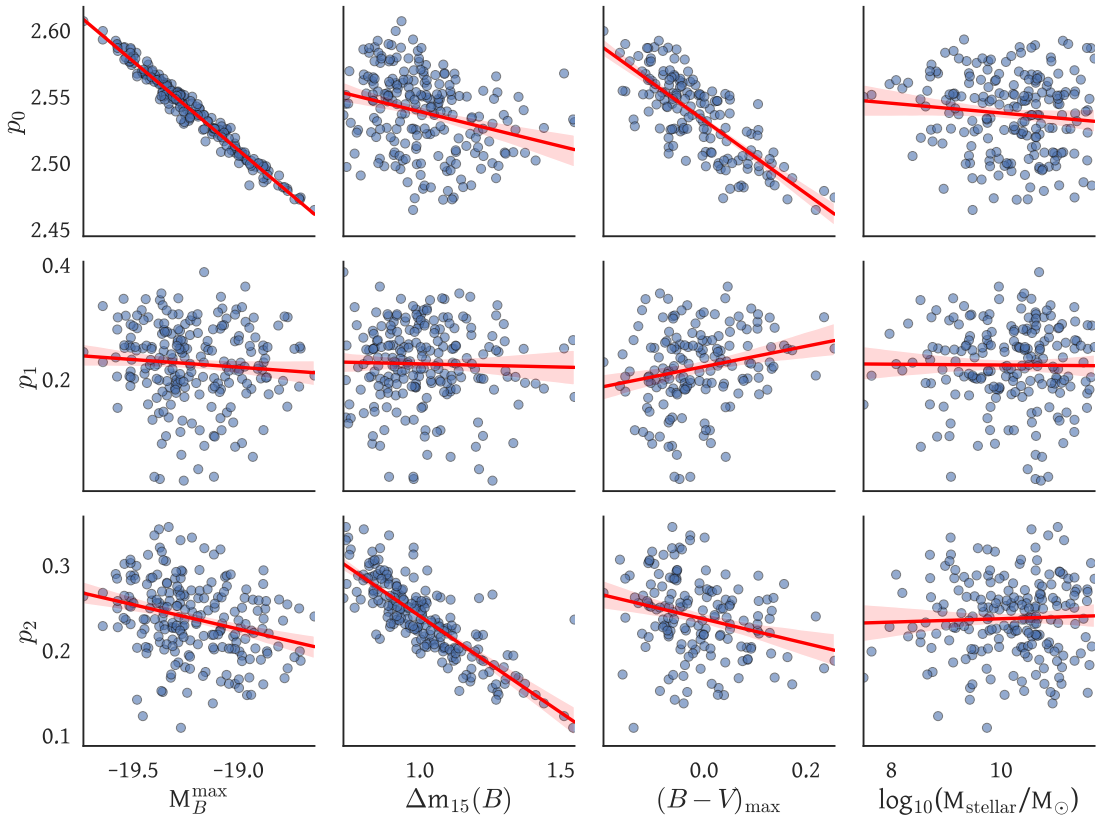

FIGURE 5.6: NMF coefficients vs PISCOLA light-curve parameters and host galaxy mass for the SNe in Figure 5.2. From the 214 SNe, only 156 have $(B-V)_{max}$ values. Uncertainties are not shown for visualisation. Linear regressions are represented by red lines.

TABLE 5.1: Number of supernovae discarded at different stages of the analysis (Chapter 5).

Discarding reason	**low-z**	**SDSS**	**SNLS**	**PS1**	**Total**	**Cumulative number discarded**
(a)	59	129	71	97	356	356
(b)	1	19	8	22	50	406
(c)	0	12	40	6	58	464
Initial sample	74	230	130	186	620	
Total discarded	60	160	119	125	464	
Remaining SNe	14	70	11	61	156	

Notes. The reasons for discarding SNe are:
(a) Incomplete phase coverage.
(b) Un-physical looking light curve.
(c) No $(B-V)_{max}$ value.

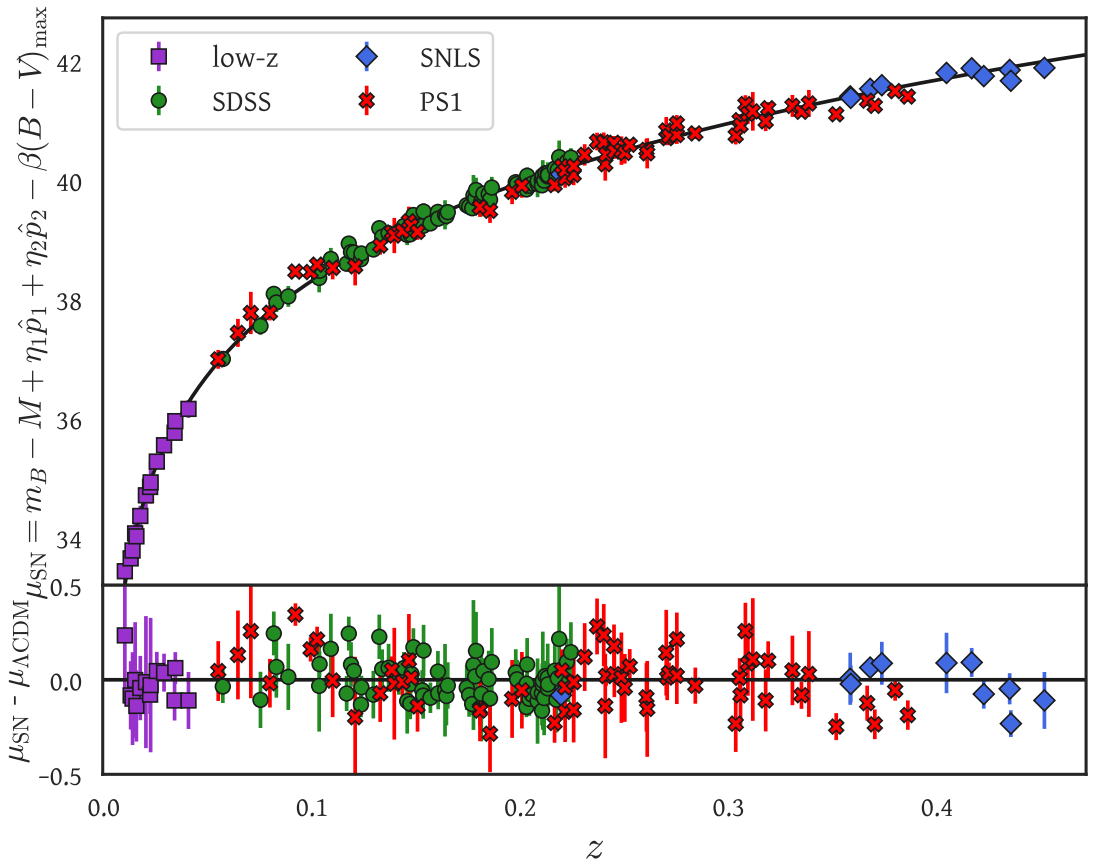

FIGURE 5.7: Hubble diagram (**top** panel) and residual (**bottom** panel) for the SNe in the sample, using the PISCOLA standardisation and cosmology from this work.

I included uncertainties and covariances for my light-curve parameters, uncertainties in redshift (σ_z), uncertainties due to peculiar velocities (σ_{pec}; adopting 300 km s^{-1}) and uncertainties from stochastic gravitational lensing (σ_{lens}). I also included an intrinsic scatter term (σ_{int}) such that $\chi^2_{red} = 1$. Distance bias correction (Section 1.3.8) is not included as a separate analysis would be required. However, I do not expect it to be significant due to the need for a $(B-V)_{max}$ measurement in my analysis, which translates into an implicit redshift cut; see the redshift ranges for the different surveys in Figure 5.7. Furthermore, as I am mainly interested in comparing my results with those from SALT2 (see next section), using the same sample of SNe, the same or a very similar bias correction would need to be applied to the results of SALT2, cancelling each other out. The resulting Hubble diagram is shown in Figure 5.7, while the MCMC results of the parameters are shown in Figure 5.8.

5.3.2 Hubble Residuals: PISCOLA vs SALT2

I now compare this simple PISCOLA parametrization with SALT2 using the same sample of 156 SNe. The results for SALT2 are shown in Figure 5.9. In Figure 5.10, I show

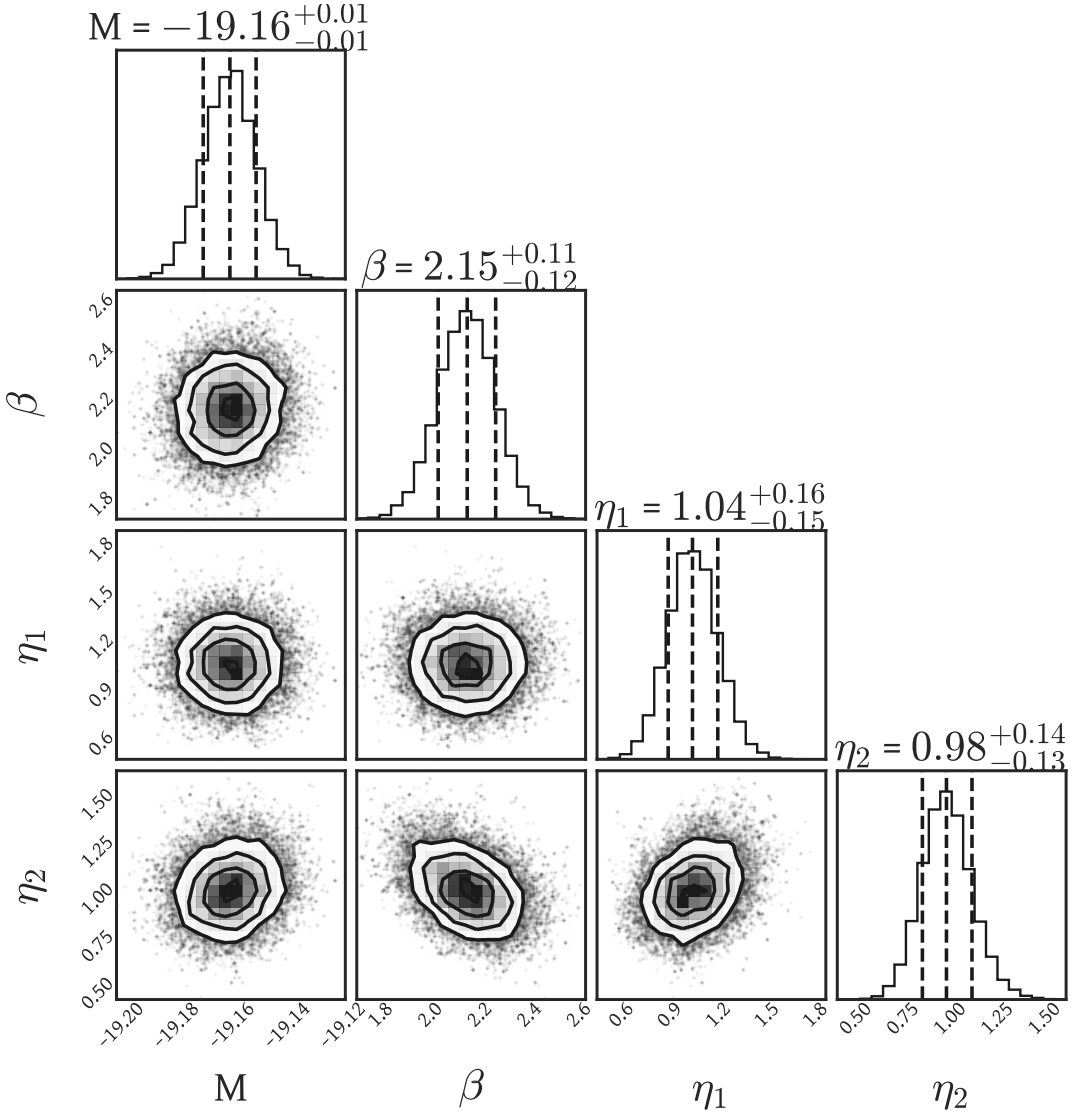

FIGURE 5.8: MCMC results of the nuisance parameters used for the standardisation of the SNe Ia in the Hubble diagram (Figure 5.7).

the comparison of the Hubble residuals (between measured and theoretical distances) using parameters derived from the PISCOLA light curves and from SALT2. PISCOLA obtains a similar r.m.s. value of 0.118 mag compared to SALT2 (0.111 mag), indicating it as a competitive method. The performance difference in r.m.s. of 0.007 mag is small. I note, however, that, although PISCOLA does not outperform SALT2, using it for cosmological analyses is but a limited demonstration of its true potential as a general purpose light-curve fitter.

The nuisance parameters obtained by using PISCOLA and SALT2 are summarised in Table 5.2. For SALT2, I found a similar value for α and a slightly lower value for β than those reported in Scolnic et al. (2018b), possibly due to the subsample used in this work. The value for M is different between both approaches, but as a normalisation factor this has no effect on the analysis. The value of β is smaller with PISCOLA, indicating the

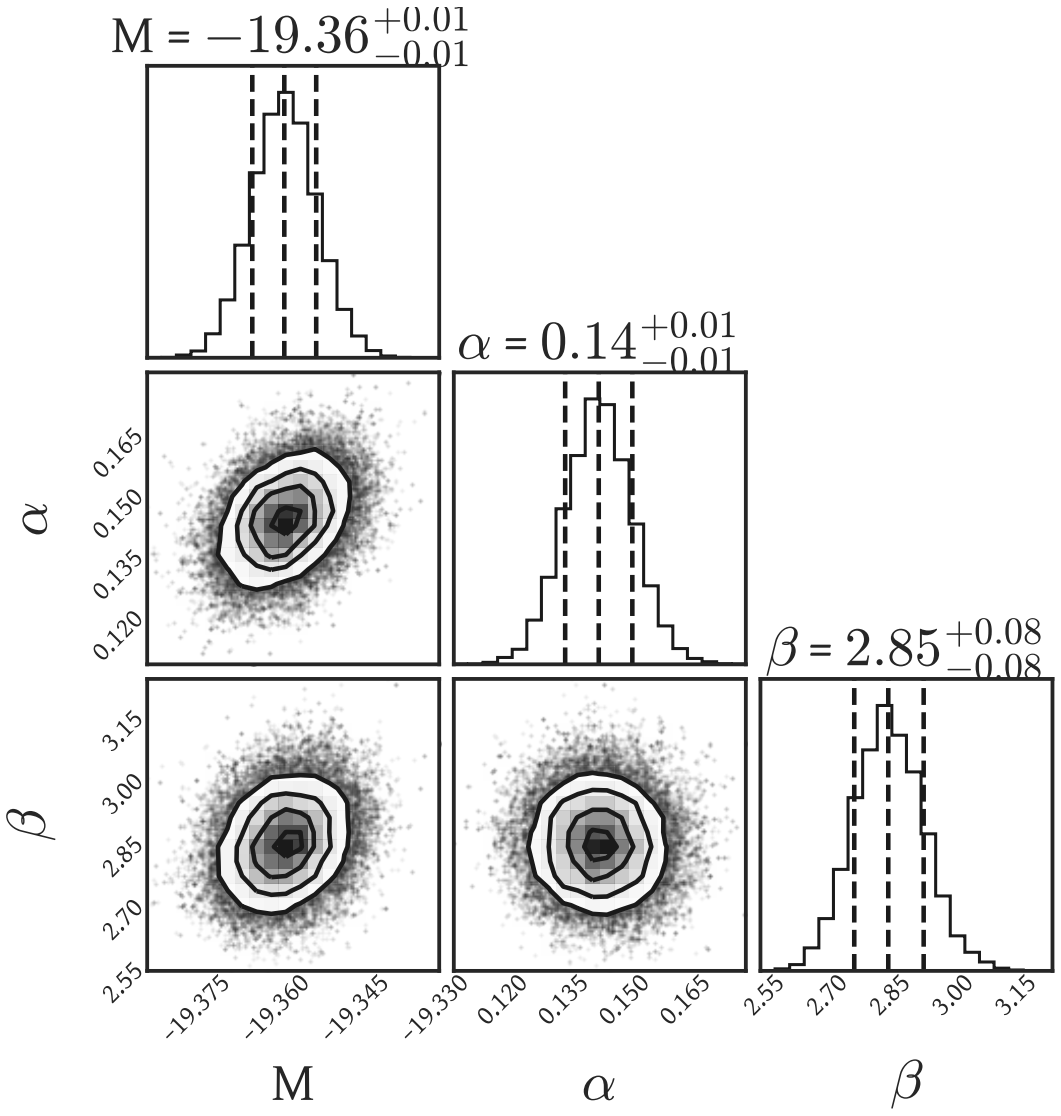

FIGURE 5.9: MCMC results for the standardisation of the SNe Ia using SALT2.

colour correction is not as large as with SALT2, possibly implying that some of the colour contribution is accounted for in p_1 and/or p_2 (note also the slight correlation between β and η_2 in Figure 5.8). The stretch-like parameters, p_1 and p_2, distribute as quasi-Gaussians over $\sim 0.0 - 0.4$ with mean values of ~ 0.2 (see Figure 5.4), so the correction from $\eta_1 p_1 + \eta_2 p_2$ is larger than αx_1. This is consistent with the possibility that some of the contribution from colour is absorbed by the p_1 and/or p_2 parameters. Finally, I obtain a lower σ_{int} with PISCOLA than with SALT2, but this is also a reflection of the larger uncertainties, where the main contributor to the uncertainty budget is $(B - V)_{\text{max}}$, an effect of the GP light-curve fits.

I also examined the dependence of Hubble residual on host-galaxy stellar mass, the so-called 'mass step' (e.g., Kelly et al., 2010; Lampeitl et al., 2010; Sullivan et al., 2010), by using the stellar mass values from Scolnic et al. (2018b). I found a mass-step value

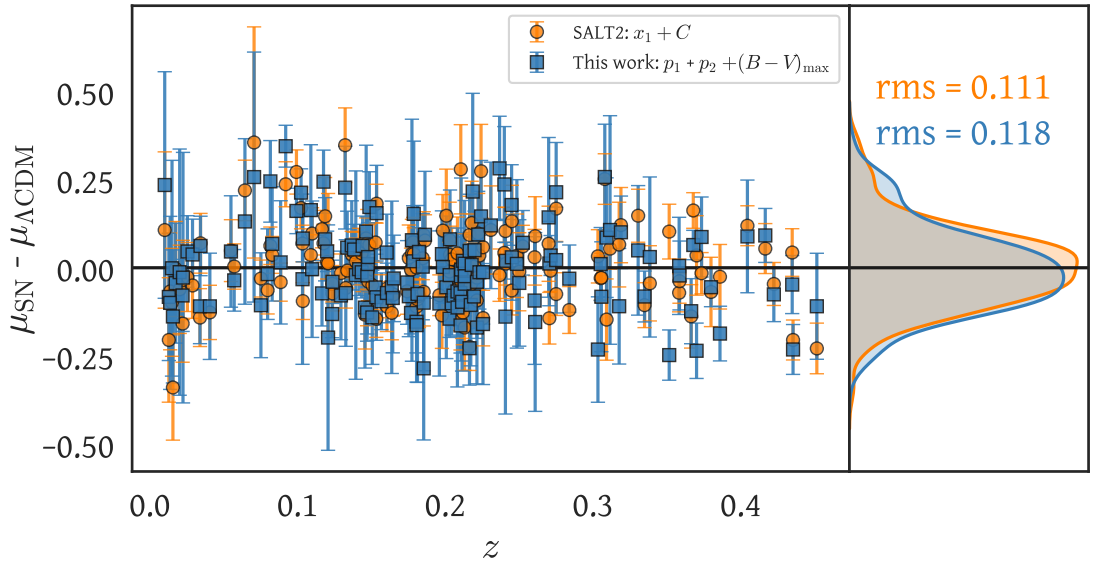

FIGURE 5.10: Hubble Residual comparison between the parametrization derived in this work and the standard parametrization from SALT2.

TABLE 5.2: Nuisance parameters from the cosmological analysis for SALT2 and PISCOLA.

Parameter	SALT2	PISCOLA
M	$-19.36^{+0.01}_{-0.01}$	$-19.16^{+0.01}_{-0.01}$
β	$2.85^{+0.08}_{-0.08}$	$2.15^{+0.11}_{-0.12}$
α	$0.14^{+0.01}_{-0.01}$	-
η_1	-	$1.04^{+0.16}_{-0.15}$
η_2	-	$0.98^{+0.14}_{-0.13}$
σ_{int}	0.068	0.047

Notes. The uncertainties in σ_{int} are negligible (<0.001) in both cases.

of -0.052 ± 0.022 mag (2.4σ; see Figure 5.11) and -0.071 ± 0.016 mag (4.4σ; see Figure 5.12) for PISCOLA and SALT2, respectively, for a step at $M_{\text{stellar}} = 10^{10} M_{\odot}$. The PISCOLA value is therefore consistent with the value obtained with SALT2 and with previous work (e.g., Sullivan et al., 2010; Betoule et al., 2014; Scolnic et al., 2018b; Kelsey et al., 2021; Boone et al., 2021), although lower and less significant.

5.4 Further Exploration

The results of the light-curve decomposition in Section 5.2 depend on the phase range considered. I explored different ranges with lower limits of -8, -10 and -12 days, and upper limits of $+12$, $+15$ and $+18$ days. As not all SNe have the same coverage, I used

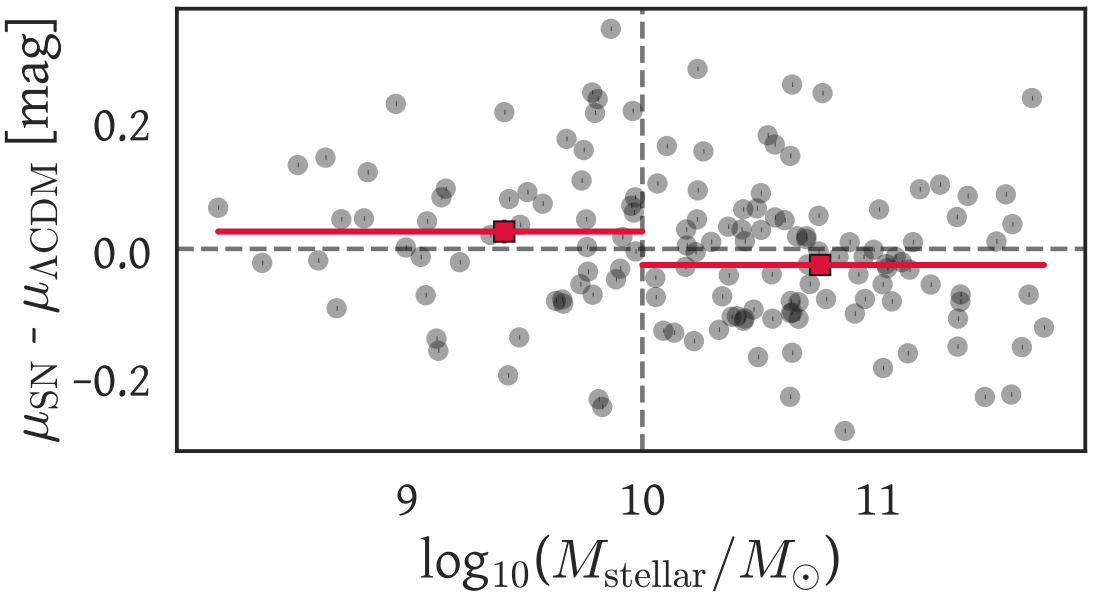

FIGURE 5.11: PISCOLA Hubble residuals as a function of host galaxy stellar mass. Uncertainties are not shown for better visualisation. A host galaxy mass step of -0.052 ± 0.022 mag (2.4σ) was obtained. The vertical dashed line marks the location of the step at $M_{stellar} = 10^{10} M_{\odot}$.

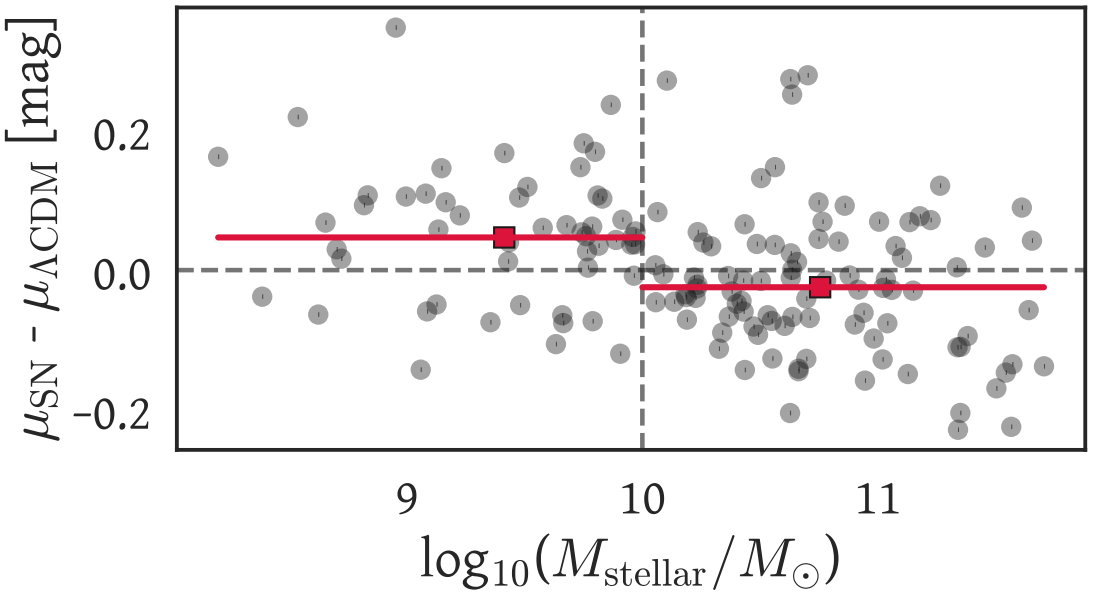

FIGURE 5.12: Hubble residual from SALT2 as a function of host galaxy mass. Uncertainties are not shown for better visualisation. A host galaxy mass step of -0.071 ± 0.016 mag (4.4σ) was obtained. The vertical dashed line marks the location of the step at $M_{stellar} = 10^{10} M_{\odot}$.

an initial sample of 264 SNe in common for all the ranges. Data outside of these phase ranges are usually more incomplete. 50 SNe were discarded for having un-physical-looking light curves, as previously described, leaving 214 SNe. From these 214 SNe, only 156 SNe had $(B-V)_{\max}$ values, which make up the sample used for building the Hubble Diagram (Section 5.3.1).

My full analysis (Sections 5.2 and 5.3) was performed for these phase ranges and the Hubble residual r.m.s. values are summarised in Table 5.3. The range of $[-10, +15]$ d produced the smallest r.m.s.. Although naively it might be expected that larger ranges would contain more light-curve information in the NMF components, the fits can also be less reliable at early or late epochs. For example, the ranges starting at -12 days produce the largest r.m.s. values, due to less reliable fits from the larger observational uncertainties at these early epochs. A similar behaviour is seen for the ranges ending at $+18$ d. The range of $[-10, +15]$ d produces the best combination between information incorporated and reliable fits.

The shape and information contained in the different NMF components also depends on the number of components chosen. I repeated the analysis using two, four and five components for the phase range of $[-10, +15]$ d. The resultant components are shown in Figures 5.13, 5.14 and 5.15, respectively. For all the decompositions, components 0, 1 and 2 have a relatively similar contribution to the light curve. For the two-component decomposition, component 1 also contributes to the luminosity around and after peak, as it has no component 2. Components 4 and 5, where present, have a general contribution along the light curve and apparently further help explain the variability in SN Ia light curves, but with no direct physical interpretation.

Using two components resulted in a worse result (Hubble residual r.m.s. of 0.141 mag), while using four and five components produced similar results as that with three components (both with a Hubble residual r.m.s. of 0.121 mag). I conclude that two components are not sufficient to capture the variability of SNe Ia. On the other hand, as the number of components increases it is hard to determine if there is any physical interpretation and/or contribution to the light-curve standardisation. The results suggest that three components is optimal with the current data, each component with clear physical interpretation.

To summarise the sample used for the cosmological analysis, of the 620 SNe that PISCOLA successfully fit (obtained $m_B^{\max}$), only 264 have phase coverage in the B-band between -12 and $+18$ days. There are more SNe with smaller phase-range coverage, but to ensure a fair comparison, I use the sample from the largest phase-range coverage I tested, which has SNe in common with all the other phase ranges. Of these 264 SNe, 50 had unphysical-looking light curves from visual inspection (see the example in Figure 5.1) and were removed, leaving 214 SNe on which the NMF analysis was

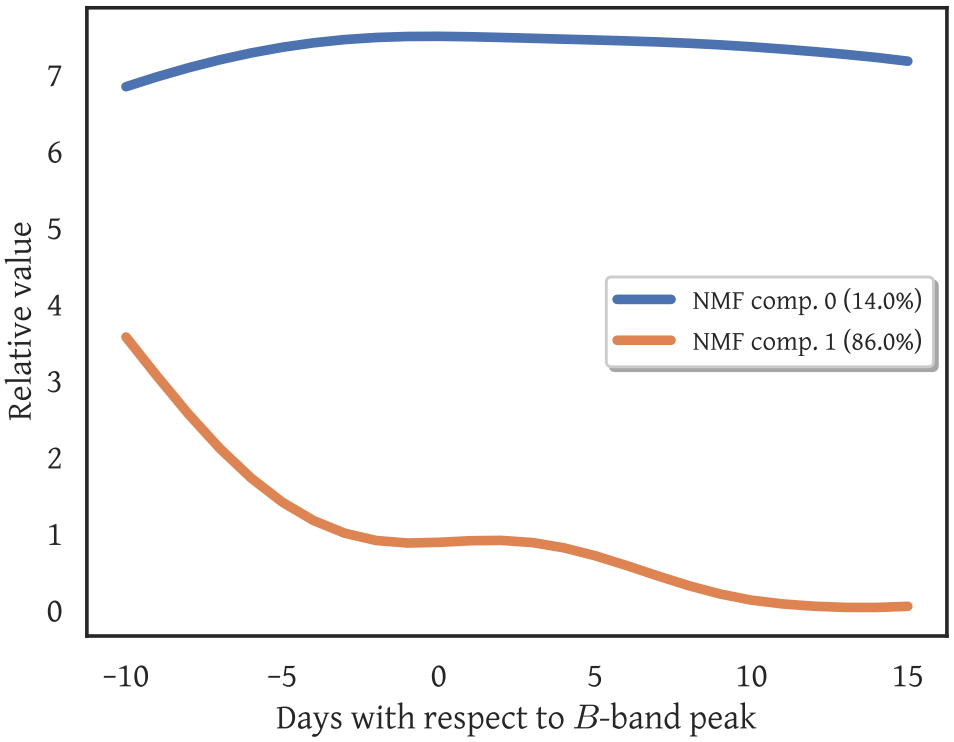

FIGURE 5.13: The description is the same as in Figure 5.3, but for two components.

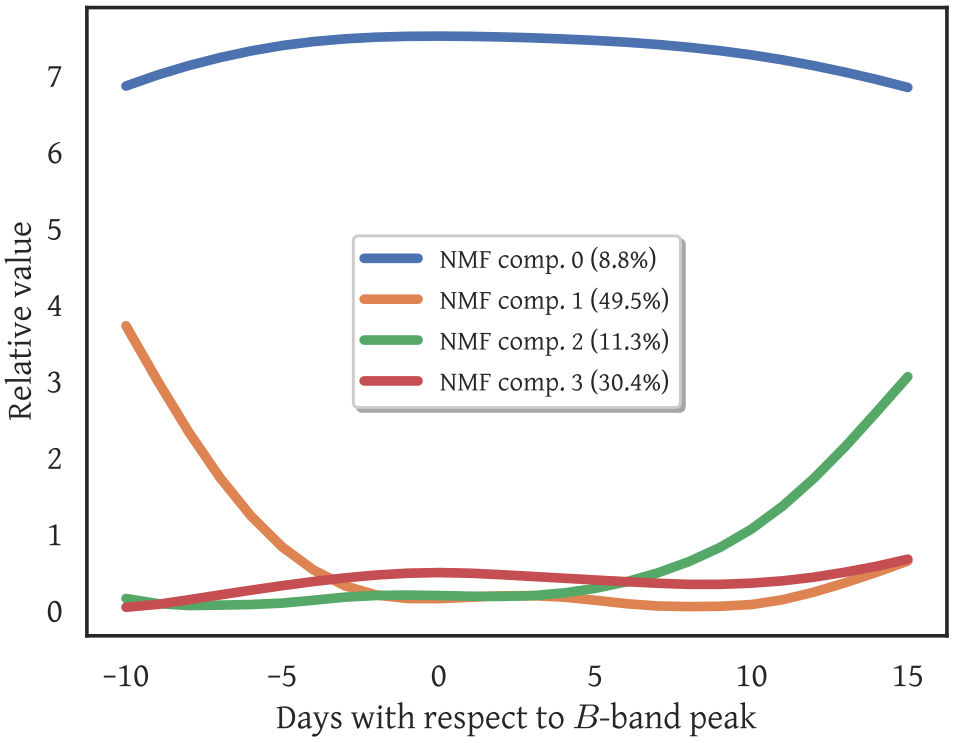

FIGURE 5.14: The description is the same as in Figure 5.3, but for four components.

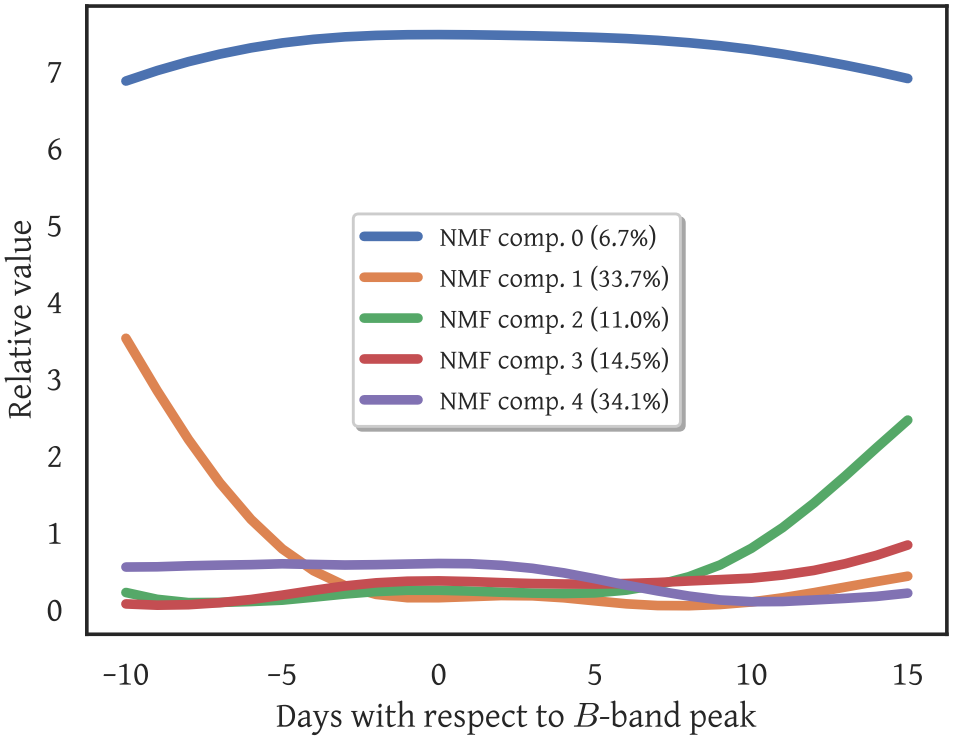

FIGURE 5.15: The description is the same as in Figure 5.3, but for five components.

TABLE 5.3: Hubble residual (HR) RMS for our method using different combinations of light-curve phase ranges. The range that gave the lowest RMS is marked in bold font. The same final sample of 156 SNe was used for for all these analyses.

min. phase (days)	max. phase (days)	HR RMS (mag)
−8	+12	0.125
−8	+15	0.120
−8	+18	0.123
−10	+12	0.123
−10	**+15**	**0.118**
−10	+18	0.122
−12	+12	0.125
−12	+15	0.125
−12	+18	0.127

Notes. The HR r.m.s. for the same sample, using SALT2, is 0.111 mag.

performed. Finally, from these 214 SNe, only 156 have $(B-V)_{\max}$ and form our final cosmological sample. I note that, although the cuts in the sample are severe, this is a proof-of-concept analysis with the idea of exploring new approaches and thus requires a 'golden' sample, removing possible biases.

In this chapter, I have provided a proof-of-concept analysis of SN Ia light curves. By using an NMF decomposition, I showed that the components extracted can be physically interpreted and compared to standard light-curve parameters. Furthermore, the coefficients related to these components can be used for the standardisation of SNe Ia, leading to similar results as well-established light-curve fitters, such as SALT2. The exact number of components and phase range used can affect the results, where we found a 'sweet-spot ' for the standardisation of SNe Ia with three NMF components and a phase range between -10 and $+15$ days.

PISCOLA is not only a tool that allows the user to fit SN Ia light curves and estimate distances, but also gives the opportunity to explore the astrophysics of these objects. In the next chapter, I look into the PISCOLA SED model and study the differences with the SALT2 SED model, focusing specifically on the change of colour as a function of wavelength and time.

Chapter 6

Type Ia Supernova Colour Law

In the previous chapter, I showed that PISCOLA, together with an appropriate machine-learning light-curve analysis, is a powerful tool for the standardisation of SNe Ia. In this chapter, I take a different turn and explore the astrophysics behind these objects.

The SN colour is the light-curve parameter that contributes most to the standardisation of SNe Ia. It is related to the physics, progenitors and environments of SNe Ia, and is a complicated parameter as there are several factors that may contribute to variations in the observed colour (e.g., SN circumstellar material or host galaxy extinction).

The wavelength-dependent variation of colour in SNe Ia is known as the 'colour-variation law' or 'colour law' (CL). SALT2 describes the CL as a wavelength-dependent function that does not vary in time or as a function of x_1 (see equation (1.27)). I can also use the PISCOLA mangling fits to estimate a CL, in a similar fashion to SALT2. The mangling function at $t_B^{\max}$ (see Section 3.3) describes how the colour of a SN varies with respect to a base SED template and therefore gives me a method to estimate the relative CL for a single SN (i.e., the mangling function is equal to $(B-V)_{\max}$ multiplied by the CL).

6.1 PISCOLA Colour Law

I divided the cosmological sample of SNe Ia used in the previous chapter (156 SNe) into bins of 0.05 mag in colour, and calculated their average mangling function in each bin. I then fit a third-order polynomial, optimising across all bins of $(B-V)_{\max}$ simultaneously, to obtain a functional form for the CL following the assumption that the CL is wavelength-dependent only (as in equation (1.27)). I note that only data between $\sim$3500 and $\sim$7000 Å is used for this as not all SNe have coverage bluer than 3500 Å, especially at low redshifts. High-z SNe get their ultraviolet (UV) wavelengths redshifted to optical wavelengths at the observer's frame. However, most of the SNe with rest-frame UV coverage do not have PISCOLA-measured $(B-V)_{\max}$ as the rest-frame V

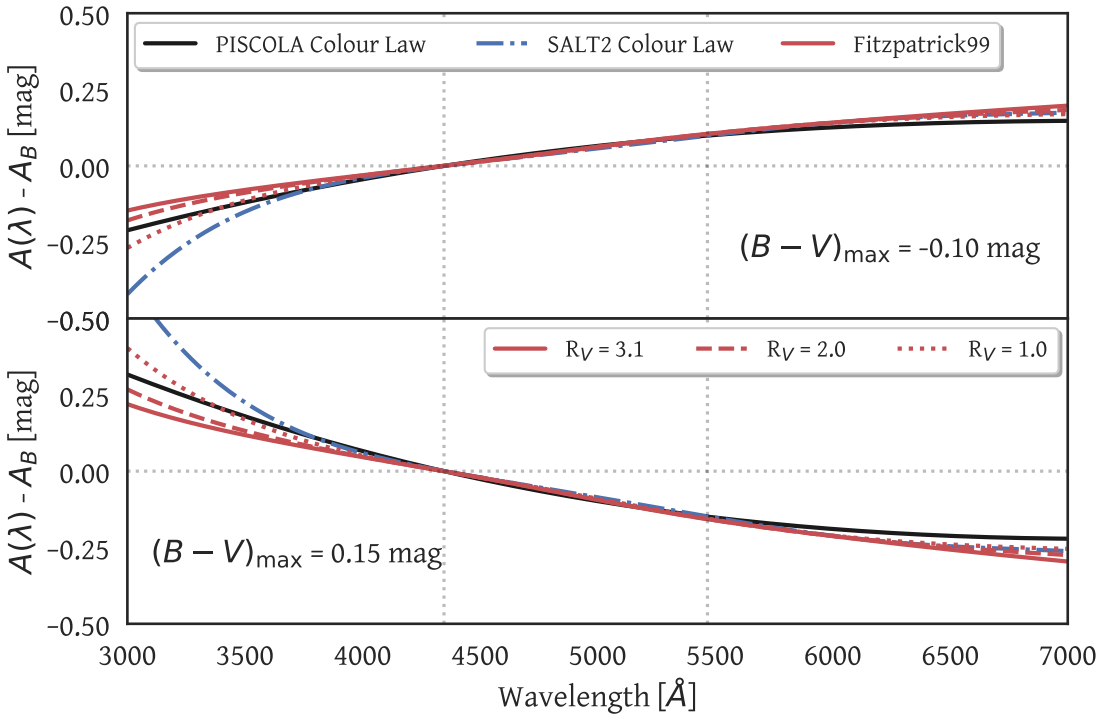

FIGURE 6.1: The colour law obtained with PISCOLA (solid black line) compared to that from SALT2 (dash-dotted blue line) and a Fitzpatrick (1999, Fitzpatrick99) extinction law for different R_V values (red lines). The vertical dotted lines mark the effective wavelengths of the B and V bands. This comparison is shown for two different $(B-V)_{\max}$ values (-0.10 and 0.15 mag). Similarities with the dust extinction laws is seen in both cases.

band gets redshifted outside the filters' range, so are not used for the estimation of the PISCOLA CL.

In Figure 6.1, I compare this CL against that of SALT2 and the extinction law from Fitzpatrick (1999) for three different values of the total-to-selective extinction ratio, R_V, and two different $(B-V)_{\max}$ values (-0.10 and 0.15 mag). The PISCOLA CL agrees with the Fitzpatrick (1999) extinction law with $R_V < 3.1$. Similar findings have been reported in previous work (e.g., Burns et al., 2014; Amanullah et al., 2015; Sasdelli et al., 2016; Brout & Scolnic, 2021; Thorp et al., 2021).

When comparing with the SALT2 CL, there is agreement at optical wavelengths, but some deviation towards the UV. However, as previously mentioned, the data around 3000 Å is limited and thus the PISCOLA CL at these wavelengths is merely an extrapolation.

The colour dispersion, i.e., the scatter around the CL, is also of importance to quantify the disagreement. SALT2 includes its CL in its model (equation (1.27)), possibly limiting its behaviour, and it is estimated during the training phase, while we estimate it after the PISCOLA fitting and correction process of the SNe Ia, almost directly from the data. In Figure 6.2, I compare the CLs of PISCOLA and SALT2 at $(B-V)_{\max}$

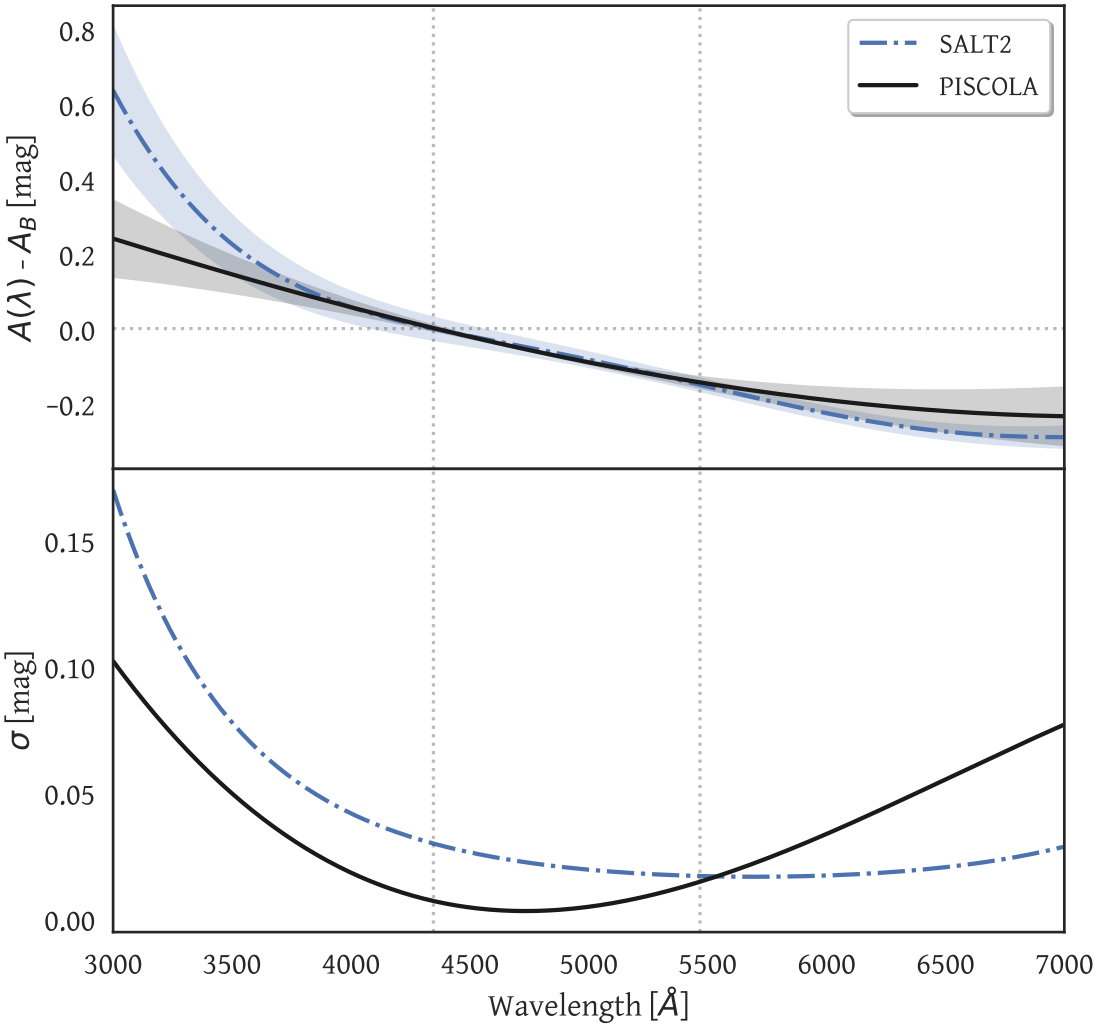

FIGURE 6.2: **Top** panel: CL obtained with PISCOLA (solid black line) compared to the CL from SALT2 (dash-dotted blue line) for $(B-V)_{\max} = 0.15$ mag. The shaded areas represent their respective colour dispersions. **Bottom** panel: Colour dispersion comparison between PISCOLA (solid black line) and SALT2 (dash-dotted blue line). The vertical dotted lines mark the effective wavelengths of the B and V bands.

$= 0.15$ mag, but also include their respective colour dispersions. I note that, despite the differences in the estimation of the CLs, they agree (considering the colour disperson), especially in the range used for calculating the PISCOLA CL (∼3500–7000 Å).

This was also tested with the simulations of Section 4.3.1, where I found similar results. Furthermore, by changing the shape of the CL of the simulations, PISCOLA is able to retrieve a CL that agrees with it within uncertainties (1σ at $\gtrsim$3500 Å; see Figure 6.3).

The colour dispersion indicates that PISCOLA has a larger scatter towards the near-IR, but similar in the UV, compared to SALT2. The shape of the colour dispersion curve from PISCOLA could be a consequence of a combination of three factors. The first is due to the smaller observational uncertainties in the B and V bands, where much of the flux of a SN Ia emerges, and larger uncertainties at redder and bluer wavelengths. The

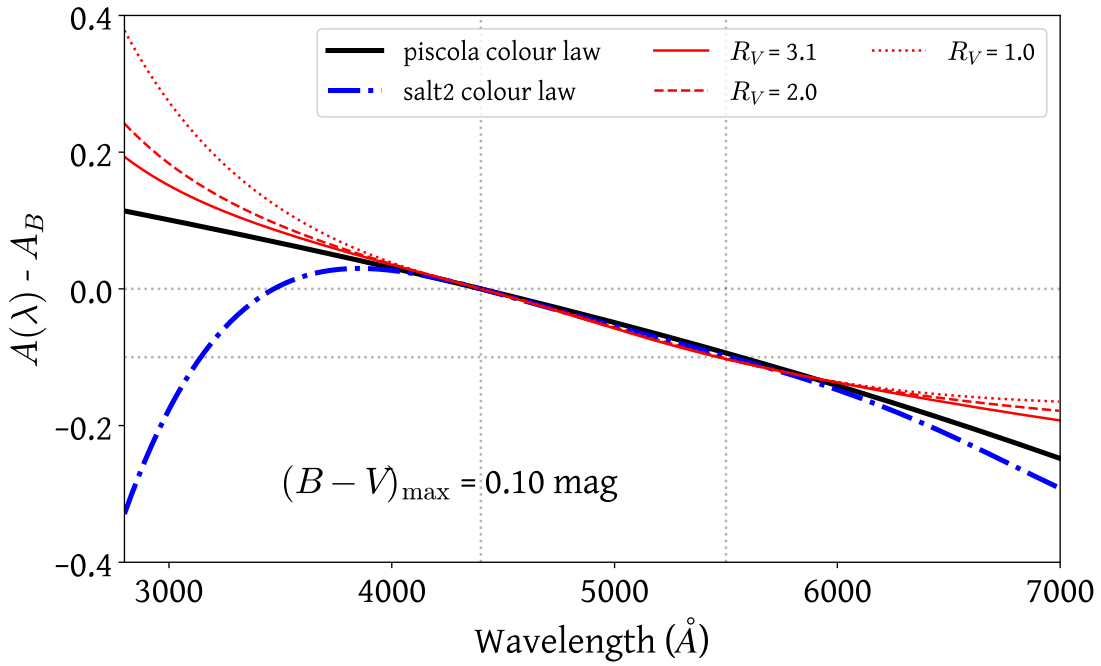

FIGURE 6.3: The description is the same as in Figure 6.1 but for $(B-V)_{\max} = 0.10$ mag and a SALT2 model with a different (artificial) CL shape. PISCOLA is able to retrieve a CL that agrees with that of SALT2 (at $\gtrsim$3500 Å) even after changing the shape of the CL in the SALT2 model.

second is due to the reduced number of SNe covering bluer and redder wavelengths (around 3500 Å and 7000 Å respectively) compared to the range around B and V. The third is that there may be a difference in the CL for different SNe.

The differences in CLs are important as they can represent differences in the underlying physics of SNe Ia. The SALT2 model only incorporates near-UV observations of high-z SNe (e.g., from SNLS) as these wavelengths are redshifted to optical wavelengths and can be observed with ground-based telescopes. In principle, the characteristics of these SNe could be intrinsically different to those at lower redshift (e.g., Ellis et al., 2008; Maguire et al., 2012). This may introduce biases in the SALT2-measured colour. The CL obtained with PISCOLA agrees with the average extinction law measured in the MW (with low values of R_V) within the uncertainties, implying that the remaining variation (intrinsic scatter) in SNe Ia may be driven by dust of similar properties to that in our galaxy. I note that Brout & Scolnic (2021) found that the remaining variation could be explained by dust with different properties to that in our galaxy, although using a SALT2 CL.

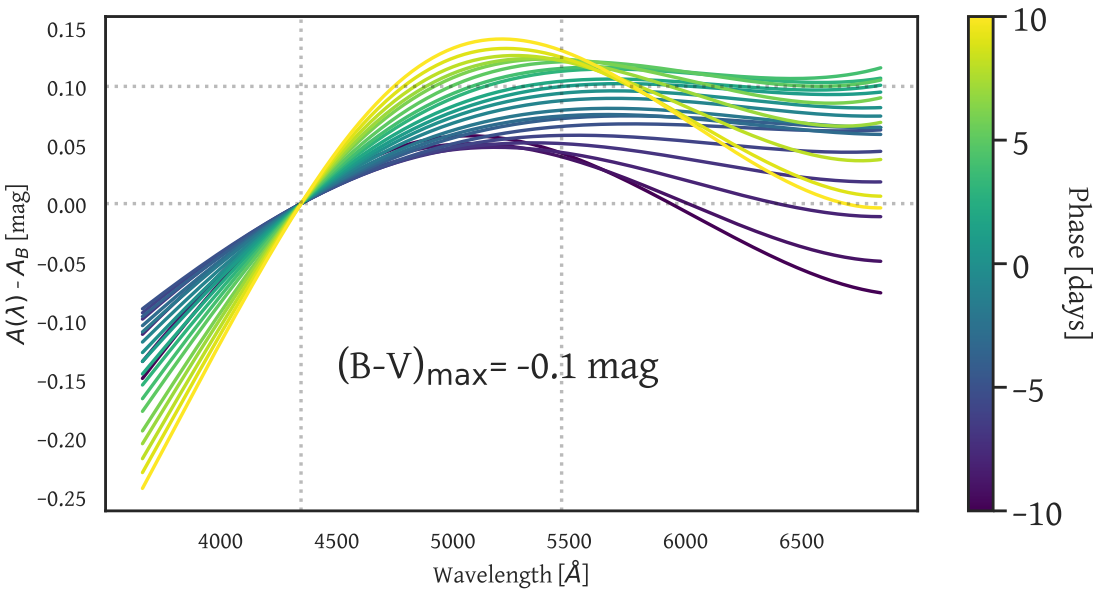

FIGURE 6.4: PISCOLA average mangling functions of SNe, with $(B-V)_{\max} = -0.1$ mag, at different phases between -10 and $+10$ days (colour-coded according to the bar on the right). The vertical dotted lines mark the effective wavelengths of the B and V bands while the horizontal lines mark the respective $A_V - A_B$ value at phase 0 days.

6.2 Testing Phase Dependence

As was mentioned above, SALT2 assumes a constant CL that does not depend on the phase of the SNe. Here I test whether or not PISCOLA retrieves a phase-independent CL. In Figure 6.4, I show the average mangling function of SNe with $(B-V)_{\max} = -0.1$ mag (the colour bin with the most SNe), at different phases between -10 and $+10$ days. A phase-dependent evolution of the mangling function (hence CL) seems to be observed, which would be inconsistent with the assumption of SALT2. However, the dispersion for the different phases can be relatively large. For phases around 0 days, the dispersion is similar to that shown in the bottom panel of Figure 6.2, but for much later or earlier phases, the dispersion can even double. Thus, this apparent evolution is not significant and the PISCOLA CL is consistent with the phase-independent CL of SALT2.

To further test this results, I studied the effect that the x_1-dependent component of the SALT2 SED model (M_1 in equation (1.27)) has on colour as a function of phase (see Figure 6.5). I remind the reader that the x_1-dependent component of the SED is not included in the PISCOLA fits. The SNe Ia sample used in this chapter has in average $x_1 \sim 0$, taking the values from Scolnic et al. (2018b). Furthermore, I note that, despite different x_1 contributions having different colour evolution (Figure 6.5), x_1 does not depend on phase. Therefore, the x_1-dependent component of the SALT2 SED is unable to explain any evolution in the CL.

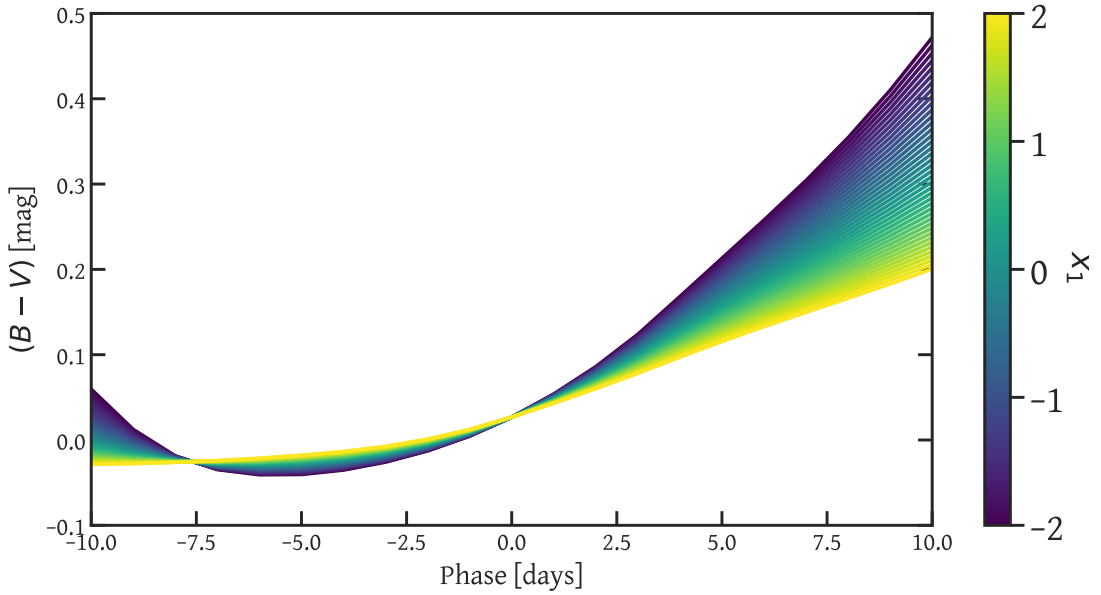

FIGURE 6.5: $(B-V)$ evolution for the SALT2 SED time-series template including the x_1-dependent component, M_1, as a function of phase, for different values of SALT2-x_1 (colour-coded according to the bar on the right).

To eliminate the effect of redshift in the apparent CL evolution (SALT2 is trained mostly with low-z SNe), I also estimated the CL as a function of phase for different bins of redshift. I found similar CL shapes for all the tested bins, all consistent with no CL evolution.

6.3 Exploring the SNe Ia Colour Law with DES

In order to corroborate the findings from the previous sections of this chapter, I decided to use a different sample. DES was a 6-year survey covering a large portion on the Southern sky using the Dark Energy Camera (DECam Flaugher et al., 2015) in the 4-m Blanco telescope at the Cerro Tololo Inter-American Observatory. The survey includes a 5-year transient survey, 'DES-SN', optimised for the purpose of observing SNe Ia for cosmology over a redshift range $0.2 < z < 1.2$ (Smith et al., 2020, and references therein), with characteristics similar to those of SNLS and PS1 (e.g., average cadence of 7 days).

For this work, I use the public 3-year sample of spectroscopically classified SNe Ia (DES-SN3YR; Abbott et al., 2019), which consist of 207 SNe Ia in the redshift range $0.02 < z < 0.85$, and supplement it with 122 low-z SNe Ia from CfA3, CfA4 and CSP (also included in the Pantheon sample) used for the cosmological analysis in Abbott et al. (2019), with a total of 329 SNe Ia (I will refer to the joint sample as the DES-SN3YR). Using SNe Ia across a wide range of z prevents biases from possible selection effects, as previously

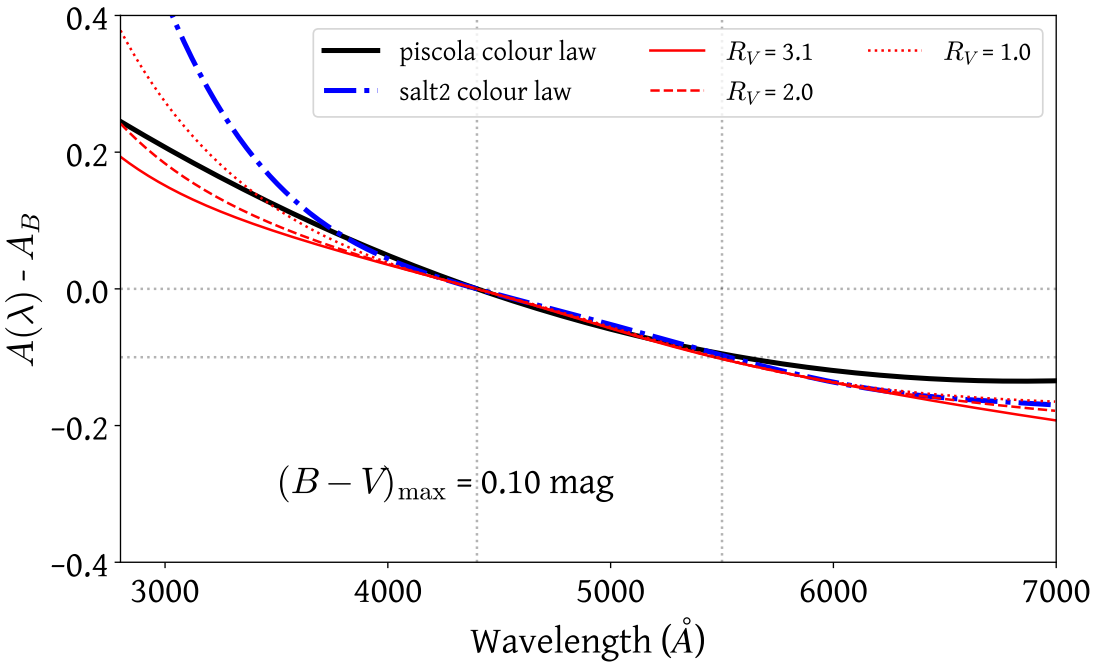

FIGURE 6.6: The colour law obtained with PISCOLA (solid black line) compared to that from SALT2 (dash-dotted blue line) for the DES-SN3YR sample. A Fitzpatrick (1999, Fitzpatrick99) extinction law with different R_V values is shown for reference (red lines). The vertical dotted lines mark the effective wavelengths of the B and V bands. This comparison is shown for a $(B-V)_{\max}$ value of 0.10 mag).

mentioned (e.g., selection of intrinsically different populations by using only high-z SNe).

I made sure to use the proper set of filters, magnitudes systems and photometry (e.g., Burke et al., 2018; Brout et al., 2019), available online[1]. The DES-SN3YR sample was fitted with PISCOLA in a similar fashion to the Pantheon sample (Chapter 4). 280 SNe were successfully fitted ($m_B^{\max}$ measured), where most of the 'failed ' SNe were those from the low-z surveys without peak coverage. The higher successful rate compared to the surveys in the Pantheon sample is given by the better data quality, due to the superior camera and z-band response used in DES (Smith et al., 2020).

Using this sample, I estimate the PISCOLA CL as described in Section 6.1. The result is shown in Figure 6.6, where I compare it with the SALT2 CL and a Fitzpatrick (1999) extinction law with different R_V values, as before. I note that the CL obtained with both samples, DES and Pantheon, are very similar. This does not only help validate PISCOLA by proving that PISCOLA is consistent, but also corroborates the CL obtained in Section 6.1.

Given this result, I do not expect to see a CL evolution, as before (Section 6.2), for the DES-SN3YR sample. In the left panels of Figure 6.7, I show the mangling functions/-CLs for SNe with $(B-V)_{\max}$ between -0.2 and 0.25 mag (PISCOLA-measured colour

[1] https://des.ncsa.illinois.edu/releases/sn

range for the sample), and their dependence on phase (colour coded). Similar results were found as with the Pantheon sample. In the right panels of Figure 6.7, I show the $A_V - A_B$ (i.e., the difference between the values of the CL at the effective wavelengths of the V and B bands) evolution as a function of phase for the different $(B-V)_{\rm max}$ values. As can be seen, these are all consistent with no evolution (i.e., a horizontal straight line).

I note that A_x is commonly used to refer to the extinction value in x band, however, the CL might not necessarily be driven (completely) by dust. I use this nomenclature to follow the convention used in other works for easier comparison (e.g., Guy et al., 2005, 2007).

To conclude this chapter, by using SNe Ia from the Pantheon sample, PISCOLA retrieves a CL consistent with that of SALT2, but with hints of some, but not significant deviation towards the UV. This CL is also consistent with dust extinction laws with $R_V < 3.1$ (i.e., smaller values than those found in the MW). By studying the CL as a function of phase, I found that the PISCOLA CL is consistent with a phase-independent CL, as that from SALT2. Analysing a separate sample of SNe Ia from DES, I found similar results, providing further validation for PISCOLA.

In this chapter, I have shown how important it is to find new ways of extracting new information to help better understand the explosion mechanisms and progenitors of SNe Ia. This allows us to understand the link between different types of SNe and the bigger picture of how they are all connected. Thus, In the following chapter, I study the astrophysics of SNe II, by analysing a particular case of this type of objects.

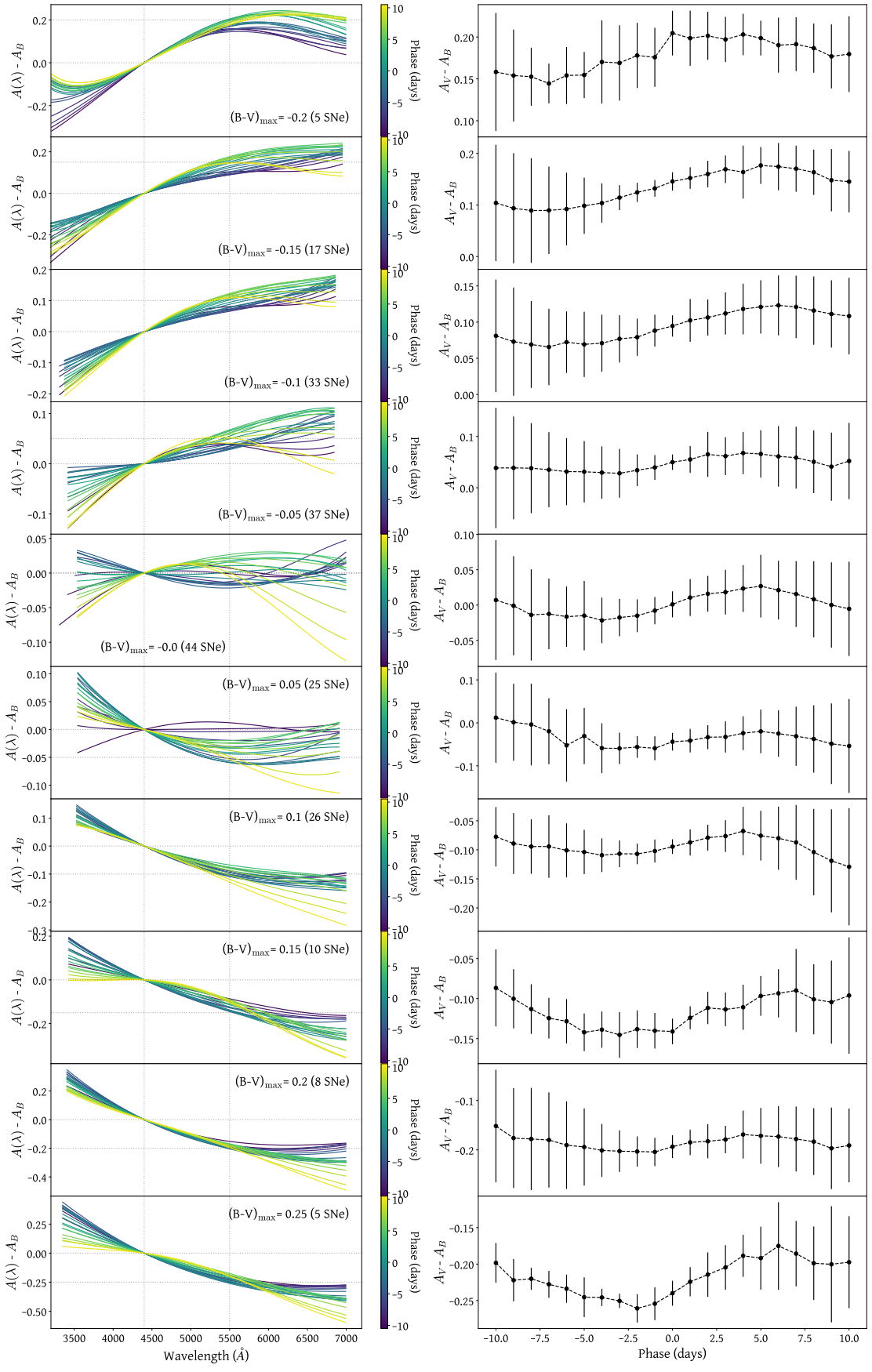

FIGURE 6.7: **Left** panels: PISCOLA average mangling functions of SNe Ia with $(B-V)_{\max}$ between -0.2 and 0.25 mag at different phases between -10 and $+15$ days (colour-coded according to the bar on the right). The vertical dotted lines mark the effective wavelengths of the B and V bands while the horizontal lines mark the respective $A_V - A_B$ values at phase 0 days. **Right** panels: $A_V - A_B$ as a function of phase.

Chapter 7

Supernova 2016aqf

In the previous chapter, I showed the importance of studying the astrophysics of SNe Ia, through different wavelengths. In this chapter, I move my focus to studying the astrophysical properties of SNe II to expand my knowledge of the SN 'landscape'. More specifically, I study the particular case of a low-luminosity (LL) SN II, SN 2016aqf. This 'extreme' case of SN can be key in understanding the progenitor scenarios and explosion mechanisms of SNe II and CCSNe in general. This chapter is based on the work published by Müller-Bravo et al. (2020)

7.1 Low-Luminosity Type II SNe

SNe II show a large diversity in luminosities, with peak V-band maximum absolute magnitudes ranging from ~ -13.5 to ~ -19 mag, and an average of about -16.7 mag (Anderson et al., 2014). With the increasing number of telescopes and surveys, several LL SNe II, generally events with $V \gtrsim -16$ mag (e.g., Kulkarni & Kasliwal, 2009; Smartt et al., 2015, however, see Pastorello 2012), have been found in the past decades (e.g., Turatto et al., 1998; Pastorello, 2012; Spiro et al., 2014; Lisakov et al., 2018).

The prototype of this faint sub-class is SN 1997D (de Mello et al., 1997; Turatto et al., 1998). SN 1997D displayed a low luminosity and low expansion velocity. However, it was discovered several weeks after peak, with no well-constrained explosion epoch. The first statistical study of this sub-class was presented by Pastorello et al. (2004), who found the class to be characterised by narrow spectral lines (P-Cygni profiles) and low expansion velocities (a few 1000 km s^{-1} during the late photospheric phase), suggesting low explosion energies ($E_{\rm exp} \lesssim$ few times 10^{50} erg). Their bolometric luminosity during the recombination ranges between $\sim 10^{41}$ erg s^{-1} and $\sim 10^{42}$ erg s^{-1}, with SN 1999br (Pastorello et al., 2004) and SN 2010id (Gal-Yam et al., 2011) being the faintest SNe II discovered. They also show lower luminosity in their exponential-decay tail than the

bulk of SNe II, which reflects their low ^{56}Ni masses ($M_{Ni} \lesssim 10^{-2}$ $M_{\odot}$), in agreement with the low explosion energies, as expected from the M_{Ni}–E_{exp} relation found in different studies (e.g., Pejcha & Prieto, 2015; Kushnir, 2015; Müller et al., 2017). Spiro et al. (2014) have since expanded the statistical study of LL SNe II, adding several objects and finding similar characteristics to those found by Pastorello et al. (2004). While the current sample of nebular-phase (late-time) spectra of LL SNe II is growing, the study of additional events with better cadence and higher S/N data is essential for understanding their observed diversity.

The nebular [O I] $\lambda\lambda$6300, 6364 doublet and Ni/Fe abundance ratio, measured from the [Fe II] λ7155 and [Ni II] λ7378 lines, are very important for the understanding of the inner structure of the progenitor and the explosion mechanism dynamics of SNe II and possibly CCSNe in general (Section 1.1.1). The latter lines are found in several LL SNe II, probably due to their lower expansion velocity de-blending them. However, there are few studies of this ratio, mainly due to the lack of late-time spectra. In the rest of this chapter I present the study of SN 2016aqf, a well-observed (i.e., excellent spectral and photometric coverage) LL SN II, discovered soon after explosion.

7.2 Observations, reductions and host galaxy

7.2.1 SN Photometry and Spectroscopy

SN 2016aqf (ASASSN-16cc) was discovered on 2016 February 26 at 04:33:36 UTC (57444.19 MJD) by the All-Sky Automated Survey for Supernovae[1] (ASAS-SN; Shappee et al., 2014) at RA = 05h46m23^{s}.91 and Dec. = -52° 05$'$18$''$.9, in the galaxy NGC 2101 (Brown et al., 2016) at $z = 0.004016$ (Lauberts & Valentijn, 1989). On 2016 February 27, SN 2016aqf was classified as a SN II (Hosseinzadeh et al., 2016; Jha & Miszalski, 2016). Based on the low luminosity of the host ($M_B = -17.66$ mag as in Gutiérrez et al. 2018, although see Section 7.2.2), Claudia Gutiérrez commenced a follow-up campaign with the extended Public ESO Spectroscopic Survey of Transient Objects (ePESSTO; Smartt et al., 2015) as part of the programme 'SNe II in Low-luminosity host galaxies'.

The final pre-explosion non-detection in the V-band, reported three days before the date of classification by ASAS-SN (57442 MJD), has a limiting magnitude $\sim$ 16.7 mag, which does not give a strong constraint on the explosion epoch. Previous non-detections have similar limiting magnitudes. Hence, I decided to estimate the explosion epoch using the spectral matching technique (e.g., Anderson et al., 2014; Gutiérrez et al., 2017). I used GELATO[2] (Harutyunyan et al., 2008) to find good spectral matches to the highest resolution spectrum of SN 2016aqf, as it is also one of the first spectra taken (57446

[1] http://www.astronomy.ohio-state.edu/assassin/index.shtml
[2] https://gelato.tng.iac.es/gelato/

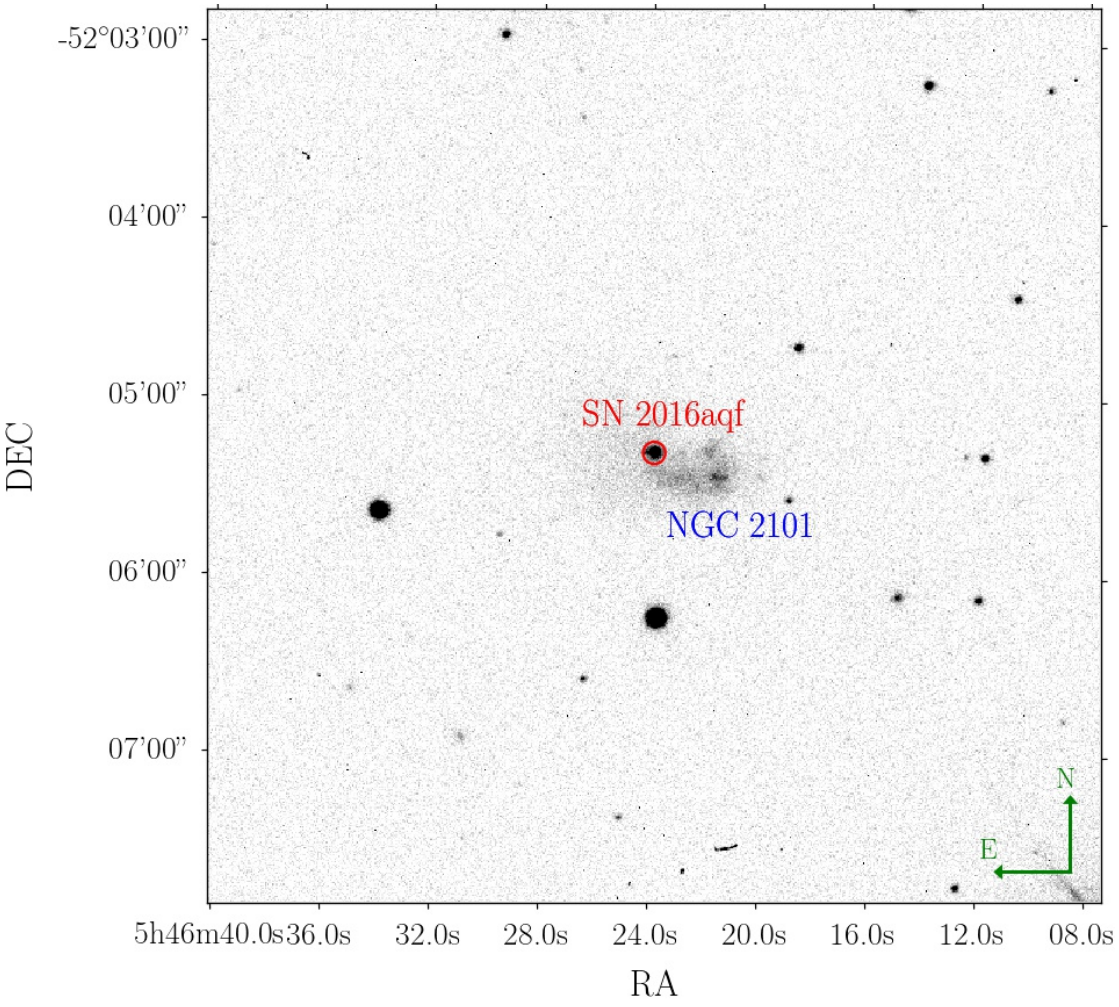

FIGURE 7.1: *r*-band image of NGC 2101 with SN 2016aqf marked. Data from the 1.0-m Las Cumbres Observatory telescopes (MJD = 57514, 74 days after explosion).

MJD). From the best matching templates, I calculated a mean epoch of the spectrum of ∼6 days after explosion and a mean error added with the standard deviation of the explosion epochs in quadrature of ∼ 4 days. This gives an explosion epoch of MJD 57440.19±4 (slightly different to the estimated epoch in Gutiérrez et al. 2018 as they used the non-detection).

Optical *BVgri* imaging of SN 2016aqf was obtained with the 1.0-m telescope network of the Las Cumbres Observatory (LCO; Brown et al., 2013) as part of both ePESSTO and the 'Las Cumbres Observatory SN Key Project', with data taken from 8 to 311 d after explosion. All photometric data were reduced following the prescriptions described by Firth et al. (2015). This pipeline subtracts a deep reference image constructed using data obtained in the *BVgri* bands three years after the first detection of SN 2016aqf to remove the host-galaxy light using a point-spread-function (PSF) matching routine. SN photometry is then measured from the difference images using a PSF-fitting technique. Figure 7.1 shows the SN position within the host galaxy. The photometry of SN 2016aqf is presented in Table A.1 in Appendix A.

Spectroscopic observations were obtained with the ESO Faint Object Spectrograph and Camera version 2 (EFOSC2; Buzzoni et al., 1984) at the 3.58-m ESO New Technology Telescope (NTT), the FLOYDS spectrograph (Brown et al., 2013) on the Faulkes Telescope South (FTS), and the Robert Stobie Spectrograph (RSS; Burgh et al. 2003; Kobulnicky et al. 2003) at the Southern African Large Telescope (SALT). FLOYDS spectra were taken as part of the 'Las Cumbres Observatory SN Key Project'. The observations include phases from 2 to 348 d after explosion (all phases in this chapter are relative to the estimated explosion epoch of SN 2016aqf). EFOSC2 spectra, obtained with grism #13, cover 3500–9300 Å at a 21.2 Å resolution, the FLOYDS spectra have wavelength coverage of $\sim$3200 – 10000 Å with a resolution of $\sim$ 18 Å, and the RSS spectrum (Jha & Miszalski, 2016) covers 3600–9200 Å at $\sim$ 7 Å resolution. The data reduction of the EFOSC2 spectra was performed using the PESSTO pipeline[3] (Smartt et al., 2015), while the FLOYDS data were reduced using the PYRAF-based FLOYDSSPEC pipeline[4] (Valenti et al., 2014). Spectral information is summarised in Table A.2 in Appendix A.

7.2.2 Host Galaxy

Photometry of NGC 2101 was obtained with the LCO 1.0-m telescope network, and spectroscopy with the Focal Reducer/low dispersion Spectrograph 2 in the Very Large Telescope, around three years after the SN explosion (2019 February 6 at 04:38:48 UTC). I estimated a galaxy distance of $\mu = 30.16 \pm 0.27$ mag (see Section 7.3.2), consistent with the Tully-Fisher value of $\mu = 30.61 \pm 0.80$ mag, as reported in the NASA/IPAC Extragalactic Database[5] (NED). Adopting the distance estimated in this work, the galaxy has $M_B = -17.22 \pm 0.34$ mag, which is consistent with the value reported in Gutiérrez et al. (2018, -17.66 mag) given the large uncertainties from the reported distance. I use the total corrected B-band apparent magnitude, with the total B-band magnitude error as reported in HyperLEDA, using error propagation. The radial velocity corrected for Local Group infall onto Virgo is 883 ± 3 km s^{-1} (Theureau et al., 1998; Terry et al., 2002), as reported in HyperLEDA[6] (Makarov et al., 2014), a value which I use to estimate the corrected redshift of SN 2016aqf.

From the spectrum of the H II region at the position of the SN, I measure the emission line fluxes of Hα, Hβ, [N II] and [O III]. I estimated the star-formation rate (SFR) from the Hα line as SFR = $2.3 \pm 0.6 \times 10^{-1}$ M$_\odot$ yr^{-1}, using the calibration from Kennicutt & Evans (2012), where the uncertainty is driven by the uncertainty in the distance. Using the calibration of Marino et al. (2013), I then estimated a gas-phase metallicity of (12 + log(O/H))$_{O3N2}$ $= 8.144 \pm 0.025$ dex and (12 + log(O/H))$_{N2}$ $= 8.134 \pm 0.042$ dex, i.e., below the solar value of 8.69 dex (Asplund et al., 2009). This is low compared to many

[3] https://github.com/svalenti/pessto
[4] https://github.com/svalenti/FLOYDS_pipeline
[5] http://ned.ipac.caltech.edu/
[6] http://leda.univ-lyon1.fr/

other SN II host galaxies, but not uncommon (e.g., Anderson et al., 2016). However, the metallicity does not follow the relation found with the Fe II λ5018 pseudo-equivalent-width (pEW; a measure of the strength/intensity of a spectral line with respect to a *pseudo*-continuum) evolution measured from SN 2016aqf (e.g., Dessart et al., 2014; Anderson et al., 2016; Gutiérrez et al., 2018). This may be caused by the lower temperatures in LL SNe II which causes the earlier appearance of the Fe II lines in these objects (Gutiérrez et al., 2017).

7.3 Data Analysis

7.3.1 Extinction corrections

I adopt a MW reddening value of $E(B-V)_{\rm MW} = 0.047$ mag, and correct my photometry using the prescription of Schlafly & Finkbeiner (2011) and the Cardelli et al. (1989) extinction law with $R_V = 3.1$. To estimate the host galaxy extinction, I investigated the EW of the Na I D ($\lambda\lambda$5889, 5895) absorption, a well-known tracer of gas, metals and dust (e.g., Richmond et al., 1994; Munari & Zwitter, 1997; Turatto et al., 2003; Poznanski et al., 2012). I note that these relations tend to have large uncertainties.

The spectrum at +6 d is the only one that seems to shows Na I D absorption lines from the MW and the host galaxy. I used the relations for one line (D_1) and two lines (D_1+D_2) from Poznanski et al. (2012), obtaining upper limits of $E(B-V) \lesssim 0.028 \pm 0.011$ mag and $E(B-V) \lesssim 0.032 \pm 0.006$ mag, respectively. This gives a weighted average value of $E(B-V) \lesssim 0.031$ mag. Given this very small level of reddening (and its uncertainty), I choose not to make an extinction correction to the SN data. I do not use other methods to estimate this value as they rely on the SN colour; de Jaeger et al. (2018) showed that the majority of colour dispersion of SNe II is intrinsic to the SN.

7.3.2 Light curve and distance

The *BVgri*-band light curves of SN 2016aqf (Figure 7.2) cover from +8 to +311 d. As the host galaxy is not in the smooth Hubble flow (where recessional velocities are dominated by the expansion of the universe), I estimated the distance to SN 2016aqf using the Standardized Candle Method (Hamuy & Pinto, 2002b), which relates the velocity of the ejecta of a SN II to its luminosity during the plateau, and the relation of Kasen & Woosley (2009, equation 17) for a redshift-independent distance estimate. I calculate the distance modulus $\mu = 30.16 \pm 0.27$ mag (10.8 ± 1.4 Mpc), which gives $M_V^{\rm max} = -14.58$ mag and a mid-plateau V-band luminosity of -14.63 mag (Section 7.4.2). Note that the plateau luminosity is slightly brighter, thus $M_V^{\rm max}$ represents the maximum luminosity from the peak closest to the bolometric peak (Section 7.3.4).

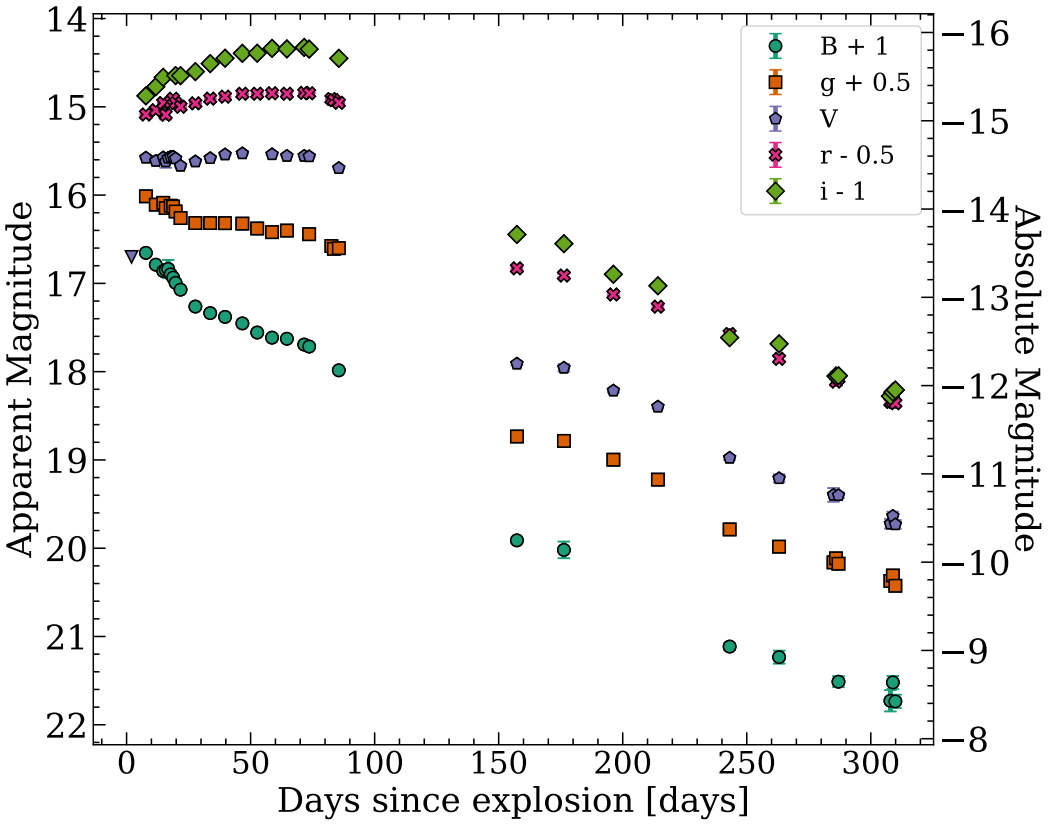

FIGURE 7.2: SN 2016aqf *BVgri*-band photometry from +8 to + 311 d. *BV* bands are in Vega magnitude system, while *gri* bands are in AB magnitude system. The last non-detection in *V* band is also shown (inverted triangle). The SN was not visible around the transition from the optically-thick to the optically-thin phase. Offsets have been applied to the photometry for visualisation purposes. As in all figures in this paper, the photometry is corrected for MW extinction but not host extinction, and the data are in the rest-frame.

I estimated $M_V^{\max}$ from the first epoch of photometry given that the last non-detection helps to obtain a good constraint.

During the plateau, the SN shows an increase in the *Vri*-bands luminosity, probably due to its low temperature which shifts the peak luminosity from the UV to redder bands more rapidly compared to normal SNe II. The gap in observations between +80 and +150 days was caused by the sun obstructing the line-of-sight, and coincides with the SN transitioning from the optically-thick to the optically-thin phase. The *V*-band decreases by ~ 2 mag across the gap in the light curve, and is an estimate of the decrease caused by the transition from plateau to nebular phase, smaller than other LL SNe II ($\sim$ 3–5 mag; e.g., Spiro et al., 2014).

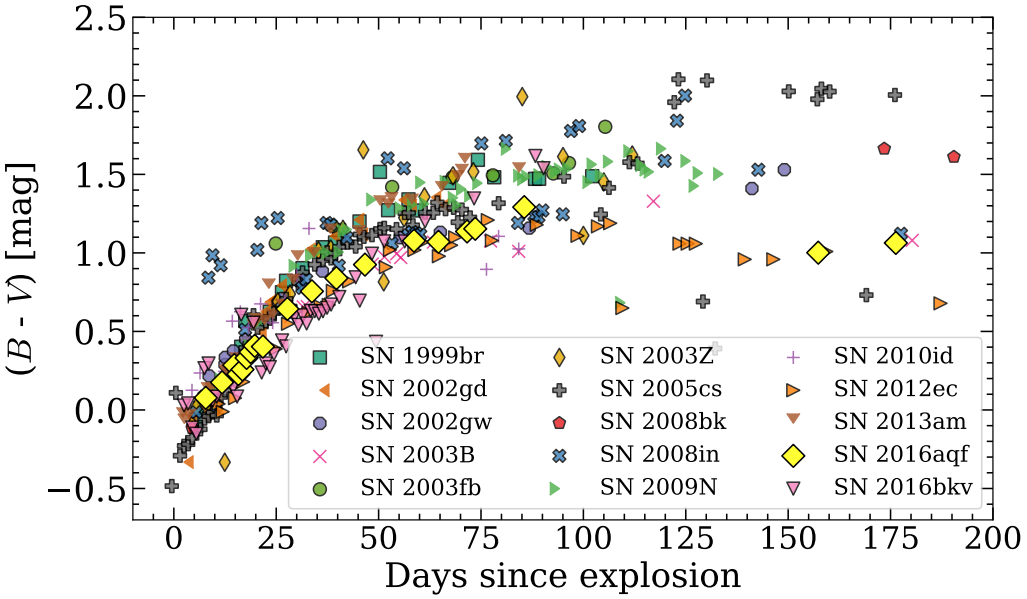

FIGURE 7.3: $(B-V)$ colour evolution of SN 2016aqf compared to my sample of LL SNe II. All data is corrected for MW and host galaxy extinction (except for those SNe with host extinction values reported as upper limits in Table A.3 in Appendix A). Notice that the dispersion generally increases with time. Uncertainties are not shown as they are relatively small in general.

7.3.3 Colour Evolution

In Figure 7.3, I show the $(B-V)$ colour curve (corrected for extinction) of SN 2016aqf during the first ∼200 days. At the beginning of the observations (+8 d) it has a colour close to 0 mag, which slowly increases to around 1.0 mag at $\sim$ +50 d and ∼1.3 mag before the gap in coverage.

For comparison, I form a sample of other LL SNe II from the literature with good data coverage and similar properties to my object: SNe 1999br (Hamuy, 2003; Pastorello et al., 2004; Gutiérrez et al., 2017), 2002gd, 2002gw , 2003B, 2003fb, 2003Z, 2004fx, 2005cs, 2008bk, 2008in, 2009N, 2010id, 2013am and 2016bkv. Note that this sample is used throughout the rest of this chapter but is later supplemented with other SNe in Section 7.5.3. These SNe and their references are in Table A.3 in Appendix A. In addition, I include SN 2012ec (Maund et al., 2013), a non-LL SN II, as a reference as it has a well-measured Ni/Fe abundance ratio, used in my later analysis. For this comparison sample, I use photometry and spectra obtained from the 'Open Supernova Catalog' (Guillochon et al., 2017) and the Weizmann Interactive Supernova Data Repository (Yaron & Gal-Yam, 2012). Note that I only used epochs with both B and V photometry to calculate the $(B-V)$ colour, without applying interpolations. The photometry of this sample is corrected for MW extinction (see Section 7.3.1), and host galaxy extinction, using the values from the references in Table A.3 in Appendix A. However,

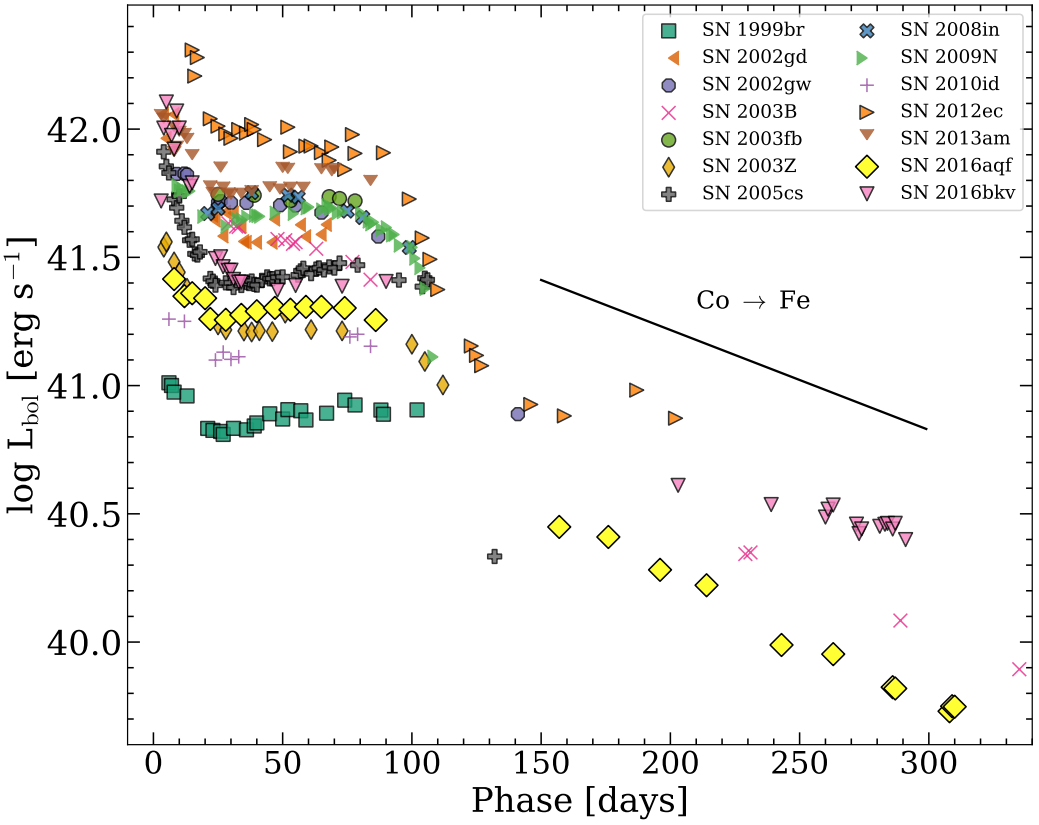

FIGURE 7.4: Bolometric light curve of SN 2016aqf compared to my LL SNe II sample. The light curves were obtained by using bolometric corrections (see Section 7.3.4 for details). All data is corrected for MW and host galaxy extinction (except for those with values reported as upper limits, see Table A.3 in Appendix A). The ^{56}Co $\rightarrow$ ^{56}Fe decay line is shown for comparison. Uncertainties are not shown for visualisation purposes

I do not correct for host galaxy extinction when the reported value is an upper limit (this does not represent a problem given the relatively small extinction values, $A_V < 0.1$ mag).

The $(B-V)$ evolution of SN 2016aqf is in general flatter than the bulk of my sample, showing similar colours at early epochs ($t \lesssim$15 days), but becoming slightly bluer at later epochs ($t \gtrsim$25 days), similar to SN 2012ec. After $\sim$100 d the dispersion in the colour evolution of my sample starts increasing, probably due to the faintness of these objects.

7.3.4 Bolometric light curve

I estimated the bolometric light curve of SN 2016aqf by applying the bolometric correction from Lyman et al. (2014) (assuming a cooling phase of 20 days). I use the $(g-i)$ colour as it shows the smallest dispersion. Most SNe in my LL SN II sample have only $BVRI$ data, so, to be consistent, I calculated their bolometric light curves by using the

$(B-I)$ colour as it has the smallest dispersion within the available bands, using the distances from Table A.3 in Appendix A. Only epochs with simultaneous B and I bands (or g and i for SN 2016aqf) were used. The light curves are shown in Figure 7.4 (SN 2008bk is not shown as it does not have epochs with simultaneous B and I coverage). Unfortunately, as the relations from Lyman et al. (2014) only work in a given colour range, I can not estimate the bolometric light curve during the nebular phase of some of the SNe.

The luminosity of SN 2016aqf at peak is $L_{\rm bol} \approx 10^{41.4}\,{\rm erg\,s^{-1}}$, estimated from the first epoch with photometry. The luminosity of SN 2016aqf during the cooling phase generally decreases less steeply than other LL SNe II. During the plateau phase, the luminosity falls to $L_{\rm bol} \approx 10^{41.3}\,{\rm erg\,s^{-1}}$, placing it in the mid-luminosity range of my sample (between SN 2005cs and SN 2002gd). After the gap, the SN has a luminosity of $L_{\rm bol} \approx 10^{40.5}\,{\rm erg\,s^{-1}}$, dropping to $L_{\rm bol} \approx 10^{39.7}\,{\rm erg\,s^{-1}}$ at $+300$ d. The exponential-decay tail is steeper than the ^{56}Co decay (0.98 mag per 100 days Woosley et al., 1989), although shallower than the decay in the V-band, presumably due to γ-ray leakage.

7.3.5 Early spectral evolution

The spectra of SN 2016aqf have narrower lines than spectra of normal SNe II, suggesting low expansion velocities and low explosion energies. Spectra obtained during the optically-thick phase are shown in Figure 7.5. During the first two weeks, the evolution is mainly dominated by a blue continuum and Balmer lines, showing P-Cygni profiles of Hα and Hβ. Fe II λ4924, λ5018, λ5169 and Ca II $\lambda\lambda\lambda$8498, 8542, 8662 then appear, becoming prominent at later epochs. The Na I D appears at around one month. Sc II/Fe II λ5531, Sc II λ5663, λ6247 and Ba II λ6142 appear at around $+50$ d. O I λ7774 is weakly present after one month.

Figure 7.6 shows the early-time spectra of SN 2016aqf with other SNe from my comparison sample. The Fe II lines are present in all SNe, although in SN 2016aqf they are generally weaker. SN 2016aqf is similar to SN 2002gw and SN 2010id, with a relatively featureless spectrum between Hβ and Hα. However, I see no major differences with the rest of the sample at $\sim +15$ d.

At around $+50$ d (Figure 7.7), SN 2016aqf resembles SN 2009N, with the difference that the Sc II/Fe II λ5531, Sc II λ5663, λ6247 and Ba II λ6142 lines are weaker (and weaker than most other SNe in my sample). O I λ7774 is seen in the spectrum of most SNe, except SN 2002gd and SN 2016bkv where the resolution of the spectra precludes a secure identification. Most SNe have very similar Fe II and Ca II NIR line profiles. SN 2016aqf does not display any other peculiarity with respect to the comparison sample. Note that host galaxy extinction may be substantial for SN 2013am (Zhang et al., 2014; Tomasella et al., 2018), explaining the drop in flux at the bluer end of this SN (Figure 7.6).

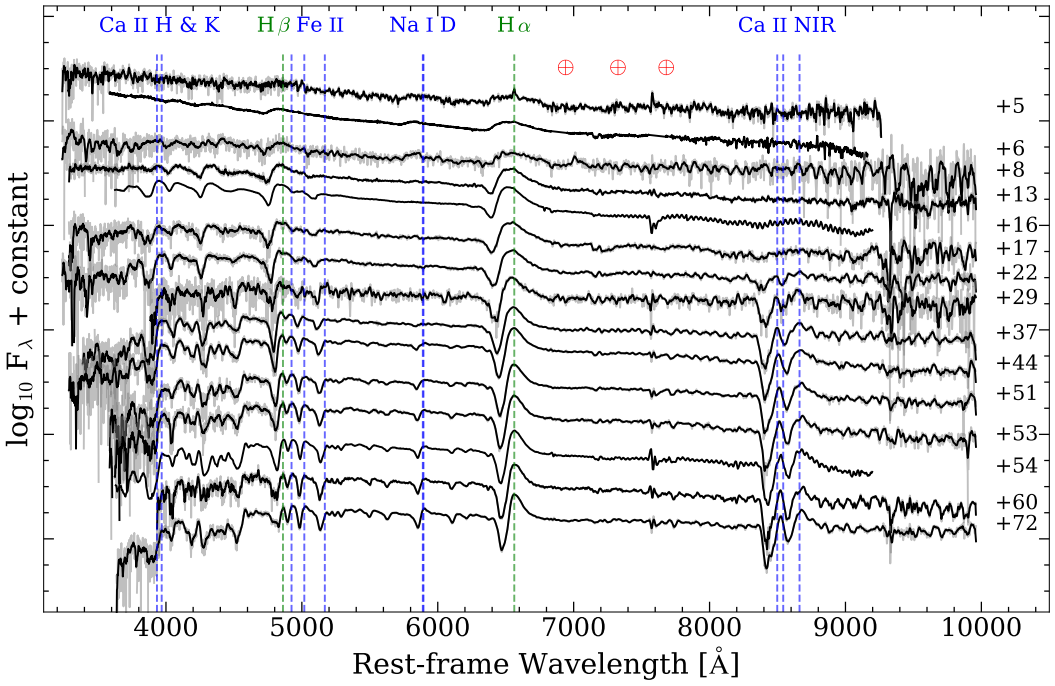

FIGURE 7.5: SN 2016aqf photospheric phase spectra. Ca II H&K, Hβ, Fe II $\lambda\lambda\lambda$4924, 5018, 5169, Na I D, Hα and Ca II NIR lines are marked. Green vertical lines denote single lines, while blue denotes doublets or triplets. Telluric (i.e., atmospheric) lines are shown by red circles with crosses. In some cases, the binned spectra (black line) are over-plotted on the original spectra (grey) for visualisation. Spectra corrected for MW extinction.

7.3.6 Nebular spectral evolution

Figure 7.8 shows the spectra taken during the optically thin phase. Hβ is present, although its strength slowly decreases at >250 d. The Fe II lines around 5000 Å are weak and hard to distinguish. The [O I] $\lambda\lambda$6300, 6364 doublet has two distinguishable components (separated by $\sim$ 62 Å), and appears after five months, becoming prominent. At five months, I see the presence of He I λ7065, [Fe II] λ7155, [Ca II] $\lambda\lambda$7291, 7323 and [Ni II] λ7378, which become prominent at later epochs. Despite being a LL SN II (i.e., having low expansion velocities), SN 2016aqf displays blended [Ca II] $\lambda\lambda$7291, 7323 lines. The presence of O I λ7774 is more prominent at these later epochs. The Ca II NIR lines are easy to distinguish given the narrow profiles.

The [O I] $\lambda\lambda$6300, 6364 and [Ca II] $\lambda\lambda$7291, 7323 lines show some very minor redshift ($\sim$ 5 Å, or $\sim$ 230 km s^{-1} and $\sim$ 200 km s^{-1}), while the He I λ7065, [Fe II] λ7155 and [Ni II] λ7378 lines are more redshifted ($\sim$ 15 Å, or $\sim$ 630 km s^{-1}, $\sim$ 630 km s^{-1} and $\sim$ 610 km s^{-1}) throughout most of the nebular phase. I also noticed that the [Ni II] λ7378 line shows almost no redshift ($\sim$ 2 Å, or $\sim$ 80 km s^{-1}) at $\sim$ +150 days before rapidly increasing to $\sim$ 10 Å ($\sim$ 400 km s^{-1}) at $\sim$ +165 days and $\sim$ 20 Å ($\sim$ 800 km s^{-1}) at $\sim$ +270 days. In addition, the [O I] $\lambda\lambda$6300, 6364 lines show a minor blueshift ($\sim$ 5

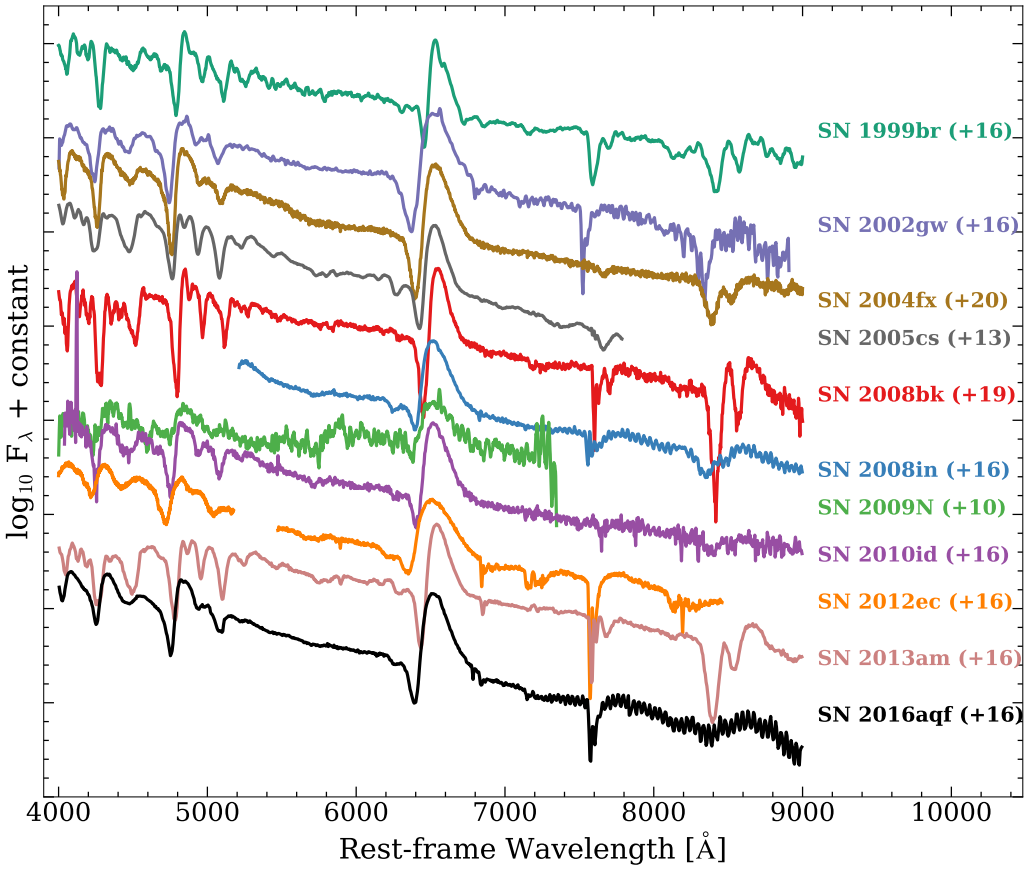

FIGURE 7.6: SN 2016aqf spectrum around +15 d (*left*) and +50 d (*right*) compared with the LL SNe II sample at similar epochs. Spectra corrected for MW and host galaxy extinction (except for those with values reported as upper limits, see Table A.3 in Appendix A).

Å, $\sim$ 230 km s^{-1}) at $\sim$ +280 days and then gets blueshifted again in about one month. These shifts could be caused by asymmetries due to clumps in different layers of the expanding envelope. It is worth mentioning that the [Fe II] λ7172 and [Ni II] λ7412 lines can contribute to the shifts in the [Fe II] λ7155 and [Ni II] λ7378 lines, respectively. However, due to the resolution of the spectra, I am unable to discern their contribution.

When I compare SN 2016aqf to other SNe at $>$ +300 d (see Figure 7.9), some of them do not show He I λ7065 (e.g., SN 2005cs and SN 2012ec). For SN 2009N, which does show this line, it has a similar strength to [Fe II] λ7155, which does not occur for other SNe. The ratio between the [O I] $\lambda\lambda$6300, 6364 lines are similar for all SNe, except for SN 2005cs, where the ratio is relatively close to 1. It can also be seen that [Ni II] λ7378 is easy to distinguish in some SNe (e.g., SN 2012ec, SN 2009N and SN 2016aqf). In the case of SN 2003B and SN 2005cs, this line is present, but it gets blended with the [Ca II] $\lambda\lambda$7291, 7323 doublet. SN 2012ec is a special case as it is the only SN that shows a higher peak in [Ni II] λ7378 than in the [Ca II] $\lambda\lambda$7291, 7323 doublet.

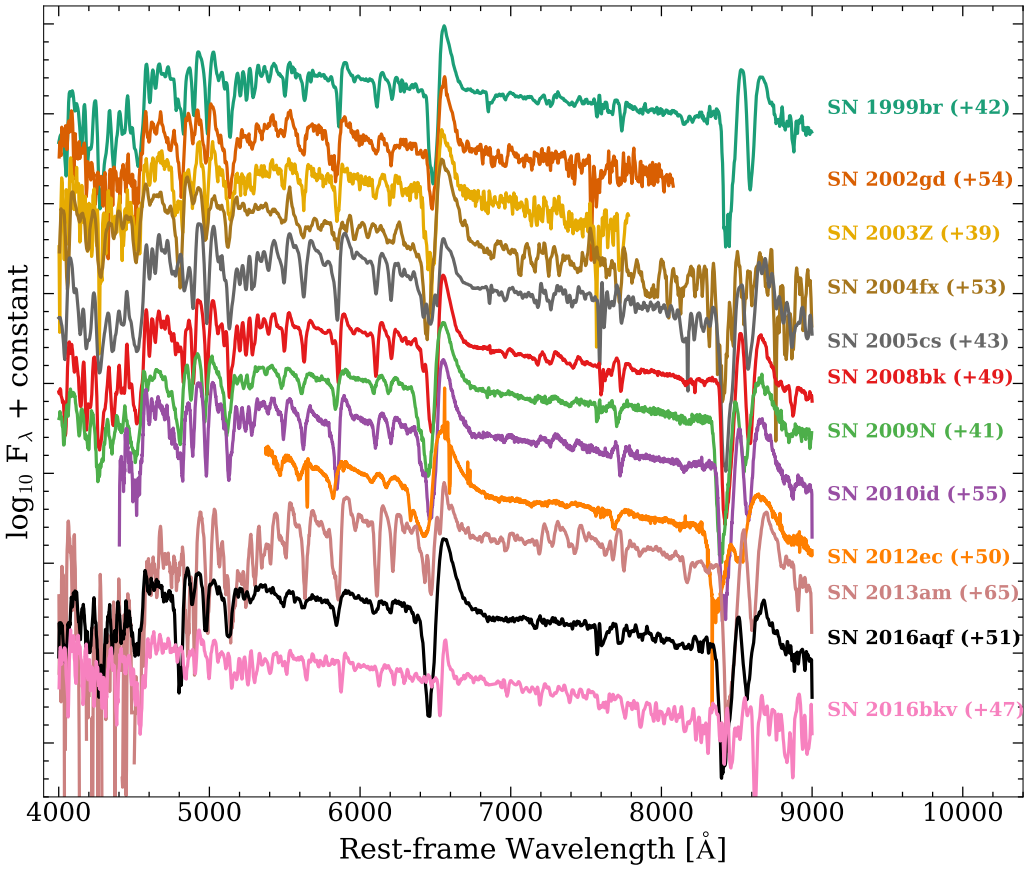

FIGURE 7.7: SN 2016aqf spectrum around +50 d (*right*) compared with the LL SNe II sample at similar epochs. Spectra corrected for MW and host galaxy extinction (except for those with values reported as upper limits, see Table A.3 in Appendix A).

7.3.7 Expansion velocity evolution

The ejecta expansion velocities were measured from the position of the absorption minima for Hβ, Fe II λ4924, Fe II λ5018, Fe II λ5169, Na I D (middle of the doublet), Ba II λ6142, Sc II λ6247 and Hα. For Hα, I also estimated the expansion velocity from the full-width at half-maximum (FWHM; width of a spectral line measured at half the maximum amplitude) of the emission by using $v = c \times \mathrm{FWHM}/\lambda_{\mathrm{rest}}$, where c is the speed of light, λ_{rest} is the rest-frame wavelength of the line, and FWHM is corrected for the instrumental resolution. I include uncertainties in the measurement of the absorption minima, from the host galaxy recession velocity (3 km s^{-1}, as reported in HyperLEDA[7]; Makarov et al. 2014), the maximum rotation velocity of the galaxy (44.2 km s^{-1}, as reported in HyperLEDA) and from the instrumental resolution, all added in quadrature. The major contribution to the uncertainty comes from the instrumental resolution.

The expansion velocity curves are shown in Figure 7.10. The velocities of Hα and Hβ are relatively high ($\gtrsim$ 8000 km s^{-1}) at very early epochs ($t \lesssim$ 10 days) and drop to

[7] http://leda.univ-lyon1.fr

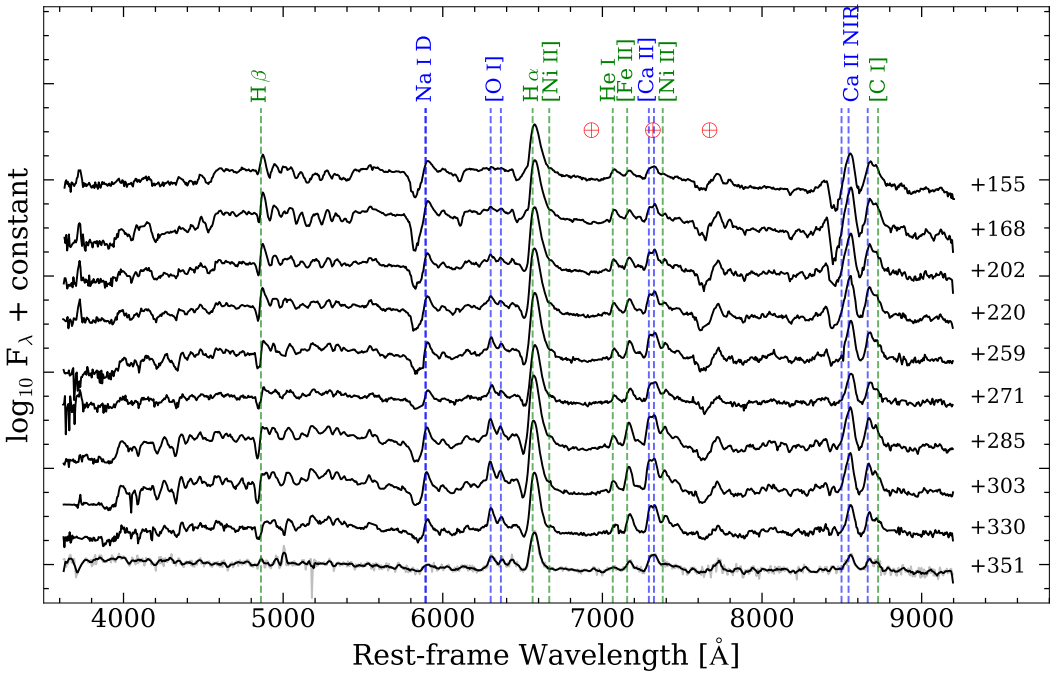

FIGURE 7.8: SN 2016aqf nebular phase spectroscopy. Hα, Hβ, Na I D, [O I] $\lambda\lambda$6300, 6364, [Ni II] λ6667, He I λ7065, [Fe II] λ7155, [Ca II] $\lambda\lambda$7291, 7323, [Ni II] λ7378 and Ca II NIR lines are shown for guidance. The rest of the description is the same as in Figure 7.5.

$\sim$ 5000 and 4000 km s^{-1} at $\sim$50 days, respectively, decreasing at a slower rate afterwards. The Hα velocity estimated from the FWHM is close to that estimated from the absorption minima as shown by Gutiérrez et al. (2017). The velocities of other lines decrease less drastically, from $\sim$ 5000 km s^{-1} at early epochs ($t \sim 10$ d), for the Fe II lines, dropping down to $\sim$ 3000 km s^{-1} at $\sim$ 50 d and relatively constant thereafter.

In general, the expansion velocity curves of SN 2016aqf fall within the bulk of my sample and follow the general trend, although some of the velocities seem to decrease faster during the first 50 days after explosion.

7.4 Physical Parameters

7.4.1 Nickel Mass

The M_{Ni} is one of the main physical parameters that characterises CCSNe in general as it is formed very close to the core (within a few thousand kilometers; e.g., Kasen & Woosley 2009). I estimated the nickel mass of SN 2016aqf by using different methods: (i) Arnett (1996), (ii) Hamuy (2003), (iii) Maguire et al. (2012) and (iv) Jerkstrand et al.

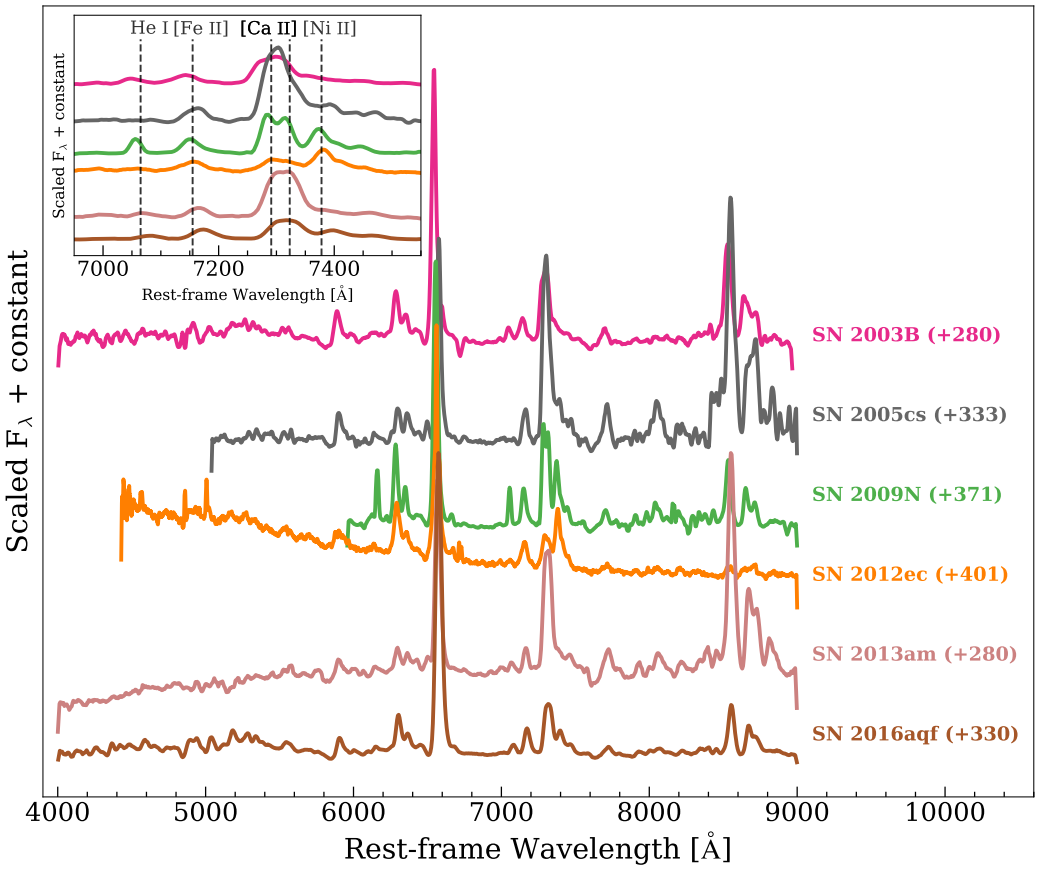

FIGURE 7.9: SN 2016aqf spectrum around +330 d compared with the LL SN II sample at similar epochs. The spectra were normalised by their peak Hα flux. *Embedded figure*: zoom-in around $\sim$ 7250 Å. The rest-frame position of the He I λ7065, [Fe II] λ7155, [Ca II] $\lambda\lambda$7291, 7323 and [Ni II] λ7378 lines are shown. Spectra corrected for MW host galaxy extinction (except for those with values reported as upper limits, see Table A.3 in Appendix A).

(2012). For more information regarding the different relations used for the estimation of M_{Ni}, see Appendix B.

For (i), (ii) and (iv), I used the bolometric luminosity of the exponential-decay tail at +200 days, calculated in Section 7.3.4 by interpolating with GPs and including the distance of the SN for (ii). In the case of (iii), I measured the FWHM of H_α at +351 days, correcting it for the FWHM of the instrument. The M_{Ni} values obtained with the different methods were $M_{Ni} = 0.008^{+0.002}_{-0.002}$, $0.011^{+0.003}_{-0.003}$, $0.014^{+0.009}_{-0.007}$ and $0.007^{+0.001}_{-0.001}$ $M_\odot$, respectively, with a weighted mean and a weighted standard error of the mean of $M_{Ni} = 0.008 \pm 0.002\ M_\odot$.

7.4.2 Explosion Energy, Ejected Mass and Progenitor Radius

Popov (1993) derived analytical relations for the estimation of the explosion energy

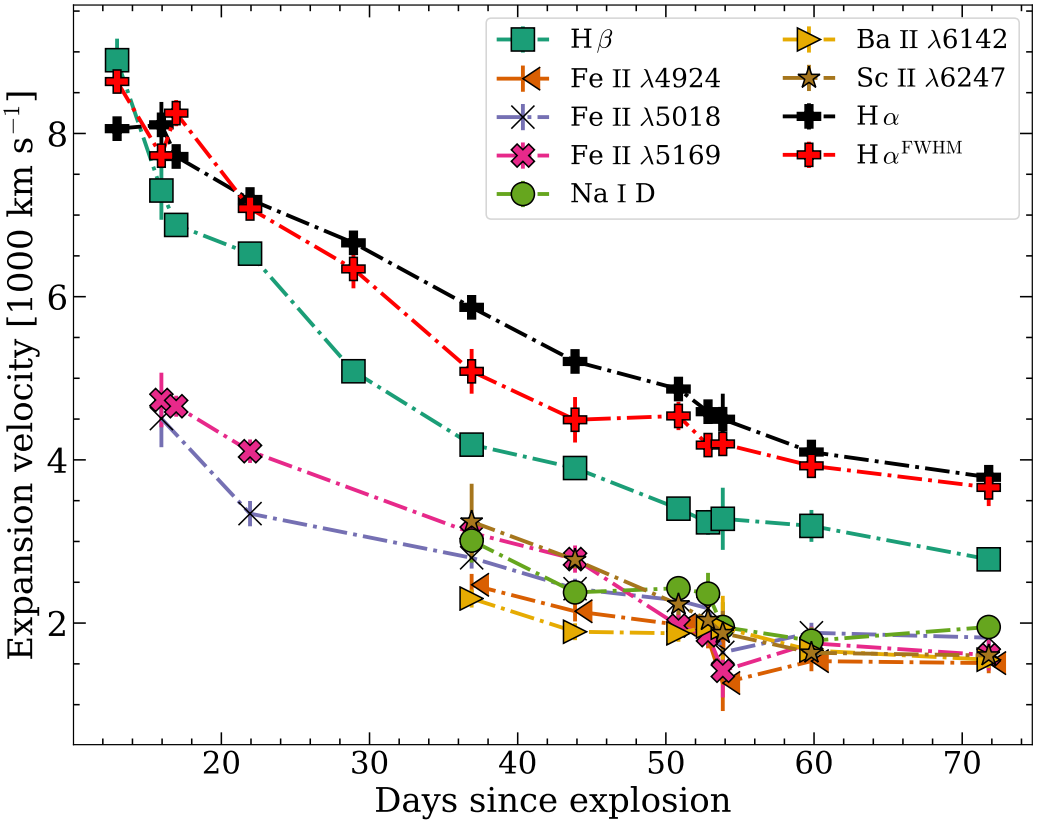

FIGURE 7.10: SN 2016aqf expansion velocities for H β, Fe II λ4924, Fe II λ5018, Fe II λ5169, Na I D (middle of the doublet), Ba II λ6142, Sc II λ6247 and H α. For H α I also estimated the expansion velocity from the FWHM; see text for details.

(E_{exp}), ejected envelope mass (M_{env}) and the progenitor radius prior to outburst (R_{prog}) for SNe II-P (following a similar analysis by Litvinova & Nadezhin 1985). These parameters are related to different light-curve properties and M_{Ni}. Thus, they are essential for the characterisation of SNe II and CCSNe in general. The relations found by Popov (1993) are:

$$\log_{10}(E_{exp}) = 4.0\ \log_{10}\ t_p + 0.4\ M_V + 5.0\ \log_{10}(v_{ph}) - 4.311, \tag{7.1}$$

$$\log_{10}(M_{env}) = 4.0\ \log_{10}\ t_p + 0.4\ M_V + 3.0\ \log_{10}(v_{ph}) - 2.089, \tag{7.2}$$

$$\log_{10}(R_{prog}) = -2.0\ \log_{10}\ t_p - 0.8\ M_V - 4.0\ \log_{10}(v_{ph}) - 4.278, \tag{7.3}$$

where M_V is the V-band absolute magnitude at the middle of the plateau, t_p is the duration of the plateau in days (as in Hamuy 2003), v_{ph} is the expansion velocity of the photosphere at $t_p/2$ (usually measured from the Fe II λ5169 line, as a good tracer of the photosphere) in 10^3 km s^{-1}. E_{exp} is expressed in 10^{51} erg, and M_{env} and R_{prog} in solar units. I measured $M_V = -14.63 \pm 0.27$ mag for which I used GPs to interpolate the light curve. By using the relativistic Doppler shift, I obtained $v_{ph} = 2068 \pm 167$ km s^{-1} from

the Fe II λ5169 absorption line minima. Finally, I use $t_p = 97.9 \pm 7.2$ days, for which I assumed the same value of SN 2003fb (see Anderson et al., 2014), adding its uncertainty in quadrature, as these SNe have relatively similar evolution around the transition ($t \gtrsim +50$ days) in the V band (see Appendix C.1 for a detailed comparison). With these values for SN 2016aqf, I obtained $E_{exp} = (0.24 \pm 0.13) \times 10^{51}$ erg, $M_{env} = 9.31 \pm 4.26$ $M_\odot$ and $R_{prog} = 152 \pm 94$ $R_\odot$. The large uncertainties mainly come from the velocity, specifically, from the instrumental resolution, and from the distance uncertainty used in calculating the absolute magnitude. I compared these results with similar relations found in the literature (e.g., Kasen & Woosley, 2009; Shussman et al., 2016; Sukhbold et al., 2016; Kozyreva et al., 2019; Goldberg et al., 2019; Kozyreva et al., 2020), obtaining similar results.

SN 2016aqf follows the E_{exp}–M_{Ni} (e.g., Pejcha & Prieto, 2015; Müller et al., 2017) and M_{env}–E_{exp} relations (e.g., Pejcha & Prieto, 2015) found in SNe II. If I assume a neutron star ($\sim 1.4\,M_\odot$) as the compact remnant left behind after the explosion, the progenitor of SN 2016aqf should be a red supergiant star with $\sim 10.7\,M_\odot$. This is a lower limit, as some mass loss is expected due to various processes, e.g., winds (e.g. Dessart et al., 2013a). Finally, R_{prog} is well within the normal estimated values of RSG radii, although on the lower end (e.g., Pejcha & Prieto, 2015; Müller et al., 2017), but consistent with other estimations for this sub-class of SNe (e.g., Chugai & Utrobin, 2000; Zampieri et al., 2003; Pastorello et al., 2009; Roy et al., 2011).

7.5 Discussion

7.5.1 Progenitor Mass

The progenitors of SNe II have been extensively studied through pre-SN images (e.g. Smartt, 2009, 2015) and hydrodynamical models (e.g. Bersten et al., 2011; Dessart et al., 2013a; Martinez & Bersten, 2019). Although there remain some disagreements in the estimated physical properties, such progenitor mass and radius (e.g., Utrobin & Chugai, 2009; Dessart et al., 2013a, for discussions of this discrepancy), there have been recent major improvements due to better cadence observations.

The [O I] $\lambda\lambda$6300, 6364 nebular-phase lines have also been shown to be good tracers of the core mass of CCSN progenitors (e.g., Elmhamdi et al., 2003; Sahu et al., 2006; Maguire et al., 2010), as at these later epochs one is observing deeper into the progenitor structure. Spectral modelling of the nebular phase has shown good agreement with this and can be used to estimate the progenitor mass (e.g., J12; J14; J18). In order to estimate the progenitor mass of SN 2016aqf, I used the spectral synthesis models from J14 and J18 for progenitors with three different ZAMS masses: 9, 12 and 15 $M_\odot$. The 9 $M_\odot$ model has an initial ^{56}Ni mass of 0.0062 $M_\odot$ while the other two models have an

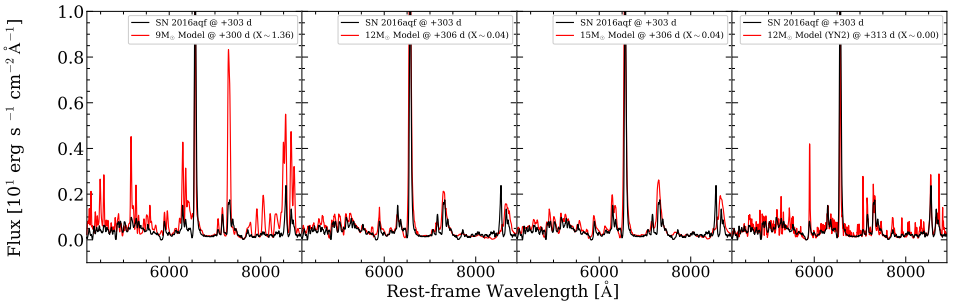

FIGURE 7.11: *First three panels (from left to right)*: Spectral synthesis models of SNe II from J14 and J18. Three spectral synthesis models at $\sim$ +300 d from different progenitor masses: 9 (left), 12 (centre) and 15 $M_\odot$ (right). X is the scaling factor (see Section 7.5.1). The 12 and 15 $M_\odot$ models fit the spectrum better than the 9 $M_\odot$ model, including the [O I] $\lambda\lambda$6300, 6364 lines. *Last panel*: YN2 model of 12 $M_\odot$ from Lisakov et al. (2017). There is a relatively good agreement with some of the Ca and the [O I] λ6300, 6364 lines, however, most other lines are over-predicted.

initial ^{56}Ni mass of 0.062 $M_\odot$. I compare the nebular spectra of SN 2016aqf with the models at two different epochs each (see Figure 7.11 for models at +300 days). The models are scaled by exp((t_{mod} - t_{SN})/111.4), where t_{mod} is the epoch of the spectrum of the models, t_{SN} is the epoch of the spectrum of the SN and 111.4 is the *e*-folding time (in days) of the ^{56}Co. The models are also scaled by the SN M_{Ni}, M_{Ni}^{SN}/M_{Ni}^{mod}, and by the inverse square of the SN distance, $(d_{mod}/d_{SN})^2$. The luminosity of some lines, like [O I] λ6300, 6364, scale relatively linearly with the M_{Ni} (e.g., J14), thus, it is reasonably accurate to compare the models re-scaled to match the M_{Ni} of my observed SN. χ^2 values were calculated to quantify these comparisons as well.

From Figure 7.11, I see that the 12 and 15 $M_\odot$ models present similar results, reproducing several lines. They can partially reproduce the [O I] λ6300 line, but the latter does not reproduce the [O I] λ6364 line very well. However, these models under-predict the [Fe II] λ7155 line and do not reproduce the [Ni II] λ7378 line and Ca II NIR triplet. The 9 $M_\odot$ mostly over-predicts the flux of lines, but does a good job reproducing the He I λ7065 and [Fe II] λ7155 lines. In terms of χ^2 values, the 12 $M_\odot$ model is slightly better than the 15 $M_\odot$ one, while the 9 $M_\odot$ model has a poorer fit. In addition, the 12 $M_\odot$ model is relatively consistent with the mass estimate from Section 7.4.2, within the uncertainty. I also measured [O I]/[Ca II] flux ratios (e.g., Maguire et al., 2010) between $\sim$ 0.5–0.7, which are consistent with the 12 $M_\odot$ model and roughly consistent with the 15 $M_\odot$ model. Finally, I found that the models reproduce lines better at later epochs ($\gtrsim$ 300 d) than at early epochs ($<$ 300 d). J18 found the same pattern.

There seems to be a very weak detection of [Ni II] λ6667 (see Figure 7.8), partially blended with H α, and the 9 $M_\odot$ model predicts similar fluxes for this line and [Ni II] λ7378, due to the high optical depths (Figure 20 of J18). Note that this model has only primordial (i.e., pre-explosion) nickel in the hydrogen-zone, no synthesised ^{58}Ni, and a different setup compared to the other two (e.g., no mixing applied, J18). As the model

prediction for [Ni II] λ7378 is too weak, one can argue the detection of synthesised nickel. The 9 $M_\odot$ model over-predicts the [O I] λ6300, 6364 lines, including most other lines. As mentioned above, J18 had similar results at these early epochs, however, this model showed better agreement at later epochs (e.g., $>$ 350 d for SN 2005cs). I did not find better agreement at later epochs.

In order to expand my analysis, I also compared SN 2016aqf with the progenitor models from Lisakov et al. (2017), specifically, the YN models of 12 $M_\odot$ (a set of piston-driven explosion with ^{56}Ni mixing) as their M_{Ni} (0.01 $M_\odot$) agree perfectly with my estimation, apart from agreeing with other physical parameters (e.g., $E_{exp} = 2.5 \times 10^{50}$ erg, M_{env} = 9.45 $M_\odot$) as well. This comparison, which was done in the same way as with the other models above, is shown in Figure 7.11 for the YN2 model as well. As can be seen, the model predicts some of the Ca and the [O I] λ6300, 6364 lines relatively well. Nonetheless, most of the other lines are over-predicted. Other models from Lisakov et al. (2017) did not show better agreement. However, the fact that both 12 $M_\odot$ models (from J14 and Lisakov et al. 2017) partially agree with the [O I] λ6300, 6364 lines (the main tracers of the ZAMS mass) strengthen the conclusion that the progenitor is probably a $\sim$ 12 $M_\odot$ RSG star.

Neither the 9 $M_\odot$ model from J18 nor the YN 12 $M_\odot$ models from Lisakov et al. (2017) have macroscopic mixing. The consistent overproduction of narrow core lines in both models (see Figure 7.11) suggests that mixing is necessary, which the models from J14 have.

In conclusion, this shows that the current models have problems predicting the observed diversity of LL SNe II, probably due to the incomplete physics behind these explosions (e.g., assumptions of mixing, ^{56}Ni mass, rotation). In other words, there is a need of more models with different parameters that can help to understand the observed behaviour of these SNe. As such, I can not exclude a 9 $M_\odot$ nor a 15 $M_\odot$ progenitor. Thus, I conclude that the progenitor of SN 2016aqf had a ZAMS mass of 12 $\pm$ 3 $M_\odot$. A more detailed modelling of the progenitor is needed to improve these constraints, although this is beyond the scope of this work.

7.5.2 He I λ7065

The He I λ7065 nebular line has been studied with theoretical modelling (e.g., Dessart et al. 2013b; J18), giving a diagnostic of the He shell. These models predict the appearance of this line in SNe II with low mass progenitors as more massive stars have more extended oxygen shell, shielding the He shell from gamma-ray deposition. However, some LL SNe II do not show this line in their spectra (e.g., SN 2005cs; see Figure 7.9). SN 2016aqf shows the clear presence of He I λ7065 throughout the entire nebular coverage. I also see the presence of [C I] λ8727, although it gets partially blended with the

Ca II NIR triplet. I expect to see this carbon line as a result of the He shell burning, so the presence of both lines (He I λ7065 and [C I] λ8727) is consistent with the theoretical prediction. Thus, I believe that SN 2016aqf is a good case study to provide further understanding of the He shell zone through theoretical models. Furthermore, following the discussion from J18, I conclude that this is a Fe core SN and not an electron-capture SN (ECSN; Moriya et al., 2014; Doherty et al., 2017; Hiramatsu et al., 2021), as the latter lacks lines produced in the He layer.

7.5.3 Ni/Fe abundance ratio

As discussed above, the nebular spectra of SNe II contain a lot of information regarding the progenitors as one is looking deeper into its structure. J15a discussed the importance of the ratio between the [Ni II] λ7378 and [Fe II] λ7155 lines as indicator of the Ni/Fe abundance ratio. These elements are synthesised very close to the progenitor core and, for this reason, their abundances are affected by the inner structure of the progenitor and the explosion dynamics. More specifically, iron-group yields are directly affected mainly by three properties: temperature, density and neutron excess of the fuel (for a more detailed account, see J15b). For this reason, studying iron-group abundances is key to understanding SNe II.

SN 2016aqf is the only SN II to date with a relatively extensive coverage of the evolution of [Ni II] λ7378 (most other SNe with the presence of this line only have at most $\sim$2 epochs showing it). In Figure 7.12, I show the evolution in time of the flux of [Ni II] λ7378 and [Fe II] λ7155, and their luminosity ratio. I estimated the fluxes by fitting Gaussians to the profiles. Uncertainties were estimated by repeating the measurements and assuming different continuum levels.

I note that the evolution of the luminosity ratio reaches a quasi-constant value after $\sim$170 days since the explosion. This suggests that at relatively late nebular phase the Ni/Fe abundance ratio is constant as the temperature should not vary much (see J15a), although clumps in the ejecta might cause deviations from the measured values. After removing the value at $\sim+155$ days (as the SN might still be in the transition to the optically thin phase) I report a Ni/Fe luminosity ratio weighted mean of 0.906 and a standard deviation of 0.062. The standard deviation gives us a more conservative estimation of the uncertainty in the Ni/Fe luminosity ratio than the uncertainty in the weighted mean.

I follow J15a to estimate the Ni II/Fe II ratio and in turn the Ni/Fe abundance ratio. From the ratio between the luminosity of the [Fe II] λ7155 line and M_{Ni}, I then obtained a temperature constraint of $T = 3919^{+215}_{-257}$ K. With these values I estimated the Ni/Fe abundance ratio to be $0.081^{+0.009}_{-0.010}$, or $\sim$1.4 times the solar ratio (0.056, Lodders 2003).

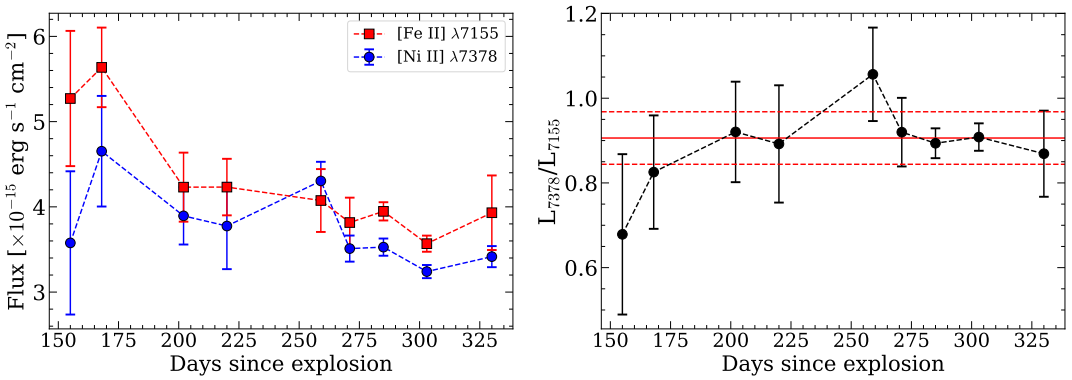

FIGURE 7.12: **Left panel:**[Ni II] λ7378 and [Fe II] λ7155 lines fluxes. **Right panel:** Luminosity ratio of these lines. The weighted average (solid red line) with a one standard deviation (dashed red lines) are shown for guidance. The value at $\sim +150$ days was removed for these calculations.

However, there are several things I need to take into consideration. Contribution to the [Fe II] λ7155 and [Ni II] λ7378 lines does not come only from synthesised material, but also from primordial Fe and Ni in the H-zone (J15a). The contribution can be significant ($\sim$ 40 per cent) and depends on the model and epoch. Unfortunately, the effect of primordial contamination is not easy to remove without detailed theoretical modelling. Nonetheless, it is plausible that the [Fe II] λ7155 and [Ni II] λ7378 lines are greatly dominated by synthesised Fe and Ni at relatively early epochs ($\lesssim$ 300 d), although I am uncertain at which epochs the effect from primordial Fe and Ni starts becoming important (J18). The line ratio can also be affected at very early epochs ($\lesssim$ 200 d), as the SN can still be during the optically-thick phase when opacity plays an important role.

Few other SNe have been reported to show [Ni II] λ7378. It is possible that this line is mainly visible in LL SNe II, where the expansion velocities are lower, producing narrower, de-blended line profiles. However, it is also seen in non-LL SNe II, other CCSNe (e.g., SN 2006aj; Maeda et al., 2007; Mazzali et al., 2007) and type Ia SNe (SNe Ia; e.g. Maeda et al., 2010). I searched for objects in my LL SN II comparison sample with spectra in which I could detect [Fe II] λ7155 and [Ni II] λ7378 to measure the Ni/Fe abundance ratio as for SN 2016aqf. I also expanded this sample to include other LL SNe II: 1997D, 2003B, 2005cs, 2008bk, 2009N and 2013am.

SN 1997D and SN 2008bk were not included in my initial sample as they lack good publicly available data. I also include SN 2012ec as it is a well-studied case. In the case of SN 1997D, I measured the ratio at two different epochs, but I used one (at $\sim +384$ days) of those, given that the other value (at $\sim +250$ days) had relatively large uncertainties. For SN 2009N, I took an average between the two values I was able to measure (at $\sim +372$ and $+412$ days) as they were relatively similar. SN 2016bkv was not included as the M_{Ni} values obtained in Nakaoka et al. (2018) and Hosseinzadeh et al. (2018) for this SN are not consistent with each other ($\sim$ 0.01 $M_\odot$ and 0.0216 $M_\odot$, respectively), this

TABLE 7.1: Ni/Fe abundance ratio values used in this work.

SN	Ni/Fe	σ_-	σ_+
1997D	0.079	0.025	0.014
2003B	0.057	0.021	0.018
2005cs	0.084	0.012	0.012
2007aa	0.074	0.006	0.006
2008bk	0.046	0.042	0.017
2009N	0.101	0.018	0.017
2012A	0.028	0.022	0.016
2012aw	0.084	0.022	0.016
2012ec	0.2	0.07	0.07
2013am	0.108	0.017	0.018
2016aqf	0.081	0.010	0.009

being necessary for an accurate estimation of the Ni/Fe abundance ratio. For the rest of the SNe, only one value was obtained. Several other LL SNe II show the presence of [Ni II] λ7378, but it is either blended with other lines or the SNe lack some of the parameters needed to estimate the Ni/Fe abundance ratio.

To expand my analysis, I looked into other physical parameters related to the Ni/Fe abundance ratio. For example, J15b further analyse and compare this ratio against theoretical models. Some of these models show that at lower progenitor mass, the Ni/Fe abundance ratio should be higher. Unfortunately, not many LL SNe II have measured progenitor masses from pre-SN images, so I increase my sample by adding non-LL SNe II as several of these do (e.g., Smartt, 2015), while they also show the presence of [Fe II] λ7155 and [Ni II] λ7378 in their spectra. I do not include SNe with estimates of the progenitor mass from other methods as they depend on more assumptions than the pre-SN images method, making these estimates less reliable. The SNe included are: SN 2007aa (Anderson et al., 2014; Gutiérrez et al., 2017), SN 2012A (Tomasella et al., 2013) and SN 2012aw (Fraser et al., 2012). All these SNe are included in Table A.3 in Appendix A. For SN 2007aa, I calculated the ejected nickel mass to be M_{Ni} = 0.032 $\pm$ 0.009 $M_\odot$ (I estimated this value using the relation from Hamuy 2003 and other values from Anderson et al. 2014) and estimated the Ni/Fe abundance ratio also as part of this work. For the other two SNe II, I took the values from J15a, assuming upper and lower uncertainties equal to the average of the uncertainties of the rest of the sample (not taking into account the uncertainties of SN 2012ec as they are too high). The Ni/Fe abundance ratio values for this sample are shown in Table 7.1.

In addition, I compared the Ni/Fe against other physical, light-curve and spectral parameters to investigate possible correlations. The motivation is two-fold. Firstly, I am searching for correlations that might allow indirect methods of measuring this ratio for

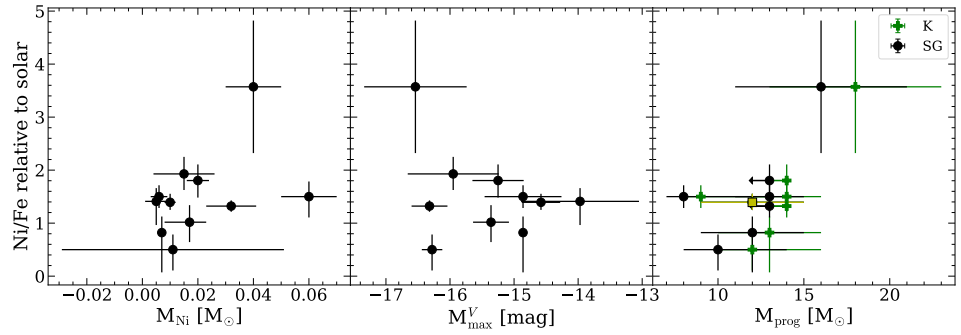

FIGURE 7.13: Ni/Fe abundance ratio versus M_{Ni}, M^V_{max} and M_{prog}. For M_{prog} I show two different progenitor models, KEPLER (K) and STARS and Geneva (SG). SN 2016aqf is shown as a yellow square in the subplot with M_{prog}, for which I assume a value of $12 \pm 3\ M_\odot$.

SNe with blended lines. Secondly, these correlations could shed light on the effect of different parameters in the observed value of Ni/Fe, as is expected for the progenitor mass, important for the theoretical modelling of SNe II.

I examined various SN parameters I thought could be somehow connected to the Ni/Fe abundance ratio. The most relevant parameters are: nickel mass (M_{Ni}); V-band maximum absolute magnitude (M^V_{max}); optically-thick phase duration (OPT_d); Fe II λ5169 expansion velocity (vel(Fe II 5169)); the progenitor mass from KEPLER (K) models (M^K_{prog}; see Smartt 2015), progenitor mass from STARS and Geneva (SG) rotating models (M^{SG}_{prog}; see Smartt 2015); explosion energy (E_{exp}); [O I] λ6300 and [O I] λ6364 luminosities at the epoch of measured Ni/Fe abundance ratio (L_{6300} and L_{6364}); and host-galaxy gas-phase metallicity ($(12 + \log(O/H))_{N2}$). The sources of the parameters values are summarised in Appendix C.2. The Ni/Fe abundance ratio versus M_{Ni}, M^V_{max} and M_{prog} are shown in Figure 7.13.

Pearson and Spearman's rank correlations were used to investigate if there is any meaningful correlation between these parameters and the Ni/Fe abundance ratio. To account for the measurement uncertainties, I use a Monte Carlo method, assuming Gaussian distributions for symmetric uncertainties, skewed Gaussian distributions for asymmetric uncertainties, and a uniform distribution (with a lower limit of $8\ M_\odot$) for upper limits in the progenitor masses.

I found no significant correlation between the parameters tested above. However, I note that the uncertainties in some parameters are significant. If I do not take into account the uncertainties I obtain a weak correlation between Ni/Fe and M^V_{max} and progenitor mass. However, these are mainly driven by one object (SN 2012ec).

This null result raises some interesting questions. I did not find a correlation between M_{Ni} and Ni/Fe abundance ratio, which is expected as one would assume the production of ^{56}Ni to track the production of ^{58}Ni and ^{54}Fe (e.g., J15b). I expected to see an

anti-correlation between progenitor mass and Ni/Fe abundance ratio, as theory predicts that lower-mass stars ($\lesssim$13 $M_\odot$) have relatively thick Si shells that more easily encompass the mass cut that separates the ejecta from the compact remnant, ejecting part of their Si layers, which produces higher Ni/Fe abundance ratios (J15b). This is supported by the models from Woosley & Weaver (1995) and Thielemann et al. (1996), but not by those of Limongi & Chieffi (2003), which uses a different explosion approach than the former two (see J15b). Having this in mind, my results either indicate that this anti-correlation can be driven by the exact choice of explosion mechanism (e.g., piston-driven explosions, neutrino mechanism, thermal bomb) and physical parameters (e.g., composition, density profile), or that low-mass stars typically do not burn and eject Si shells, but either O shells or possibly merged O-Si shells (e.g., Collins et al., 2018). This is an important constraint both for pre-SN modelling (shell mergers and convection physics that determines whether these Si shells are thin or thick) and explosion theory (which matter falls into NS and which is ejected). Finally, I also need to consider the possibility of having primordial Ni and Fe contaminating the measured Ni/Fe abundance ratio, which could affect my results (as discussed above).

As mentioned in J15b, 1D models tend to burn and eject either Si shell or O shell material that gives Ni/Fe abundance ratios of $\sim$3 and $\sim$1 times solar, respectively. Therefore, there is a clear-cut prediction that I should see a bimodal distribution of this ratio, with relatively few cases where the burning covers both shells. However, the observed distribution of my sample seems to cover the whole $\sim$1–3 range. This may suggest that the 1D picture of progenitors is too simplistic. Recent work on multi-D progenitor simulations suggest vigorous convection and shell mixing inside the progenitor (e.g., Müller et al. 2016; Collins et al. 2018; Yadav et al. 2020, and references therein). If this happens, Si and O shells could smear together and burning such a mixture would give rise to Ni/Fe abundance ratios covering the observed range depending on the relative masses of the two components.

7.6 Conclusions for the analysis on SN 2016aqf

Theoretical modelling has shown that the Ni/Fe abundance ratio, which can be estimated from the [Ni II] λ7378/[Fe II] λ7155 lines ratio, gives an insight of the inner structure of progenitors and explosion mechanism dynamics. To date, very few SNe II have shown these lines in their spectra, most of them been LL SNe II. This could be due to their lower explosion energies (hence lower expansion velocities) which facilitates the de-blending of lines, although these have also been found in one SN Ic and SNe Ia.

SN 2016aqf has a similar spectral evolution to other SNe of this faint sub-class and has a bolometric luminosity and expansion velocities that follow the bulk behaviour

of LL SNe II. When comparing its nebular spectra to spectral synthesis models to constraint the progenitor mass through the [O I] $\lambda\lambda$6300, 6364 lines, I find a relatively good agreement with progenitors of 12 (using two model grids) and 15 $M_{\odot}$. However, due to uncertainties (e.g., mixing) in the other models, I cannot exclude lower mass ($\sim 9\ M_{\odot}$) progenitors. In addition, I noted that the lack of macroscopic mixing seen in some models produce too much fine structure in the early nebular spectra, which would need to be considered in future modelling. Hence, I conclude that the progenitor of SN 2016aqf had a ZAMS mass of $12 \pm 3\,M_{\odot}$. To further constraint the progenitor mass, a more detailed modelling would be required, although this is outside the scope of this work.

As observed from the theoretical modelling of SNe II progenitors, the presence of He I λ7065 and [C I] λ8727 in the spectra is linked to the (at least partial) burning of the He shell, which would suggest that SN 2016aqf is a Fe-core SN instead of an ECSN.

SN 2016aqf is a unique case as it has an extended spectral coverage showing the evolution of [Ni II] λ7378 and [Fe II] λ7155 lines for over 150 days. The ratio between these lines appears to be relatively constant (at $t \gtrsim +170$ days), which would suggest that one spectrum at a relatively late epoch would be enough to measure this quantity. An optimal epoch range to measure this ratio is $\sim$200–300 days, given that at earlier epochs the SN can still be in the optically-thick phase, when the high opacity blocks the contribution from the lines, and at later epochs the contribution from primordial Fe and Ni is more important. This could vary from SN to SN, so a larger sample with extensive coverage of the [Ni II] λ7378 and [Fe II] λ7155 lines is required to properly constrain this. When comparing to a sample of SNe II (LL and non-LL included) with measured Ni/Fe abundance ratio, the SN 2016aqf value falls within the middle of the distribution.

I did not find any anti-correlation between ZAMS mass and Ni/Fe abundance ratio as predicted by theory. I believe this could mean one of two things. On the one hand, as some models predict this anti-correlation, but others do not, this trend could be driven by the choice of explosion mechanism (e.g., piston-driven explosions, neutrino mechanism, thermal bomb) and physical parameters (e.g., composition, density profile). On the other hand, this could mean that low-mass stars ($\lesssim$13 $M_{\odot}$) typically do not burn and eject Si shells, but instead O shells or possibly merged O-Si shells which would alter the produced Ni/Fe abundance ratio. However, one must keep in mind that there is the possibility of having contamination of primordial Ni and Fe, which can be significant (up to $\sim$ 40 per cent) and epoch dependent.

The current picture of 1D progenitors may be too simplistic, as higher dimensional effects, like mixing and convection, can play an important role, which could help reproduce the observed distribution of Ni/Fe abundance ratio.

I note that nebular-phase spectral coverage of SNe II is essential for the study of these objects. While there exist a number of SN II nebular spectra in the literature, additional

higher cadence and higher S/N observations are required to help improve theoretical models.

In this chapter, I have shown the importance of studying the astrophysics of SNe as one can learn much about the progenitor scenarios and explosions mechanisms and how these affect the observables one measures. From this kind of analysis, one can understand the link between the different types of SNe and the bigger picture of the SN 'landscape'. In the next and final chapter, I summarise my thesis.

Chapter 8

Summary

In this thesis, I have presented PISCOLA, a new SN Ia light-curve fitter developed by me, with the goal of offering a different alternative to current fitters, together with a new approach for the analysis of SN Ia light curves in the search of an improved standardisation of these objects as cosmological probes. Additionally, I studied the astrophysics of SNe Ia and SNe II in the context of the SN 'landscape'. In this final chapter, I summarise this work.

8.1 PISCOLA

PISCOLA is a data-driven interpolation method, for fitting light-curves of SNe Ia (but generic enough to fit other types of SNe) which relies on GPs. This code can be applied to any observer-frame SN light-curves, and produces rest-frame light-curves as its principal output. PISCOLA can additionally estimate rest-frame light-curve parameters, such as peak magnitudes, colours, and light-curve shapes.

I tested PISCOLA by applying it to SN Ia data from the Pantheon sample, both simulated and real. With simulations of SNe Ia for different cadences and observational uncertainties, I found that PISCOLA is reliable for observational cadences of $\lesssim 7$ days for typical current SN Ia samples, provided relatively loose constraints on data coverage around peak luminosity and S/N are used. When comparing PISCOLA outputs on real data and comparing to light-curve fits with the SALT2 light-curve fitter, I see small but significant ($>3\sigma$) differences in light-curve parameters, including peak rest-frame B-band magnitude. However, with no ground-truth for these tests, I argue that such differences may be expected due to calibration and/or different assumptions used in the two techniques.

8.2 Light-Curve Analysis

I then demonstrated a scientific use of PISCOLA by analysing the rest-frame B-band light curves of the Pantheon SN Ia sample using NMF, a machine-learning decomposition algorithm, to search for alternative standardisations of these objects. The extracted components can be physically interpreted and even be used to study the astrophysics of these objects. I compared the NMF coefficients with different SN Ia parameters, and used them to build a Hubble diagram. I tested different combinations of light-curve phase ranges and numbers of components for the decomposition, and found the best results were based on B-band light curves with a phase range of $[-10, +15]$ d and three components. This parametrization produces an r.m.s. in the Hubble residual similar to that of SALT2 (0.118 and 0.111 mag, respectively), showing the promise of this new framework. I stress that, although PISCOLA does not outperform SALT2 in this particular case, this is but a limited demonstration of what this general-purpose light-curve fitter can do.

8.3 Colour Law of SNe Ia

PISCOLA uses a smooth GP interpolation to adjust its base SED template to an observed SN colour (a mangling function). This mangling function encodes information on the CL of SNe Ia. I estimated a functional form for this CL by fitting a third-order polynomial and compared it with the SALT2 CL and Fitzpatrick (1999) extinction laws with different R_V values. I found that the PISCOLA CL agrees with an extinction law with $R_V \lesssim 3.1$, but also with the SALT2 CL. Although there could be some slight (but not significant) disagreement towards the UV, a possible cause is the extrapolation of the PISCOLA CL bluer than $\sim$3500 Å.

I also calculated the CL as a function of phase to test the assumption of SALT2, a time-independent CL, finding good agreement with this hypothesis. To further study this, I used a separate sample of SNe Ia from DES. These SNe were fitted and analysed in a similar fashion to those of the Pantheon SNe Ia sample, finding a similar shape and behaviour in the CL. Furthermore, the DES SNe Ia sample provided another way of validating PISCOLA.

8.4 SN 2016aqf: a Low-Luminosity SNe II

I studied SN 2016aqf, a LL SN II with a good photometric and spectral coverage, presenting a unique opportunity for future theoretical modelling. The late-time nebular

spectra are of special interest as they provide information that can help unveil the astrophysics of these objects. Theoretical modelling has shown that [O I] $\lambda\lambda 6300, 6364$ nebular lines are a good tracer of the ZAMS mass of CCSNe. Additionally, The ratio between the [Ni II] $\lambda 7378$ and [Fe II] $\lambda 7155$ nebular lines gives an insight of the inner structure of progenitors and explosion mechanism dynamics. By studying SN 2016aqf, I found that this ratio seems constant at late phases ($\sim 200 - 300$ days after explosion). Using a sample of SNe II (LL and non-LL SNe), I studied the correlation of this line ratio with different physical parameters. However, I did not find any correlations predicted by theoretical modelling. Furthermore, the observed distribution of Ni/Fe ratios does not agree with that predicted by the models, hence implying that the current status of progenitors and explosion modelling may be too simplistic.

8.5 Looking into the Future

8.5.1 Analysis of SNe Ia and PISCOLA

Future plans will involve upgrades of PISCOLA. This includes the use of a 'stretch'-dependent time-series SED, a mangling function in two-dimensions (wavelength and time) and exploring alternative GP models, for example, using different kernels and different bounds for the hyper-parameters. This may produce more accurate light-curve fits and mangling functions.

PISCOLA can be used on other current and future samples of SNe Ia as it gives the opportunity to study the astrophysics of these objects in a different way other fitter do. For instance, the study of the CL using SNe from LSST may result of great importance for future cosmological analyses. Even more, PISCOLA can be used on SNe Ia samples with NIR (e.g., CSP, CfA) as it does not have the wavelength limitations other fitter have and has proven to be better at fitting relatively well-sampled SNe Ia, compared to SALT2.

Finally, I emphasise that although my tests have been based around applications to SNe Ia, PISCOLA is generic so that, with an appropriate time-series SED for K-corrections, it can fit any type of optical transient to estimate rest-frame light-curves and luminosities. For instance, SED templates for type Ib, Ic and II SNe already exist (e.g., Vincenzi et al., 2019). Thus future applications will involve the fitting of other types of SNe as well.

8.5.2 Astrophysics of CCSNe

In the previous chapter, I showed that the nebular-phase coverage of CCSNe is crucial for understanding their astrophysics. However, the current samples are relatively

limited, mainly due to the faint luminosities at this late epochs. Fortunately, several facilities (e.g., NTT) have been increasing the samples of well-observed CCSNe. Additionally, very early data can further help constrain the progenitors and explosion mechanism of these objects. Therefore, combining observations of larger samples and improved theoretical modelling are key for the better understanding of the astrophysics of CCSNe. Thus, I will gather a larger sample of well-sampled objects with this end. PISCOLA also presents an alternative option to studying these phenomena and will be used in future work.

Appendix A

Tables

In this appendix chapter I provide tables summarising the photometry, spectra and spectral properties of SN 2016aqf and the SN II sample used in Chapter 7.

TABLE A.1: SN 2016aqf *BVgri*-band photometry between +5 and +311 days. *BV* bands are in Vega magnitude system, while *gri* bands are in AB magnitude system.

MJD	Phase	B	σ_B	V	σ_V	g	σ_g	r	σ_r	i	σ_i
57448	8	15.851	0.006	15.851	0.006	15.851	0.006	15.851	0.006	15.851	0.006
57452	12	15.985	0.005	15.985	0.005	15.985	0.005	15.985	0.005	15.985	0.005
57455	15	16.057	0.010	16.057	0.010	16.057	0.010	16.057	0.010	16.057	0.010
57456	16	16.045	0.034	16.045	0.034	16.045	0.034	16.045	0.034	16.045	0.034
57457	17	16.033	0.103	16.033	0.103	-	-	-	-	-	-
57458	18	16.095	0.039	16.095	0.039	16.095	0.039	16.095	0.039	-	-
57459	19	16.131	0.008	16.131	0.008	16.131	0.008	16.131	0.008	16.131	0.008
57460	20	16.190	0.005	16.190	0.005	16.190	0.005	16.190	0.005	16.190	0.005
57462	22	16.268	0.031	16.268	0.031	16.268	0.031	16.268	0.031	16.268	0.031
57468	28	16.459	0.009	16.459	0.009	16.459	0.009	16.459	0.009	16.459	0.009
57474	34	16.534	0.010	16.534	0.010	16.534	0.010	16.534	0.010	16.534	0.010
57480	40	16.576	0.008	16.576	0.008	16.576	0.008	16.576	0.008	16.576	0.008
57487	47	16.650	0.009	16.650	0.009	16.650	0.009	16.650	0.009	16.650	0.009
57493	53	16.754	0.015	16.754	0.015	16.754	0.015	16.754	0.015	16.754	0.015
57499	59	16.812	0.014	16.812	0.014	16.812	0.014	16.812	0.014	16.812	0.014
57505	65	16.824	0.015	16.824	0.015	16.824	0.015	16.824	0.015	16.824	0.015
57512	72	16.890	0.017	16.890	0.017	-	-	16.890	0.017	16.890	0.017
57514	74	16.912	0.012	16.912	0.012	16.912	0.012	16.912	0.012	16.912	0.012
57523	83	-	-	-	-	16.258	0.007	16.258	0.007	-	-
57524	84	-	-	-	-	16.289	0.008	16.289	0.008	-	-
57526	86	17.182	0.030	17.182	0.030	17.182	0.030	17.182	0.030	17.182	0.030
57598	158	19.108	0.034	19.108	0.034	19.108	0.034	19.108	0.034	19.108	0.034
57617	177	19.216	0.095	19.216	0.095	19.216	0.095	19.216	0.095	19.216	0.095
57684	244	20.311	0.041	20.311	0.041	20.311	0.041	20.311	0.041	20.311	0.041
57704	264	20.430	0.074	20.430	0.074	20.430	0.074	20.430	0.074	20.430	0.074
57726	286	-	-	19.546	0.077	19.546	0.077	-	-	-	-
57727	287	-	-	-	-	19.795	0.049	19.795	0.049	19.795	0.049
57728	288	20.709	0.063	20.709	0.063	20.709	0.063	20.709	0.063	20.709	0.063
57749	309	20.925	0.120	20.925	0.120	20.925	0.120	20.925	0.120	20.925	0.120
57750	310	20.717	0.073	20.717	0.073	20.717	0.073	20.717	0.073	20.717	0.073
57751	311	20.932	0.076	20.932	0.076	20.932	0.076	20.932	0.076	20.932	0.076

TABLE A.2: Spectra description. The UTC dates mark the beginning of the exposures. Phase with respect to the explosion epoch (MJD 57440.19).

UTC Date	MJD	Phase	Range [Å]	Resolution [Å]	Telescope/Instrument
2016-02-27T09:54:44.475	57445.4	5	3250 - 9300	18.0	FTS/FLOYDS-S
2016-02-27T21:00:25.837	57445.9	6	3600 - 9200	7.0	SALT/RSS
2016-03-01T11:24:32.205	57448.5	8	3250 - 10000	18.0	FTS/FLOYDS-S
2016-03-06T10:09:18.022	57453.4	13	3300 - 10001	18.0	FTS/FLOYDS-S
2016-03-09T04:39:49.731	57456.2	16	3640 - 9235	21.2	NTT/EFOSC2
2016-03-10T12:46:20.372	57457.5	17	3299 - 10000	18.0	FTS/FLOYDS-S
2016-03-15T10:13:25.851	57462.4	22	3250 - 10000	18.0	FTS/FLOYDS-S
2016-03-22T11:10:18.554	57469.5	29	3900 - 9999	18.0	FTS/FLOYDS-S
2016-03-30T09:29:37.393	57477.4	37	3401 - 10000	18.0	FTS/FLOYDS-S
2016-04-06T08:58:10.460	57484.4	44	3299 - 9999	18.0	FTS/FLOYDS-S
2016-04-13T10:06:55.453	57491.4	51	3599 - 10000	18.0	FTS/FLOYDS-S
2016-04-15T08:39:52.609	57493.4	53	3600 - 10000	18.0	FTS/FLOYDS-S
2016-04-16T00:26:16.687	57494.1	54	3645 - 9239	21.2	NTT/EFOSC2
2016-04-22T08:55:30.146	57500.4	60	3950 - 10000	18.0	FTS/FLOYDS-S
2016-05-04T09:27:45.944	57512.4	72	3650 - 10000	18.0	FTS/FLOYDS-S
2016-07-26T09:49:26.448	57595.4	155	3645 - 9239	21.2	NTT/EFOSC2
2016-08-08T09:39:55.699	57608.4	168	3639 - 9233	21.2	NTT/EFOSC2
2016-09-11T08:20:03.866	57642.3	202	3640 - 9233	21.2	NTT/EFOSC2
2016-09-29T07:23:09.743	57660.3	220	3636 - 9232	21.2	NTT/EFOSC2
2016-11-07T07:57:09.799	57699.3	259	3639 - 9232	21.2	NTT/EFOSC2
2016-11-19T04:31:19.658	57711.2	271	3636 - 9231	21.2	NTT/EFOSC2
2016-12-03T06:56:26.427	57725.3	285	3639 - 9232	21.2	NTT/EFOSC2
2016-12-21T05:55:04.628	57743.2	303	3640 - 9233	21.2	NTT/EFOSC2
2017-01-17T02:55:39.708	57770.1	330	3639 - 9233	21.2	NTT/EFOSC2
2017-02-07T02:46:40.051	57791.1	351	3640 - 9233	21.2	NTT/EFOSC2

TABLE A.3: SN II sample used throughout this work. The data for this sample were taken from the references cited in column References.

SN	z	M_{Ni} [$M_\odot$]	σ^-_{Ni} [$M_\odot$]	σ^+_{Ni} [$M_\odot$]	μ [mag]	σ_μ [mag]	A_V(MW) [mag]	A_V(Host) [mag]	Host	References
1997D	0.004059	0.005	0.004	0.004	30.74	0.92	0.057	$\lesssim$0.060	NGC 1536	Turatto et al. (1998), Zampieri et al. (2003) Spiro et al. (2014)
1999br	0.00323	0.002	0.001	0.001	30.97	0.83	0.063	0.000	NGC 4900	Hamuy (2003), Pastorello et al. (2004), Gutiérrez et al. (2017)
2002gd	0.00892	¡0.003	-	-	32.87	0.35	0.178	0.000	NGC 7537	Spiro et al. (2014), Gutiérrez et al. (2017)
2002gw	0.01028	0.012	0.004	0.003	32.98	0.23	0.051	0.000	NGC 922	Anderson et al. (2014), Galbany et al. (2016), Gutiérrez et al. (2017)
2003B	0.00424	0.017	0.009	0.006	31.11	0.28	0.072	0.180	NGC 1097	Blondin et al. (2006), Anderson et al. (2014), Galbany et al. (2016), Gutiérrez et al. (2017)
2003fb	0.01754	¿0.017	-	-	34.43	0.12	0.482	-	UGC 11522	Papenkova et al. (2003), Anderson et al. (2014), Gutiérrez et al. (2017)
2003Z	0.0043	0.005	0.003	0.003	31.70	0.60	0.104	0.000	NGC 2742	Utrobin et al. (2007), Spiro et al. (2014)
2004fx	0.00892	0.014	0.006	0.004	32.82	0.24	0.274	0.000	MCG -02-14-003	Park & Li (2004), Anderson et al. (2014), Gutiérrez et al. (2017)
2005cs	0.002	0.006	0.003	0.003	29.46	0.60	0.095	0.171	M 51	Pastorello et al. (2006), Pastorello et al. (2009), Spiro et al. (2014)
2007aa	0.004887	0.032	0.009	0.009	31.95	0.27	0.070	0.000	NGC 4030	Anderson et al. (2014), Gutiérrez et al. (2017), This Work
2008bk	0.000767	0.007	0.001	0.001	27.68	0.13	0.052	0.000	NGC 7793	Van Dyk et al. (2012), Anderson et al. (2014), Spiro et al. (2014) , Gutiérrez et al. (2017)
2008in	0.005224	0.012	0.005	0.005	30.60	0.20	0.060	0.080	NGC 4303	Roy et al. (2011), Anderson et al. (2014), Gutiérrez et al. (2017)
2009N	0.003456	0.020	0.004	0.004	31.67	0.11	0.056	0.100	NGC 4487	Takáts et al. (2014), Anderson et al. (2014), Spiro et al. (2014), Gutiérrez et al. (2017)
2010id	0.01648	-	-	-	32.86	0.50	0.162	0.167	NGC 7483	Gal-Yam et al. (2011), Spiro et al. (2014)
2012A	0.0025	0.011	0.004	0.004	29.96	0.15	0.085	$\sim$0.010	NGC 3239	Tomasella et al. (2013), J15a
2012aw	0.0026	0.060	0.010	0.010	29.97	0.03	0.074	0.143	NGC 3351	Fraser et al. (2012), Bose et al. (2013), J14, J15a
2012ec	0.00469	0.040	0.015	0.015	31.19	0.13	0.071	0.372	NGC 1084	Barbarino et al. (2015), J15a
2013am	0.002692	0.015	0.006	0.011	30.54	0.40	0.066	1.705	NGC 3623	Zhang et al. (2014); Tomasella et al. (2018)
2016aqf	0.004016	0.008	0.002	0.002	30.16	0.27	0.146	$\lesssim$0.096	NGC 2101	This Work
2016bkv	0.002	0.0216	0.0014	0.0014	30.79	0.05	0.045	$\lesssim$0.016	NGC 3184	Nakaoka et al. (2018), Hosseinzadeh et al. (2018)

TABLE A.4: pEW for several lines during the optically thick phase and H_α FWHM. These values are not corrected for instrument resolution. Phase with respect to the explosion epoch.

Phase	pEW(H_β) [Å]	pEW(Fe II 4924) [Å]	pEW(Fe II 5018) [Å]	pEW(Fe II 5169) [Å]	pEW(Na I D) [Å]	pEW(Ba II 6142) [Å]	pEW(Sc II 6247) [Å]	pEW(H_α) [Å]	FWHM(H_α) [Å]
13	31.7 ± 3.1	-	-	-	-	-	-	19.0 ± 0.9	189.7 ± 2.5
16	34.0 ± 2.0	-	1.3 ± 0.1	12.7 ± 0.4	-	-	-	29.2 ± 3.2	170.0 ± 2.6
17	33.9 ± 0.8	-	-	13.7 ± 0.4	-	-	-	31.3 ± 3.1	181.3 ± 3.5
22	51.0 ± 2.6	-	16.3 ± 0.6	19.3 ± 1.5	-	-	-	46.0 ± 2.0	156.0 ± 1.7
29	32.3 ± 1.5	-	-	-	-	-	-	62.0 ± 7.0	140.0 ± 5.2
37	37.7 ± 1.2	6.3 ± 0.8	16.2 ± 0.8	23.7 ± 7.6	6.9 ± 1.3	3.2 ± 0.5	4.1 ± 1.0	62.3 ± 4.5	113.0 ± 6.0
44	43.3 ± 1.5	8.2 ± 0.4	19.3 ± 1.5	31.3 ± 2.3	9.4 ± 0.9	5.1 ± 0.4	3.9 ± 0.7	65.7 ± 3.2	100.3 ± 6.1
51	42.0 ± 1.0	11.7 ± 1.1	20.7 ± 1.2	31.0 ± 2.0	16.8 ± 0.3	6.0 ± 0.6	5.0 ± 0.5	65.3 ± 3.5	101.3 ± 3.8
53	47.3 ± 2.3	12.8 ± 0.7	22.0 ± 1.0	34.0 ± 1.7	19.7 ± 2.3	9.6 ± 1.0	7.8 ± 1.5	64.0 ± 2.6	93.7 ± 3.2
54	55.0 ± 3.6	11.7 ± 0.5	20.3 ± 0.6	33.7 ± 2.1	24.0 ± 1.7	8.9 ± 1.6	5.0 ± 0.4	68.7 ± 1.5	94.0 ± 3.0
60	45.3 ± 2.9	14.3 ± 0.5	23.0 ± 1.0	37.0 ± 3.0	24.0 ± 2.6	11.0 ± 1.1	7.1 ± 0.3	66.0 ± 2.6	88.3 ± 2.5
71	37.0 ± 1.7	17.7 ± 0.6	25.0 ± 1.0	40.3 ± 1.5	30.7 ± 2.1	15.3 ± 1.2	7.2 ± 0.5	62.0 ± 2.6	82.7 ± 5.0

TABLE A.5: FWHM for lines during the optically-thin phase. Values are corrected for the instrument resolution.

Phase [days]	FWHM([O I] 6300) [Å]	FWHM([O I] 6364) [Å]	FWHM(H_α) [Å]	FWHM(He I 7065) [Å]	FWHM([Fe II] 7155) [Å]
155	-	-	43.8 ± 0.6	47.8 ± 3.1	41.2 ± 2.1
168	29.5 ± 2.1	18.7 ± 2.1	40.0 ± 0.6	36.3 ± 2.6	36.3 ± 2.0
202	33.6 ± 1.5	20.8 ± 2.1	40.5 ± 0.6	30.3 ± 1.0	34.3 ± 1.2
220	38.2 ± 6.7	23.6 ± 1.2	38.2 ± 0.6	32.7 ± 1.0	34.7 ± 1.5
259	24.9 ± 2.5	17.8 ± 1.2	37.8 ± 0.6	24.4 ± 1.5	34.3 ± 1.5
271	24.4 ± 2.5	20.8 ± 2.1	39.4 ± 0.6	23.0 ± 1.5	34.7 ± 1.5
285	27.5 ± 2.1	20.8 ± 3.8	35.9 ± 0.6	28.7 ± 1.5	32.4 ± 1.2
303	28.2 ± 2.5	22.2 ± 4.0	35.4 ± 0.6	27.0 ± 0.6	29.5 ± 1.5
330	28.2 ± 1.5	24.9 ± 2.1	35.9 ± 0.6	28.2 ± 2.1	34.7 ± 1.2
351	39.7 ± 3.6	19.8 ± 4.4	37.8 ± 0.6	70.9 ± 9.0	43.4 ± 4.0

Appendix B

Nickel Mass estimation for SNe II

In the literature there are various methods to estimate the ^{56}Ni mass for SNe II. In this chapter, I present the ones I used in Chapter 7.

B.1 Arnett's Rule

Arnett (1996) found a relation between $M_{\rm Ni}$ of SNe II and their luminosity during the exponential-decay tail, known as Arnett's rule. For instance, one can use SN 1987A, an extremely well-observed and well-studied SN, as comparison to obtain the following relation:

$$M_{\rm Ni} = 0.075 \times \frac{L_{\rm SN}}{L_{\rm 87A}} {\rm M}_{\odot}. \tag{B.1}$$

By using the bolometric light curve calculated in Section 7.3.4, interpolating with GPs to obtain the luminosity at 200 days after the explosion, I obtain $M_{\rm Ni} = 0.008 \pm 0.001$ $\rm M_{\odot}$.

B.2 Modified Arnett's Rule

Hamuy (2003) formed a relation between the bolometric luminosity of the exponential-decay tail and $M_{\rm Ni}$, in a similar fashion to Arnett (1996). The bolometric luminosity is then given by:

$$log_{10}\, L_{\rm tail} = \frac{-[m_{V,\rm tail} - A_{\rm MW}(V) - A_{\rm Host}(V) + BC] + 5\, log_{10}(D) - 8.14}{2.5} \tag{B.2}$$

where $L_{\rm tail}$ is the tail luminosity in erg s^{-1} at 200 days after the explosion, D is the distance in cm, BC is a bolometric correction that permits one to transform V magnitudes into bolometric magnitudes, and the additive constant, 8.14, provides the conversion from Vega magnitudes into cgs units. $A_{\rm MW}(V)$ and $A_{\rm Host}(V)$ are the V-band extinction values for our galaxy and the host galaxy of the SN. From SN 1987A and SN 1999em, Hamuy (2001b) found that $BC = 0.26 \pm 0.06$.

Using the relation above, $M_{\rm Ni}$ is obtained as follows:

$$M_{\rm Ni} = (7.866 \times 10^{-44})\, L_{\rm tail}\, exp\Big[\frac{(t_{\rm tail} - t_0)/(1+z) - 6.1}{111.26}\Big] {\rm M}_\odot, \tag{B.3}$$

where t_0 is the time of explosion, $t_{\rm tail}$ is the time at which the luminosity is measure during the exponential-decay tail (i.e., +200 days) and z is the SN redshift. 6.1 is the half-life (in days) of ^{56}Ni and 111.26 is the e-folding time (in days) of the ^{56}Co decay. From this, I obtain $M_{\rm Ni} = 0.011 \pm 0.003$ M$_\odot$.

B.3 ^{56}Ni Mass – Hα FWHM relation

Maguire et al. (2012) found a relation between $M_{\rm Ni}$ and the Hα FWHM given by:

$$M_{\rm Ni} = A \times 10^{B \times FWHM_{\rm corr}} {\rm M}_\odot, \tag{B.4}$$

where the coefficients have values of $B = 0.0233 \pm 0.0041$ and $A = 1.81^{+1.05}_{-0.68} \times 10^{-3}$. FWHM$_{\rm corr}$ is the FWHM of H$_\alpha$, corrected by the spectral resolution of the instrument, during the nebular phase ($\sim 350 - 550$ days). From this relation, using the FWHM of Hα from the spectrum at +348 days, I obtain $M_{\rm Ni} = 0.014^{+0.009}_{-0.007}$ M$_\odot$, where I used FWHM$_{\rm inst}$ = 21.2 Å, taken from grism #13 in EFOSC2 (as given in the ESO website[1]).

B.4 Theoretical Approach

J12 also gives a relation to estimate $M_{\rm Ni}$ from the early exponential-decay tail, assuming full trapping, that the deposited energy is instantaneously re-emitted and that no other energy source has any influence, i.e.:

$$L_{^{56}{\rm Co}}(t) = 9.92 \times 10^{41} \frac{M_{\rm Ni}}{0.07 M_\odot} \left(e^{-t/111.4\ d} - e^{-t/8.8\ d}\right) {\rm erg\ s}^{-1}, \tag{B.5}$$

[1] https://www.eso.org/sci/facilities/lasilla/instruments/efosc/inst/Efosc2Grisms.html

where 0.07 is the ^{56}Ni mass of SN 1987A (in $M_\odot$), and 111.4 and 8.8 are the *e*-folding time (in days) of the ^{56}Co and ^{56}Ni decays, respectively. With this, I obtain $M_{\rm Ni} = 0.007 \pm 0.001\ M_\odot$.

The exact values of some of the parameters, such as $M_{\rm Ni}$ of SN 1987A, may slightly vary between the different implementations in this chapters due to differences in the approaches.

Appendix C

Further details for Chapter 7

In this chapter, I describe further details used in Chapter 7.

C.1 *V*-band comparison for SN 2016aqf

Given that SN 2016aqf was not visible for a period of time, I do not have observations of the transition from the plateau phase to the nebular phase. To estimate the duration of the plateau, I therefore compared the V-band light curve of SN 2016aqf with other LL SNe II in my sample. I found that the V band of SN 2003fb has a similar shape (see Figure C.1), if normalised by the luminosity at 50 days after the explosion. For this reason, I decided to use the plateau duration of SN 2003fb (adding its uncertainty in quadrature) for SN 2016aqf.

C.2 SN II sample: Parameters and Correlations

Below I describe the sources of the parameters used for the analysis in Section 7.5.3. Not every SN has every parameter measured. All the values for SN 2016aqf come from this work unless otherwise mentioned:

1. Ni/Fe abundance ratio: these come from this work except for SN 2012A, SN 2012aw and SN 2012ec, the three of them coming from J15a (table 4 in J15a for the former two).
2. M_{Ni}: these were obtained from the references in Table A.3. Note that I estimate M_{Ni} for SN 2007aa in this work.
3. M^{B}_{host}: these were obtained from Gutiérrez et al. (2018).

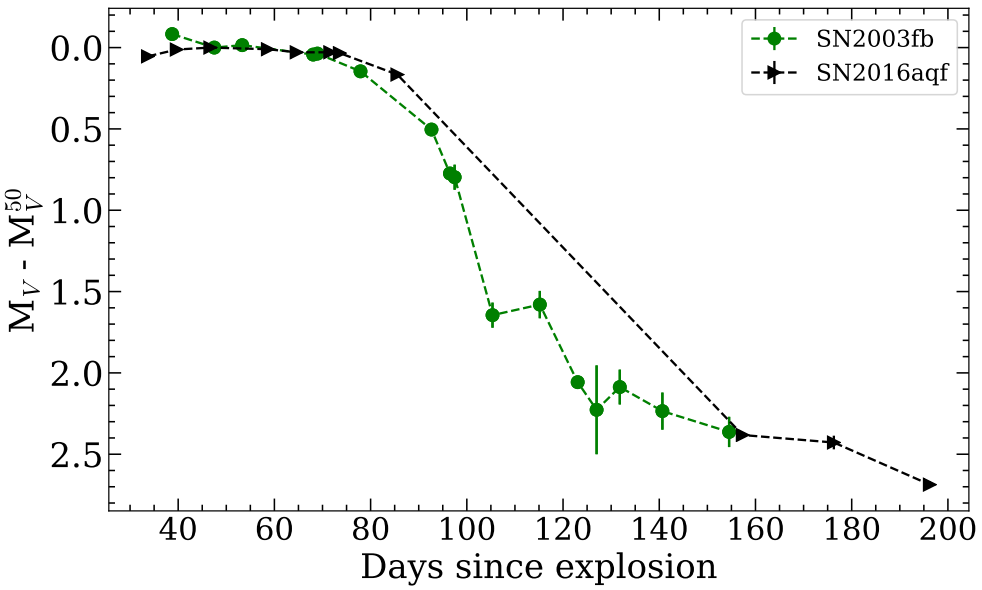

FIGURE C.1: V-band comparison between the light curves of SN 2016aqf and SN 2013fb. The y-axis is V-band absolute magnitude minus V-band absolute magnitude at $+50$ days. The evolution of both light curves is very similar.

4. M^V_{max}: these were obtained from Gutiérrez et al. (2018), except for SN 2012ec which comes from Barbarino et al. (2015) and SN 2013am which comes from Zhang et al. (2014).

5. s_2: these were obtained from Gutiérrez et al. (2018).

6. OPT_d: these were obtained from Gutiérrez et al. (2018), including SN 2016aqf, except for SN 2012A, SN 2012aw and SN 2012ec, which came from table 10 in Barbarino et al. (2015) with an assumed uncertainty of ± 10 d.

7. vel(Fe II 5169): taken from Spiro et al. (2014), except for SN 2012A, SN 2012aw and SN 2012ec which come from table 10 in Barbarino et al. (2015) with an assumed uncertainty of $\pm$ 300 km s^{-1} and SN 2013am which comes from Zhang et al. (2014).

8. pEW(Fe II 5169): obtained from Gutiérrez et al. (2018).

9. vel(Na I D): obtained from Gutiérrez et al. (2018).

10. M^K_{prog} and M^{SG}_{prog}: these values come from Smartt (2015).

11. E_{exp}: these values come from Barbarino et al. (2015), except for SN 2005cs which comes from Pastorello et al. (2009).

12. L_{6300} and L_{6364}: these values come from this work.

13. $(12 + \log(O/H))_{N2}$: these values come from Anderson et al. (2016).

References

Abbott, T. M. C., Allam, S., Andersen, P., et al. 2019, , 872, L30

Alam, S., Ata, M., Bailey, S., et al. 2017, , 470, 2617

Alekseev, E. N., Alekseeva, L. N., Krivosheina, I. V., & Volchenko, V. I. 1988, Soviet Astronomy Letters, 14, 41

Alekseev, E. N., Alekseeva, L. N., Volchenko, V. I., & Krivosheina, I. V. 1987, Soviet Journal of Experimental and Theoretical Physics Letters, 45, 589

Allen, J. T., Hewett, P. C., Maddox, N., Richards, G. T., & Belokurov, V. 2011, , 410, 860

Altavilla, G., Ruiz-Lapuente, P., Balastegui, A., et al. 2009, , 695, 135

Amanullah, R., Johansson, J., Goobar, A., et al. 2015, , 453, 3300

Ambikasaran, S., Foreman-Mackey, D., Greengard, L., Hogg, D. W., & O'Neil, M. 2016, IEEE Transactions on Pattern Analysis and Machine Intelligence, 38, 252

Anderson, J. P. 2019, , 628, A7

Anderson, J. P., González-Gaitán, S., Hamuy, M., et al. 2014, , 786, 67

Anderson, J. P., Gutiérrez, C. P., Dessart, L., et al. 2016, Astronomy and Astrophysics, 589, A110

Angus, C. R., Smith, M., Sullivan, M., et al. 2019, , 487, 2215

Arnett, D. 1996, Supernovae and Nucleosynthesis: An Investigation of the History of Matter from the Big Bang to the Present

Arnett, W. D. 1966, Canadian Journal of Physics, 44, 2553

—. 1978, , 219, 1008

—. 1979, , 230, L37

—. 1980, , 237, 541

—. 1982, The Astrophysical Journal, 253, 785

Arnett, W. D., & Clayton, D. D. 1970, , 227, 780

Ashall, C., Mazzali, P., Sasdelli, M., & Prentice, S. J. 2016, , 460, 3529

Asplund, M., Grevesse, N., Sauval, A. J., & Scott, P. 2009, , 47, 481

Astier, P., Guy, J., Regnault, N., et al. 2006, , 447, 31

Avelino, A., Friedman, A. S., Mandel, K. S., et al. 2019, , 887, 106

Baade, W., & Zwicky, F. 1934a, Proceedings of the National Academy of Science, 20, 259

—. 1934b, Proceedings of the National Academy of Science, 20, 254

—. 1934c, Physical Review, 46, 76

Barbarino, C., Dall'Ora, M., Botticella, M. T., et al. 2015, , 448, 2312

Barbary, K. 2016, extinction v0.3.0, Zenodo, doi:10.5281/zenodo.804967

Barbary, K., rbiswas4, Goldstein, D., et al. 2016, sncosmo/sncosmo: v1.4.0, v.v1.4.0, Zenodo, doi:10.5281/zenodo.168220

Barbon, R., Capaccioli, M., & Ciatti, F. 1975, , 44, 267

Barbon, R., Ciatti, F., & Rosino, L. 1973, , 25, 241

—. 1979, , 72, 287

Benetti, S., Cappellaro, E., Mazzali, P. A., et al. 2005, , 623, 1011

Bersten, M. C., Benvenuto, O., & Hamuy, M. 2011, , 729, 61

Bersten, M. C., & Mazzali, P. A. 2017, Light Curves of Type I Supernovae, ed. A. W. Alsabti & P. Murdin (Cham: Springer International Publishing), 723–735

Bessell, M. S. 1990, , 102, 1181

—. 2005, , 43, 293

Bethe, H. A., & Wilson, J. R. 1985, , 295, 14

Betoule, M., Marriner, J., Regnault, N., et al. 2013, , 552, A124

Betoule, M., Kessler, R., Guy, J., et al. 2014, , 568, A22

Bionta, R. M., Blewitt, G., Bratton, C. B., et al. 1987, , 58, 1494

Blanton, M. R., & Roweis, S. 2007, , 133, 734

Blondin, S., Dessart, L., Leibundgut, B., et al. 2006, , 131, 1648

Bloom, J. S., Kasen, D., Shen, K. J., et al. 2012, , 744, L17

Bohlin, R. C., & Gilliland, R. L. 2004a, , 128, 3053

—. 2004b, , 127, 3508

Bohlin, R. C., Gordon, K. D., & Tremblay, P. E. 2014, , 126, 711

Boone, K., Aldering, G., Antilogus, P., et al. 2021, , 912, 71

Bose, S., Kumar, B., Sutaria, F., et al. 2013, , 433, 1871

Brout, D., & Scolnic, D. 2021, , 909, 26

Brout, D., Sako, M., Scolnic, D., et al. 2019, , 874, 106

Brown, J. S., Bersier, D., Stanek, K. Z., et al. 2016, The Astronomer's Telegram, 8736, 1

Brown, T. M., Baliber, N., Bianco, F. B., et al. 2013, , 125, 1031

Burbidge, E. M., Burbidge, G. R., Fowler, W. A., & Hoyle, F. 1957, Rev. Mod. Phys., 29, 547

Burgh, E. B., Nordsieck, K. H., Kobulnicky, H. A., et al. 2003, Society of Photo-Optical Instrumentation Engineers (SPIE) Conference Series, Vol. 4841, Prime Focus Imaging Spectrograph for the Southern African Large Telescope: optical design, ed. M. Iye & A. F. M. Moorwood, 1463–1471

Burke, D. L., Rykoff, E. S., Allam, S., et al. 2018, , 155, 41

Burns, C. R., Stritzinger, M., Phillips, M. M., et al. 2011, The Astronomical Journal, 141, 19

—. 2014, The Astrophysical Journal, 789, 32

Burrows, A., & Lattimer, J. M. 1986, , 307, 178

Buta, R. J. 1982, , 94, 578

Buzzoni, B., Delabre, B., Dekker, H., et al. 1984, The Messenger, 38, 9

Cadonau, R., Sandage, A., & Tammann, G. A. 1985, Type I Supernovae as Standard Candles, ed. N. Bartel, Vol. 224, 151

Calzetti, D., Armus, L., Bohlin, R. C., et al. 2000, , 533, 682

Cao, Y., et al. 2013, , 775, L7

Cardelli, J. A., Clayton, G. C., & Mathis, J. S. 1989, The Astrophysical Journal, 345, 245

Carter, P., Beutler, F., Percival, W. J., et al. 2018, , 481, 2371

Chevalier, R. A. 1977, in Supernovae, ed. D. N. Schramm (Dordrecht: Springer Netherlands), 53–61

Childress, M. J., Hillier, D. J., Seitenzahl, I., et al. 2015, Monthly Notices of the Royal Astronomical Society, 454, 3816

Chugai, N. N., & Utrobin, V. P. 2000, , 354, 557

Colgate, S. A., & McKee, C. 1969, The Astrophysical Journal, 157, 623

Colgate, S. A., & White, R. H. 1966, , 143, 626

Collins, C., Müller, B., & Heger, A. 2018, , 473, 1695

Conley, A., Howell, D. A., Howes, A., et al. 2006, , 132, 1707

Conley, A., Sullivan, M., Hsiao, E. Y., et al. 2008, The Astrophysical Journal, 681, 482

Conley, A., Guy, J., Sullivan, M., et al. 2011, The Astrophysical Journal Supplement Series, 192, 1

Contreras, C., Hamuy, M., Phillips, M. M., et al. 2010, The Astronomical Journal, 139, 519

Cormier, D., & Davis, T. M. 2011, , 410, 2137

Couch, S. M. 2017, Philosophical Transactions of the Royal Society of London Series A, 375, 20160271

Cousins, A. W. J. 1976, , 81, 25

Cowan, J. J., & Thielemann, F.-K. 2004, Physics Today, 57, 10.47

de Jaeger, T., Stahl, B. E., Zheng, W., et al. 2020a, , 496, 3402

de Jaeger, T., González-Gaitán, S., Anderson, J. P., et al. 2015, , 815, 121

de Jaeger, T., Anderson, J. P., Galbany, L., et al. 2018, Monthly Notices of the Royal Astronomical Society, 476, 4592

de Jaeger, T., Galbany, L., González-Gaitán, S., et al. 2020b, , 495, 4860

de Mello, D., Benetti, S., & Massone, G. 1997, International Astronomical Union Circular, 6537, 1

Dessart, L., Hillier, D. J., Waldman, R., & Livne, E. 2013a, , 433, 1745

Dessart, L., Waldman, R., Livne, E., Hillier, D. J., & Blondin, S. 2013b, , 428, 3227

Dessart, L., Gutierrez, C. P., Hamuy, M., et al. 2014, , 440, 1856

Dhawan, S., Jha, S. W., & Leibundgut, B. 2018, , 609, A72

Dodelson, S. 2003, Modern cosmology (Elsevier)

Doggett, J. B., & Branch, D. 1985, , 90, 2303

Doherty, C. L., Gil-Pons, P., Siess, L., & Lattanzio, J. C. 2017, , 34, e056

Doi, M., Tanaka, M., Fukugita, M., et al. 2010, , 139, 1628

Doroshkevich, A., Tucker, D. L., Allam, S., & Way, M. J. 2004, , 418, 7

Elias, J. H., Frogel, J. A., Hackwell, J. A., & Persson, S. E. 1981, The Astrophysical Journal, 251, L13

Elias, J. H., Matthews, K., Neugebauer, G., & Persson, S. E. 1985, The Astrophysical Journal, 296, 379

Elias-Rosa, N., Van Dyk, S. D., Li, W., et al. 2010, , 714, L254

Ellis, R. S., Sullivan, M., Nugent, P. E., et al. 2008, , 674, 51

Elmhamdi, A., Danziger, I. J., Chugai, N., et al. 2003, , 338, 939

Ertl, T., Janka, H. T., Woosley, S. E., Sukhbold, T., & Ugliano, M. 2016, , 818, 124

Falk, S. W., & Arnett, W. D. 1977, The Astrophysical Journal Supplement Series, 33, 515

Filippenko, A. V. 1988, , 96, 1941

—. 1997, , 35, 309

Filippenko, A. V., Richmond, M. W., Matheson, T., et al. 1992a, , 384, L15

Filippenko, A. V., Richmond, M. W., Branch, D., et al. 1992b, , 104, 1543

Fink, M., Hillebrandt, W., & Röpke, F. K. 2007, , 476, 1133

Fink, M., Röpke, F. K., Hillebrandt, W., et al. 2010, , 514, A53

Firth, R. E., Sullivan, M., Gal-Yam, A., et al. 2015, Monthly Notices of the Royal Astronomical Society, 446, 3895

Fitzpatrick, E. L. 1999, , 111, 63

Fitzpatrick, E. L., & Massa, D. 2007, , 663, 320

Flaugher, B., Diehl, H. T., Honscheid, K., et al. 2015, , 150, 150

Folatelli, G., Phillips, M. M., Burns, C. R., et al. 2010, , 139, 120

Foley, R. J., Papenkova, M. S., Swift, B. J., et al. 2003, , 115, 1220

Foley, R. J., Challis, P. J., Chornock, R., et al. 2013, , 767, 57

Foley, R. J., Scolnic, D., Rest, A., et al. 2018, , 475, 193

Fraser, M., Maund, J. R., Smartt, S. J., et al. 2012, , 759, L13

Freedman, W. L., Burns, C. R., Phillips, M. M., et al. 2009, The Astrophysical Journal, 704, 1036

Frieman, J. A., Bassett, B., Becker, A., et al. 2008, , 135, 338

Fukugita, M., Ichikawa, T., Gunn, J. E., et al. 1996, , 111, 1748

Gal-Yam, A. 2017, Observational and Physical Classification of Supernovae, ed. A. W. Alsabti & P. Murdin, 195

Gal-Yam, A., Ofek, E. O., & Shemmer, O. 2002, , 332, L73

Gal-Yam, A., Leonard, D. C., Fox, D. B., et al. 2007, , 656, 372

Gal-Yam, A., Kasliwal, M. M., Arcavi, I., et al. 2011, , 736, 159

Gal-Yam, A., Arcavi, I., Ofek, E. O., et al. 2014, , 509, 471

Galbany, L., Hamuy, M., Phillips, M. M., et al. 2016, , 151, 33

Gall, E. E. E., Kotak, R., Leibundgut, B., et al. 2016, , 592, A129

Ganeshalingam, M., Li, W., & Filippenko, A. V. 2011, , 416, 2607

Gao, L., De Lucia, G., White, S. D. M., & Jenkins, A. 2004, , 352, L1

Goldberg, J. A., Bildsten, L., & Paxton, B. 2019, , 879, 3

Goldhaber, G., Groom, D. E., Kim, A., et al. 2001, , 558, 359

González-Gaitán, S., Tominaga, N., Molina, J., et al. 2015, , 451, 2212

Gordon, K. D., Clayton, G. C., Misselt, K. A., Landolt, A. U., & Wolff, M. J. 2003, , 594, 279

Graur, O., Rodney, S. A., Maoz, D., et al. 2014, , 783, 28

Groh, J. H., Georgy, C., & Ekström, S. 2013, , 558, L1

Guillochon, J., Parrent, J., Kelley, L. Z., & Margutti, R. 2017, , 835, 64

Gunn, J. E., Carr, M., Rockosi, C., et al. 1998, , 116, 3040

Gutiérrez, C. P., Anderson, J. P., Hamuy, M., et al. 2017, The Astrophysical Journal, 850, 89

Gutiérrez, C. P., Anderson, J. P., Sullivan, M., et al. 2018, Monthly Notices of the Royal Astronomical Society, 479, 3232

Guy, J., Astier, P., Nobili, S., Regnault, N., & Pain, R. 2005, , 443, 781

Guy, J., Astier, P., Baumont, S., et al. 2007, Astronomy and Astrophysics, 466, 11

Guy, J., Sullivan, M., Conley, A., et al. 2010, Astronomy and Astrophysics, 523, A7

Hamuy, M. 2003, , 582, 905

Hamuy, M., Phillips, M. M., Maza, J., et al. 1995, The Astronomical Journal, 109, 1

Hamuy, M., Phillips, M. M., Wells, L. A., & Maza, J. 1993, , 105, 787

Hamuy, M., & Pinto, P. A. 2002a, , 566, L63

—. 2002b, , 566, L63

Hamuy, M., Phillips, M. M., Suntzeff, N. B., et al. 1996, The Astronomical Journal, 112, 2408

Hamuy, M., Pinto, P. A., Maza, J., et al. 2001, , 558, 615

Hamuy, M., Phillips, M. M., Suntzeff, N. B., et al. 2003, , 424, 651

Hamuy, M. A. 2001a, PhD thesis, The University of Arizona

—. 2001b, PhD thesis, The University of Arizona

Harkness, R. P., Wheeler, J. C., Margon, B., et al. 1987, , 317, 355

Harris, W. E., Fitzgerald, M. P., & Reed, B. C. 1981, , 93, 507

Harutyunyan, A. H., et al. 2008, , 488, 383

Hayden, B. T., Garnavich, P. M., Kessler, R., et al. 2010, , 712, 350

He, S., Wang, L., & Huang, J. Z. 2018, , 857, 110

Hicken, M., Garnavich, P. M., Prieto, J. L., et al. 2007, , 669, L17

Hicken, M., Wood-Vasey, W. M., Blondin, S., et al. 2009a, , 700, 1097

Hicken, M., Challis, P., Jha, S., et al. 2009b, The Astrophysical Journal, 700, 331

Hicken, M., Challis, P., Kirshner, R. P., et al. 2012, , 200, 12

Hillebrandt, W., & Niemeyer, J. C. 2000, , 38, 191

Hiramatsu, D., Howell, D. A., Van Dyk, S. D., et al. 2021, Nature Astronomy, 5, 903

Hirata, K., Kajita, T., Koshiba, M., et al. 1987, , 58, 1490

Hoeflich, P., Khokhlov, A., Wheeler, J. C., et al. 1996, The Astrophysical Journal, 472, L81

Höflich, P., Dragulin, P., Mitchell, J., et al. 2013, Frontiers of Physics, 8, 144

Hosseinzadeh, G., Yang, Y., McCully, C., et al. 2016, The Astronomer's Telegram, 8748, 1

Hosseinzadeh, G., Valenti, S., McCully, C., et al. 2018, , 861, 63

Howell, D. A., Sullivan, M., Nugent, P. E., et al. 2006, , 443, 308

Hoyle, F., & Fowler, W. A. 1960, , 132, 565

Hsiao, E. Y., Conley, A., Howell, D. A., et al. 2007, , 663, 1187

Hubble, E. 1929, Proceedings of the National Academy of Science, 15, 168

Hubeny, I., & Mihalas, D. 2014, Theory of stellar atmospheres: an introduction to astrophysical non-equilibrium quantitative spectroscopic analysis, Vol. 26 (Princeton University Press)

Hunter, D. J., et al. 2009, , 508, 371

Iben, I., J., & Tutukov, A. V. 1984, , 54, 335

Ilkov, M., & Soker, N. 2012, , 419, 1695

Inserra, C., Smartt, S. J., Gall, E. E. E., et al. 2018, , 475, 1046

Janka, H. T. 2001, , 368, 527

Janka, H.-T. 2017, Neutrino-Driven Explosions, ed. A. W. Alsabti & P. Murdin, 1095

Janka, H. T., & Mueller, E. 1996, , 306, 167

Jerkstrand, A., Ertl, T., Janka, H. T., et al. 2018, , 475, 277

Jerkstrand, A., Fransson, C., Maguire, K., et al. 2012, , 546, A28

Jerkstrand, A., Smartt, S. J., Fraser, M., et al. 2014, , 439, 3694

Jerkstrand, A., Timmes, F. X., Magkotsios, G., et al. 2015a, , 807, 110

Jerkstrand, A., Smartt, S. J., Sollerman, J., et al. 2015b, , 448, 2482

Jha, S., Riess, A. G., & Kirshner, R. P. 2007, , 659, 122

Jha, S., Kirshner, R. P., Challis, P., et al. 2006, The Astronomical Journal, 131, 527

Jha, S. W., & Miszalski, B. 2016, The Astronomer's Telegram, 8749, 1

Johnson, H. L. 1955, Annales d'Astrophysique, 18, 292

—. 1966, , 4, 193

Johnson, H. L., & Harris, D. L. 1954, , 120, 196

Johnson, H. L., Mitchell, R. I., Iriarte, B., & Wisniewski, W. Z. 1966, Communications of the Lunar and Planetary Laboratory, 4, 99

Johnson, H. L., & Morgan, W. W. 1953, , 117, 313

Jones, D. O., Scolnic, D. M., Foley, R. J., et al. 2019, , 881, 19

Jönsson, J., Sullivan, M., Hook, I., et al. 2010, , 405, 535

Kasen, D., & Woosley, S. E. 2009, , 703, 2205

Kashi, A., & Soker, N. 2011, , 417, 1466

Kattner, S., Leonard, D. C., Burns, C. R., et al. 2012, Publications of the Astronomical Society of the Pacific, 124, 114

Kelly, P. L., Hicken, M., Burke, D. L., Mandel, K. S., & Kirshner, R. P. 2010, , 715, 743

Kelsey, L., Sullivan, M., Smith, M., et al. 2021, , 501, 4861

Kennicutt, R. C., & Evans, N. J. 2012, Annual Review of Astronomy and Astrophysics, 50, 531

Kessler, R., Becker, A. C., Cinabro, D., et al. 2009a, , 185, 32

Kessler, R., Bernstein, J. P., Cinabro, D., et al. 2009b, , 121, 1028

Kessler, R., Guy, J., Marriner, J., et al. 2013, , 764, 48

Khatami, D. K., & Kasen, D. N. 2019, , 878, 56

Kim, A., Goobar, A., & Perlmutter, S. 1996, , 108, 190

Kim, A. G., Thomas, R. C., Aldering, G., et al. 2013, , 766, 84

Kimeldorf, G. S., & Wahba, G. 1970, The Annals of Mathematical Statistics, 41, 495

Kirshner, R. P., & Kwan, J. 1974, , 193, 27

Klein, R. I., & Chevalier, R. A. 1978, , 223, L109

Kobulnicky, H. A., Nordsieck, K. H., Burgh, E. B., et al. 2003, Society of Photo-Optical Instrumentation Engineers (SPIE) Conference Series, Vol. 4841, Prime focus imaging spectrograph for the Southern African large telescope: operational modes, ed. M. Iye & A. F. M. Moorwood, 1634–1644

Kochanek, C. S. 2014, , 785, 28

Kourkchi, E., Tully, R. B., Anand, G. S., et al. 2020, , 896, 3

Kowal, C. T. 1968, , 73, 1021

Kozyreva, A., Nakar, E., & Waldman, R. 2019, , 483, 1211

Kozyreva, A., Nakar, E., Waldman, R., Blinnikov, S., & Baklanov, P. 2020, arXiv e-prints, arXiv:2003.14097

Kron, G. E., White, H. S., & Gascoigne, S. C. B. 1953, , 118, 502

Kroupa, P. 2001, , 322, 231

Kroupa, P., Weidner, C., Pflamm-Altenburg, J., et al. 2013, The Stellar and Sub-Stellar Initial Mass Function of Simple and Composite Populations, ed. T. D. Oswalt & G. Gilmore, Vol. 5, 115

Kulkarni, S., & Kasliwal, M. M. 2009, in Astrophysics with All-Sky X-Ray Observations, ed. N. Kawai, T. Mihara, M. Kohama, & M. Suzuki, 312

Kushnir, D. 2015, arXiv e-prints, arXiv:1506.02655

Lambourne, R. J. 2010, Relativity, gravitation and cosmology (Cambridge University Press)

Lampeitl, H., Nichol, R. C., Seo, H. J., et al. 2010, , 401, 2331

Landolt, A. U. 1992, , 104, 340

—. 2007, , 133, 2502

Lauberts, A., & Valentijn, E. A. 1989, The surface photometry catalogue of the ESO-Uppsala galaxies

Lee, D. D., & Seung, H. S. 1999, , 401, 788

Leibundgut, B. 1990, , 229, 1

Li, W., Filippenko, A. V., Chornock, R., et al. 2003, , 115, 453

Li, W., Leaman, J., Chornock, R., et al. 2011, , 412, 1441

Limongi, M., & Chieffi, A. 2003, , 592, 404

Lisakov, S. M., Dessart, L., Hillier, D. J., Waldman, R., & Livne, E. 2017, , 466, 34

—. 2018, , 473, 3863

Litvinova, I. Y., & Nadezhin, D. K. 1985, Soviet Astronomy Letters, 11, 145

Lochner, M., Scolnic, D. M., Awan, H., et al. 2018, arXiv e-prints, arXiv:1812.00515

Lodders, K. 2003, , 591, 1220

Lundmark, K. 1932, Handbuch der Astrophysik, 5, 210

Lyman, J. D., Bersier, D., & James, P. A. 2014, Monthly Notices of the Royal Astronomical Society, 437, 3848

Maddox, S. J., Efstathiou, G., Sutherland, W. J., & Loveday, J. 1990, , 242, 43

Maeda, K., Taubenberger, S., Sollerman, J., et al. 2010, , 708, 1703

Maeda, K., Kawabata, K., Tanaka, M., et al. 2007, The Astrophysical Journal, 658, L5

Magee, L. 1998, The American Statistician, 52, 20

Maguire, K., Di Carlo, E., Smartt, S. J., et al. 2010, , 404, 981

Maguire, K., Sullivan, M., Ellis, R. S., et al. 2012, , 426, 2359

Makarov, D., Prugniel, P., Terekhova, N., Courtois, H., & Vauglin, I. 2014, , 570, A13

Malmquist, K. G. 1922, Meddelanden fran Lunds Astronomiska Observatorium Serie I, 100, 1

—. 1925, Meddelanden fran Lunds Astronomiska Observatorium Serie I, 106, 1

Maoz, D., Mannucci, F., & Nelemans, G. 2014, , 52, 107

Marino, R. A., Rosales-Ortega, F. F., Sánchez, S. F., et al. 2013, Astronomy and Astrophysics, 559, A114

Martinez, L., & Bersten, M. C. 2019, , 629, A124

Maund, J. R., Fraser, M., Smartt, S. J., et al. 2013, , 431, L102

Mazzali, P. A., Maurer, I., Valenti, S., Kotak, R., & Hunter, D. 2010, , 408, 87

Mazzali, P. A., Röpke, F. K., Benetti, S., & Hillebrandt, W. 2007, Science, 315, 825

Mazzali, P. A., Deng, J., Maeda, K., et al. 2002, , 572, L61

Minkowski, R. 1941, , 53, 224

Moriya, T. J., Tominaga, N., Langer, N., et al. 2014, , 569, A57

Müller, B., Viallet, M., Heger, A., & Janka, H.-T. 2016, , 833, 124

Müller, T., Prieto, J. L., Pejcha, O., & Clocchiatti, A. 2017, , 841, 127

Müller-Bravo, T. E., Sullivan, M., Smith, M., et al. 2021, , arXiv:2110.11340

Müller-Bravo, T. E., Gutiérrez, C. P., Sullivan, M., et al. 2020, , 497, 361

Munari, U., & Zwitter, T. 1997, Astronomy and Astrophysics, 318, 269

Nakaoka, T., Kawabata, K. S., Maeda, K., et al. 2018, , 859, 78

Narlikar, J. V. 2002, An introduction to cosmology (Cambridge University Press)

Navarro, J. F., Frenk, C. S., & White, S. D. M. 1996, , 462, 563

Nomoto, K., Iwamoto, K., Nakasato, N., et al. 1997, , 621, 467

Nomoto, K., Thielemann, F. K., & Yokoi, K. 1984, , 286, 644

Nomoto, K., Uenishi, T., Kobayashi, C., et al. 2003, in From Twilight to Highlight: The Physics of Supernovae, ed. W. Hillebrandt & B. Leibundgut, 115

Nugent, P., Kim, A., & Perlmutter, S. 2002, , 114, 803

Nugent, P. E., Sullivan, M., Cenko, S. B., et al. 2011, , 480, 344

ODonnell, J. E. 1994, , 422, 158

Oke, J. B. 1965, , 3, 23

—. 1974, , 27, 21

Oke, J. B., & Gunn, J. E. 1983, , 266, 713

Oke, J. B., & Sandage, A. 1968, , 154, 21

Paatero, P., & Tapper, U. 1994, Environmetrics, 5, 111

Padmanabhan, N., Schlegel, D. J., Finkbeiner, D. P., et al. 2008, , 674, 1217

Papenkova, M., Li, W., Lotoss/Kait, et al. 2003, , 8143, 2

Park, S., & Li, W. 2004, , 8431, 2

Pastorello, A. 2012, Memorie della Societa Astronomica Italiana Supplementi, 19, 24

Pastorello, A., Zampieri, L., Turatto, M., et al. 2004, , 347, 74

Pastorello, A., Sauer, D., Taubenberger, S., et al. 2006, , 370, 1752

Pastorello, A., Smartt, S. J., Mattila, S., et al. 2007, , 447, 829

Pastorello, A., Valenti, S., Zampieri, L., et al. 2009, , 394, 2266

Pejcha, O., & Prieto, J. L. 2015, , 806, 225

Pejcha, O., & Thompson, T. A. 2012, , 746, 106

—. 2015, , 801, 90

Pereira, R., Thomas, R. C., Aldering, G., et al. 2013, , 554, A27

Perley, D. A., Fremling, C., Sollerman, J., et al. 2020, , 904, 35

Perlmutter, S., Gabi, S., Goldhaber, G., et al. 1997, , 483, 565

Perlmutter, S., Aldering, G., Goldhaber, G., et al. 1999, , 517, 565

Pesce, D. W., Braatz, J. A., Reid, M. J., et al. 2020, , 891, L1

Phillips, M. M. 1993, , 413, L105

Phillips, M. M., Lira, P., Suntzeff, N. B., et al. 1999, , 118, 1766

Piro, A. L., Chang, P., & Weinberg, N. N. 2010, , 708, 598

Planck Collaboration, Ade, P. A. R., Aghanim, N., et al. 2014a, , 571, A15

—. 2014b, , 571, A16

Planck Collaboration, Aghanim, N., Arnaud, M., et al. 2016a, , 594, A11

Planck Collaboration, Ade, P. A. R., Aghanim, N., et al. 2016b, , 594, A13

—. 2016c, , 594, A16

Planck Collaboration, Aghanim, N., Akrami, Y., et al. 2020a, , 641, A5

—. 2020b, , 641, A6

Podsiadlowski, P. 1992, , 104, 717

Popov, D. V. 1993, , 414, 712

Poznanski, D., Prochaska, J. X., & Bloom, J. S. 2012, , 426, 1465

Prentice, S. J., Mazzali, P. A., Pian, E., et al. 2016, , 458, 2973

Prentice, S. J., Ashall, C., James, P. A., et al. 2019, , 485, 1559

Pskovskii, I. P. 1977, , 21, 675

Pskovskii, Y. P. 1984, , 28, 658

Rasmussen, C. E., & Williams, C. K. I. 2006, Gaussian Processes for Machine Learning

Ren, B., Pueyo, L., Zhu, G. B., Debes, J., & Duchêne, G. 2018, , 852, 104

Rest, A., Scolnic, D., Foley, R. J., et al. 2014, , 795, 44

Richmond, M. W., Treffers, R. R., Filippenko, A. V., et al. 1994, , 107, 1022

Riess, A. G., Press, W. H., & Kirshner, R. P. 1995, , 438, L17

—. 1996, , 473, 88

Riess, A. G., Filippenko, A. V., Challis, P., et al. 1998, , 116, 1009

Riess, A. G., Kirshner, R. P., Schmidt, B. P., et al. 1999, , 117, 707

Riess, A. G., Strolger, L.-G., Tonry, J., et al. 2004, , 607, 665

Riess, A. G., Strolger, L.-G., Casertano, S., et al. 2007, , 659, 98

Riess, A. G., Rodney, S. A., Scolnic, D. M., et al. 2018, , 853, 126

Rodney, S. A., Riess, A. G., Strolger, L.-G., et al. 2014, , 148, 13

Rodríguez, Ó., Clocchiatti, A., & Hamuy, M. 2014, , 148, 107

Roy, R., Kumar, B., Benetti, S., et al. 2011, , 736, 76

Ruiz-Lapuente, P., Jeffery, D. J., Challis, P. M., et al. 1993, , 365, 728

Sahu, D. K., Anupama, G. C., Srividya, S., & Muneer, S. 2006, , 372, 1315

Sako, M., Bassett, B., Becker, A. C., et al. 2018, , 130, 064002

Salpeter, E. E. 1955, , 121, 161

Sandage, A. 1961, The Hubble Atlas of Galaxies

Sanders, N. E., Soderberg, A. M., Gezari, S., et al. 2015, , 799, 208

Sasdelli, M., Ishida, E. E. O., Hillebrandt, W., et al. 2016, , 460, 373

Saunders, C., Aldering, G., Antilogus, P., et al. 2018, , 869, 167

Scalzo, R. A., Aldering, G., Antilogus, P., et al. 2010, , 713, 1073

Schlafly, E. F., & Finkbeiner, D. P. 2011, , 737, 103

Schlafly, E. F., Finkbeiner, D. P., Jurić, M., et al. 2012, , 756, 158

Schlegel, D. J., Finkbeiner, D. P., & Davis, M. 1998, , 500, 525

Schlegel, E. M. 1990, , 244, 269

Schuecker, P., Böhringer, H., Collins, C. A., & Guzzo, L. 2003, , 398, 867

Schultz, G. V., & Wiemer, W. 1975, , 43, 133

Scolnic, D., & Kessler, R. 2016, , 822, L35

Scolnic, D., Rest, A., Riess, A., et al. 2014, , 795, 45

Scolnic, D., Casertano, S., Riess, A., et al. 2015, , 815, 117

Scolnic, D. M., Lochner, M., Gris, P., et al. 2018a, arXiv e-prints, arXiv:1812.00516

Scolnic, D. M., Jones, D. O., Rest, A., et al. 2018b, , 859, 101

Seitenzahl, I. R., & Townsley, D. M. 2017, Nucleosynthesis in Thermonuclear Supernovae, ed. A. W. Alsabti & P. Murdin (Cham: Springer International Publishing), 1–24

Shappee, B. J., Prieto, J. L., Grupe, D., et al. 2014, , 788, 48

Shivvers, I., Modjaz, M., Zheng, W., et al. 2017, , 129, 054201

Shussman, T., Nakar, E., Waldman, R., & Katz, B. 2016, arXiv e-prints, arXiv:1602.02774

Sim, S. A., Röpke, F. K., Hillebrandt, W., et al. 2010, , 714, L52

Smartt, S. J. 2009, , 47, 63

—. 2015, , 32, e016

Smartt, S. J., Valenti, S., Fraser, M., et al. 2015, , 579, A40

Smith, J. A., Tucker, D. L., Kent, S., et al. 2002, , 123, 2121

Smith, M., D'Andrea, C. B., Sullivan, M., et al. 2020, , 160, 267

Sollerman, J., Mörtsell, E., Davis, T. M., et al. 2009, , 703, 1374

Spiro, S., Pastorello, A., Pumo, M. L., et al. 2014, , 439, 2873

Stritzinger, M. D., Phillips, M. M., Boldt, L. N., et al. 2011, , 142, 156

Sukhbold, T., Ertl, T., Woosley, S. E., Brown, J. M., & Janka, H. T. 2016, , 821, 38

Sullivan, M., Conley, A., Howell, D. A., et al. 2010, , 406, 782

Sumiyoshi, K. 2002, Progress of Theoretical Physics Supplement, 146, 258

Suzuki, N., Rubin, D., Lidman, C., et al. 2012, , 746, 85

Taddia, F., Stritzinger, M. D., Bersten, M., et al. 2018, , 609, A136

Takáts, K., Pumo, M. L., Elias-Rosa, N., et al. 2014, , 438, 368

Tammann, G. A., & Leibundgut, B. 1990, , 236, 9

Terry, J. N., Paturel, G., & Ekholm, T. 2002, , 393, 57

Theureau, G., Rauzy, S., Bottinelli, L., & Gouguenheim, L. 1998, , 340, 21

Thielemann, F.-K., Nomoto, K., & Hashimoto, M.-A. 1996, , 460, 408

Thorp, S., Mandel, K. S., Jones, D. O., Ward, S. M., & Narayan, G. 2021, arXiv e-prints, arXiv:2102.05678

Tomasella, L., Cappellaro, E., Fraser, M., et al. 2013, , 434, 1636

Tomasella, L., Cappellaro, E., Pumo, M. L., et al. 2018, , 475, 1937

Tonry, J. L., Schmidt, B. P., Barris, B., et al. 2003, , 594, 1

Tripp, R. 1998, , 331, 815

Tröster, T., Sánchez, A. G., Asgari, M., et al. 2020, , 633, L10

Trumpler, R. J. 1930, , 42, 214

Turatto, M., Benetti, S., & Cappellaro, E. 2003, in From Twilight to Highlight: The Physics of Supernovae, ed. W. Hillebrandt & B. Leibundgut, 200

Turatto, M., Mazzali, P. A., Young, T. R., et al. 1998, , 498, L129

Tytgat, M. H. G. 2009, 52 p

Ugliano, M., Janka, H.-T., Marek, A., & Arcones, A. 2012, , 757, 69

Utrobin, V. P., & Chugai, N. N. 2009, , 506, 829

Utrobin, V. P., Chugai, N. N., & Pastorello, A. 2007, , 475, 973

Valenti, S., Sand, D., Pastorello, A., et al. 2014, , 438, L101

Valenti, S., Howell, D. A., Stritzinger, M. D., et al. 2016, , 459, 3939

Van Dyk, S. D., Davidge, T. J., Elias-Rosa, N., et al. 2012, , 143, 19

Vincenzi, M., Sullivan, M., Firth, R. E., et al. 2019, , 489, 5802

Wang, B., Meng, X.-C., Wang, X.-F., & Han, Z.-W. 2008, , 8, 71

Waxman, E., & Katz, B. 2017, Shock Breakout Theory, ed. A. W. Alsabti & P. Murdin, 967

Waxman, E., Mészáros, P., & Campana, S. 2007, , 667, 351

Webbink, R. F. 1984, , 277, 355

Wheeler, J. C., & Harkness, R. P. 1990, Reports on Progress in Physics, 53, 1467

Whelan, J., & Iben, Icko, J. 1973, , 186, 1007

White, S. D. M., Navarro, J. F., Evrard, A. E., & Frenk, C. S. 1993, , 366, 429

Wong, K. C., Suyu, S. H., Chen, G. C. F., et al. 2020, , 498, 1420

Woosley, S. E., Arnett, W. D., & Clayton, D. D. 1973, , 26, 231

Woosley, S. E., Heger, A., & Weaver, T. A. 2002, Reviews of Modern Physics, 74, 1015

Woosley, S. E., Pinto, P. A., & Hartmann, D. 1989, , 346, 395

Woosley, S. E., Taam, R. E., & Weaver, T. A. 1986, , 301, 601

Woosley, S. E., & Weaver, T. A. 1995, The Astrophysical Journal Supplement Series, 101, 181

Yadav, N., Müller, B., Janka, H. T., Melson, T., & Heger, A. 2020, , 890, 94

Yaron, O., & Gal-Yam, A. 2012, , 124, 668

Zampieri, L., Pastorello, A., Turatto, M., et al. 2003, , 338, 711

Zhang, J., Wang, X., Mazzali, P. A., et al. 2014, , 797, 5

Zhu, G., & Ménard, B. 2013, , 770, 130

Zwicky, F. 1933, Helvetica Physica Acta, 6, 110

Zwicky, F. 1965, in Stellar Structure - Stars and Stellar Systems, ed. L. H. Aller & D. B. McLaughlin, 367